

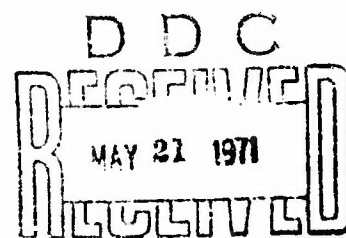
AD723343

Bulletin 40
Part 4
(of 7 Parts)

THE SHOCK AND VIBRATION BULLETIN

DECEMBER 1969

A Publication of
THE SHOCK AND VIBRATION
INFORMATION CENTER
Naval Research Laboratory, Washington, D.C.



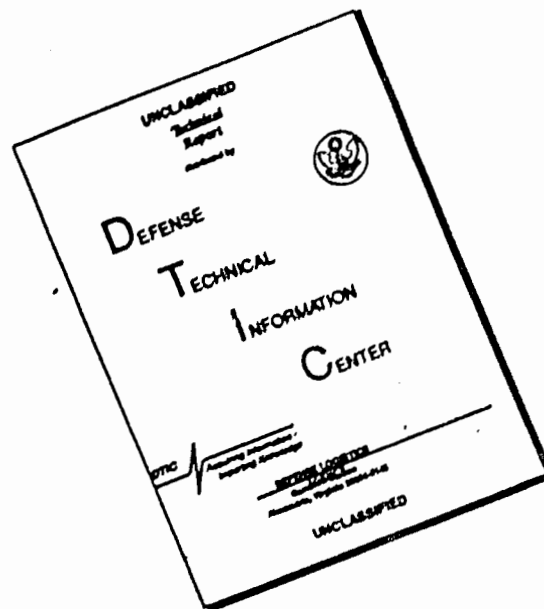
Office of
The Director of Defense
Research and Engineering

This document has been approved for public release and sale; its distribution is unlimited.

Reproduced by
NATIONAL TECHNICAL
INFORMATION SERVICE
Springfield, Va. 22151

243

DISCLAIMER NOTICE



THIS DOCUMENT IS BEST QUALITY AVAILABLE. THE COPY FURNISHED TO DTIC CONTAINED A SIGNIFICANT NUMBER OF PAGES WHICH DO NOT REPRODUCE LEGIBLY.

APPROVED BY	
DATE	WHITE SECTION <input checked="" type="checkbox"/>
DOE	DIFF SECTION <input type="checkbox"/>
UNCLASSIFIED	<input type="checkbox"/>
JUSTIFICATION	
BY	
DISTRIBUTION/AVAILABILITY CODES	
DISC.	AVAIL. NO. OF SPECIAL
A	21

SYMPOSIUM MANAGEMENT

THE SHOCK AND VIBRATION INFORMATION CENTER

William W. Mutch, Director
 Henry C. Pusey, Coordinator
 Rudolph H. Volin, Coordinator
 Edward H. Schell, Coordinator
 Katherine G. Jahnel, Clerk Typist

Bulletin Production

Graphic Arts Branch, Technical Information Division,
 Naval Research Laboratory

BLANK PAGES
 DELETED
 FROM
 DOCUMENT

Bulletin 40
Part 4
(of 7 Parts)

THE SHOCK AND VIBRATION BULLETIN

DECEMBER 1969

**A Publication of
THE SHOCK AND VIBRATION
INFORMATION CENTER
Naval Research Laboratory, Washington, D.C.**

The 40th Symposium on Shock and Vibration was held at the Chamberlin Hotel, Fort Monroe, Virginia and the NASA Langley Research Center, Hampton, Virginia, on 21-23 October 1969. The National Aeronautics and Space Administration was host.

**Office of
The Director of Defense
Research and Engineering**

CONTENTS

PART 4

Dynamics

FURTHER COMPARISONS OF CONSISTENT MASS MATRIX SCHEMES	1
R. M. Mains, Washington University, St. Louis, Missouri	
SHOCK SPECTRA FOR STATISTICALLY MODELLED STRUCTURES	17
R. H. Lyon, Bolt Beranek and Newman Inc., Cambridge, Massachusetts	
REVIEW OF MODAL SYNTHESIS TECHNIQUES AND A NEW APPROACH	25
S. Hou, Bellcomm, Inc., Washington, D. C.	
ROTATING ELEMENTS IN THE DIRECT STIFFNESS METHOD OF DYNAMIC ANALYSIS WITH EXTENSIONS TO COMPUTER GRAPHICS	41
M. E. Novak, The Boeing Company, Vertol Division, Philadelphia, Pennsylvania	
DYNAMIC RESPONSE OF BEAMS TO MOVING PRESSURE LOADS AS RELATED TO TRACKED AIR CUSHION VEHICLES	47
J. F. Wilson, Duke University, Durham, North Carolina	
*THE DESIGN OF A STRUCTURAL MEMBER ANALYSIS PROGRAM FOR AN INTERACTIVE COMPUTER SYSTEM	63
W. D. Pilkey, University of Virginia, Charlottesville, Virginia, and R. Nielsen and M. Steler, COM/CODE Corporation, Washington, D. C.	
*DYNAMIC RESPONSE OF A SINGLE-DEGREE-OF-FREEDOM ELASTIC-PLASTIC SYSTEM SUBJECTED TO A HALF SINE PULSE	67
M. Wohltmann, Martin Marietta Corporation, Orlando, Florida	
*PROPAGATION OF YIELDING IN A BILINEAR HYSTERETIC BEAM AND DISTRIBUTED FOUNDATION UNDER DYNAMIC PULSE LOADING	81
J. R. Mays, University of Colorado, Denver, Colorado	
PLASTIC MODELS FOR DYNAMIC STRUCTURAL ANALYSIS	89
W. A. Elliott, Chevrolet Division, GMC, Detroit, Michigan	
FATIGUE DESIGN OF ELECTRONIC EQUIPMENT	97
L. W. Root, Collins Radio Company, Cedar Rapids, Iowa	
MODEL STUDIES TO DETERMINE LOW-FREQUENCY NOISE REDUCTION OF SPACECRAFT	103
A. W. Mueller, NASA Langley Research Center, Hampton, Virginia	
*COMBUSTION INSTABILITY TESTS OF THE SATURN IB FIRST STAGE	109
W. S. Parker, Chrysler Corporation, New Orleans, Louisiana	
DYNAMIC ANALYSIS OF A HIGH-SPEED LINKLESS AMMUNITION CONVEYOR SYSTEM	115
C. B. Basye and B. R. Scheller, Emerson Electric Company, St. Louis, Missouri	

*This paper not presented at Symposium.

STRESS WAVES IN MULTILAYERED CYLINDERS AND CONICAL FRUSTUMS	127
J. C. S. Yang and A. E. Seigel, Naval Ordnance Laboratory, Silver Spring, Maryland	
CAVITY EFFECT ON PANEL FLUTTER - JUST HOW SIGNIFICANT?	139
N. H. Zimmerman and C. E. Lemley, McDonnell Aircraft Company, St. Louis, Missouri	
AN EIGENVALUE PROBLEM SOLUTION OF A THREE-DIMENSIONAL PIPING SYSTEM	147
P. Bezler, Brookhaven National Laboratory, Upton, New York, and J. R. Curreri, Polytechnic Institute of Brooklyn, Brooklyn, New York	
DESIGN MODEL BASED ON OBSERVED MODES OF VIBRATION OF AUSTRALIAN CSIRO 210-FT RADIO TELESCOPE	155
J. A. Macinante, CSIRO, National Standards Laboratory, Sydney, Australia	
UPPER AND LOWER BOUNDS TO TORSIONAL FREQUENCIES OF NONUNIFORM SHAFTS AND APPLICATIONS TO MISSILES	163
N. Rubinstein, V. G. Sigillito and J. T. Stadter, Applied Physics Laboratory, JHU, Silver Spring, Maryland	
*DETERMINATION OF DYNAMIC LOADS AND RESPONSE OF A SPACE VEHICLE USING FLIGHT DATA	171
S. Hou, Bellcomm, Inc., Washington, D. C.	
*STIFFNESS MATRIX OF A BEAM-COLUMN INCLUDING SHEAR DEFORMATION	187
H. Saunders, General Electric Company, Philadelphia, Pennsylvania	
*LIQUID-STRUCTURE COUPLING IN CURVED PIPES	197
L. C. Davidson and J. E. Smith, Naval Ship Research and Development Laboratory, Annapolis, Maryland	
*DISTRIBUTION OF EIGENVALUES IN CONICAL SHELLS,	209
D. K. Miller and F. D. Hart, North Carolina State University, Raleigh, North Carolina	
*DYNAMIC RESPONSE OF STRUCTURAL SHIELD TO A TRAVELING PRESSURE PULSE	217
A. M. Rodriguez and P. N. Mathur, Aerospace Corporation, San Bernardino, California	
*ANALYSIS OF THE RELATIVE MOTION OF THE PEM MOD-IV TETHERED CANISTER AND THE ATLAS BOOSTER	225
T. L. Alley, Aerospace Corporation, San Bernardino, California	

PART 1

CLASSIFIED

(Unclassified Titles)

EFFECT OF EQUIPMENT MASS ON THE SHOCK MOTIONS OF DECKS

E. A. Thornton, Naval Ship Research and Development Center, Portsmouth,
Virginia

CORRELATION OF A RESULTANT VELOCITY CHANGE TO AN UNDERWATER EXPLOSION FORCING-FUNCTION

W. F. Peete, Jr., Naval Undersea Research and Development Center, Pasadena,
California

*This paper not presented at Symposium.

PREDICTION OF THE TRANSIENT RESPONSE OF A CYLINDRICAL ELASTIC SHELL TO SPHERICAL UNDERWATER SHOCK WAVES BY THE ACOUSTIC WAVE-SHELL INTERACTION THEORY

H. Huang and Y. F. Wang, Naval Ship Research and Development Laboratory, Annapolis, Maryland

STRUCTURAL EVALUATION OF SHIPBOARD WEAPON SYSTEMS--NSRDC PARTICIPATION IN OPERATION PRAIRIE FLAT

L. R. Hill, Jr., Naval Ship Research and Development Center, Washington, D. C.

THE RESPONSE OF WHIP ANTENNAS TO AIR BLAST

W. E. Gilbert, Naval Ship Research and Development Center, Washington, D. C.

THE EFFECT OF LIQUIDS ON THE DYNAMIC MOTIONS OF IMMERSED SOLIDS

R. J. Fritz, General Electric Company, Schenectady, New York

SHOCK LOADING AND RESPONSE OF HELICOPTER STRUCTURES DUE TO WEAPON BLAST

P. A. Cox, W. E. Baker, S. Silverman, and P. S. Westine, Southwest Research Institute, San Antonio, Texas

THE RESPONSE OF LONG WIRE ROPE ANTENNAS TO AIR BLAST

W. R. Conley, Naval Ship Research and Development Center, Washington, D. C.

***BUILDING BLOCK APPROACH TO MULTI-MASS THREE DIMENSIONAL SHOCK AND VIBRATION ANALYSIS OF SHIPBOARD EQUIPMENT (D-DAM)**

M. R. Kulina and J. P. Wilson, Curtiss-Wright Corporation, Wood-Ridge, New Jersey

PART 2

Shock

AN EXPERIMENTAL APPROACH TO UNDERSTANDING SHOCK RESPONSE

M. W. Oleson, Naval Research Laboratory, Washington, D. C.

EXPLOSIVE SHOCK

W. H. Roberts, Martin Marietta Corporation, Orlando, Florida

MODAL VELOCITY AS A CRITERION OF SHOCK SEVERITY

H. A. Gaberson, Naval Civil Engineering Laboratory, Pt. Hueneme, California, and R. H. Chalmers, Naval Electronics Laboratory Center, San Diego, California

THE SIMULTANEOUS APPLICATION OF TRANSIENT AND STEADY STATE DYNAMIC EXCITATIONS IN A COMBINED ENVIRONMENT TEST FACILITY SIMULATING SHIPBOARD ENVIRONMENTS

T. B. Jones, Jr., Hughes Aircraft Company, Fullerton, California

***PERIODIC SHOCK EXCITATION OF ELASTIC STRUCTURES**

D. Krajcinovic, Ingersoll-Rand Research Inc., Princeton, New Jersey, and G. Herrmann, Northwestern University, Evanston, Illinois

SHOCK ANALYSIS OF FLUID SYSTEMS USING ACOUSTIC IMPEDANCE AND THE FOURIER TRANSFORM: APPLICATION TO WATERHAMMER PHENOMENA

A. A. Winquist, Norton AFB, San Bernardino, California, and R. C. Binder, University of Southern California, Los Angeles, California

*This paper not presented at Symposium.

- DRAG ON FREE FLIGHT CYLINDERS IN A BLAST WAVE**
S. B. Mellsen, Defense Research Establishment Suffield, Alberta, Canada
- ANALYTICAL AND EXPERIMENTAL RESULTS OF LATTICE TYPE STRUCTURES
SUBJECTED TO A BLAST LOADING**
R. Geminder, Mechanics Research, Inc., Los Angeles, California
- *LATERAL RESPONSE OF SLIGHTLY CURVED COLUMNS UNDER LONGITUDINAL
PULSE LOAD**
T. L. Anderson, University of Idaho, Moscow, Idaho, and M. L. Moody,
University of Colorado, Denver, Colorado
- RESPONSES OF AIRCRAFT STRUCTURES SUBJECTED TO BLAST LOADING**
N. M. Isada, R. K. Koegler and D. O. Bliven, Cornell Aeronautical Laboratory,
Inc., Buffalo, New York
- PREDICTION OF BLAST-VALVE RESPONSE USING MODELS**
R. G. McCoy, G. Nevruinean and E. F. Witt, Bell Telephone Laboratories,
Whippany, New Jersey
- *TESTING THE RESPONSE OF GAS TURBINES TO AIR BLAST**
J. C. Muirhead, R. Naylor and C. G. Coffey, Defense Research Establishment
Suffield, Alberta, Canada
- TRANSIENT WAVEFORM CONTROL OF ELECTROMAGNETIC VIBRATION TEST
EQUIPMENT**
J. D. Favour and J. M. LeBrun, The Boeing Company, Seattle, Washington,
and J. P. Young, NASA Goddard Space Flight Center, Greenbelt, Maryland
- AN IMPROVED ELECTRODYNAMIC SHAKER SHOCK TECHNIQUE**
J. R. Moser and D. Garner, Texas Instruments Inc., Dallas, Texas
- PROTUBERANCE EFFECTS ON LIMITER-EQUIPPED HARD LANDING
PAYLOADS**
J. L. McCarty and J. T. Howlett, NASA Langley Research Center, Hampton,
Virginia
- IMPACT TESTS OF NUCLEAR FUEL MATRICES USING A VACUUM TUBE
LAUNCHER**
H. W. Nunez, Sandia Corporation, Albuquerque, New Mexico
- DEVELOPMENT OF 100,000 G TEST FACILITY**
R. L. Bell, Endevco Corporation, Pasadena, California
- *ON THE INTERPRETATION AND APPLICATION OF SHOCK TEST RESULTS IN
ENGINEERING DESIGNS**
Chi-Hung Mok, General Electric Company, Philadelphia, Pennsylvania
- METHODS OF COMPUTING STRUCTURAL RESPONSE OF HELICOPTERS TO
WEAPONS' MUZZLE AND BREECH BLAST**
W. E. Baker, S. Silverman, P. A. Cox, Jr., and D. Young, Southwest Research
Institute, San Antonio, Texas
- SHOCK TESTING FOR EQUIPMENT IN PROTECTIVE STRUCTURES**
M. M. Dembo and C. C. Huang, U. S. Army Engineer Division, Huntsville,
Alabama

*This paper not presented at Symposium.

PART 3

Vibration

ANALYSIS OF RANDOM RESPONSES FOR CALCULATION OF FATIGUE DAMAGE

C. C. Osgood, RCA Astro-Electronics Division, Princeton, New Jersey

VIBRATION TRENDS ANALYSIS

A. Y. Edelberg, The Boeing Company, Washington, D. C.

THE RADIATION RESISTANCE OF CYLINDRICAL SHELLS EXHIBITING AXISYMMETRIC MODE SHAPES

C. J. Runkle, Chemstrand Research Center, Durham, North Carolina, and
F. D. Hart, North Carolina State University, Raleigh, North Carolina

MODEL SENSITIVITY STUDY OF A CONICAL REENTRY VEHICLE TO AERODYNAMICALLY INDUCED ACOUSTIC LOADING

L. E. Chaump and J. K. Merchant, General Electric Company, Philadelphia,
Pennsylvania

ACOUSTIC RESPONSE OF A SPACECRAFT SOLAR PANEL USING NORMAL MODE METHOD

A. Stroeve, TRW Systems Group, Redondo Beach, California

COMPUTER PROGRAMS FOR PREDICTION OF STRUCTURAL VIBRATIONS DUE TO FLUCTUATING PRESSURE ENVIRONMENTS

T. N. Lee and W. L. Swanson, Chrysler Corporation Space Division, Huntsville,
Alabama

MODAL DENSITIES OF SPHERICAL SHELLS

H. Kunieda, NASA Ames Research Center, Moffett Field, California

PREDICTION OF INTERFACE RANDOM AND TRANSIENT ENVIRONMENTS THROUGH THE USE OF MECHANICAL IMPEDANCE CONCEPTS

G. K. Jones and F. J. On, NASA Goddard Space Flight Center, Greenbelt, Maryland

***FACTORS OF SAFETY FOR UNMANNED SPACECRAFT STRUCTURES**

S. M. Kaplan, General Electric Company, Philadelphia, Pennsylvania

***RESPONSE OF RECTANGULAR PLATES TO MOVING LOADS BY A FINITE ELEMENT PROCEDURE**

S. K. Danile, University of Baroda, Baroda, India, and L. J. Feser,
University of Colorado, Boulder, Colorado

***VIBRATORY RESPONSE OF PRINTED CIRCUIT BOARDS**

N. M. Isada, State University of New York, Buffalo, New York, and J. C. Shear,
Eastman Kodak Company, Rochester, New York

***NONLINEAR PARAMETRIC RESPONSE OF PLATES UNDER RANDOM LOADS**

T. P. Shyu and J. H. Somerset, Syracuse University, Syracuse, New York

***VIBRATION OF CELLULAR CYLINDRICAL SHELLS**

M. C. Patel, Brown Engineering Company, Huntsville, Alabama, and S. I. Hayek,
Pennsylvania State University, University Park, Pennsylvania

***ANALYSIS OF SINUSOIDAL AND RANDOM VIBRATION ENERGIES**

J. N. Tait, Naval Air Development Center, Johnsville, Pennsylvania

*This paper not presented at Symposium.

APOLLO LUNAR MODULE VIBRATIONS DURING FLIGHT AND GROUND TESTS

W. D. Dorland and J. D. Johnston, Jr., NASA Manned Spacecraft Center, Houston, Texas

STRUCTURAL QUALIFICATION OF THE ORBITING ASTRONOMICAL OBSERVATORY
W. B. Keegan, NASA Goddard Space Flight Center, Greenbelt, Maryland

THE ENVIRONMENTAL TESTING OF EXPLOSIVE STORES IN THE UNITED KINGDOM

C. Higham, Ordnance Board, London England, and D. A. E. Carter, Environmental Test Center, Foulness, England

A UNIQUE MODEL, SUSPENSION, AND EXCITATION SYSTEM FOR LAUNCH VEHICLE DYNAMICS STUDIES

J. Pearson and B. J. Gambucci, NASA Ames Research Center, Moffett Field, California

LOAD APPLICATION AND CONTROL SYSTEMS UTILIZED TO SIMULATE COMBINED LOADS ENVIRONMENT FOR SATURN V - APOLLO SPACECRAFT

G. D. Shipway, Wyle Laboratories, Norco, California

IMPEDANCE SIMULATION VIBRATION TEST FIXTURES FOR SPACECRAFT TESTS

T. D. Scharton, Bolt Beranek and Newman Inc., Van Nuys, California

VIBRATION ANALYSIS OF AN INERTIAL REFERENCE UNIT

B. M. Ishino, Autonetics, Anaheim, California

***PULSED-RANDOM VIBRATION TESTING**

H. L. Stewart, McDonnell Aircraft Company, St. Louis, Missouri

***AXIAL RESPONSE OF A HIGH-SPEED, GAS-LUBRICATED, ROTOR-BEARING ASSEMBLY TO SHOCK AND VIBRATION**

P. R. Spencer and P. W. Curwen, Mechanical Technology, Inc., Latham, New York, and H. B. Tryon, NASA Lewis Research Center, Cleveland, Ohio

MULTI-ENVIRONMENT TEST SYSTEM FOR SEQUENTIAL TIMERS

V. G. Ames, U. S. Army Frankford Arsenal, Philadelphia, Pennsylvania

***ON THE SELF EXCITED VIBRATIONS OF A CIRCULAR CYLINDER IN UNIFORM FLOW**

D. W. Sallet, University of Maryland, College Park, Maryland

PART 5

Damping and Isolation

REDUCTION OF VIBRATIONS IN AEROSPACE STRUCTURES BY ADDITIVE DAMPING

D. I. G. Jones and J. P. Henderson, Air Force Materials Laboratory, Wright-Patterson AFB, Ohio, and A. D. Nashif, University of Dayton, Dayton, Ohio

VIBRATION ISOLATION WITH NONLINEAR DAMPING

J. E. Ruzicka and T. F. Derby, Barry Controls, Watertown, Massachusetts

*This paper not presented at Symposium.

THE CONTROL OF VIBRATIONS WITH VISCOELASTIC MATERIALS

P. Grootenhuis, Imperial College of Science and Technology, London, England

SONIC FATIGUE RESISTANCE OF STRUCTURES INCORPORATING A CONSTRAINED VISCOELASTIC CORE

M. D. Lamoree and W. L. LaBarge, Lockheed-California Company, Burbank, California

EXPERIMENTS ON INELASTIC DAMPING OF SPACE VEHICLE DUCTS

G. E. Bowie, W. A. Compton and J. V. Long, Solar Division of International Harvester Company, San Diego, California

TRANSVERSE VIBRATIONS OF LAMINATED PLATES WITH VISCOELASTIC LAYER DAMPING

F. Abdulhadi, IBM Corporation, Rochester, Minnesota

COMPARISON OF THE GEIGER THICK PLATE TEST AND THE VIBRATING COMPOSITE BEAM TEST FOR THE EVALUATION OF THE EFFECTIVENESS OF VIBRATION DAMPING MATERIALS

D. R. Blenner, Lord Manufacturing Company, Erie, Pennsylvania, and
T. J. Dudek, General Tire and Rubber Company, Akron, Ohio

AN AEROSPACE ENERGY ABSORBER APPLIED TO HIGHWAY SAFETY

W. E. Woolam, Southwest Research Institute, San Antonio, Texas

***DETERMINATION OF THE COMPLEX MOBILITY AND IMPEDANCE MATRICES FOR DAMPED LUMPED PARAMETER LINEAR DYNAMIC SYSTEMS**

J. J. Engblom, Hughes Aircraft Company, Culver City, California

'WAGGING TAIL' VIBRATION ABSORBER

R. G. Barclay and P. W. Humphrey, NASA Goddard Space Flight Center, Greenbelt, Maryland

A SIMPLE DEVICE FOR ATTENUATION OF LONGITUDINAL ELASTIC STRESS WAVES

J. P. O'Neill and C. J. Tirman, TRW Systems Group, Redondo Beach, California

ANALYSIS OF SHOCK MITIGATION FOR GLASS SUBMERSIBLES

J. C. S. Yang, Naval Ordnance Laboratory, Silver Spring, Maryland

REDUCTION IN VIBRATION OF THE CH-47C HELICOPTER USING A VARIABLE TUNING VIBRATION ABSORBER

J. J. O'Leary, The Boeing Company, Philadelphia, Pennsylvania

RESPONSE AND OPTIMIZATION OF AN ISOLATION SYSTEM WITH RELAXATION TYPE DAMPING

T. F. Derby and P. C. Calcaterra, Barry Controls, Watertown, Massachusetts

THE RESPONSE OF MECHANICAL SHOCK ISOLATION ELEMENTS TO HIGH RATE INPUT LOADING

R. L. Eshleman and P. N. Rao, IIT Research Institute, Chicago, Illinois

RATIONAL ANALYSIS OF A TWO-DEGREE-OF-FREEDOM FLEXURE-TORSION SYSTEM FOR REDUCTION OF CERTAIN TYPES OF FLUTTER

M. J. Klep, North American Rockwell Corporation, Los Angeles, California, and R. C. Binder, University of Southern California Los Angeles, California

*This paper not presented at Symposium.

**DESIGN AND DEVELOPMENT OF A SHOCK ISOLATION EVALUATION SYSTEM
FOR HIGH RATE INPUT LOADING**

P. N. Rao and K. E. Hofer, IIT Research Institute, Chicago, Illinois

***A STUDY OF AMPLITUDE FREQUENCY PLOTS WITH NONLINEAR DAMPING**

G. F. Brammeier, Brown Engineering Company, Huntsville, Alabama

VIBRATIONS OF MULTICORE SANDWICH BEAMS

V. P. Roske, Jr., Air Force Missile Development Center, Holloman AFB,
New Mexico, and C. W. Bert, University of Oklahoma, Norman, Oklahoma

***THE USE OF POLYURETHANE FOAM FOR SHOCK AND VIBRATION ISOLATION
OF AVIONICS COMPONENTS**

W. E. Arthur and T. Carreil, North American Rockwell Corporation, Los
Angeles, California, and J. Nirschl, U. S. Army Electronics Command,
Ft. Monmouth, New Jersey

***THE ANALYTIC MODELING OF OPEN-CELL FOAMS AS SHOCK AND VIBRATION
ELEMENTS**

T. Liber, IIT Research Institute, Chicago, Illinois, and H. Epstein, University
of Minnesota, Minneapolis, Minnesota

PART 6

Transportation

SIMULATION OF DYNAMIC LOADS ON EJECTED MISSILES

C. R. Perry, The Boeing Company, Seattle, Washington

**WIND TUNNEL SIMULATION OF FLIGHT VIBRATION AND ACOUSTIC LEVELS ON
AN EXTERNAL STORE**

K. A. Herzing and S. N. Schwantes, Honeywell Inc., Hopkins, Minnesota

A METHOD TO SIMULATE GUNFIRE INDUCED VIBRATION ENVIRONMENT

J. A. Hutchinson and R. N. Hancock, LTV Aerospace Corporation, Dallas, Texas

**THE SHOCK AND VIBRATION EXPERIENCED BY NAVAL AVIONICS DURING
ARRESTED LANDING**

V. M. Foxwell, Jr., Westinghouse Aerospace Division, Baltimore, Maryland

**A SURVEY OF PRACTICAL PROBLEMS ENCOUNTERED IN REPRODUCING THE
CAPTIVE FLIGHT ENVIRONMENT BY MEANS OF SHAKERS AND SHOCK TEST
MACHINES**

W. Tustin, Tustin Institute of Technology, Inc., Santa Barbara, California

**STANDARD ARM CAPTIVE CARRY LIFE EXPECTANCY PREDICTION AND
VIBRATION QUALIFICATION TESTING**

B. N. Downing, General Dynamics Corporation, Pomona, California

RAILROAD TRANSPORTABILITY CRITERIA

R. Kennedy, U. S. Army Transportation Engineering Agency, Ft. Eustis, Virginia

**MEASURED VIBRATION RIDE ENVIRONMENTS OF A STOL AIRCRAFT AND A
HIGH-SPEED TRAIN**

J. J. Catherines, NASA Langley Research Center, Hampton, Virginia

THRESHOLD-TYPE RECORDERS

L. J. Pursifull, U. S. Army Transportation Engineering Agency, Ft. Eustis,
Virginia

*This paper not presented at Symposium.

RAIL VEHICLE DYNAMIC STUDIES

J. L. Sewall, R. V. Parrish and B. J. Durling, NASA Langley Research Center,
Hampton, Virginia

A PROCEDURE FOR DETERMINING DAMAGE BOUNDARIES

J. W. Goff and S. R. Pierce, Michigan State University, School of Packaging,
East Lansing, Michigan

**EVALUATION OF A FRAGILITY TEST METHOD AND SOME PROPOSALS FOR
SIMPLIFIED METHODS**

E. H. Schell, Shock and Vibration Information Center, Washington, D. C.

PANEL DISCUSSION ON FRAGILITY

PART 7

Instrumentation and Data Analysis

**THE RESPONSE OF TRANSDUCERS TO THEIR ENVIRONMENT: THE PROBLEM
OF SIGNAL AND NOISE**

P. K. Stein, Arizona State University, Tempe, Arizona

**A SIMPLIFIED METHOD FOR MEASURING STATIC AND DYNAMIC DISPLACEMENT
OF VIBRATING SYSTEMS**

P. T. JaQuay, Air Force Flight Dynamics Laboratory, Wright-Patterson AFB,
Ohio

**INSTRUMENTATION FOR MEASUREMENT OF VIBRATORY MOTION AND MECHANICAL
IMPEDANCE WITHIN ASSEMBLED AEROSPACE EQUIPMENT**

C. T. Morrow, LTV Research Center, Anaheim, California

**APPLICATIONS OF HOLOGRAPHY TO HIGH-FREQUENCY VIBRATIONS AND
TRANSIENT RESPONSE**

R. Aprahamian and D. A. Evensen, TRW Systems Group, Redondo Beach, California

LOW-FREQUENCY PORTABLE VIBRATION MEASURING AND RECORDING SYSTEM

S. A. Clevenson, D. J. Martin and A. C. Dibble, NASA Langley Research Center,
Hampton, Virginia

MEASUREMENT OF THE TOTAL STRUCTURAL MOBILITY MATRIX

J. E. Smith, Naval Ship Research and Development Laboratory, Annapolis,
Maryland

***DEVELOPMENT OF A SMALL TRANSMITTER FOR HIGH INTENSITY SHOCK
ENVIRONMENT**

E. L. Kirkley, Radiation Inc., Melbourne, Florida

PREDICTABLE SHOCK PULSE BY MODIFIED FOURIER TRANSFORMS

C. W. Young, Johnson-Williams Division, Bacharach Instrument Company,
Mountain View, California

**ON-LINE COMPUTER APPLICATIONS FOR THE APOLLO 'SHORT-STACK'
COMBINED ENVIRONMENTS TEST PROGRAM**

D. J. Bozich, Wyle Laboratories, Huntsville, Alabama

DYNAMIC DATA ANALYSIS SYSTEM

M. O. Michelich, The Boeing Company, Seattle, Washington

*This paper not presented at Symposium.

***A DYNAMIC DATA COMPENSATION TECHNIQUE FOR SEISMIC TRANSDUCERS**
G. L. Schulz and W. E. Baker, University of New Mexico, Albuquerque,
New Mexico

**AIR DAMPED HIGH-G ACCELEROMETER AND WIDE BAND VELOCIMETER FOR
SHOCK STUDY IN FREE MASS UNDER SEVERE AIR BLAST**
Y. T. Li and S. Y. Lee, Massachusetts Institute of Technology, Cambridge,
Massachusetts

Ship Shock

**A SURVEY OF THE INFORMATION NEEDS OF INDUSTRY IN DESIGNING TO MEET
NAVY SHIPBOARD SHOCK REQUIREMENTS**
H. C. Pusey, Shock and Vibration Information Center, Washington, D. C.

**A CONVERSATIONAL TIMESHARING COMPUTER PROGRAM FOR DYNAMIC
SHOCK ANALYSIS**
B. A. Bott, General Electric Company, Groton, Connecticut, and R. G. Gauthier,
General Dynamics Corporation, Groton, Connecticut

CRITERIA FOR MODE SELECTION IN THE DDAM PROCEDURE
M. Pakstys, Jr., General Dynamics Corporation, Groton, Connecticut

**APPLICATION OF PERTURBATION TECHNIQUES TO THE NAVY'S DYNAMIC
DESIGN ANALYSIS METHOD**
J. T. Higney, Gibbs & Cox, Inc., New York, New York

AN ANALYSIS OF SPECTRUM DIP IN UNDERWATER SHOCK
R. J. Scavuzzo and D. D. Raftopoulos, The University of Toledo, Toledo, Ohio

DYNAMIC ANALYSIS OF SUBMERGED SHIP STRUCTURE AND EQUIPMENT
D. B. Ehrenpreis, David Ehrenpreis Consulting Engineers, New York, New York

DYNAMIC BEHAVIOR OF PARTIALLY CONSTRAINED SHIP GRILLAGES
C. S. Smith, Naval Construction Research Establishment, Dunfermline, Fife,
Scotland, and D. Faulkner, British Navy Staff, Washington, D. C.

***AN ENVIRONMENTAL VIBRATION RECORDER**
R. E. Schauer and W. P. Foster, Naval Ship Research and Development Center,
Washington, D. C.

***2K SYSTEM APPROACH FOR VIBRATION AND SHOCK PROTECTION FOR
SHIPBOARD EQUIPMENTS**
C. M. Salerno, Barry Controls, Watertown, Massachusetts

***PORTABLE INSTRUMENTS FOR USE IN CONNECTION WITH SHIPBOARD
VIBRATION CODES**
R. K. Brown and A. Hagen, Naval Ship Research and Development Center,
Washington, D. C.

*This paper not presented at Symposium.

SUPPLEMENT

RIGID AND RESILIENT SHIPBOARD PIPING SYSTEMS: WHAT CONSTITUTES ACCEPTABLE SHOCK PERFORMANCE/QUALIFICATION?

D. M. C. Hurt, Naval Ship Engineering Center, Hyattsville, Maryland

DAMPING VALUES OF NAVAL SHIPS OBTAINED FROM IMPULSE LOADINGS

W. P. Foster and H. F. Alma, Naval Ship Research and Development Center,
Washington, D. C.

CATAPULT-EXCITED MAST-ISLAND VIBRATION ON AN AIRCRAFT CARRIER

A. Hagen and K. McConnell, Naval Ship Research and Development Center,
Washington, D. C.

COMPRESSED-AIR LAUNCHERS

H. M. Cole, Naval Ordnance Laboratory, Silver Spring, Maryland

EQUIPMENT CABINET MOUNTING FOR SHIPBOARD SHOCK

P. V. Roberts, Raytheon Company, Bedford, Massachusetts, and A. Smith,
Canadian Naval Engineering Test Establishment, Montreal, Canada

RESPONSE OF THE LOW SPEED FAE AND HELICOPTER TRAP WEAPONS (HTW) TO CAPTIVE-FLIGHT VIBRATION

W. W. Parmenter, Naval Weapons Center, China Lake, California

RESPONSE OF TIAS MECHANICAL MODEL DURING LABORATORY SINE AND RANDOM VIBRATION COMPARED TO INFLIGHT AND VIBROACOUSTIC RESPONSES

P. Bouclin and L. G. Janetzko, Naval Weapons Center, China Lake, California

PANEL DISCUSSION ON CAPTIVE FLIGHT DESIGN AND TEST CRITERIA

DYNAMICS

FURTHER COMPARISONS OF CONSISTENT MASS MATRIX SCHEMES

R. M. Mains
Professor of Civil and Environmental Engineering
Washington University
St. Louis, Missouri

The work presented by the author at the 39th Symposium^{(1)*} has been extended and carried through to comparisons of stresses. An exponent error in generating the flexibility matrix has been found and corrected, which led to approximately 8% increase in the frequencies affected. Three more comparative solutions have been included: the different mass formulations, as before, but with a linear-coordinate stiffness derived from the full linear-plus-rotational stiffness. This linear stiffness produced stresses about 6% different from the stresses calculated from the stiffness matrix obtained by inversion of the flexibility matrix.

The shear and bending stresses in mode 1 for the various solutions are compared first. Then the square roots of the sums of the squares of the bending stresses across the modes are compared for the first six modes. The algebraic sums of the bending stresses across the modes are also compared for the first six modes. The results show that the maximum stresses, upon which design decisions would be based, are essentially the same for all ten of the different solutions, with the range of values about 5%. For any one coordinate station away from the maximum areas, larger differences did occur as would be expected. The simple sum of the stresses across the modes was interesting to observe in that it was consistent between the various solutions and followed the same pattern as the square roots of the sums of the squares. (All of the calculations and comparisons were carried through for 12 modes in each solution, and the material presented herein has been selected to show the general character of the results in condensed format. The full data are available on request from the author.)

The solution to the Timoshenko⁽²⁾ beam problem, published by T. C. Huang⁽³⁾ for the beam with rotatory inertia and shear effects, has been calculated for numerical values of frequency for the beam discussed herein. The results are included in the comparison of the various frequencies obtained from the lumped parameter solutions.

I. SUMMARY AND CONCLUSIONS

The responses of a cantilever beam to step-velocity shock, with shear flexibility and rotatory inertia effects included, have been calculated for ten different formulations of the problem: three different forms of stiffness and three different forms of mass in various combinations. The solutions were carried through to the calculation of stress amplitudes in the lowest 12 modes, the accumulated sums of stresses across the modes, and the square roots of the accumulated sums of squares across the modes. Through mode 6, the agreement between the various solutions was generally better than ± 5 percent on the average, and was frequently better than ± 2 percent. No one solution or

group of solutions stood out as more consistent or more correct than any other. For design decisions, any one of the solutions would produce the same result. The double problem size required by the inclusion of rotational coordinates was not worth the extra computing cost, and the additional eigenvalue calculation required by the "consistent mass" schemes was not worth the extra cost. Twenty linear degrees of freedom with pro-rated diagonal mass was just as good as forty degrees of freedom with consistent mass, at less than half the cost.

* Superscripts refer to items in the list of references.

II. CORRECTION TO DEFLECTION INFLUENCE COEFFICIENT MATRIX

In working further on the cantilever beam problem previously reported,⁽¹⁾ additional data and information have been developed which are discussed below. (The essential data on the problem and a sketch of the system are reproduced in the appendix for convenient reference.) First, an exponent misprint in the generation of the deflection influence coefficient matrix (Table 7, reference 1) was discovered and corrected. The error was in the shear flexibility term, making that contribution too large, so that the corrected flexibility is smaller. The corrected flexibility matrix is shown in Table 1, with the 20-20 element about 4 percent smaller than before.

III. CALCULATION OF REDUCED STIFFNESS MATRIX FROM SYSTEM STIFFNESS

The rotational coordinates were eliminated from the system stiffness to leave a reduced stiffness matrix with linear coordinates only, by means of the equation:

$$K_{11}^* = K_{11} - K_{12}K_{22}^{-1}K_{21} \quad (1)$$

in which K_{11}^* = reduced stiffness matrix

K_{11} contains coordinates to be retained

K_{22} contains coordinates to be eliminated

K_{12}, K_{21} are the coupling matrices

In this computation, the inverse of K_{22} was multiplied against K_{22} , and the result was an identity matrix with off-diagonal elements no larger than 10^{-16} . An excerpt from the system stiffness matrix is shown in Table 2, and the reduced system stiffness is shown in Table 3.

The reduced system stiffness and the deflection influence coefficient matrix are theoretically inverses of each other, so the two were multiplied to see how good they were. The largest off-diagonal element was 0.78×10^{-3} . When the flexibility matrix was conditioned, inverted, and multiplied against itself, the largest off-diagonal element was 0.4×10^{-3} , or a factor of 2 better. The reduction of the system stiffness was done by a 14-digit computation on the IBM 360 and fed into the other computations at the IBM 7072 limit of 9 digits. Even with this kind of computation and careful cross checking, the reduced system stiffness, KLIN1, and the stiffness resulting from the inversion of the flexibility matrix, KLIN2, were different. In order to evaluate this difference, the rest of the computations were carried through for KLIN1 and KLIN2 separately.

IV. THEORETICAL SOLUTION

During the presentation of the previous work, the author's attention was called to a solution in closed form of the Timoshenko⁽²⁾ beam problem by T. C. Huang⁽³⁾. That solution has been checked, and numerical results have been calculated for the lowest 12 modes. The frequency equation according to Huang is:

$$2 + [b^2(r^2 - s^2)^2 + 2] \cosh ba \cos b\beta$$

$$- \frac{b(r^2 + s^2)}{(1 - b^2 r^2 s^2)^{\frac{1}{2}}} \sinh ba \sin b\beta = 0 \quad (2)$$

in which

$$b^2 = \frac{m l^4}{EI} \omega^2 \quad (3)$$

$$r^2 = \frac{I}{A l^2} \quad (4)$$

$$s^2 = \frac{2(1+\nu)}{k} \frac{I}{A l^2} \quad (5)$$

$$\alpha^2 = \frac{1}{2} \left\{ - (r^2 + s^2) + [(r^2 - s^2)^2 + 4/b^2]^{\frac{1}{2}} \right\} \quad (6)$$

m = mass per unit length

l = total length

I = moment of inertia of cross-section

A = area of cross-section

ν = Poisson's ratio

k = shear form factor

E = Young's modulus

ω = frequency in radians/sec.

An examination of eq. (2) shows that it is highly transcendental, and no direct calculation for b is possible. Consequently, an iterative solution was set up and carried through on the IBM 7072 after some hand computations showed that 7-place log tables would not be adequate. The solution is very touchy, and depends on the small difference of large numbers because of the dominance of the hyperbolic functions after the third or fourth mode.

V. COMPARISON OF FREQUENCIES

The frequencies are compared for two theoretical and ten lumped-parameter solutions as follows:

1. THEORY 1 - theoretical solution without shear or rotatory inertia
2. THEORY 2 - theoretical solution with shear and rotatory inertia
3. RMM - lumped parameter by the author's usual way
4. ARCH - lumped parameter with Archer's mass⁽⁴⁾
5. MCCY - lumped parameter with McCalleys mass⁽⁵⁾

6. RMOD - lumped parameter by author modified to match MCCY higher frequencies
7. RMM LIN 1 }
 8. ARCH LIN 1 } lumped parameter with KLIN 1
 9. MCCY LIN 1 } from reduced system stiffness
10. RMM LIN 2 }
 11. ARCH LIN 2 } lumped parameter with KLIN 2
 12. MCCY LIN 2 } from inverse of flexibility

Table 4 shows the frequencies in the column order given above for the lowest 12 modes. If one compares the lumped parameter values with the theoretical values in column 2, the differences range from - 3.3% to + 4.3% in mode 1, -1.9% to + 6.9% in mode 6, and - 12.1% to +16.8% in mode 12. If one looks at these lowest twelve modes, it is difficult to argue that any set of frequencies is better than column 3, which is far the simplest to obtain.

VI. CALCULATION OF RESPONSES TO 100 IN/SEC. STEP VELOCITY

Since the object of many dynamic analyses is to produce some numbers representing stresses, the calculations were carried through for the stresses produced by a step-velocity shock of 100 in/sec. The modal response amplitudes were calculated by:

$$R = X_0 \left[\frac{1}{\omega_0} * X_0^T * M * 100 \right] \quad (7)$$

in which R = modal response amplitudes

X_0 = modal matrix by columns

M = mass matrix

In this equation, X_0 has been normalized such that

$$X_0^T M X_0 = I \quad (8)$$

Also, the $X_0^T M$ multiplication was done as a matrix times vector computation, and the resulting vector was diagonalized before completing the computation. In this way, the modes were kept separate until the end.

Once the response amplitudes had been calculated, they were applied directly to the unassembled stiffness matrix to get the shears and moments on each end of each beam segment. This was easy for the 40 x 40 matrices, since they contained both moment and shear. The 20 x 20 linear matrices could not be handled this way, and the effective force at each mass point had to be calculated as:

$$F_e = M R \omega^2 \quad (9)$$

These effective forces were then used to calculate shears and moments in standard fashion. Stresses, of course, result directly from shears and moments.

Table 5 shows the bending stresses in mode 1, and Table 6 shows the shear stresses in the same mode.

VII. COMBINATIONS OF MODAL STRESSES

One of the most difficult problems to resolve in a dynamic analysis is how to combine the stress amplitudes obtained from the various modes since they are amplitudes of sinusoidal functions, each mode at a different frequency. The most probable value of the combined functions is the square root of the sums of the squares of the amplitudes, and half the values will exceed this value. This most probable value was computed for the successively increasing numbers of modes through the lowest 12. The results for the bending stresses through mode 6 are shown in Table 7.

For comparison, the simple sum of stress amplitudes through successively increasing modes was also calculated, using whatever algebraic sign came through the computation. This is justifiable because the $X_0^T M$ product determines the sign R, regardless of whether X_0 is multiplied by (-1) or not. The later multiplication by X_0 with its (-1) would cancel out the sign multiplier on X_0^T . The simple sums of the bending stresses through mode 6 are shown in Table 8.

It is worth noting that the simple sums do produce the same result in the various solutions, even though about half of the eigenvectors were negative in comparison to any one selected as standard. It is also worth noting that the simple sum stress for the first few coordinates is consistently about 1.6 times the square root of sum of squares values.

XIII. HOW MANY MODES TO USE

The modal effective mass is frequently used to determine how many modes are needed for an adequate solution. With the normalization on X_0 shown in eq. (8), it follows that

$$M X_0 X_0^T M = M \quad (10)$$

$$\text{or} \quad (X_0^T M)^2 = M \quad (11)$$

If the modal effective mass is defined as $(X_0^T M)^2$, then all of the effective masses must add to the total mass. On this basis it is argued that enough modes must be taken for the effective masses to sum to 95 percent of the total mass, or some other percentage.

The author prefers to consider that, however the problem is laid out, a loop in a mode needs about 3 coordinate stations in order for it to be properly represented in the analysis, just as in a Fourier analysis of a signal. So

with 20 coordinate stations, 6 or 7 loops are the maximum that can be well represented. An examination of the mode shapes showed that the 6th modes all had 3 coordinates per loop, while 6 of the 10 solutions for the 7th mode had loops with only 2 stations.

Table 9 shows the accumulated sum down the modes of the modal effective mass divided by the total mass. All of the solutions show an accumulation of effective mass in excess of 96 percent of the total mass in the lowest six modes. This observation, plus the mode shape observation cited in the previous paragraph, plus the observation that after mode six the various solutions show increasing divergence, leads to the conclusion that six modes are an adequate number to represent the solution to the problem.

It is interesting to observe that the various consistent mass schemes sum to more than 100 percent of the total mass after mode 8 or 10, as the case may be. Whether this observation is significant or not is not yet determined.

LIST OF REFERENCES

1. Mains, R. M., "Comparisons of Consistent Mass Matrix Schemes," Shock and Vibration Bull., no. 39, part 3.
2. Timoshenko, S. P., "On the Correction for Shear of the Differential Equation for the Transverse Vibration of Prismatic Bars," Phil. Mag. v41, p744, 1921.
3. Huang, T. C., "The Effect of Rotatory Inertia and of Shear Deformation on the Frequency and Normal Mode Equations of Uniform Beams with Simple End Conditions," Jour. App. Mech. ASME, Dec. 1961, p579.
4. Archer, J. S., "Consistent Mass Matrix for Distributed Mass Systems," Jour. Struct. Div. ASCE, v89, ST4, Aug. 1963.
5. McCalley, R. B., Jr., "Mass Matrix for a Prismatic Beam Segment," Rept. No. KAPL-M-6913, Knolls Atomic Power Lab, General Electric Co., Schenectady, N. Y., Mar. 1968.

Table 1
CORRECTED DEFLECTION INFLUENCE COEFFICIENT MATRIX

	1	2	3	4	5	6	7	8	9	10
1	0.48311E-04	0.75335E-05	0.10294E-05	0.13028E-05	0.15781E-05	1	0.18493E-05	0.21226E-05	0.23958E-05	0.26691E-05
2	0.75335E-04	0.20892E-05	0.31532E-05	0.42931E-05	0.53331E-05	2	0.64311E-05	0.75281E-05	0.86171E-05	0.97102E-05
3	0.75335E-04	0.31532E-05	0.58212E-05	0.82804E-05	0.10740E-04	3	0.13149E-04	0.15638E-04	0.18117E-04	0.20512E-04
4	0.13028E-05	0.42931E-05	0.82804E-05	0.12862E-04	0.17234E-04	4	0.21606E-04	0.25978E-04	0.30350E-04	0.34722E-04
5	0.42931E-05	0.82804E-05	0.16735E-04	0.25606E-04	0.34477E-04	5	0.43348E-04	0.52219E-04	0.61090E-04	0.69961E-04
6	0.82804E-05	0.16735E-04	0.34477E-04	0.52219E-04	0.69961E-04	6	0.87703E-04	0.10544E-03	0.12325E-03	0.14106E-03
7	0.16735E-04	0.34477E-04	0.69961E-04	0.10544E-03	0.14106E-03	7	0.21230E-03	0.24792E-03	0.28354E-03	0.31916E-03
8	0.34477E-04	0.69961E-04	0.10544E-03	0.14106E-03	0.17668E-03	8	0.43348E-03	0.52219E-03	0.61090E-03	0.69961E-03
9	0.69961E-04	0.10544E-03	0.14106E-03	0.17668E-03	0.21230E-03	9	0.87703E-03	0.10544E-03	0.12325E-03	0.14106E-03
10	0.10544E-03	0.14106E-03	0.17668E-03	0.21230E-03	0.24792E-03	10	0.43348E-03	0.52219E-03	0.61090E-03	0.69961E-03
11	0.14106E-03	0.17668E-03	0.21230E-03	0.24792E-03	0.28354E-03	11	0.87703E-03	0.10544E-03	0.12325E-03	0.14106E-03
12	0.17668E-03	0.21230E-03	0.24792E-03	0.28354E-03	0.31916E-03	12	0.87703E-03	0.10544E-03	0.12325E-03	0.14106E-03
13	0.21230E-03	0.24792E-03	0.28354E-03	0.31916E-03	0.35478E-03	13	0.87703E-03	0.10544E-03	0.12325E-03	0.14106E-03
14	0.24792E-03	0.28354E-03	0.31916E-03	0.35478E-03	0.39040E-03	14	0.87703E-03	0.10544E-03	0.12325E-03	0.14106E-03
15	0.28354E-03	0.31916E-03	0.35478E-03	0.39040E-03	0.42602E-03	15	0.87703E-03	0.10544E-03	0.12325E-03	0.14106E-03
16	0.31916E-03	0.35478E-03	0.39040E-03	0.42602E-03	0.46164E-03	16	0.87703E-03	0.10544E-03	0.12325E-03	0.14106E-03
17	0.35478E-03	0.39040E-03	0.42602E-03	0.46164E-03	0.49726E-03	17	0.87703E-03	0.10544E-03	0.12325E-03	0.14106E-03
18	0.39040E-03	0.42602E-03	0.46164E-03	0.49726E-03	0.53288E-03	18	0.87703E-03	0.10544E-03	0.12325E-03	0.14106E-03
19	0.42602E-03	0.46164E-03	0.49726E-03	0.53288E-03	0.56850E-03	19	0.87703E-03	0.10544E-03	0.12325E-03	0.14106E-03
20	0.46164E-03	0.49726E-03	0.53288E-03	0.56850E-03	0.60412E-03	20	0.87703E-03	0.10544E-03	0.12325E-03	0.14106E-03

EXCERPT FROM K SYSTEM= 1,1 TO 12,7' 13,16 TO 28,22' 29,34 TO 40,40

1	0.57722E 07	-0.23283E-08	-0.28861E 07	0.86583E 07	0.00000E 00	0.00000E 00	0.00000E 00
2	-0.37253E-08	0.18370E 09	-0.86583E 07	-0.39900E 08	0.00000E 00	0.00000E 00	0.00000E 00
3	-0.28861E 07	-0.86583E 07	0.57722E 07	-0.23283E-08	-0.28861E 07	0.86583E 07	0.00000E 00
4	0.86583E 07	-0.39900E 08	-0.37253E-08	0.18370E 09	-0.86583E 07	0.39900E 08	0.00000E 00
5	0.00000E 00	0.00000E 00	-0.28861E 07	-0.86583E 07	0.57722E 07	-0.23283E-08	-0.28861E 07
6	0.00000E 00	0.00000E 00	0.86583E 07	-0.39900E 08	-0.37253E-08	0.18370E 09	-0.86583E 07
7	0.00000E 00	0.00000E 00	0.00000E 00	0.00000E 00	0.00000E 00	-0.86583E 07	0.57722E 07
8	0.00000E 00	0.00000E 00	0.00000E 00	0.00000E 00	0.86583E 07	-0.39900E 08	-0.37253E-08
9	0.00000E 00	0.00000E 00	0.00000E 00	0.00000E 00	0.00000E 00	0.00000E 00	-0.28861E 07
10	0.00000E 00	0.00000E 00	0.00000E 00	0.00000E 00	0.00000E 00	0.00000E 00	0.86583E 07
11	0.00000E 00	0.00000E 00	0.00000E 00	0.00000E 00	0.00000E 00	0.00000E 00	0.00000E 00
12	0.00000E 00	0.00000E 00	0.00000E 00	0.00000E 00	0.00000E 00	0.00000E 00	0.00000E 00
13	0.86583E 07	0.00000E 00	0.00000E 00	0.00000E 00	0.00000E 00	0.00000E 00	0.00000E 00
14	-0.39900E 08	0.00000E 00	0.00000E 00	0.00000E 00	0.00000E 00	0.00000E 00	0.00000E 00
15	-0.23283E-08	0.28861E 07	0.86583E 07	0.00000E 00	0.00000E 00	0.00000E 00	0.00000E 00
16	0.18370E 09	-0.86583E 07	-0.39900E 08	0.00000E 00	0.00000E 00	0.00000E 00	0.00000E 00
17	-0.86583E 07	0.57722E 07	-0.23283E-08	0.18370E 09	-0.86583E 07	0.39900E 08	0.00000E 00
18	-0.39900E 08	-0.37253E-08	0.18370E 09	-0.86583E 07	0.57722E 07	-0.23283E-08	0.00000E 00
19	0.00000E 00	-0.28861E 07	-0.86583E 07	0.57722E 07	-0.23283E-08	-0.28861E 07	0.86583E 07
20	0.00000E 00	0.86583E 07	-0.39900E 08	-0.37253E-08	0.18370E 09	-0.86583E 07	-0.23283E-08
21	0.00000E 00	0.00000E 00	0.00000E 00	0.86583E 07	-0.39900E 08	-0.37253E-08	0.18370E 09
22	0.00000E 00	0.00000E 00	0.00000E 00	0.00000E 00	0.00000E 00	0.00000E 00	-0.28861E 07
23	0.00000E 00	0.00000E 00	0.00000E 00	0.00000E 00	0.00000E 00	0.00000E 00	-0.86583E 07
24	0.00000E 00	0.00000E 00	0.00000E 00	0.00000E 00	0.00000E 00	0.86583E 07	-0.39900E 08
25	0.00000E 00	0.00000E 00	0.00000E 00	0.00000E 00	0.00000E 00	0.00000E 00	0.00000E 00
26	0.00000E 00	0.00000E 00	0.00000E 00	0.00000E 00	0.00000E 00	0.00000E 00	0.00000E 00
27	0.00000E 00	0.00000E 00	0.00000E 00	0.00000E 00	0.00000E 00	0.00000E 00	0.00000E 00
28	0.00000E 00	0.00000E 00	0.00000E 00	0.00000E 00	0.00000E 00	0.00000E 00	0.00000E 00
29	0.00000E 00	0.00000E 00	0.00000E 00	0.00000E 00	0.00000E 00	0.00000E 00	0.00000E 00
30	0.00000E 00	0.00000E 00	0.00000E 00	0.00000E 00	0.00000E 00	0.00000E 00	0.00000E 00
31	0.86583E 07	0.00000E 00	0.00000E 00	0.00000E 00	0.00000E 00	0.00000E 00	0.00000E 00
32	-0.39900E 08	0.00000E 00	0.00000E 00	0.00000E 00	0.00000E 00	0.00000E 00	0.00000E 00
33	-0.23283E-08	-0.28861E 07	0.86583E 07	0.00000E 00	0.00000E 00	0.00000E 00	0.00000E 00
34	0.18370E 09	-0.86583E 07	-0.39900E 08	0.00000E 00	0.00000E 00	0.00000E 00	0.00000E 00
35	-0.86583E 07	0.57722E 07	-0.23283E-08	0.18370E 09	-0.86583E 07	0.39900E 08	0.00000E 00
36	-0.39900E 08	-0.37253E-08	0.18370E 09	-0.86583E 07	0.57722E 07	-0.23283E-08	0.00000E 00
37	0.00000E 00	-0.28861E 07	-0.86583E 07	0.57722E 07	-0.23283E-08	-0.28861E 07	0.86583E 07
38	0.00000E 00	0.86583E 07	-0.39900E 08	-0.37253E-08	0.18370E 09	-0.86583E 07	-0.23283E-08
39	0.00000E 00	0.00000E 00	0.00000E 00	0.86583E 07	-0.39900E 08	-0.37253E-08	0.18370E 09
40	0.00000E 00	0.00000E 00	0.00000E 00	0.00000E 00	0.00000E 00	0.00000E 00	-0.28861E 07

CORRECTED DEFLECTION INFLUENCE

7

TABLE 4

COMPARISON OF FREQUENCIES, CYCLES / SEC

	THEORY1	THEORY2	RMM	ARCH	MCCY	RMCY
1	0.16753F C2	0.16691E 02	0.16676E 02	0.16520E 02	0.16700F C2	0.16673F C2
2	0.10500E 03	0.10232E 03	0.10192E 03	0.10292E 03	0.10215E 03	0.10216E 03
3	0.29402E 03	0.27711E 03	0.27534E 03	0.27393E 03	0.27757E 03	0.27643E 03
4	0.57517F C3	0.51943E 03	0.51464E 03	0.52409F 03	0.52242E 03	0.51794E 03
5	0.95236E 03	0.81563F 03	0.80501F 03	0.83986E 03	0.82648F 03	0.81170F 03
6	0.14227E C4	0.11523E 04	0.11314E 04	0.12014E 04	0.11803E 04	0.11426E 04
7	0.19471E 04	0.15186E 04	0.14806E 04	0.16037E 04	0.15701E 04	0.14658E 04
8	0.26455E C4	0.19063E 04	0.18416E 04	0.20377E 04	0.20077E 04	0.18624E C4
9	0.33680E 04	0.23092E 04	0.22050E 04	0.24938E 04	0.24097E 04	0.22300E 04
10	0.42445E C4	0.27225E 04	0.25630E 04	0.29605E 04	0.29555E 04	0.25608E 04
11	0.51852E 04	0.31431E 04	29089E 04	0.34153E 04	0.34498E 04	0.29379F C4
12	0.62199E 04	0.35682E 04	0.32370E 04	0.38176F 04	0.38886E 04	0.32657E 04
13	0.73486E 04	0.39962E 04	0.35424E 04	0.41980E 04	0.42476E 04	0.35092E 04
14	0.85714E C4	0.44256E 04	0.38209E 04	0.46395E 04	0.47303E 04	0.38446E 04
15	0.98893E C4	0.48554E 04	0.40690E 04	0.51133E 04	0.52593E 04	0.40887E 04
16	0.11299E 05	0.52847E 04	0.42837E 04	0.55786E 04	0.58543F 04	0.42988E C4
17	0.12804E C5	0.57128E 04	0.44626E 04	0.60072E 04	0.64861E 04	0.44731E 04
18	0.14403E 05	0.61390E 04	0.46037E 04	0.63720E 04	0.70426E 04	0.46100E 04
19	0.16096E 05	0.65623E 04	0.47055E 04	0.66472E 04	0.75192E 04	0.47085E 04
20	0.17884E 05	0.69813E 04	0.47671E 04	0.68145E C4	0.78552E 04	0.47678E 04

	RMMLIN1	ARCHLIN1	MCCYLIN1	RAMLIN2	ARCHLIN2	MCCYLIN2
1	0.17674E C2	0.17557E 02	0.17540E 02	0.16518E 02	0.16419E 02	0.16396E C2
2	0.10298E 03	0.10350E 03	0.10363E 03	0.10264E 03	0.10316E 03	0.10328E 03
3	0.27789E 03	0.28122E 03	0.28235E 03	0.27789E 03	0.28121E 03	0.28204E 03
4	0.52173E C3	0.53316E 03	0.53607E 03	0.52175E 03	0.53318E 03	0.53609E C3
5	0.81976E 03	0.84827F 03	0.85570E 03	0.81976E 03	0.84827E 03	0.85570E 03
6	0.11561E 04	0.12147E 04	0.12304E 04	0.11561E 04	0.12146E 04	0.12304E 04
7	0.15162F 04	0.16219E 04	0.16513F 04	0.15162E 04	0.16219E 04	0.16513E 04
8	0.18874E 04	0.20609E 04	0.21112E 04	0.18874E 04	0.20609E 04	0.21112E 04
9	0.22591E 04	0.25241E 04	0.26046E 04	0.22591E 04	0.25241E 04	0.26046E C4
10	0.26225E 04	0.30046E 04	0.31267E 04	0.26225E 04	0.30045E 04	0.31267E 04
11	0.29705E C4	0.34955E 04	0.36730E 04	0.29706E 04	0.34956E 04	0.36731E C4
12	0.32972E 04	0.39898E 04	0.42385E 04	0.32972E 04	0.39898E 04	0.42385E 04
13	0.35828E 04	0.44796E 04	0.48165E 04	0.35828E 04	0.44796E 04	0.48155E 04
14	0.38698E 04	0.49552E 04	0.53974E 04	0.38698E 04	0.49553E 04	0.53977E 04
15	0.41092E 04	0.54055E 04	0.59684E 04	0.41090E 04	0.54054E 04	0.59680F C4
16	0.43144E 04	0.58182E 04	0.65106F 04	0.43143E 04	0.58180E 04	0.65106E 04
17	0.44838E C4	0.61788E 04	0.70014E 04	0.44836E 04	0.61786E 04	0.70012E 04
18	0.46164E 04	0.64737E 04	0.74145E 04	0.46162E 04	0.64735E 04	0.74141E 04
19	0.47114E 04	0.66917E 04	0.77250E 04	0.47115E 04	0.66917E 04	0.77250E 04
20	0.47686E 04	0.69249E 04	0.79158E 04	0.47686E 04	0.69249E 04	0.79159E C4

TABLE 5
COMPARISON OF BENDING STRESSES, PSI, MOOE 1

	RMM	ARCH	MCCY	RMOD	RMMLIN1
1	0.21365E 05	0.20941E 05	0.21392E 05	0.21382E 05	0.22553E 05
2	0.19787E 05	0.19457E 05	0.19812E 05	0.19804E 05	0.20892E 05
3	0.18216E 05	0.17952E 05	0.18237E 05	0.18230E 05	0.19235E 05
4	0.16649E 05	0.16449E 05	0.16666E 05	0.16661E 05	0.17585E 05
5	0.15104E 05	0.14963E 05	0.15109E 05	0.15103E 05	0.15949E 05
6	0.13551E 05	0.13470E 05	0.13577E 05	0.13568E 05	0.14333E 05
7	0.12065E 05	0.11992E 05	0.12068E 05	0.12077E 05	0.12746E 05
8	0.10573E 05	0.10585E 05	0.10584E 05	0.10593E 05	0.11196E 05
9	0.91746E 04	0.92152E 04	0.91719E 04	0.91607E 04	0.96947E 04
10	0.77982E 04	0.78727E 04	0.77815E 04	0.78129E 04	0.82526E 04
11	0.65007E 04	0.65549E 04	0.65118E 04	0.64951E 04	0.68819E 04
12	0.52769E 04	0.53606E 04	0.52594E 04	0.52853E 04	0.55952E 04
13	0.41588E 04	0.42453E 04	0.41607E 04	0.41532E 04	0.44058E 04
14	0.31447E 04	0.32209E 04	0.31105E 04	0.31539E 04	0.33276E 04
15	0.22491E 04	0.23217E 04	0.22482E 04	0.22371E 04	0.23746E 04
16	0.15433E 04	0.15770E 04	0.14639E 04	0.14128E 04	0.15613E 04
17	0.85698E 03	0.94899E 03	0.88590E 03	0.94874E 03	0.90238E 03
18	0.31291E 03	0.43385E 03	0.33985E 03	0.41933E 03	0.41262E 03
19	0.15636E 03	-0.31766E 01	0.21225E 02	0.10268E 03	0.10687E 03
20	-0.77169E 02	0.13765E 02	0.63516E 02	-0.10987E 03	0.00000E 00

	ARCHLIN1	MCCYLIN1	RMMLIN2	ARCHLIN2	MCCYLIN2
1	0.22434E 05	0.22418E 05	0.21150E 05	0.21054E 05	0.21029E 05
2	0.20782E 05	0.20767E 05	0.19589E 05	0.19501E 05	0.19477E 05
3	0.19133E 05	0.19120E 05	0.18032E 05	0.17950E 05	0.17929E 05
4	0.17473E 05	0.17481E 05	0.16482E 05	0.16407E 05	0.16388E 05
5	0.15865E 05	0.15854E 05	0.14945E 05	0.14877E 05	0.14860E 05
6	0.14258E 05	0.14248E 05	0.13427E 05	0.13366E 05	0.13351E 05
7	0.12679E 05	0.12671E 05	0.11936E 05	0.11883E 05	0.11869E 05
8	0.11138E 05	0.11130E 05	0.10482E 05	0.10435E 05	0.10423E 05
9	0.96442E 04	0.96381E 04	0.90730E 04	0.90322E 04	0.90221E 04
10	0.82097E 04	0.82046E 04	0.77206E 04	0.76859E 04	0.76774E 04
11	0.68462E 04	0.68420E 04	0.64358E 04	0.64069E 04	0.63998E 04
12	0.55663E 04	0.55630E 04	0.52305E 04	0.52070E 04	0.52013E 04
13	0.43831E 04	0.43806E 04	0.41170E 04	0.40985E 04	0.40941E 04
14	0.33104E 04	0.33086E 04	0.31082E 04	0.30942E 04	0.30910E 04
15	0.23624E 04	0.23611E 04	0.22171E 04	0.22072E 04	0.22049E 04
16	0.15533E 04	0.15525E 04	0.14572E 04	0.14506E 04	0.14492E 04
17	0.89776E 03	0.89730E 03	0.84186E 03	0.83809E 03	0.83724E 03
18	0.41052E 03	0.41031E 03	0.38478E 03	0.38306E 03	0.38267E 03
19	0.10633E 03	0.10628E 03	0.99609E 02	0.99163E 02	0.99066E 02
20	0.00000E 00	0.00000E 00	0.00000E 00	0.00000E 00	0.00000E 00

TABLE 6
COMPARISON OF SHEAR STRESSES, PSI, MODE 1

	RMM	ARCH	MCCY	RMOD	RMMLIN1
1	0.72561E 03	0.67487E 03	0.72701E 03	0.72676E 03	0.76455E 03
2	0.72574E 03	0.68547E 03	0.72714E 03	0.72663E 03	0.76412E 03
3	0.72305E 03	0.69071E 03	0.72458E 03	0.72356E 03	0.76240E 03
4	0.72062E 03	0.68892E 03	0.72716E 03	0.72229E 03	0.75892E 03
5	0.70796E 03	0.68483E 03	0.71640E 03	0.71960E 03	0.75279E 03
6	0.71461E 03	0.68266E 03	0.70464E 03	0.70745E 03	0.74343E 03
7	0.68509E 03	0.68381E 03	0.69148E 03	0.68381E 03	0.73031E 03
8	0.68637E 03	0.65569E 03	0.67614E 03	0.67742E 03	0.71291E 03
9	0.65059E 03	0.63271E 03	0.65313E 03	0.66336E 03	0.69077E 03
10	0.62373E 03	0.61348E 03	0.63907E 03	0.61995E 03	0.66347E 03
11	0.60200E 03	0.60075E 03	0.59178E 03	0.60712E 03	0.63064E 03
12	0.56113E 03	0.55217E 03	0.56751E 03	0.55345E 03	0.59197E 03
13	0.52023E 03	0.50874E 03	0.50874E 03	0.52530E 03	0.54718E 03
14	0.46141E 03	0.46907E 03	0.48316E 03	0.46269E 03	0.49607E 03
15	0.41032E 03	0.41160E 03	0.40132E 03	0.41158E 03	0.43844E 03
16	0.29142E 03	0.32848E 03	0.34514E 03	0.41156E 03	0.37417E 03
17	0.28119E 03	0.26461E 03	0.23518E 03	0.19685E 03	0.30315E 03
18	0.27610E 03	0.21343E 03	0.24159E 03	0.18789E 03	0.22532E 03
19	0.89481E 02	0.25563E 03	0.19430E 03	0.12910E 03	0.14067E 03
20	0.10992E 03	0.16665E 02	-0.29384E 02	0.14956E 03	0.49169E 02

	ARCHLIN1	MCCYLIN1	RMMLIN2	ARCHLIN2	MCCYLIN2
1	0.76044E 03	0.75984E 03	0.71849E 03	0.71522E 03	0.71431E 03
2	0.76001E 03	0.75942E 03	0.71807E 03	0.71480E 03	0.71390E 03
3	0.75839E 03	0.75779E 03	0.71650E 03	0.71324E 03	0.71234E 03
4	0.75486E 03	0.75426E 03	0.71309E 03	0.70985E 03	0.70896E 03
5	0.74875E 03	0.74817E 03	0.70721E 03	0.70400E 03	0.70312E 03
6	0.73946E 03	0.73889E 03	0.69828E 03	0.69511E 03	0.69424E 03
7	0.72642E 03	0.72587E 03	0.68576E 03	0.68265E 03	0.68181E 03
8	0.70912E 03	0.70859E 03	0.66919E 03	0.66616E 03	0.66534E 03
9	0.68711E 03	0.68660E 03	0.64813E 03	0.64520E 03	0.64442E 03
10	0.65996E 03	0.65949E 03	0.62221E 03	0.61940E 03	0.61866E 03
11	0.62732E 03	0.62688E 03	0.59110E 03	0.58844E 03	0.58775E 03
12	0.58886E 03	0.58847E 03	0.55454E 03	0.55204E 03	0.55140E 03
13	0.54433E 03	0.54398E 03	0.51227E 03	0.50997E 03	0.50939E 03
14	0.49350E 03	0.49319E 03	0.46413E 03	0.46204E 03	0.46153E 03
15	0.43618E 03	0.43591E 03	0.40995E 03	0.40810E 03	0.40766E 03
16	0.37224E 03	0.37202E 03	0.34963E 03	0.34806E 03	0.34769E 03
17	0.30159E 03	0.30142E 03	0.28309E 03	0.28182E 03	0.28152E 03
18	0.22416E 03	0.22405E 03	0.21029E 03	0.20934E 03	0.20913E 03
19	0.13995E 03	0.13988E 03	0.13120E 03	0.13061E 03	0.13048E 03
20	0.48918E 02	0.48894E 02	0.45627E 02	0.45622E 02	0.45577E 02

TABLE 7

SQUARE ROOT OF ACCUMULATED SUM OF SQUARES OF BENDING STRESS, MODE 1 TO 6

	RMM	ARCH	MCCY	RMOD	RMMLIN1
1	0.23845E 05	0.23475E 05	0.23889E 05	0.23861E 05	0.25183E 05
2	0.20987E 05	0.20657E 05	0.20985E 05	0.21005E 05	0.22217E 05
3	0.18990E 05	0.18764E 05	0.19037E 05	0.19003E 05	0.20067E 05
4	0.17392E 05	0.17242E 05	0.17456E 05	0.17402E 05	0.18314E 05
5	0.16149E 05	0.16044E 05	0.16175E 05	0.16152E 05	0.16923E 05
6	0.15242E 05	0.15217E 05	0.15301E 05	0.15262E 05	0.15895E 05
7	0.14503E 05	0.14516E 05	0.14580E 05	0.14516E 05	0.15015E 05
8	0.13776E 05	0.13838E 05	0.13841E 05	0.13794E 05	0.14211E 05
9	0.13221E 05	0.13258E 05	0.13229E 05	0.13217E 05	0.13563E 05
10	0.12670E 05	0.12706E 05	0.12658E 05	0.12682E 05	0.12946E 05
11	0.12002E 05	0.12048E 05	0.12029E 05	0.12000E 05	0.12224E 05
12	0.11317E 05	0.11412E 05	0.11363E 05	0.11326E 05	0.11503E 05
13	0.10650E 05	0.10749E 05	0.10720E 05	0.10649E 05	0.10786E 05
14	0.97810E 04	0.98312E 04	0.98173E 04	0.97811E 04	0.98648E 04
15	0.87557E 04	0.87885E 04	0.87825E 04	0.87491E 04	0.88089E 04
16	0.78012E 04	0.78430E 04	0.78424E 04	0.77704E 04	0.78084E 04
17	0.65263E 04	0.64826E 04	0.65805E 04	0.65020E 04	0.64561E 04
18	0.43965E 04	0.41232E 04	0.43367E 04	0.43232E 04	0.42253E 04
19	0.17733E 04	0.13153E 04	0.15672E 04	0.16742E 04	0.15583E 04
20	0.12919E 03	0.21320E 03	0.12441E 03	0.12356E 03	0.00000E 00

	ARCHLIN1	MCCYLIN1	RMMLIN2	ARCHLIN2	MCCYLIN2
1	0.25079E 05	0.25074E 05	0.23734E 05	0.23647E 05	0.23627E 05
2	0.22157E 05	0.22163E 05	0.20854E 05	0.20817E 05	0.20812E 05
3	0.20049E 05	0.20065E 05	0.18837E 05	0.18844E 05	0.18852E 05
4	0.18292E 05	0.18301E 05	0.17233E 05	0.17234E 05	0.17238E 05
5	0.16910E 05	0.16918E 05	0.15998E 05	0.16007E 05	0.16012E 05
6	0.15929E 05	0.15947E 05	0.15126E 05	0.15181E 05	0.15199E 05
7	0.15087E 05	0.15115E 05	0.14386E 05	0.14478E 05	0.14505E 05
8	0.14323E 05	0.14360E 05	0.13704E 05	0.13833E 05	0.13871E 05
9	0.13731E 05	0.13783E 05	0.13161E 05	0.13344E 05	0.13398E 05
10	0.13134E 05	0.13189E 05	0.12633E 05	0.12833E 05	0.12889E 05
11	0.12385E 05	0.12429E 05	0.11983E 05	0.12153E 05	0.12197E 05
12	0.11667E 05	0.11709E 05	0.11324E 05	0.11494E 05	0.11536E 05
13	0.11000E 05	0.11056E 05	0.10660E 05	0.10879E 05	0.10934E 05
14	0.10142E 05	0.10215E 05	0.97820E 04	0.10064E 05	0.10136E 05
15	0.92013E 04	0.93081E 04	0.87605E 04	0.91564E 04	0.92633E 04
16	0.83618E 04	0.85160E 04	0.77853E 04	0.83413E 04	0.84956E 04
17	0.70487E 04	0.72140E 04	0.64475E 04	0.70415E 04	0.72070E 04
18	0.46464E 04	0.47631E 04	0.42231E 04	0.46447E 04	0.47615E 04
19	0.17107E 04	0.17526E 04	0.15580E 04	0.17106E 04	0.17525E 04
20	0.00000E 00	0.00000E 00	0.00000E 00	0.00000E 00	0.00000E 00

TABLE 8
ACCUMULATED SUM OF BENDING STRESSES, MODE 1 TO 6

	RM4	ARCH	MCCY	RMOD	RMMLIN1
1	0.37959E 05	0.37920E 05	0.38583E 05	0.37929E 05	0.39695E 05
2	0.24245E 05	0.24129E 05	0.24734E 05	0.24204E 05	0.25785E 05
3	0.14093E 05	0.13515E 05	0.13832E 05	0.14089E 05	0.15552E 05
4	0.83895E 04	0.77698E 04	0.78566E 04	0.84376E 04	0.97900E 04
5	0.63839E 04	0.60034E 04	0.59277E 04	0.64391E 04	0.76578E 04
6	0.61418E 04	0.61059E 04	0.60620E 04	0.62012E 04	0.72404E 04
7	0.58344E 04	0.59979E 04	0.60652E 04	0.58505E 04	0.66754E 04
8	0.44345E 04	0.46839E 04	0.47873E 04	0.44255E 04	0.50851E 04
9	0.23112E 04	0.24489E 04	0.25172E 04	0.22619E 04	0.27968E 04
10	0.36898E 03	0.38795E 03	0.33245E 03	0.37186E 03	0.80099E 03
11	-0.50040E 03	-0.55330E 03	-0.65750E 03	-0.48520E 03	-0.97000E 02
12	-0.21922E 03	-0.15454E 03	-0.38146E 03	-0.16999E 03	0.14530E 03
13	0.58291E 03	0.78758E 03	0.59509E 03	0.61182E 03	0.85022E 03
14	0.10322E 04	0.13142E 04	0.11767E 04	0.10439E 04	0.11705E 04
15	0.67412E 03	0.97519E 03	0.94171E 03	0.63559E 03	0.70794E 03
16	-0.17830E 03	0.82700E 02	0.11800E 02	-0.33320E 03	-0.24710E 03
17	-0.10225E 04	-0.70051E 03	-0.77500E 03	-0.93496E 03	-0.10059E 04
18	-0.12020E 04	-0.82355E 03	-0.10053E 04	-0.10707E 04	-0.10554E 04
19	-0.51955E 03	-0.45116E 03	-0.53739E 03	-0.53910E 03	-0.48929E 03
20	-0.11721E 03	0.82139E 02	0.94995E 02	-0.12835E 03	0.00000E 00

	ARCHLIN1	MCCYLIN1	RMMLIN2	ARCHLIN2	MCCYLIN2
1	0.39176E 05	0.39060E 05	0.37848E 05	0.37342E 05	0.37196E 05
2	0.24840E 05	0.24608E 05	0.24093E 05	0.23161E 05	0.22902E 05
3	0.14526E 05	0.14275E 05	0.14016E 05	0.13001E 05	0.12727E 05
4	0.90144E 04	0.88328E 04	0.84093E 04	0.76435E 04	0.74414E 04
5	0.72767E 04	0.72017E 04	0.64305E 04	0.60596E 04	0.59671E 04
6	0.71672E 04	0.71711E 04	0.61637E 04	0.60997E 04	0.60891E 04
7	0.66776E 04	0.66953E 04	0.57438E 04	0.57562E 04	0.57604E 04
8	0.49525E 04	0.49246E 04	0.42937E 04	0.41694E 04	0.41320E 04
9	0.24662E 04	0.23801E 04	0.21359E 04	0.18135E 04	0.17190E 04
10	0.37454E 03	0.26005E 03	0.26049E 03	-0.15865E 03	-0.27916E 03
11	-0.45150E 03	-0.54540E 03	-0.52910E 03	-0.87650E 03	-0.97520E 03
12	-0.31880E 02	-0.76820E 02	-0.19046E 03	-0.36140E 03	-0.40968E 03
13	0.82099E 03	0.81549E 03	0.59796E 03	0.57423E 03	0.56635E 03
14	0.11588E 04	0.11551E 04	0.98868E 03	0.98187E 03	0.97679E 03
15	0.58802E 03	0.55075E 03	0.58464E 03	0.46803E 03	0.43031E 03
16	-0.50320E 03	-0.57960E 03	-0.32400E 03	-0.57810E 03	-0.65450E 03
17	-0.13114E 04	-0.14011E 04	-0.10478E 04	-0.13525E 04	-0.14420E 04
18	-0.12825E 04	-0.13482E 04	-0.10733E 04	-0.13002E 04	-0.13656E 04
19	-0.57318E 03	-0.59709E 03	-0.49355E 03	-0.57747E 03	-0.60121E 03
20	0.00000E 00	0.00000E 00	0.00000E 00	0.00000E 00	0.00000E 00

TABLE 9
ACCUMULATED SUM OF MASS RATIOS , DOWN THE COLUMNS

	RMH	ARCH	MCCY	RMOD	RMMLIN1
1	0.62883E 00	0.62988E 00	0.63036E 00	0.62921E 00	0.62489E 00
2	0.82475E 00	0.82436E 00	0.82472E 00	0.82526E 00	0.82599E 00
3	0.89296E 00	0.89503E 00	0.89479E 00	0.89365E 00	0.89461E 00
4	0.92839E 00	0.92964E 00	0.92919E 00	0.92920E 00	0.93024E 00
5	0.94998E 00	0.95384E 00	0.95334E 00	0.95085E 00	0.95195E 00
6	0.96434E 00	0.96847E 00	0.96799E 00	0.96521E 00	0.96630E 00
7	0.97437E 00	0.98253E 00	0.98233E 00	0.97519E 00	0.97622E 00
8	0.98156E 00	0.99204E 00	0.99205E 00	0.98231E 00	0.98323E 00
9	0.98679E 00	0.10041E 01	0.10048E 01	0.98744E 00	0.98825E 00
10	0.99062E 00	0.10142E 01	0.10153E 01	0.99116E 00	0.99186E 00
11	0.99341E 00	0.10305E 01	0.10354E 01	0.99386E 00	0.99445E 00
12	0.99543E 00	0.10429E 01	0.10593E 01	0.99580E 00	0.99631E 00

	ARCHLIN1	MCCYLIN1	RMMLIN2	ARCHLIN2	MCCYLIN2
1	0.62569E 00	0.62581E 00	0.62839E 00	0.62928E 00	0.62937E 00
2	0.82752E 00	0.82796E 00	0.82578E 00	0.82729E 00	0.82759E 00
3	0.89687E 00	0.89745E 00	0.89455E 00	0.89681E 00	0.89726E 00
4	0.93318E 00	0.93394E 00	0.93024E 00	0.93318E 00	0.93381E 00
5	0.95557E 00	0.95650E 00	0.95197E 00	0.95557E 00	0.95637E 00
6	0.97054E 00	0.97165E 00	0.96631E 00	0.97054E 00	0.97152E 00
7	0.98103E 00	0.98231E 00	0.97623E 00	0.98104E 00	0.98218E 00
8	0.98856E 00	0.99000E 00	0.98324E 00	0.98857E 00	0.98987E 00
9	0.99405E 00	0.99564E 00	0.98826E 00	0.99405E 00	0.99551E 00
10	0.99807E 00	0.99980E 00	0.99187E 00	0.99807E 00	0.99968E 00
11	0.10010E 01	0.10029E 01	0.99446E 00	0.10010E 01	0.10028E 01
12	0.10032E 01	0.10052E 01	0.99632E 00	0.10032E 01	0.10051E 01

Appendix

The essential data on the problem and a sketch of the system are copied here from the previous work, so that less reference to it is required.

TABLE 1.

STIFFNESS FOR ELEMENT LBS. INS. RAD.

	1	2	3	4
1	0.28861E 07	0.86583E 07	-0.28861E 07	0.86583E 07 y_1
2	0.86583E 07	0.91850E 08	-0.86583E 07	-0.39900E 08 θ_1
3	-0.28861E 07	-0.86583E 07	0.28861E 07	-0.86583E 07 y_2
4	0.86583E 07	-0.39900E 08	-0.86583E 07	0.91850E 08 θ_2

TABLE 2.

A. MASS ACCORDING TO RHM AS USUALLY DONE

	1	2	3	4
1	0.63788E-02	0.00000E 00	0.00000E 00	0.00000E 00
2	0.00000E 00	0.24319E-01	0.00000E 00	0.00000E 00
3	0.00000E 00	0.00000E 00	0.63788E-02	0.00000E 00
4	0.00000E 00	0.00000E 00	0.00000E 00	0.24319E-01

B. MASS ACCORDING TO ARCHER

	1	2	3	4
1	0.47385E-02	0.40095E-02	0.16403E-02	-0.23693E-02
2	0.40095E-02	0.43740E-02	0.23693E-02	-0.32805E-02
3	0.16403E-02	0.23693E-02	0.47385E-02	-0.40095E-02
4	-0.23693E-02	-0.32805E-02	-0.40095E-02	0.43740E-02

C. MASS ACCORDING TO RHM MODIFIED TO MATCH MCCALLEY'S

	1	2	3	4
1	0.63788E-02	0.00000E 00	0.00000E 00	0.00000E 00
2	0.00000E 00	0.13176E-01	0.00000E 00	0.00000E 00
3	0.00000E 00	0.00000E 00	0.63788E-02	0.00000E 00
4	0.00000E 00	0.00000E 00	0.00000E 00	0.13176E-01

(Table II continued)

D.MASS ACCORDING TO MCCALLEY - LINEAR ONLY

	1	2	3	4
1	0.43095E-02	0.32764E-02	0.20693E-02	-0.31024E-02
2	0.32764E-02	0.38367E-02	0.31024E-02	-0.38178E-02
3	0.20693E-02	0.31024E-02	0.43095E-02	-0.32764E-02
4	-0.31024E-02	-0.38178E-02	-0.32764E-02	0.38367E-02

E.MASS ACCORDING TO MCCALLEY - ROTATIONAL ONLY

	1	2	3	4
1	0.28008E-04	-0.44871E-03	-0.28008E-04	-0.44871E-03
2	-0.44871E-03	0.13268E-01	0.44871E-03	0.51621E-02
3	-0.28008E-04	0.44871E-03	0.28008E-04	0.44871E-03
4	-0.44871E-03	0.51621E-02	0.44871E-03	0.13268E-01

F.MASS ACCORDING TO MCCALLEY - LINEAR + ROTATION

	1	2	3	4
1	0.43375E-02	0.28277E-02	0.20413E-02	-0.35511E-02
2	0.28277E-02	0.17105E-01	0.35511E-02	0.13442E-02
3	0.20413E-02	0.35511E-02	0.43375E-02	-0.28277E-02
4	-0.35511E-02	0.13442E-02	-0.28277E-02	0.17105E-01

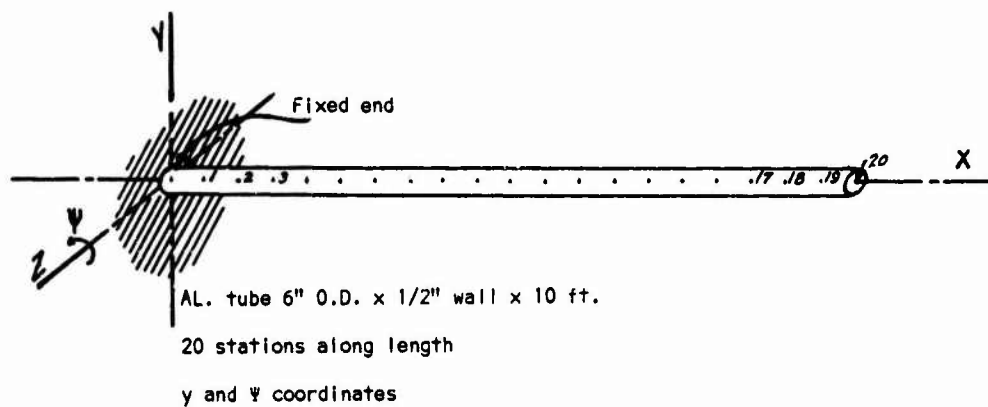


Fig. 1

CANTILEVER BEAM SYSTEM

DISCUSSION

Mr. Verga (Haleltine Corp.): It was enlightening to see that for the first mode, and possibly up to the sixth mode, in a cantilever beam we could neglect the rotary mass and the shear.

Mr. Mains: I do not advocate this in general.

Mr. Verga: In the case of shear, you did not discuss the effect of the ratio of the length to moment of inertia. If the moment of inertia becomes quite large, then the shear might have greater effect.

Mr. Mains: The shear flexibility was the order of $2/3$ of the bending flexibility because the length of the element was equal to its diameter.

Mr. Verga: The length of the cantilever?

Mr. Mains: Yes, 10 foot cantilever, 20 stations, 6 inches outside diameter. The length of the segment was the same as its diameter.

SHOCK SPECTRA FOR STATISTICALLY MODELLED STRUCTURES

Richard H. Lyon
Bolt Beranek and Newman Inc.
Cambridge, Massachusetts 02138

Shock sensitive equipments used in aerospace and marine structures are exposed to complex transient loadings. The transient at an equipment mounting has phase and amplitude spectra that fluctuate. If the equipment has several important modes of vibration, there arises a question of how to combine the transient responses of the several modes of oscillation into a single maximum expected response. The amplitude and phase spectra of the exciting transient are statistically modelled. The slope of the phase spectrum at the resonance frequency of a mode determines the time of the response maximum for that mode, giving a distribution of times of maximum response. This distribution, along with the amplitude spectrum, governs the distribution for maximum of the summed response of modes.

INTRODUCTION

The extreme displacement attained by any portion of the surface of a flexible structure when its attachments (edges, base, etc.) undergo a prescribed transient motion is probably not solvable in a deterministic way, except for quite elementary cases. If calculations of such responses are to include the possibility of irregularities in boundary conditions, uncertainties in resonance frequencies, and variations in the amplitude and phase spectra of the applied transient, then a statistical approach may be most appropriate.

The purpose of this article is to suggest a starting point for statistical analysis of the transient response of multi-dof systems. The emphasis therefore is on developing an approach rather than getting detailed answers. The practicality of this approach will have to be tested in future applications.

THE TRANSIENT VIBRATION OF MULTI-DOF SYSTEMS

We consider the system sketched in Fig. 1. The structural frame undergoes a transient motion $y(t)$. The structure deforms due to its inertial tendency to

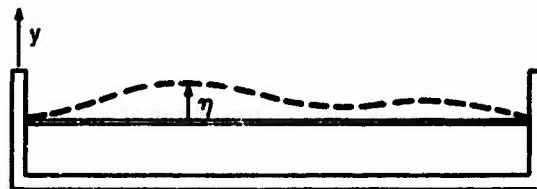


Fig. 1 - Flexible structure excited by frame motion

remain in place. In Fig. 2, we show how the "rigid translation" and surface deformation can be combined to be equivalent to this frame excitation. Thus, the total displacement of the surface is

$$\eta(\vec{p}, t) = y(t) + \eta_1(\vec{p}, t) \quad (1)$$

where the induced displacement $\eta_1(\vec{p}, t)$ is the solution of

$$\rho_s \frac{\partial^2 \eta_1}{\partial t^2} + \beta \frac{\partial \eta_1}{\partial t} + \rho_s \kappa^2 c_l^2 \nabla^2 \eta_1 = -\rho_s \ddot{y}_s \quad (2)$$

The motion η_1 is decomposed into eigenfunctions of the ∇^2 operator that

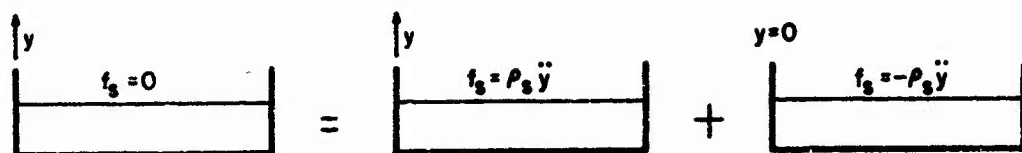


Fig. 2 - Decomposition of frame excitation into rigid body and deformation components

individually satisfy the boundary conditions and are normalized:

$$V^4 \psi_m(\vec{\rho}) = k_m^4 \psi_m(\vec{\rho})$$

$$\int \psi_m(\vec{\rho}) \psi_n(\vec{\rho}) d\vec{\rho} = \delta_{mn} \quad (3)$$

$$\eta_1(\vec{\rho}, t) = \sum_m N_m(t) \psi_m(\vec{\rho})$$

$$N_m = \int d\vec{\rho} \eta_1(\vec{\rho}, t) \psi_m(\vec{\rho}) \quad (4)$$

The time dependence is expressed through the Fourier transform pairs

$$F\{N_m(t)\} = N_m(\omega) = \int_{-\infty}^{\infty} dt e^{i\omega t} N_m(t)$$

$$F^{-1}\{N_m(\omega)\} = N_m(t) = \frac{1}{2\pi} \int_{-\infty}^{\infty} d\omega e^{-i\omega t} N_m(\omega) \quad (5)$$

Similarly, the Fourier transform of the excitation $y(t)$ is the complex function $Y(\omega)$. If we use Eqs. (4) and (5) in Eq. (2), and apply Eq. (3), we get

$$\{-\omega^2(1-i\eta) + \omega_m^2\} U_m(\omega) = \omega^2 y_s(\omega) A_p \langle \psi_m \rangle_\rho \quad (6)$$

where $\omega_m^2 = k_m^4 / \rho_s$, $\eta = \beta / \omega$, A_p is the surface area of the plate, and $\langle \dots \rangle_\rho$ means a spatial average over the surface.

The straightforward way of solving Eq. (6) is to consider a particular displacement $y(t)$ - a rectangular pulse, for example - and a particular structure with known eigenfunctions - a supported plate, for example - and calculate the N_m 's term by term, add them up and find the time history of vibration at any desired position. However, if the structure is not so ideal, and if the fixture motion $y(t)$ is not so simple, then the straightforward approach may not be a practical procedure. In the remainder of this paper, we shall explore an

approximate procedure that may be more useful and economical of effort.

TRANSIENT MOTION OF A SINGLE RESONATOR

The modal displacement is given by

$$N_m(t) = \frac{1}{2\pi} A_p \langle \psi_m \rangle \times \int_{-\infty}^{\infty} d\omega \frac{\omega^2 Y(\omega)}{(\omega - \omega_1)(\omega - \omega_2)} e^{-i\omega t} \quad (7)$$

where $\omega_1 = \omega_m(-1-i\eta/2)$, $\omega_2 = \omega_m(1-i\eta/2)$. The range of integration in Eq. (7) covers three regions of different dynamical behavior: stiffness controlled, $|\omega| < \omega_m$; mass controlled, $|\omega| > \omega_m$; and resonant or damping controlled $|\omega| \approx \omega_m$.

The stiffness controlled term is

$$\frac{1}{2\pi} \int_{-\omega_m}^{\omega_m} \frac{\omega^2 Y(\omega)}{\omega_m^2} e^{-i\omega t} d\omega \equiv -a_m^{(-)}(t) \omega_m^{-2} \quad (8)$$

This is the deformation of the mode due to inertial reaction to fixture acceleration frequency components less than the modal resonance frequency.

The mass controlled term is

$$-\frac{1}{2\pi} \int_{|\omega| > \omega_m} d\omega e^{-i\omega t} Y(\omega) = -y_m^{(+)}(t) \quad (9)$$

These components represent the "limp" behavior of the structure. The inertia of the panel causes the motion at frequency components above ω_m to be the negative of the fixture motion. At these frequencies, the mode "stands still".

The damping controlled motion is that most often calculated in transient

response problems:

$$\frac{1}{2\pi} \int \frac{-\omega^2 Y(\omega) e^{-i\omega t}}{(\omega - \omega_1)(\omega - \omega_2)} d\omega =$$

$$\frac{1}{2\pi} \int_{\text{near } \omega_1} \frac{-\omega_m^2 |Y(\omega_m)| e^{-i\omega t + i\phi(\omega)}}{(\omega - \omega_1)(\omega_1 - \omega_2)} d\omega$$

$$+ \frac{1}{2\pi} \int_{\text{near } \omega_2} d\omega \frac{-\omega_m^2 |Y(\omega_m)| e^{-i\omega t + i\phi(\omega)}}{(\omega_2 - \omega_1)(\omega - \omega_2)}$$

where ϕ is the phase spectrum of Y . We expand $\phi(\omega)$ about $\omega = -\omega_m$ for the first integral

$$\phi(\omega) \approx \phi(-\omega_m) + \phi'(\omega_m) \cdot (\omega + \omega_m)$$

and about $\omega = \omega_m$ for the second

$$\phi(\omega) \approx \phi(\omega_m) + \phi'(\omega_m)(\omega - \omega_m).$$

Since $y(t)$ is real, $\phi(\omega)$ is an odd function of ω and ϕ' is an even function. When these are placed into the integral, the result is

$$\frac{1}{2\pi} \int \dots = \omega_m |y(\omega_m)| e^{-\omega_m \eta t / 2} \times \sin[\omega_m t - \phi(\omega_m)] u_{-1}(t - \tau_m)$$

where the time delay τ_m is the derivative of the excitation phase spectrum, $\tau_m = \phi'(\omega_m)$, and $u_{-1}(t)$ is the unit step function at $t=0$.

The total displacement is found, according to Eq. (1) by adding $y(t)$ to η_1 which yields

$$\begin{aligned} \eta(\vec{p}, t) = & \sum_m A_p \langle \psi_m \rangle \psi_m(\vec{p}) \\ & \times \{ \omega_m |Y(\omega_m)| e^{-\omega_m \eta t / 2} \\ & \times \sin[\omega_m t - \phi(\omega_m)] u_{-1}(t - \tau_m) \\ & + y_m^{(-)}(t) - a_m^{(-)}(t) \omega_m^{-2} \}. \end{aligned}$$

Comparing expressions for $a_m^{(-)}$ and $y_m^{(-)}$, and noting that $\omega^2 \ll \omega_m^2$ for $|\omega| < \omega_m$, we can neglect $a_m^{(-)}/\omega_m^2$ and write

$$\begin{aligned} \eta(\vec{p}, t) = & \sum_m A_p \langle \psi_m \rangle \psi_m(\vec{p}) \\ & \times \{ \omega_m |Y(\omega_m)| e^{-\omega_m \eta t / 2} \\ & \times \sin[\omega_m t - \phi(\omega_m)] u_{-1}(t - \tau_m) \\ & + y_m^{(-)}(t) \}. \end{aligned} \quad (10)$$

Equation (10) forms the basis of our discussion. It says that the structural motion has two components - a quasistatic inertial deflection of each mode due to excitation frequency components below the modal frequency and a resonant oscillation. The amplitude of the resonant component is proportional to the magnitude of the excitation spectrum at the resonance frequency. The phase of the oscillation is governed by the phase of the excitation spectrum. In addition, there is a time delay before onset of the oscillation which is equal to the frequency derivative of the excitation phase at ω_m .

As mentioned above, the parameters ω_m and ϕ_m may be regarded as random parameters, drawn from a statistical population of structures. Similarly, we might also treat $\phi(\omega_m)$ and τ_m as random variables describing a set of possible transients. In Fig. 3, we indicate another way this might be done. The magnitude and phase spectra of a pulse are drawn, and their values as well as the slope $\phi'(\omega)$ at $\omega = \omega_m$ are noted. These become parameters for the summation of modal transient responses. Whether the populations are formed *ad hoc*, or whether they are random samples of a prescribed function, the extreme value of the motion will be a random variable. Thus, a proper expression for the shock spectra will be the confidence coefficient that the extreme value of response does not exceed a certain amplitude. A family of shock spectra will then be generated for each case, and "equivalent" transients (sine pulse, ramp, etc.) would be designated by the confidence coefficient corresponding to the extreme values of response they generate.

In the remainder of this paper, we shall briefly examine two cases - the extreme transient response of a one-dof system to a rectangular pulse - and the space average transient response of a two dimensional plate to the same input.

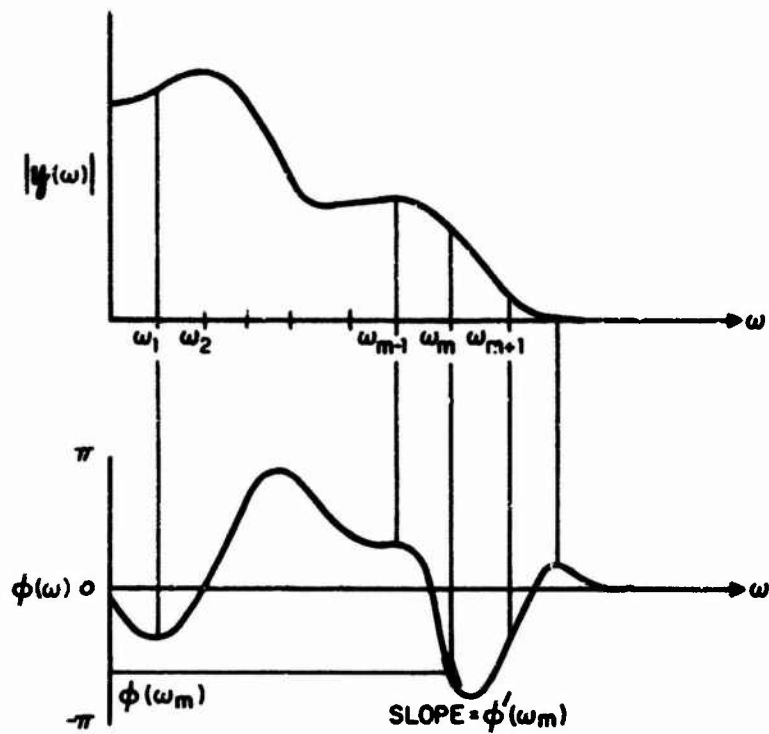


Fig. 3 - Sampling of excitation magnitude and phase spectra by structural resonances

A TEST CASE-RESPONSE OF RESONATOR TO SQUARE PULSE

Suppose that $y(t)$ is the function shown in Fig. 4. Its phase and amplitude spectra are shown in Fig. 5. The time delay of resonant motion is $\phi' = t_0/2$. If $\omega_0 t_0 \ll 1$, then t_0 is small compared to the oscillation period and $Y(\omega_m) = y_0 t_0$. The resonant motion is

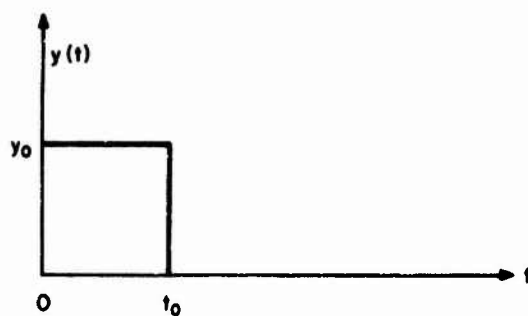


Fig. 4 - Rectangular displacement pulse at base of resonator

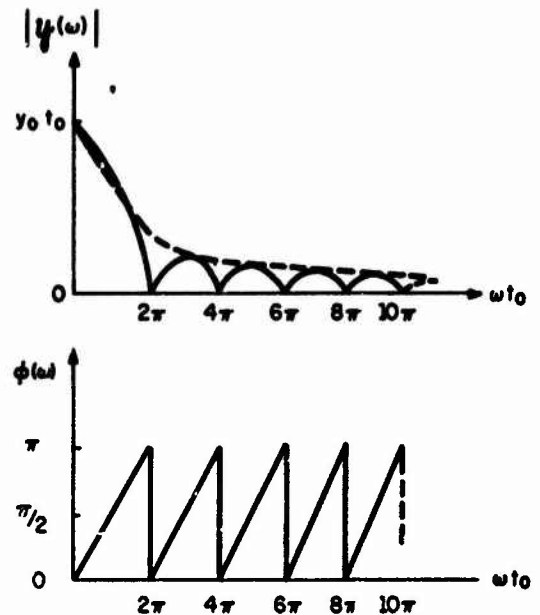


Fig. 5 - Magnitude and phase spectra of rectangular pulse

$$\eta_{res}(t) = y_0 \omega_0 t_0 e^{-\omega_0 \eta t / 2} \times \sin \omega_0 (t - t_0 / 2) u_{-1}(t - t_0 / 2), \quad (11)$$

which has the approximate maximum value $y_0 \omega_0 t_0$, as long as the damping loss factor η is small. The stiffness controlled motion is

$$y_m^{(-)}(t) = \frac{1}{\pi} y_0 \omega_0 t_0 \frac{\sin \omega_0 (t - t_0 / 2)}{\omega_0 (t - t_0 / 2)} \quad (12)$$

where we have assumed $y(\omega) = y_0 t_0 \exp[i\omega t_0 / 2]$. If we combine Eqs. (11) and (12), we get the composite motion shown in Fig. 6a. At the other extreme, when $\omega_0 t_0$ is large, $|Y(\omega)|$ is small, and the mass controlled motion will dominate. The displacement will then be

$$\eta(t) = y(t),$$

as shown in Fig. 6b. Clearly, in this case

$$\eta_{max} = y_0.$$

THE AVERAGE RESPONSE OF A SET OF MODES TO A RECTANGULAR PULSE

Taking guidance from our preceding example, we can generally consider two classes of modes — low-frequency modes of order less than M that have damping

controlled response, and high-frequency modes that move with the base or fix-
ture. Thus

$$\eta(\vec{\rho}, t) = \sum_{m < M} A_p \langle \psi_m \rangle \psi_m \omega_m^2 |Y(\omega_m)| h_m(t) + y(t) \sum_{m > M} A_p \langle \psi_m \rangle \psi_m$$

where

$$h_m(t) = \omega_m^{-1} e^{-\omega_m \eta t / 2} \times \sin\{\omega_m t - \phi(\omega_m)\} u_{-1}(t - \tau_m).$$

However, since $\sum_{all\ m} \langle \psi_m \rangle \psi_m A_p \equiv 1$,

$$\eta(\vec{\rho}, t) - y(t) = \sum_{m < M} A_p \langle \psi_m \rangle \psi_m \times \{\omega_m^2 |Y(\omega_m)| h_m(t) - y(t)\}.$$

The space average displacement relative to the base is

$$\langle \eta(\vec{\rho}, t) \rangle - y(t) = \sum_{m < M} A_p \langle \psi_m \rangle^2 \times \{\omega_m^2 |Y(\omega_m)| h_m(t) - y(t)\}. \quad (13)$$

If the structure is a two dimensional plate, then the ψ_m 's are two dimensional sinusoids with an average

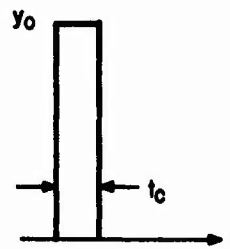
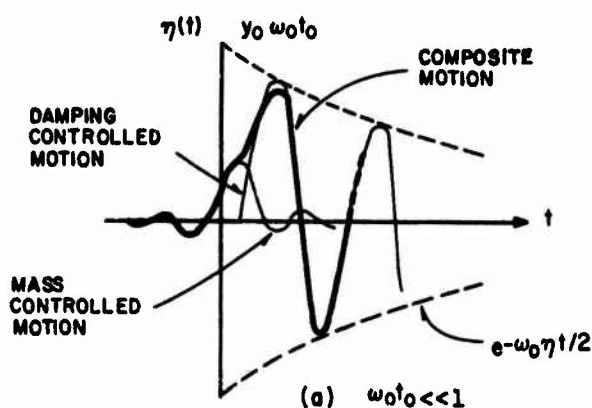


Fig. 6 — Modal displacement when oscillation period is (a) much larger than and (b) much less than the pulse length

value of the order of

$$\langle \psi_m \rangle \approx (k_m^2 A_p^{3/2})^{-1} .$$

Noting that $k_m^2 = \omega_m / \kappa c_L$, and that the ω_m 's are spaced along the frequency axis with an average spacing $\Delta\omega = 4\rho\kappa c_L / A_p$, we can estimate the second sum in Eq. (13) to be

$$y(t) \sum_{m < M} A_p k_m^{-4} A_p^{-3} \leq 10^{-2} y(t) .$$

Since this is only 1% of $y(t)$, we neglect it and get

$$\langle n(p, t) \rangle - y(t) \approx \frac{\kappa^2 c_L^2}{A_p^2} \sum_{m < M} |y(\omega_m)| h_m(t) . \quad (14)$$

We can think of Eq. (14) as a random sampling of $|y|$ by the resonance frequencies ω_m . The calculation can be carried out deterministically for a known pulse shape, or by a Monte Carlo simulation if a more complex form of $Y(\omega)$ is chosen. In any case, Eq. (13) or (14) appears to be a useful starting point for a calculation of the statistics of the transient response of a multidegree of freedom system.

DISCUSSION

Mr. Pakstys (General Dynamics Corp.): Could you explain again how you got the average mode shape for the structure you were considering?

Mr. Lyon: The average mode shape for this structure was calculated on the basis of a simply supported plate, so that the average value of the mode shape goes as one over K squared times the area. That K squared is

proportional to frequency and, since you have the average squared, you get a one over frequency squared in the multiplier on the modal response. This cancels out the other omega squared which was upstairs. It turns out for clamped plates and other kinds of boundary conditions that, for the higher modes in which this kind of analysis would be most applicable, the average value is still very close even though the mode shape is not exactly sinusoidal at the boundaries.

REVIEW OF MODAL SYNTHESIS TECHNIQUES
AND A NEW APPROACH

Shou-nien Hou
Bellcomm, Inc.
Washington, D. C.

Modal synthesis is a technique of determining mode shapes and frequencies of a large discrete mass dynamic system by breaking the system into parts, analyzing the parts, and then re-assembling the total system using selected modal information from the parts. This paper provides an interpretive review of the state-of-art in both research and aerospace applications. Comments on each technique are presented. Based on these studies, a new approach is proposed.

The new approach emphasizes ease of interpretation, mathematical simplicity, accuracy of results, and computer capability. This method can yield a spectrum of system normal frequencies in the range of interest and their associated mode shapes. Actual boundaries are imposed between parts, using either rigid body and free-free elastic modes, or only constrained elastic modes of the parts. Both compatibility and equilibrium at boundaries are satisfied for modal coupling. A simple error control scheme based on convergence of eigenvalues of the total system is used to ensure adequate selection of modes from the parts.

I. INTRODUCTION

Modal information is essential for performing vibration analysis of a structural system. When a structural system is very big, the following difficulties may be encountered:

- A. The number of degrees-of-freedom (DOF) may exceed the available computer capability for eigensolutions.
- B. The structural systems may be too large for modal vibration testing, especially when free-free boundary conditions must be simulated.
- C. A large system, such as a space vehicle, is generally built in parts and each part may be associated with different

contractors in various distant locations. An assemblage of all parts for modal testing is costly, time consuming, and difficult to handle.

Thus, modal synthesis techniques provide the following advantages:

- A. Computer capability is extended to large systems by reducing the size of matrices through partitioning and partial modal coupling.
- B. Modal information may be obtained by analysis or testing of subsystems. The subsystems are easier to handle than the total system, and their analysis or testing may be performed by different sources.

- C. Actual boundary conditions may be introduced in the synthesis scheme.
- D. A design change in one part need only modify the modal data of the changed part. The changed modal data can then be coupled with the remaining unchanged parts.

II. REVIEW OF THE STATE-OF-ART

The concepts of modal synthesis were introduced by W. C. Hurty in a series of papers⁽⁶⁻⁹⁾, the first appearing in 1960. However, no known application was made in the aerospace industry until the mid 60's. Bamford⁽²⁾ completed a computer program using Hurty's method with modification, while Goldman^(3,4) introduced a fresh approach. Since then, modal synthesis has become a popular topic in both research and industrial fields. The key point of modal synthesis is to impose a successful coupling scheme between subsystem modes, such that compatibility and equilibrium can be restored at the interfaces. The main contributors and their techniques are briefly summarized as follows:

- A. Hurty⁽⁶⁻⁹⁾ - This technique contains the following main steps:

1. Partition a system to several subsystems (parts).
2. For each part "i", set constraints at interfaces and compute mode shape matrices as follows:

$[\phi_e]_i$ = fixed constraint elastic normal modes,

$[\phi_c]_i$ = constraint modes,

$[\phi_r]_i$ = rigid body modes,

where $[\phi_c]_i$ are shapes of static displacements when each of the constraints is independently given a unit displacement, and $[\phi_e]_i$ may

contain either all normal mode shapes or the shapes of only the few lowest modes.

Then by defining:

$[\phi]_i = [\phi_r]_i [\phi_c]_i [\phi_e]_i$ = mode shape matrix,

$[m]_i$ = mass matrix,

$[k]_i$ = stiffness matrix,

$[c]_i$ = damping matrix,

$\{f\}_i$ = load matrix,

the generalized subsystem matrices are computed as

$$[m_G]_i = [\phi]_i^T [m]_i [\phi]_i,$$

$$[k_G]_i = [\phi]_i^T [k]_i [\phi]_i,$$

$$[c_G]_i = [\phi]_i^T [c]_i [\phi]_i,$$

$$\{f_G\}_i = [\phi]_i^T \{f\}_i.$$

3. Set up system equations:

$$[m]\{\ddot{p}\} + [c]\{\dot{p}\} + [k]\{p\} = \{f(t)\},$$

where

$$[m] = \begin{bmatrix} [m_G]_1 & & \\ & [m_G]_2 & \\ & & \ddots \end{bmatrix}, [k] = \begin{bmatrix} [k_G]_1 & & \\ & [k_G]_2 & \\ & & \ddots \end{bmatrix}$$

$$[c] = \begin{bmatrix} [c_G]_1 & & \\ & [c_G]_2 & \\ & & \ddots \end{bmatrix}, \{f\} = \begin{Bmatrix} \{f_G\}_1 \\ \{f_G\}_2 \\ \vdots \end{Bmatrix},$$

and $\{p\}$ is an assemblage of generalized coordinates of all subsystems.

4. Set up transformation matrix $[\beta]$ for modal coupling by restoring geometric compatibility at the interfaces. Thus $\{p\}$ can be expressed by its independent coordinates, $\{q\}$, as

$$\{p\} = [\beta] \{q\}.$$

Notice that $[\beta]$ depends entirely upon the geometric configuration of the interfaces.

5. Hence the synthesized total system equations are developed using the transformation matrix $[\beta]$:

$$[M]\{\ddot{q}\} + [C]\{\dot{q}\} + [K]\{q\} = \{F\},$$

where

$$[M] = [\beta]^T [m] [\beta],$$

$$[K] = [\beta]^T [k] [\beta],$$

$$[C] = [\beta]^T [c] [\beta],$$

$$\{F\} = [\beta]^T \{f\}.$$

- B. Bamford⁽²⁾ - A computer program based on Hurty's techniques was developed. In its subsystem processing, "attachment modes" are added for describing the shapes of motion caused by concentrated loads at unconstrained points. Thus for any subsystem "i", the mode shape matrix is defined as

$$\{\phi\}_i = \{\phi_r | \phi_c | \phi_a | \phi_e\}_i,$$

where $\{\phi_a\}_i$ contains all attachment mode shapes.

- C. Bajan, Feng, and Jaszlics⁽¹⁾ - Technique involves modal coupling and modal substitution. The former couples the subsystem modes to obtain the total system modes, while the latter provides an iteration scheme for improving accuracy through error analysis. Key steps are as follows:

1. Perform modal analysis on each subsystem i, which has known mass matrix $[m]_i$ and stiffness matrix $[k]_i$,

and obtain its mode shapes as

$$\{\phi\}_i = \{\phi_c | \phi_e\}_i,$$

where $\{\phi_c\}_i$ contains all constraint modes and $\{\phi_e\}_i$ contains all elastic modes with fixed interfaces.

2. Subsystem matrices are assembled as

$$[m] = \begin{bmatrix} [m]_1 & & \\ & [m]_2 & \\ & & \ddots \end{bmatrix}, \quad [k] = \begin{bmatrix} [k]_1 & & \\ & [k]_2 & \\ & & \ddots \end{bmatrix},$$

$$\{\phi\} = \begin{bmatrix} \{\phi\}_1 \\ \{\phi\}_2 \\ \vdots \end{bmatrix}.$$

3. Define matrix $[c]$, such that

$$\{u_s\} = [c]\{u\},$$

where $\{u_s\}$ is an assemblage of displacement vectors $\{u_s\}_i$ of all subsystems, and $\{u\}$ is the displacement vector of the system as a whole.

4. A matrix can be generated as

$$[T]_t = \{\phi\}[c] = [T_c | T_r | T_d].$$

Where $[T_c]$ contains all constraint modes, and $[T_r]$ contains subsystem elastic modes retained for modal coupling, while remainders $[T_d]$ are deleted. Thus the partial modal coupling is done by solving

$$[M]\{\ddot{q}\} + [K]\{q\} = \{0\},$$

where $[M] = [T]^T [m] [T]$,

$$[K] = [T]^T [k] [T],$$

$$[T] = [T_c \ T_r].$$

Solutions give

$$\{q\} = [Q]\{\lambda\},$$

where $[Q]$ and $\{\lambda\}$ are the participation matrix and the vector of generalized coordinates, respectively. Hence

$$\{u_s\} = ([T] [Q])\{\lambda\} = [\psi]\{\lambda\},$$

where $[\psi]$ contains approximate mode shapes of the system through such partial coupling.

5. Set a new $[T]$ by retaining certain modes from $[\psi]$ and certain unused modes of $[T_d]$, which are defined as objective modes $[\psi_0]$ and replacement modes $[T_{rep}]$, respectively:

$$[T] = [\psi_0 \ T_{rep}].$$

Then go through modal analysis as shown in step 4, and get a new $[T]$. Such a process, which is called "modal substitution" will be repeated until satisfactory eigenvalues are obtained.

Replacement modes may also be obtained from deleted modes in $[\psi]$ of previous cycles when all modes in $[T_d]$ are used. Selection of replacement modes are based on their individual contribution of error to the eigensolution, which is automatized through a "modal selection algorithm".

- D. Goldman^(3,4) - Use rigid body modes and free-free elastic modes of parts for synthesis. Modal couplings are performed by eliminating the terms of internal forces at connection

interfaces from equations of motion through the compatibility relations. Key steps are as follows:

1. Modal equations of motion of all subsystems are assembled as:

$$\{\ddot{p}_e\} + [\omega_e^2]\{p_e\} = [\phi_{eb}]^T \{F_c\},$$

$$\{\ddot{p}_r\} = [M_r]^{-1} [\phi_{rb}]^T \{F_c\},$$

where

$\{p_e\}$ = Generalized coordinates for elastic motions,

$\{p_r\}$ = Generalized coordinates for rigid body motions,

$[\omega_e^2]$ = Frequencies of elastic modes in subsystems,

$[\phi_{eb}]$ = Elastic mode shapes at interfaces of subsystems with unit generalized mass,

$[\phi_{rb}]$ = Rigid body mode shapes at interfaces of subsystems,

$\{F_c\}$ = All internal forces at connection interfaces.

2. The geometric compatibility regarding displacements at the connection interfaces provides relations as

$$[\phi_{eb}]\{p_e\} + [\phi_{rb}]\{p_r\} = \{0\}.$$

3. Multiplying the first equation of motion by $[\phi_{eb}]$ and the second one by $[\phi_{rb}]$, the sum of these two equations gives

$$\{F_c\} = [E]^{-1} [\phi_{eb}] [\omega_e^2] \{p_e\},$$

$$\text{where } [E] = [\phi_{eb}][\phi_{eb}]^T$$

$$+ [\phi_{rb}][M_r]^{-1} [\phi_{rb}]^T.$$

4. Thus, replacing $\{F_c\}$ by the above expression, the first equation of motion becomes

$$\{\ddot{p}_e\} + [L]\{p_e\} = \{0\},$$

$$\text{where } [L] = [\omega_e]([I]$$

$$- [\phi_{eb}]^T [E]^{-1} [\phi_{eb}]) [\omega_e].$$

This gives the form of eigensolution for the whole system.

E. Martin Marietta Co., Denver, Colorado⁽⁵⁾ - Empirical coupling techniques are developed for computing modal data of a space vehicle which contains a main structure and several branch structures. Key steps are as follows:

1. Each branch "i" is treated as a cantilever by fixing it at its attaching point to the main structure, and then performing a modal analysis for each branch through the following equations of motions:

$$[m_b] \{\ddot{u}_b\}_i + [k_b] \{u_b\}_i = \{0\},$$

where $[m_b]$, $[k_b]$, and $\{u_b\}$ are the mass matrix, stiffness matrix, and displacements of branch "i". The mode shapes so obtained are defined as $[\phi_b]_i$, and the generalized coordinates are $\{p_b\}_i$.

2. Then perform modal analysis for the main structure by treating all branches as rigid appendages:

$$[m_m]\{\ddot{u}_m\} + [k_m]\{u_m\} = \{0\},$$

where $[m_m]$, $[k_m]$ and $\{u_m\}$ are the mass matrix, stiffness matrix, and displacements for the main structure. The mode shapes so obtained are defined as $[\phi_m]$, and the generalized coordinates are $\{p_m\}$.

3. Assume that motion in any branch "i" is given by $\{u_b\}_i$ plus the rigid body motion $[T]_i \{u_m\}$ caused by the motion at the attaching point. Thus

$$\{u\} = \begin{bmatrix} I & & \\ T_1 & I & \\ T_2 & & I & \\ \vdots & & & \ddots & \\ \vdots & & & & \ddots & \end{bmatrix} \begin{Bmatrix} \{u_m\} \\ \{u_b\}_1 \\ \{u_b\}_2 \\ \vdots \end{Bmatrix}$$

$$= \begin{bmatrix} [\phi_m] & & & \\ [T_1][\phi_m] & [\phi_b]_1 & & \\ [T_2][\phi_m] & & [\phi_b]_2 & \\ \vdots & & & \ddots \end{bmatrix} \begin{Bmatrix} \{p_m\} \\ \{p_b\}_1 \\ \{p_b\}_2 \\ \vdots \end{Bmatrix} = [\delta] \{p\}$$

4. Thus the system equation for eigensolution after modal coupling is

$$[M]\{\ddot{p}\} + [K]\{p\} = \{0\},$$

where

$$[M] = [\delta]^T \begin{bmatrix} [m_m] & & & \\ & [m_b]_1 & & \\ & & [m_b]_2 & \\ & & & \ddots \end{bmatrix} [\delta],$$

$$[K] = [\delta]^T \begin{bmatrix} [K_m] & & & \\ & [K_b]_1 & & \\ & & [K_b]_2 & \\ & & & \ddots \end{bmatrix} [\delta].$$

III. COMMENTS ON EXISTING TECHNIQUES

- A. Hurty and Bamford were concerned with determining response after obtaining modal information by synthesis. However, solving for modal information alone, the loading and damping terms introduced by Hurty and the attachment modes introduced by Bamford need not be included in the synthesis scheme. The reasons are:

- (1) Only the homogeneous solutions are needed from the equations of motion.
- (2) Damping effects to normal frequencies are negligible if the system is lightly damped. For heavily damped cases, the equations of motion will be coupled and solutions will be difficult to obtain.

However, if modal information of parts are obtained by testing, and such testing must introduce constraints which may not be at the interface between parts, Bamford's techniques will provide data for synthesis and a check of testing.

- B. Bajan, Feng, and Jaszlics have laid out a clear scheme for obtaining constraint modes. Their ideas for automatic modal selection by error analysis and substitution scheme are impressive. However, formulations are complicated and involve a lot of computations. The number of objective modes and replacement modes used for each cycle remains arbitrary. In addition, the matrix $[c]$ is based on relations in cartesian coordinates between the whole system and subsystems and is not the coupling between subsystem modal vectors.

- C. The most attractive point of Goldman's technique is the use of free-free subsystem modes. Thus constraint modes as used by other techniques are not needed. In addition,

the method always leads to an eigensolution of a single matrix $[L]$ (see Section II E.4.). Thus the eigensolution for the synthesized total system equations are easy to handle. Since Goldman's system equation of elastic motions after coupling has a number of DOF equal to the sum of elastic DOF of the subsystems, the total DOF of the fully coupled system is not the same as the actual DOF of the system. This may introduce error.

- D. Techniques used by Martin Marietta Company are empirical in nature and may yield close solutions when the branch systems are of far less effect to the main system in terms of mass and frequency range. In addition, since no relative motions are allowed among DOF's at the interface (constraint modes are not used), the number of mass points at the connection interface should be as few as possible; the best is one.

IV. THE NEW APPROACH

Based on previous studies, a new approach emphasizing ease of interpretation, mathematical simplicity, accuracy of results, and potential computer capability is presented. This new approach is guided by the following considerations:

Whenever eigensolution routines are capable of handling free-free systems, subsystems should be unconstrained, unless constraints physically exist at the boundary. Thus, computation for constraint modes may be eliminated if free-free elastic modes are introduced from the parts.

The main goal of the approach is to yield modal information, and thus forcing functions and damping need not be considered. Concentrating on undamped free vibration will simplify the formulation and the computation scheme.

Connection interfaces between parts should be simple with as few DOF involved as possible.

Rigid body modes of subsystems are included since they have significant effect on the lowest elastic modes obtained through modal coupling. However, the effects on the higher modes are negligible.

The computation scheme should include a method for selecting proper modes, and in an adequate number from each subsystem for partial modal coupling. The method uses a simple error analysis technique, the main purpose of which is to insure convergence of results.

A. Subsystem Analysis

Partition a structural system in parts. Each part is considered as free-free unless it is physically constrained. Then perform modal analysis of each part (say part i) to obtain its normal frequencies $\{\omega_i^2\}$ and mode shapes $\{\phi_i\}$. The portion of $\{\phi_i\}$ at interfaces is designated as $\{\phi_{ic}\}$. Rigid body modes are treated as free-free elastic modes having zero frequencies. All mode shapes are normalized to unit generalized mass. For convenience of explanation, suppose a system is partitioned into two parts, A and B, which have n_A and n_B modes participating in the synthesis, respectively. Let n_r be the number of degrees-of-freedom at the connection interface.

For part A, we have

$$\{\ddot{p}_A\} + [\omega_A^2]\{p_A\} = [\phi_{AC}]^T \{F_A\} \quad (1)$$

and

$$\{u_A\} = [\phi_A]\{p_A\}, \quad (2)$$

where

$\{p_A\}$ = Vector of generalized coordinates

$\{u_A\}$ = Vector of displacements in physical coordinates

$\{F_A\}$ = Internal forces acting on the connection interface between parts.

Let $\{u_{AC}\}$ be the portion of $\{u_A\}$ on the connection interface, and the remaining portion be $\{u_{Ar}\}$, equation (2) can be partitioned as

$$\begin{Bmatrix} u_{Ar} \\ u_{AC} \end{Bmatrix} = \begin{bmatrix} \phi_{Ar} \\ \phi_{AC} \end{bmatrix} \{p_A\}. \quad (3)$$

Using the same expressions for part B, we have

$$\{\ddot{p}_B\} + [\omega_B^2]\{p_B\} = [\phi_{BC}]^T \{F_B\}, \quad (4)$$

$$\{u_B\} = [\phi_B]\{p_B\}, \quad (5)$$

and

$$\begin{Bmatrix} u_{Br} \\ u_{BC} \end{Bmatrix} = \begin{bmatrix} \phi_{Br} \\ \phi_{BC} \end{bmatrix} \{p_B\}. \quad (6)$$

B. Compatibility Conditions

The required conditions for geometric compatibility at the connection interface provide n_r equations as follows:

$$\{u_{AC}\} = \{u_{BC}\}, \quad (7)$$

or

$$[\phi_{AC}]\{p_A\} = [\phi_{BC}]\{p_B\}. \quad (8)$$

Letting $n_A > n_r$, $[\phi_{AC}]$ can be partitioned as

$$[\phi_{AC}] = [\phi_{AC}^S \mid \phi_{AC}^r], \quad (9)$$

where $[\phi_{AC}^S]$ is a square matrix, and $[\phi_{AC}^r]$ contains the remainders. Thus, from equation (8), we have

$$[\phi_{AC}^S] [\phi_{AC}^r] \begin{Bmatrix} p_A^S \\ p_A^r \end{Bmatrix} = [\phi_{BC}^r] p_B^r, \quad (10)$$

and

$$\begin{aligned} (p_A^S) &= -[\phi_{AC}^S]^{-1} [\phi_{AC}^r] (p_A^r) \\ &+ [\phi_{AC}^S]^{-1} [\phi_{BC}^r] (p_B^r). \end{aligned} \quad (11)$$

This gives an expression for $(n_A + n_B)$ generalized coordinates $\{p\}$ in terms of $(n_A + n_B - n_r)$ independent coordinates $\{q\}$:

$$\{p\} = [T] \{q\}, \quad (12)$$

where

$$\{p\} = \begin{Bmatrix} p_A \\ p_B \end{Bmatrix} = \begin{Bmatrix} p_A^S \\ p_A^r \\ p_B^r \end{Bmatrix}, \quad \{q\} = \begin{Bmatrix} p_A^r \\ p_B^r \end{Bmatrix}, \quad (13)$$

$$[T] = \begin{bmatrix} -[\phi_{AC}^S]^{-1} [\phi_{AC}^r] & [\phi_{AC}^S]^{-1} [\phi_{BC}^r] \\ [I] & [0] \\ [0] & [I] \end{bmatrix} \quad (14)$$

C. System Equations by Modal Coupling

The uncoupled modal information of the parts can be assembled as follows:

$$\begin{aligned} \begin{Bmatrix} p_A \\ p_B \end{Bmatrix} + \begin{bmatrix} \frac{2}{\omega_A^2} & 0 \\ 0 & \frac{2}{\omega_B^2} \end{bmatrix} \begin{Bmatrix} p_A \\ p_B \end{Bmatrix} \\ = \begin{bmatrix} T & 0 \\ \phi_{AC}^r & \phi_{BC}^r \end{bmatrix} \begin{Bmatrix} F_A \\ F_B \end{Bmatrix} \end{aligned} \quad (15)$$

By substituting compatibility equation (12) and then restoring symmetry, we have

$$\begin{aligned} [T]^T [T] (\ddot{q}) + [T]^T \begin{bmatrix} \frac{2}{\omega_A^2} & 0 \\ 0 & \frac{2}{\omega_B^2} \end{bmatrix} [T] (q) \\ = [T]^T \begin{bmatrix} T & 0 \\ \phi_{AC}^r & \phi_{BC}^r \end{bmatrix} \begin{Bmatrix} F_A \\ F_B \end{Bmatrix}. \end{aligned} \quad (16)$$

Since the term on the right hand side of equation (16) is equal to zero (see next section), we get $(n_A + n_B - n_r)$ coupled system equations as:

$$[m] \ddot{q} + [k] q = \{0\}, \quad (17)$$

where

$$\begin{aligned} [m] &= \text{Pseudo mass matrix} \\ &= [T]^T [T], \end{aligned}$$

$$[k] = \text{Pseudo stiffness matrix}$$

$$= [T]^T \begin{bmatrix} \frac{2}{\omega_A^2} & 0 \\ 0 & \frac{2}{\omega_B^2} \end{bmatrix} [T].$$

Performing a modal analysis of equation (17), we obtain normal frequencies of the system and shape vectors $\{\phi\}$. Hence, the mode shapes of the total system are

$$\{\phi\} = \begin{bmatrix} \phi_A & 0 \\ 0 & \phi_B \end{bmatrix} [T] \{\psi\}. \quad (18)$$

D. Equilibrium Check

Since $\{F_A\}$ and $\{F_B\}$ are equal and opposite internal forces acting at the connection interface, and since there are no external forces imposed on the system, the system must be in equilibrium at the interface if the right hand side of equation (17) is truly a zero vector. From the right hand side of equation (16), we have

$$\begin{aligned}
& [T]^T \left[\begin{array}{c|c} \phi_{AC}^T & 0 \\ \hline 0 & \phi_{BC}^T \end{array} \right] \begin{Bmatrix} F_A \\ F_B \end{Bmatrix} \\
& = \left[\begin{array}{cc|cc} -[\phi_{AC}^r]^T & [\phi_{AC}^s]^T & -1, T & [I] \\ \hline [\phi_{BC}^r]^T & [\phi_{AC}^s]^T & -1, T & [0] \end{array} \right] \left[\begin{array}{c|c} [\phi_{AC}^s]^T & [0] \\ \hline [\phi_{AC}^r]^T & [0] \\ \hline [0] & [\phi_{BC}^T]^T \end{array} \right] \begin{Bmatrix} F_A \\ F_B \end{Bmatrix} \\
& = \left[\begin{array}{cc|c} -[\phi_{AC}^r]^T & [\phi_{AC}^s]^T & -1, T \\ \hline [\phi_{BC}^r]^T & [\phi_{AC}^s]^T & -1, T \end{array} \right] \left[\begin{array}{c} [\phi_{AC}^s]^T + [\phi_{AC}^r]^T \\ \hline [\phi_{BC}^T]^T \end{array} \right] \begin{Bmatrix} F_A \\ F_B \end{Bmatrix} \\
& = \left[\begin{array}{c|c} [0] & \\ \hline [\phi_{BC}^T]^T (F_A) + [\phi_{BC}^T]^T (F_B) & \end{array} \right] = \begin{Bmatrix} 0 \\ 0 \end{Bmatrix} \quad (19)
\end{aligned}$$

(NOTE: $\{F_A\} + \{F_B\} = \{0\}$ at interface)

Thus both compatibility and equilibrium conditions are satisfied at the connection interface.

E. Selection of Subsystem Modes Using Error Index

As we know, the real advantage of modal synthesis can only be achieved by partial modal coupling, that is using a small number of selected subsystem modes. However, the accuracy of the results is also decreased when fewer modes are used. Thus, a proper selection scheme is essential.

It has been found that the low (or high) frequency modes of subsystems have only dominant effect on the low (or high) frequency modes of the overall system, and the sum of all frequency squares (eigenvalues) of a system is an invariant. Thus a simple selection scheme can be set up as follows:

1. First, rearrange mode shapes and frequencies of each subsystem into an ascending order of their frequencies. Then divide the modes in each subsystem into an equal number of groups.

2. Start synthesis by using modes in the first group of all subsystems. Then sum up first n eigenvalues λ_{1k} ($k=1,2,\dots,n$) obtained from synthesis and call it C_1 :

$$C_1 = \sum_{k=1}^n \lambda_{1k} \quad (20)$$

3. More modes are used by taking successive group of modes from all subsystems. In each cycle, compute

$$C_i = \sum_{k=1}^n \lambda_{ik} \quad (21)$$

4. Thus the "Index of Convergence" is defined as

$$E_i = \left| \frac{C_{i+1} - C_i}{C_{i+1}} \right|, \quad (22)$$

which will eventually go below a predefined tolerance level when a sufficient number of modes are involved. Since all frequencies in each subsystem have been rearranged, the magnitude change in each synthesized frequency is in a monotonic fashion. Thus such an index will indicate the relative rate of improvement in frequencies when additional groups of modes are used.

F. Conclusions

In summary, this new approach offers the following advantages and special features:

1. It is easy to interpret mathematically and physically. Such simplicity makes computer programming easier.

2. Both geometric compatibilities and force equilibrium are satisfied at interfaces between parts.
3. Mode shapes and normal frequencies from parts are the only input. Constraint modes from parts are not needed.
4. The use of free-free or constrained elastic modes from the parts depends on whether physical constraints actually exist at the interface.
5. A spectrum of system normal frequencies in the range of interest and their associated mode shapes can be computed.
6. Rigid body modes are automatically included and are treated as if they are the first few free-free elastic modes with zero frequencies. They can be included or omitted for partial modal synthesis.

Three numerical examples are given in the Appendix. The first example uses total coupling for verifying the theory of the new approach. The second example demonstrates the selection of subsystem modes for partial coupling, such that modes of the total system in the frequency range of interest can be synthesized efficiently. The third example demonstrates the synthesis scheme for obtaining higher frequency modes.

APPENDIX

Numerical Examples

EXAMPLE 1

This example is intended to demonstrate the simplicity of the synthesis technique using the new approach, and also to show the accuracy of the results through total coupling. A comparison of synthesized results with direct solution of the total system is presented.

Given an elastic, uniform section, homogeneous, free-free beam, where:

L = total length = 40 in.,

r = radius of cross section = 1 in.,

ρ = weight density = 2 lbs. per cu. in.,

E = elastic modulus = 1×10^4 psi,

ν = Poisson ratio = 0.3,

A = area of cross section = 3.1416 = sq. in.,

I = sectional moment of inertia
 $\frac{1}{4} \pi r^4 = 0.7854 \text{ in.}^4$

To compute the dynamic properties through modal synthesis, partition the beam into two identical parts, and each part into ten identical segments having a length $l = 2$ in. The mass of each segment is lumped into its two ends, which are considered as nodes. Consider each node to have only two degrees of freedom, lateral translation and rotation. Thus each part has 22 DOF and 11 nodal points as shown in Figure 1.

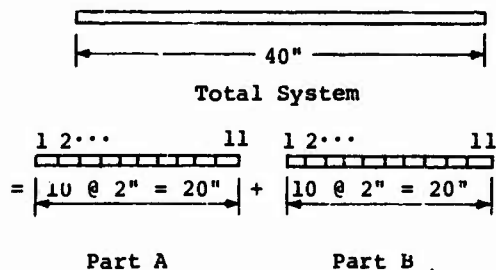


FIGURE 1

Computing frequencies and modes shapes of the parts, we have

$$[\omega_A^2] = [\omega_B^2] = \begin{bmatrix} 0 & & & & \\ & 0 & & & \\ & & 1,380 & & \\ & & & 9,765 & \\ & & & & \ddots \\ & & & & & 6,154,535 \end{bmatrix}$$

$$[\phi_A] = [\phi_B]$$

$$= \begin{bmatrix} 0.2995 & -2.9947 & 3.3432 & \dots & 1.6239 & -1.6140 \\ 0 & 0.2995 & -0.7934 & \dots & 6.7683 & -6.7255 \\ 0.2995 & -2.3955 & 1.7703 & \dots & 0.3842 & 0.3795 \\ \vdots & \vdots & \vdots & \ddots & \vdots & \vdots \\ 0.2995 & 2.9947 & 3.3432 & \dots & 1.6245 & 1.6142 \\ 0 & 0.2995 & 0.7934 & \dots & 6.7709 & -6.7266 \end{bmatrix}$$

Notice that there are two rigid body modes in each part. The interface compatibility conditions set by Equation (7) are that the displacement and rotation at node 11 of part A should be equal to the displacement and rotation at node 1 of part B. Thus the total system after synthesis has 42 DOF. According to Equations (8) and (9), $[\phi_{AC}]$ contains the last two rows of $[\phi_A]$ and $[\phi_{BC}]$ contains the first two rows of $[\phi_B]$. The $[\phi_{AC}]$ is further partitioned into a square sub-matrix $[\phi_{AC}^S]$ and the remainder $[\phi_{AC}^r]$:

$$[\phi_{AC}] =$$

$$\begin{bmatrix} 0.2995 & 2.9947 & 3.3432 & \dots & 1.6245 & 1.6142 \\ 0 & 0.2995 & 0.7934 & \dots & 6.7709 & -6.7266 \end{bmatrix}$$

$$\begin{bmatrix} S & r \\ \phi_{AC} & \phi_{AC} \end{bmatrix}$$

$$[\phi_{BC}] =$$

$$\begin{bmatrix} 0.2995 & -2.9947 & 3.3432 & \dots & 1.6239 & -1.6140 \\ 0 & 0.2995 & -0.7934 & \dots & 6.7683 & -6.7255 \end{bmatrix}$$

The 44 x 42 transformation matrix [T] for total coupling can be computed by Equation (14) as

$$[T] = \begin{bmatrix} -[\phi_{AC}^S]^{-1} [\phi_{AC}^r] & [\phi_{AC}^S]^{-1} [\phi_{BC}^r] \\ [I] & [0] \\ [0] & [I] \end{bmatrix}$$

$$= \begin{bmatrix} 15.33 & 34.01 & 51.85 & \dots & -220.59 & 219.12 \\ -2.65 & -4.44 & -6.12 & \dots & 22.60 & -22.46 \\ 1 & & & & & \\ & 1 & & & & \\ & & 1 & \dots & 1 & \\ & & & & & 1 \end{bmatrix}$$

Then compute 42 x 42 pseudo mass and stiffness matrices as

$$[m] = [T]^T [T]$$

$$[k] = [T]^T \begin{bmatrix} \omega_A^2 & & \\ & \ddots & \\ & & \omega_B^2 \end{bmatrix} [T] ,$$

and perform modal analysis for this synthesized pseudo system as shown in Equations (17) and (18).

Table 1 gives a comparison of frequencies between synthesis results and the results directly obtained from analysis of 42 DOF discretized and slopes in the first elastic mode shape (the 3rd mode). Mode shapes given by Reference (12) are also listed for comparison.

TABLE 1

COMPARISON OF FREQUENCIES (cps)

Mode No.	Direct Solution	Synthesis Results
1	0.00	0.00
2	0.00	0.00
3	1.53	1.54
4	4.17	4.18
5	8.09	8.09
6	13.21	13.22
7	19.48	19.48
8	26.83	26.84
9	35.20	35.20
10	44.51	44.52
15	103.0	103.0
20	172.8	172.8
25	252.6	252.6
30	315.5	315.5
35	361.1	361.1
40	382.3	382.3
42	394.8	394.8

TABLE 2

COMPARISON OF MODE SHAPES

(First Elastic Mode)

(A) TRANSLATIONS

Location of Node	Direct Solution	Synthesis Results	References (12)
0.0L	2.001	2.000	2.000
0.1L	1.071	1.072	1.074
0.2L	0.190	0.192	0.196
0.3L	-0.549	-0.546	-0.544
0.4L	-1.045	-1.040	-1.041
0.5L	-1.220	-1.216	-1.216
0.6L	-1.046	-1.042	-1.041
0.7L	-0.550	-0.552	-0.544
0.8L	0.189	0.184	0.196
0.9L	1.069	1.058	1.074
1.0L	1.999	1.982	2.000

TABLE 2 - Continued
COMPARISON OF MODE SHAPES
(First Elastic Mode)

(B) ROTATIONS

Location of Node	Direct Solution	Synthesis Results	Reference (12)
0.0L	-1.965	-1.973	-1.965
0.1L	-1.929	-1.939	-1.934
0.2L	-1.714	-1.737	-1.748
0.3L	-1.332	-1.332	-1.341
0.4L	-0.725	-0.725	-0.730
0.5L	0.001	0	0
0.6L	0.723	0.725	0.730
0.7L	1.331	1.332	1.341
0.8L	1.739	1.737	1.748
0.9L	1.929	1.923	1.934
1.0L	1.965	1.95	1.965

EXAMPLE 2

This example is intended to show how to select sufficient modes from parts for partial modal coupling, such that total system modes in the range of interest can be efficiently computed.

Given the same free-free beam as in Example 1 except for a hinge at midspan, if we partition the beam through this hinge and discretize the two parts the same way as Example 1, each part will also have 11 nodes and 22 DOF. The only difference is that there is only one DOF (the translation) instead of two at the interface for compatibility requirements. Since rotation of two parts at the interface may be different, the total system has 43 DOF instead of 42.

Suppose that we are interested in the lowest seven modes. The first step is to arrange modes of the two parts individually in ascending order, according to the magnitude of their frequencies. Then break the 22 modes (including 2 rigid body modes) of each part into groups:

Group No.	Modes
1	1, 2, 3, 4
2	5, 6, 7
3	8, 9, 10
4	11, 12, 13
5	14, 15, 16
6	17, 18, 19
7	20, 21, 22

Take group 1 modes from both parts for synthesis. Results will yield the 7 lowest modes of the total system. Their eigenvalues (λ_{1k}) are:

0, 0, 0, 697, 1380, 7108, 9765.

The three zeros yield three rigid body modes as shown in Figure 2.

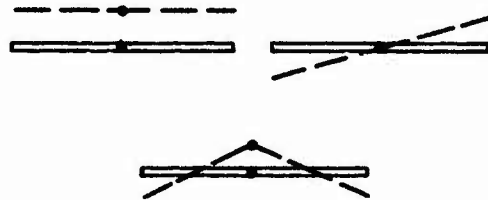


FIGURE 2

Hence

$$C_1 = \sum_{k=1}^7 \lambda_{1k} = 0 + 0 + 0 + 697 + 1380 + 7108 + 9765 = 18950.$$

Then add group 2 modes to group 1 for both parts, and synthesize again. Results yield the lowest 13 modes of the total system. However, we only take the same lowest 7 eigenvalues (λ_{2k}) and sum them:

$$C_2 = \sum_{k=1}^7 \lambda_{2k} = 18745$$

Thus the first "index of convergence" is

$$E_1 = \left| \frac{C_2 - C_1}{2} \right| = \left| \frac{18745 - 18950}{2} \right| = 109 \times 10^{-4}.$$

If additional groups of modes in both parts participate in the synthesis, we have

$$C_3 = 18739.625 \quad E_2 = 5.252 \times 10^{-4},$$

and

$$C_4 = 18739.730 \quad E_2 = 0.056 \times 10^{-4}.$$

Notice that an increase of the same number of modes from parts yields less accuracy improvement of the synthesis results, and at the same time the size of the coupled system gets larger and larger. For this particular case, since E_1 is already small enough, we may stop adding subsystem modes right after computing E_1 . This means using the lowest 7 modes (about one third of 22) from each part for synthesis. Frequencies (cps) so obtained are compared with total coupling results (22 modes from each part) as shown in Table 3.

TABLE 3

Mode No.	7 Modes From Each Part	Total Coupling
1	0.	0.
2	0.	0.
3	0.	0.
4	4.183	4.183
5	5.913	5.914
6	13.229	13.223
7	15.727	15.727

EXAMPLE 3

For the same beam as example 2, if all the modes of the total system are required, we can perform several shifts in the synthesis. Example 2 shows that 7 modes from each part will yield satisfactory results, and since we know that n_A modes from part A and n_B modes from part B with $n_r = 1$ at the interface will yield $(n_A + n_B - n_r)$ modes of the total system after synthesis, three shifts of synthesis should be sufficient, as shown in Table 4.

TABLE 4

Synthesis Shift No.	Modes From Part A	Modes From Part B	No. of Modes Synthesized
1	1 - 7	1 - 8	14
2	8 - 15	8 - 14	14
3	15 - 22	15 - 22	15

Total = 43

Frequencies (cps) so obtained are compared with total coupling results as shown in Table 5.

TABLE 5

(A) First Shift:

Mode No.	Partial Coupling	Total Coupling
1	0.	0.
2	0.	0.
3	0.	0.
4	4.183	4.183
5	5.913	5.914
6	13.227	13.223
7	15.727	15.727
8	26.855	26.840
9	29.712	29.713
10	44.556	44.520
11	47.304	47.304
12	65.820	65.739
13	68.089	68.090
14	90.836	89.956

(B) Second Shift:

15	91.683	91.683
16	109.220	116.537
17	117.613	117.613
18	141.034	144.646
19	145.171	145.171
20	171.596	172.764
21	172.917	172.917
22	221.105	221.105
23	221.105	221.105
24	238.746	239.333
25	239.388	235.388
26	263.263	266.025

TABLE 5 - Continued

(B) Second Shift - Continued

<u>Mode No.</u>	<u>Partial Coupling</u>	<u>Total Coupling</u>
27	266.304	266.304
28	289.750	291.879

(C) Third Shift:

29	292.520	292.520
30	295.087	315.529
31	316.616	316.616
32	319.742	336.304
33	337.862	337.862
34	341.014	353.738
35	355.725	355.725
36	358.416	367.466
37	369.736	369.736
38	371.549	377.147
39	379.287	379.287
40	389.971	382.303
41	394.780	394.780
42	394.808	394.808
43	394.836	394.836

BIBLIOGRAPHY

1. Bajan, R. L., Feng, C. C. and Jaszlics, I. J., "Vibration Analysis of Complex Structural Systems by Modal Substitution," The Shock and Vibration Bulletin, No. 39, January 1969, Naval Research Laboratory, Washington, D. C.
2. Bamford, R. M., "A Modal Combination Program for Dynamic Analysis of Structures," TM 33-290, Rev. No. 1, July 1967, Jet Propulsion Laboratory, Pasadena, California.
3. Goldman, R. L., "Vibration Analysis by Dynamic Partitioning," RM-305, May 1966, Martin Co., Baltimore, Maryland.
4. Goldman, R. L., "Vibration Analysis by Dynamic Partitioning," AIAA Journal, Vol. 7, No. 6, June, 1969.
5. Gwin, L. B., "Methodology Report for Docking Loads," TR ED-2002-595, August 1968, Martin Marietta Corp., Denver, Colorado.
6. Hurty, W. C., "Vibration of Structural Systems by Component Mode Synthesis," Proc. Am. Soc. Civil Engrs., Vol. 86, EM4, August 1960.
7. Hurty, W. C., "Dynamic Analysis of Structural Systems by Component Mode Synthesis," TR 32-530, January 1964, Jet Propulsion Laboratory, Pasadena, California.
8. Hurty, W. C., "Dynamic Analysis of Structural Systems Using Component Modes," AIAA Journal, Vol. 3, No. 4, April 1965.
9. Hurty, W. C., "A Criterion For Selecting Realistic Natural Modes of a Structure," TR 33-364, November 1967, Jet Propulsion Laboratory, Pasadena, California.
10. McAleese, J. D., "Method for Determining Normal Modes and Frequencies of a Launch Vehicle Utilizing Its Component Normal Modes," NASA TND-4550, May 1968, Lewis Research Center, Cleveland, Ohio.
11. MacNeal, R. H., "Vibrations of Composite Systems," Report OSR TN-SS-120, October 1954, Office of Scientific Research.
12. Young, D. and Felgar, R. P., Jr., "Tables of Characteristic Functions Representing Normal Modes of Vibration of a Beam," July 1, 1949, The University of Texas Publication, Austin, Texas.

ROTATING ELEMENTS IN THE DIRECT STIFFNESS METHOD OF DYNAMIC ANALYSIS WITH EXTENSIONS TO COMPUTER GRAPHICS

Melvin E. Novak
Dynamics Engineer, Fuselage Methods
The Boeing Company, Vertol Division
Philadelphia, Pennsylvania

A technique has been developed to include rotating elements in a direct stiffness analysis to evaluate the vibration levels of a complex structure such as a helicopter fuselage. Aerodynamic and coupled motions of the rotating elements can be included in the analysis as illustrated in an application to a tandem rotor helicopter. Vibration levels from the analysis agree with inflight test results.

A total-systems concept analysis which employs this technique and, in addition, which could utilize computer graphics is explained in this paper. This analysis combined with man-machine interaction using the scope could generate an optimum vibratory structure.

INTRODUCTION

The stiffness method of dynamic analysis has been used with confidence at the Boeing Company for ten years [1]. Complex frames have been idealized using the direct stiffness method, and good correlation has been obtained with dynamic tests [2]. Difficulty arises, however, when the structure contains rotating appendages. Structural components such as propellers and rotors on the aircraft fuselage have a significant effect on structural modes and natural frequencies, but they do not fit the general algorithms which employ the direct stiffness method.

Rotating beam vibration analysis, using methods such as Myklestad's, has developed to a point where the results obtained agree with dynamic tests. However, combining direct-stiffness analysis and beam analysis has been difficult since the vibration at the point of attachment is a function of the structure-beam interaction.

This paper considers a complex structure in three-dimensions to which rotating appendages are attached. Concentrated vibratory loads are applied at a number of structural nodes, and also, vibratory aerodynamic forces are acting along the length of the rotating elements.

DIRECT STIFFNESS METHODOLOGY

Apart from the rotating elements, the complex structure can be analyzed by the finite element-direct stiffness method described in Ref. [1]. First, the structure must be idealized as a mathematical model. Junctions or node points must be selected where structural members meet. These members may be axial-load elements, in-plane-shear elements, or bending

elements which transmit moment and shear. Each of these members contributes stiffness to the nodes to which they are attached. Each node point can have six degrees of freedom. The stiffness matrix of each structural element is determined. Then, the stiffness contributions to each degree of freedom of the structure are added together. Each degree of freedom comprises one row of a large matrix called a stiffness matrix or $[K]$, the order of which could be higher than 2000 by 2000.

In general,

$$\{F\} = [K]\{\delta\} \quad (1)$$

where $\{F\}$ is the column matrix of forces or moments at all the degrees of freedom, and $\{\delta\}$ is the matrix of deflections or rotations. If the masses and mass moments of inertia are lumped at only a portion of the degrees of freedom, then the inertial forces and torques at all the other degrees of freedom become zero. This allows partitioning of equation (1)

$$\begin{Bmatrix} F \\ 0 \end{Bmatrix} = \begin{bmatrix} K_{11} & K_{12} \\ K_{21} & K_{22} \end{bmatrix} \begin{Bmatrix} \delta_1 \\ \delta_2 \end{Bmatrix} \quad (2)$$

and through a process called reduction [1] an effective stiffness matrix of the order 300 by 300 or less is generated.

$$\{F\} = [K_{eff}]\{\delta_1\} = [K_{11} - K_{12}K_{22}^{-1}K_{21}]\{\delta_1\} \quad (3)$$

In order to include rotating elements, degrees of freedom to which the rotating elements are attached must be retained in the reduction process.

Assuming a harmonic solution, equation (3) gives

$$[M]^{-1} K_{eff} \cdot \lambda \{\delta\} = 0, \quad (4)$$

where $[M]$ is a diagonal mass matrix, λ is a natural frequency squared (eigenvalue) and $\{\delta\}$ is the matrix of modal displacements or rotations (eigenvector).

The collection of eigenvectors arranged together columnwise is called the modal matrix ϕ . It may be shown analytically that, if the eigenvalues are different from each other, $\phi^T M \phi$ is a diagonal matrix where ϕ^T is the transpose of the modal matrix. This diagonal matrix is called the effective-mass matrix.

Once the natural frequencies and mode shapes have been obtained, the damped forced response of the structure may be determined. As described in Ref. 3, the basic matrix equation is

$$[\phi^T M \phi] \{\ddot{A}\} + [\phi^T C \phi] \{\dot{A}\} + [\phi^T K \phi] \{A\} = \{\phi^T F\}, \quad (5)$$

where C is a damping matrix obtained by assuming modal damping, F is the external oscillatory exciting loads column matrix, and $\{A\}$ is a modal amplitude such that $\{X\} = [\phi] \{A\}$. $\{X\}$ is the column matrix of displacements (in inches) or of rotations (in radians). Eq. (5) is completely general in that it includes a form of structural damping, has the capability of using an external loading with sine and cosine components, and can accommodate any combination of nodal excitation. The matrix solution of Eq. (5) which is described in Ref. [3], gives the sine and cosine components of the displacements and rotations, $\{X\}$, at every retained degree of freedom due to forces, F , with sine and cosine components.

ADDITION OF ROTATING ELEMENTS

By the use of a structural mobility matrix $[H]$, the damped forced response of a complex structure may be expressed as

$$\{X\} = [H] \{F\}. \quad (6)$$

Grouping all degrees of freedom to which rotating elements are attached, Eq. (6) is partitioned as follows:

$$\begin{Bmatrix} X_1 \\ X_2 \end{Bmatrix} = \begin{bmatrix} H_{11} & H_{12} \\ H_{21} & H_{22} \end{bmatrix} \begin{Bmatrix} F_1 \\ F_2 \end{Bmatrix}, \quad (7)$$

where X_1 is a column matrix of displacements and rotations generated in their sine and cosine components, where the rotating elements are attached. The X_2 represents all other motions. F_1 is a column matrix of forces and moments with their sine and cosine components acting in degrees of freedom where the rotating elements are attached, and F_2 represents all other vibratory loads applied to the structure.

Eq. (7) then yields, for the degrees of freedom where rotating elements are attached,

$$\{X_1\} = [H_{11}] \{F_1\} + \{Q\}, \quad (8)$$

where $[H_{11}]$ is a square matrix of the mobilities in these degrees of freedom due to loads in these degrees of freedom, and $\{Q\}$ is a column matrix of constant vibratory motions equal to $[H_{12}] \{F_2\}$.

Eq. (8) expresses the damped force-displacement relationship at the boundaries between the rotating appendages and the complex structure. This relationship is defined by the properties of the structure. A similar relationship can be expressed by the aerodynamic and dynamic properties of the rotating elements per se. In matrix notation this is written as

$$\{f\} = [A] \{x\} + \{C\}, \quad (9)$$

where $\{f\}$ is a column matrix of sine and cosine components of loads at the nodes where all rotating elements are acting, and $\{x\}$ is a column matrix of phased motions of the nodes. $\{f\}$ and $\{x\}$ are in a coordinate system convenient to the rotating elements. $[A]$ is a receptive matrix expressing the change in shaft forces due to vibratory shaft motions, and $\{C\}$ is a column matrix of phased vibratory shaft forces, assuming zero vibratory motion at the point of attachment to the complex structure.

Let $[T]$ be a transformation matrix relating the coordinate systems of the rotating elements and the complex structure such that

$$\begin{Bmatrix} F_1 \\ X_1 \end{Bmatrix} = [T] \begin{Bmatrix} f \\ x \end{Bmatrix}, \quad (10)$$

then

$$\{F_1\} = [T][A][T]^{-1} \{X_1\} + [T]\{C\}. \quad (11)$$

When Eq. (8) is substituted for X_1 , Eq. (11) becomes:

$$\begin{aligned} \{F_1\} &= [T][A][T]^{-1} [H_{11}] \{F_1\} \\ &+ [T][A][T]^{-1} \{Q\} + [T]\{C\}. \end{aligned} \quad (12)$$

Finally, the boundary forces are expressed as

$$\{F_1\} = [I - TAT^{-1}H_{11}]^{-1} [TAT^{-1}Q + TC]. \quad (13)$$

These boundary forces, which are the sine and cosine components of all forces and moments in degrees of freedom to which rotating elements are attached, along with any other exciting forces, are applied in the damped forced response analysis of the complex structure.

The effective mass and the effective damping of the rotating system, as well as the coupled force-displacement relationships between orthogonal degrees of freedom in the rotating system, are all considered in the analysis because the matrix $[A]$ is square and contains sine and cosine components which express the correct phasing.

APPLICATION TO A TANDEM ROTOR HELICOPTER

The stiffness method of dynamic analysis as described has been programmed for the IBM-360 Mod 65 at Vertol Division for the analysis of fuselage vibration levels of single- and tandem-rotor helicopters in flight.

The eigenvalues and eigenvectors of a helicopter fuselage model, as illustrated in Fig. 1, are calculated by the D-46 Unified Structural Analysis Computer Program described in Ref. [1]. The final presentation of each eigenvector is the orthonormal form. This collection of eigenvectors, known as the modal matrix, is stored on tape for use as generalized coordinates in obtaining the damped forced response of the fuselage. A Total Systems Analysis Computer Program D-65 combines the Damped Forced Response Analysis of a Complex Structure Computer Program D-96 with an Aeroelastic Rotor Analysis Computer Program D-95 to calculate the inflight vibration levels of the aircraft.

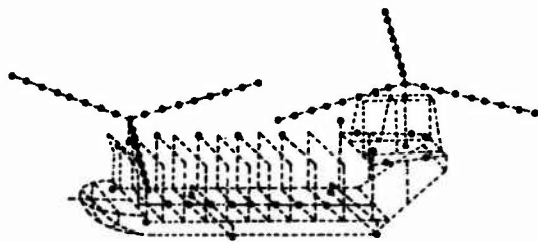


Figure 1. Structural Idealization of a Tandem-Rotor Helicopter Including a Lumped Mass-Elastic Bay Representation of the Rotor Systems

The method of rotor analysis employed in the system combines the results of an aircraft trim analysis, computer program A97, and a blade property analysis with basic flight parameters in a non-linear coupled aerodynamic system to calculate the forces and moments on the hubs of the aircraft [2]. A lumped mass system, with discrete masses and elastic bays as shown in Fig. 1, is used to idealize a rotor blade. On the blade model, airfoils are positioned at mass points for consideration of aerodynamic forces. The air velocity relative to each of these airfoils is obtained by summing contributions from wind, forward speed, vortex velocities, and the rotating, pitching, and lagging motions of the blade. The airloads are calculated using two-dimensional airfoil tables to determine lift, drag, and moment aerodynamic coefficients.

In the analysis, a system of matrices transfers load from one mass station to the next inboard station. Complexity in these transfer matrices is reduced by considering lag separate from flap and pitch. Since airloads are a function of blade position, iterations between the airloads and blade deflections are performed until convergence occurs. Shears and moments are transferred inboard to the point of attachment for all blades and are summed in a fixed-rotor shaft-disc plane system to supply the phased forcing loads for the fuselage. Hub motion is included in the analysis.

GENERATION OF REQUIRED MATRICES

As illustrated by Fig. 2, the D-65 Computer Program loops on the component analyses to generate the $[A]$, $\{C\}$, and $[H]$ matrices. The $\{C\}$ matrix is obtained by running a forward and, if needed, an aft rotor analysis with zero hub motion and extracting the desired harmonic of the vibratory shaft loads. The resulting $\{C\}$ matrix is a column matrix of the order 24 by 1 (12 by 1 for a single-rotor helicopter) containing the sine and cosine components of forces and moments in six degrees of freedom at each hub. The $[A]$ matrix is generated by looping on the rotor analysis and by inducing a vibratory shaft motion of the desired harmonic in the sine and cosine component of each available degree of freedom.

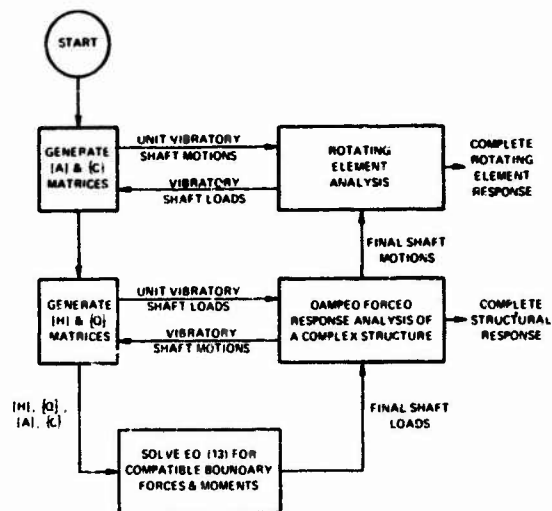


Figure 2. Flow Diagram of Total Systems Analysis Computer Program

One column of the $[A]$ is filled for each analysis by subtracting the $\{C\}$ matrix loads from the respective shaft loads resulting from each hub motion case,

$$\{f\} - \{C\} = [A] \{x\} \quad (14)$$

The $[A]$ matrix takes the following form for a tandem rotor helicopter

$$\begin{bmatrix} A_{\text{forward}} & \text{---} \\ 12 \times 12 & \text{---} \\ \text{---} & A_{\text{aft}} \\ \text{---} & 12 \times 12 \end{bmatrix}$$

The $[H]$ matrix, or mobility matrix, for the hubs of the fuselage is a full symmetric matrix. This matrix is obtained by looping on the Damped Forced Response Analysis Computer Program, inputting unit forces in every hub degree of freedom and extracting the resulting phased hub motions to fill the respective columns of the $[H]$ matrix. $\{Q\}$ is calculated by an additional damped forced response case in which all external vibratory loads are applied.

The forces and moments from the rotor analysis are calculated in the rotor shaft-disc plane coordinate system. The idealization of the fuselage and thus the resulting model displacements are given in a coordinate system which has the rotor shafts tilted in the x-z plane. Therefore, an appropriate transformation matrix is generated which corrects for this shaft tilt. It also provides for the phase difference between the two rotor systems.

Using the data which has been generated, the Total Systems Analysis Computer Program evaluates Eq. (13) for the phased vibratory rotor loads. These forces and moments are then applied in the hub degrees of freedom in the D-96 Damped Forced Response Analysis Computer Program to calculate the inflight vibratory displacements and g levels of the helicopter.

Excellent agreement with flight test results has been obtained using this procedure. Some results of the analysis for a medium size-tandem rotor transport helicopter in high speed-level flight are illustrated along with test data in Fig. 3. Twenty mode shapes were used, including six rigid body modes. The running time for the program was about seventeen minutes. Approximately sixteen minutes were used in the generation of matrix data and the solution of Eq. (13), and one minute was used for the final stiffness method portion of the program.

MATCHBOX STUDIES OF THE NEW APPROACH

Recent studies in the area of preliminary design illustrate the benefit gained from idealizing helicopter fuselages as an assemblage of rectangular boxes having the general dimensions and mass distribution of the more complex model [4]. These simplified or "Matchbox" models can be designed to have their lower natural frequencies and mode shapes very near the exact frequencies and mode shapes of the actual aircraft. Required computer running time can be greatly reduced while gross structural modifications can be studied with adequate insight into the engineering problem.

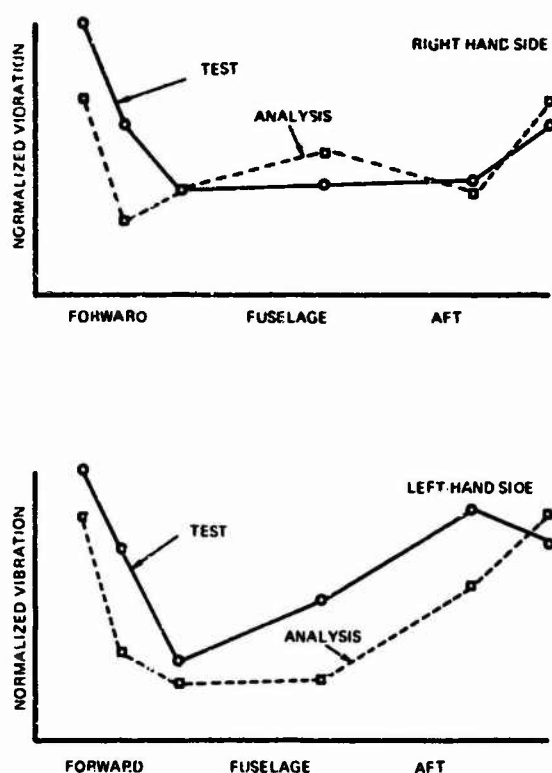


Figure 3. In-Flight Vibration Correlation

Using the "Matchbox" model concept, the new technique presented in this paper was compared with an effective mass method, another means of including rotating elements in the direct stiffness method of dynamic analysis. Identical results were obtained with the two methods when all of the off-diagonal terms in the $[A]$ matrix in Eq. 13 were set equal to zero. The reason for this phenomenon is that the effective mass techniques does not consider the effective damping and the force-displacement relationships between orthogonal degrees of freedom in the rotor system. Damping and coupling are expressed by the off-diagonal terms in the matrix $[A]$. In some cases, the consideration of these effects can make a significant difference in the calculation of the vibration levels of a complex structure. Fig. 4 shows this effect on longitudinal, lateral, and vertical vibration levels of a "Matchbox" model of a tandem-rotor helicopter at 140 knots.

APPLICATION TO COMPUTER GRAPHICS

The demand for rapid man-machine interaction and for pictorial presentation of computer results has led to widespread utilization of computer hardware such as the IBM-2250 Graphics Display Unit. Graphics programs have increased visibility into engineering problems and facilitated more rapid studies of structural modifications.

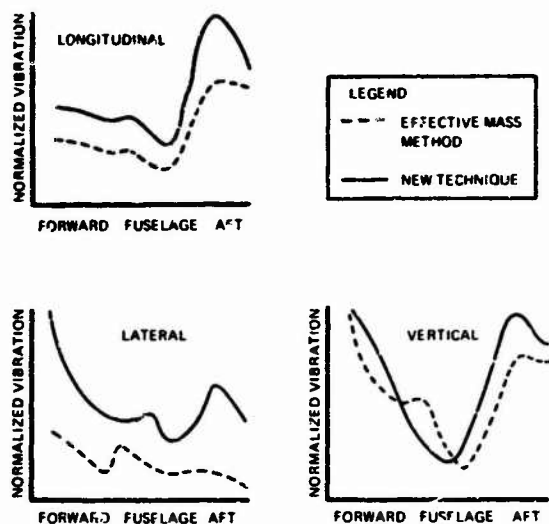


Figure 4. The Effect of Coupled Motion and Damping on the Vibration Levels of a "Matchbox" Model of a Tandem Rotor Helicopter

A computer program linking the graphics display unit to a direct stiffness analysis program [5] has been in operation at Vertol Division for more than a year. It has been used as described in Ref. [6] for cabin vibration reduction, for evaluation of self-tuning vibration absorber effectiveness, for proposal preparation, and for studies of growth versions of existing craft. A more recent application of the graphics system has been made in the area of preliminary design of new models. Fig. 5 illustrates the animated scope presentation of the CH-46A fuselage.



Figure 5. IBM 2250 Scope Display of the CH-46A Fuselage

The foreseeable goal of computer graphics application is a total systems analysis for structural optimization. An improved version of the existing vibration analysis computer graphics program would provide this capability. The generalized coordinate fuselage analysis discussed in Ref. [5] would be linked with a rotor blade analysis and trim analysis for a tandem rotor helicopter. The technique presented in this paper would be used to assure compatibility at boundaries between component systems. For example, in the program illustrated in Fig. 6, the fuselage is first trimmed for a given flight condition. Then from a rotor blade-hub load analysis program, the exciting forces and moments at the blade roots are calculated. The $[A]$, $[C]$, $[H]$, and $[Q]$ matrices are generated, and the equation for compatible boundary conditions is solved. The damped, forced response of the fuselage is then found using previously determined mode shapes. A decision can then be made at the scope as to whether or not a vibration reduction device is to be added, or if rotor blade or fuselage structure or parameters are to be changed. Recalculation can then be made to an optimum dynamic design.

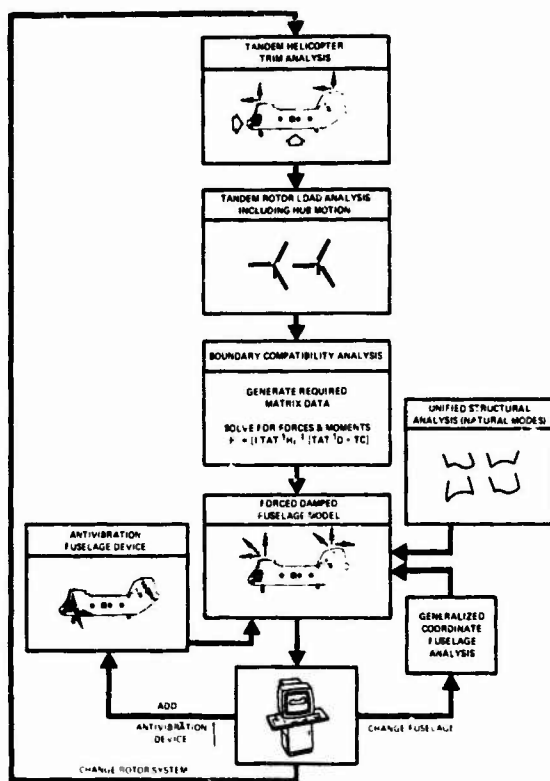


Figure 6. Optimal Design Total Systems Concept Computer Graphics Program

CONCLUSION

An accurate means of including rotating elements in the direct stiffness method for dynamic analysis is important in correlating and predicting vibration levels of certain complex structures. The method described provides this capability by considering the total rotating element-complex structure interaction. Initial efforts using this method to correlate in-flight vibration levels of a tandem-rotor helicopter have given good results.

Finally, the technique may be useful when linking large computer programs together for a total systems type-dynamic analysis program utilizing man-machine interaction graphics.

REFERENCES

1. J. J. Sciarra, "Dynamic Unified Structural Analysis Method Using Stiffness Matrices," AIAA/ASME, April 18, 1966.
2. R. Gabel, "Pvid Program, Advanced Vibration Development," Boeing-Vertol Report 107M-D-09, April 1965.
3. J. J. Sciarra, "Application of Combined Direct Stiffness and Mobility Method to Vibration Absorber Studies," ASME/MDD, Vibration Conference, Paper 67-VIBR-65, March, 1967.
4. J. J. Sciarra, "Helicopter Fuselage Vibration Prediction by Stiffness/Mobility Methods," 37th Shock and Vibration Symposium, Orlando, Florida, October, 1967.
5. J. J. Sciarra, "Helicopter Fuselage Vibration Analysis in Three Dimensions Using Computer Graphics," The Second University of Illinois Computer Graphics Conference, Urbana, Illinois, April, 1969.
6. R. R. Vlamincik, "Dynamic Structural Analysis Using a Computer Graphics Display," Aero-Space Structural Design Report, Seattle, Washington, August, 1969.

DISCUSSION

Mr. Pakstys (General Dynamics Corp.): I was interested in the eigenvalue program which was used for the IBM 360-65 computer. You modeled this with 300 dynamic degrees of freedom. How many modes were calculated, and what techniques were used?

Mr. Novak: Until very recently our capabilities were limited to approximately 140 degrees of freedom, where we used a QR transformation. We have a new technique which is available in the SSP package offered by IBM. They have routines called Eigen and Enroute which allow the use of single pre-

cision in some parts of the analysis. We have obtained a comparable correlation with 139-140 degree-of-freedom problems, using less core, and we have solved problems up to 250 degrees of freedom. Reasonable results are obtained, but we cannot compare with another method except at a lower number of degrees of freedom. These methods yield a little bit higher degree-of-freedom capability. Once we calculate approximately 30 modes, which requires nearly 37 seconds per mode, we can adjust the running time on the basis of the number of desired modes. We are always interested in the lowest modes.

**DYNAMIC RESPONSE OF BEAMS TO MOVING PRESSURE LOADS
AS RELATED TO TRACKED AIR CUSHION VEHICLES**

James F. Wilson
Duke University
Durham, North Carolina

A mathematical model is formulated to simulate the dynamic interaction of guideway spans with tracked air cushion vehicles. This model is the Bernoulli-Euler beam equation subjected to segments of uniform, moving pressures. Closed form series solutions are found by the normal mode method. Results show that, for a given span and total load, the maximum dynamic span deflections for distributed and concentrated moving loads are nearly identical, although the velocities at which these deflections occur are different. Beyond certain critical velocities (100 to 300 mph) the mean values of dynamic deflections under the pressure segments begin to decrease at increasing speed. Although the vehicle may "outrun" the static span deflection, it can never outrun its vertical accelerations during traverse. The mean value of these pressure segment accelerations always increases with increasing speed. These accelerations which may exceed 3 g's should be reduced by some means if the passengers are to travel comfortably in tracked air cushion vehicles.

INTRODUCTION

The dynamic response of structures to loads moving over them is of particular importance in high speed ground transportation. For example, elevated spans of 50 to 150 feet are currently being considered as guideways for tracked air cushioned vehicles (TACV's) cruising at 300 mph. At such speeds, these vehicles impart disturbances to the guideways which may result in span deflections which are relatively large compared to the static deflections for stationary vehicles. The purpose of this paper is to analyze the response of a guideway, represented as a beam, to moving pressure loads of the type associated with high speed TACV's. In addition to the deflection response, the vertical acceleration response of the moving pressure is examined since it is related to the riding comfort of the passengers.

The vibrations of elastic structures in response to moving loads has a rich history, extending over more than a century. Serious studies began in England motivated by the spectacular collapse of the Chester Bridge near London in 1847. In the early studies, these

structures were modeled as simply supported, slender beams with a point load moving along them at constant velocity. Willis [1] and Stokes [2] assumed that the mass of the structure was negligible in comparison to the moving mass. Stokes found an approximate expression for the ratio of the dynamic to static deflection of the beam, which was later improved upon by Timoshenko [3]. In 1905, Kryloff [4] found the dynamic deflections of a beam where its inertia was included but where the moving point load was assumed to be a constant force, without mass.

Jeffcott [5] and Inglis [6] extended all of these results to include both the mass of the moving point load and the mass of the beam. The most complete analysis, however, was done by Schallenkamp [7]. Ayre, et al, [8], [9] have further extended this work to include the two-span beam. They also reported some experimental results which check the results of Schallenkamp [10]. Harmonically varying point forces on simple beams have been studied by Timoshenko [11], Lowan [12], Pyzanova [13], and Schlak [14]. Ronaldi [15] and

Vellozzi [16] considered the response of more complex models of bridges to moving forces. Much unpublished work has also been done at MIT in the 1950's [17]. Vellozzi includes an excellent bibliography on suspension bridge dynamics. Recently, Stanisic and Hardin [18] considered the response of a beam to many moving masses, but since their basic differential equation omits a component of acceleration, correctly included by Schallenkamp [7], some of their results contain errors of unknown magnitude. The dynamics of the simply-supported, curved beam have also been a subject of recent interest [19, 20]. The dynamics of a beam on an elastic foundation, with and without damping, subjected to moving and pulsating point forces of various types, have been extensively investigated, [21-26].

In the work cited so far, the beam models have been "classical" or based on the Bernoulli-Euler theory. As the velocity of the moving load approaches the sonic speed for the beam material, the Bernoulli-Euler theory is no longer valid, and more refined beam models are needed. Such models considered by Crandall [27], Florence [28], Achenbach and Sun [29], and Steele [30-32], are especially useful when the loading is fast, as from explosions.

The purpose of this paper is to find the dynamic response of a simple beam to both a single patch and a double patch of uniform pressure, traveling along a beam at speeds much below the sonic speed of the beam material. Both the constant velocity and constant acceleration cases are discussed. The Bernoulli-Euler beam model is used, where uniform end tensions and elastic foundation effects are included. Maximum dynamic and static beam deflections are compared. Results are compared to those given by Bresse [33,34] for the response of an infinitely long band of moving pressure, and to those of Timoshenko [11] for a point force, all moving at constant velocity. The critical conditions under which large dynamic deflections and vertical accelerations may occur are discussed for two numerical examples chosen to approximate the traverse of a single tracked air cushioned vehicle over identical simple spans.

THE BEAM MODEL

The dynamic model of the beam is shown in Figure 1. The usual assumptions of elementary beam theory are made. Rotatory inertia, longitudinal vibrations, and shear deformations are neglected so that only the transverse modes of vibration are admitted. These assumptions



Figure 1. The beam model with moving, transverse pressure.

are consistent with the usual Bernoulli-Euler theory of beam vibrations [35]. All damping is neglected, including viscous material damping and external fluid damping. However, the effects of an inertia-less, elastic foundation and of a uniform longitudinal tension, are included in the equation of motion of the beam.

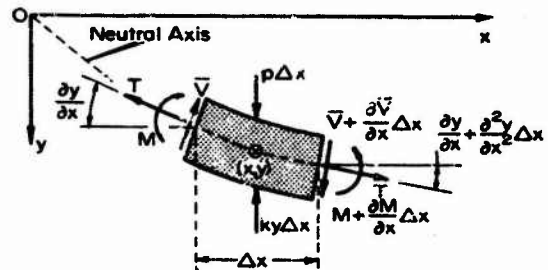


Figure 2. Forces and moments on a small element of the deflected beam.

The forces acting on a differential beam element of length Δx are shown in Figure 2. The equation of motion for small vertical displacements y of this element, subjected to a transverse pressure, or force per unit length $p=p(x,t)$, is found by applying Newton's second law in the vertical direction. When products of differential quantities above the first order are neglected, the result is

$$T \frac{\partial^2 y}{\partial x^2} \Delta x + \frac{\partial V}{\partial x} \Delta x - ky \Delta x + p \Delta x = \rho A \Delta x \frac{\partial^2 y}{\partial t^2} \quad (1)$$

where T is the longitudinal tension, V is the vertical shear force, k is the elastic constant of the foundation, and ρ and A are the mass density and the cross sectional area of the beam, respectively. From elementary beam theory, the bending moment M is related to the curvature by

$$M = -EI \frac{\partial^2 y}{\partial x^2}$$

where EI is the stiffness. Also, for moment equilibrium, $\bar{V} = \partial M / \partial x$. When these moment and shear relations are differentiated and combined with Equation (1), the governing differential equation for constant EI becomes:

$$EI \frac{\partial^4 y}{\partial x^4} - T \frac{\partial^2 y}{\partial x^2} + ky + \rho A \frac{\partial^2 y}{\partial t^2} = p \quad (2)$$

In this analysis, it is assumed that the velocity v_p of any external disturbances moving along the beam is always much less than the sonic velocity c of the longitudinal stress waves. Since $c^2 = E/\rho$ for a long, thin elastic beam, an important restriction of Equation (2) is that

$$v_p \ll \sqrt{\frac{E}{\rho}} \quad (3)$$

The vertical beam velocity, $\partial y / \partial t$ must also be less than c . In the case where $p(x, t)$ is caused by an explosion, for instance, $\partial y / \partial t$ may be of the order of c and more refined beam models must be used [27-32].

When p is known, solutions $y = y(x, t)$ to Equation (2) can be found by specifying that deflections and moments vanish at each end, or

$$\begin{aligned} y(0, t) = y(l, t) &= \frac{\partial^2 y(0, t)}{\partial x^2} \\ &= \frac{\partial^2 y(l, t)}{\partial x^2} = 0 \end{aligned} \quad (4)$$

Also, initial conditions at time $t = t_0$ must be specified in order to have a unique solution to Equation (2). These conditions are expressed as

$$y(x, t_0) = y_0(x) \quad (5a)$$

$$\frac{\partial y(x, t_0)}{\partial t} = v_0(x) \quad (5b)$$

which represent the initial displacement and initial velocity, respectively, at every point along the beam.

FREE VIBRATIONS

For free vibrations, the pressure $p = 0$. For free harmonic vibrations, the n th solution to Equation (2) is assumed in product form:

$$y_n(x, t) = Y_n(x) \sin \omega_n t \quad (5)$$

where ω_n is a real number. The function $Y_n = Y_n(x)$ is determined by substituting Equation (6) into Equation (2) or

$$Y_n^{IV} - \frac{T}{EI} Y_n'' - \frac{(\rho A \omega_n^2 - k)}{EI} Y_n = 0 \quad (7)$$

where the prime denotes differentiation with respect to x . It is not difficult to show that the only class of solutions of Equations (7) consistent with Equation (6) and the boundary conditions of Equation (4), are given by

$$Y_n(x) = \sin \frac{n\pi x}{l} \quad (8)$$

With Equation (8), Equation (7) gives the result

$$\omega_n^2 = \left[\frac{EI}{\rho A} \left(\frac{n\pi}{l} \right)^4 + \frac{T}{\rho A} \left(\frac{n\pi}{l} \right)^2 + \frac{k}{\rho A} \right] \quad (9)$$

where $n = 1, 2, 3, \dots$

The natural frequencies of the simply supported beam under uniform tension and fixed to an elastic foundation, are thus given by Equation (9). If $T = k = 0$, these frequencies depend only on the beam stiffness. If $EI = k = 0$ the frequencies are simply those of a flexible string under uniform tension T . It is also interesting to note that the critical buckling loads for this beam can be found from Equation (9), corresponding to $\omega_n = 0$ and a compressive load $N = -T$. These critical compressive loads are

$$N = \frac{n^2 \pi^2 EI}{l^2} + \left(\frac{l}{n\pi} \right)^2 k \quad (10)$$

which correspond to the Euler buckling loads when the elastic foundation is absent. If the critical compressive load at $n = 1$ is ever exceeded, ω_n becomes an imaginary number, and harmonic motion ceases to exist.

The results just obtained will be utilized to find solutions $y(x, t)$ of Equation (2) with boundary and initial conditions given by Equations (4) and (5), where p is a known function of time and position along the beam.

NORMAL MODE SOLUTION FOR ARBITRARY FORCES

Although the normal mode method is discussed by several writers, [35, 36] and these ideas will be outlined now for the sake of completeness in solving the

present problem. First, it is assumed that the solution to Equation (2) can be expanded in terms of the normal modes $Y_n(x)$ given by Equation (8) or

$$\begin{aligned} y(x,t) &= \sum_{n=1,2,\dots}^{\infty} q_n(t) Y_n(x) \\ &= \sum_{n=1}^{\infty} q_n(t) \sin \frac{n\pi x}{l} \end{aligned} \quad (11)$$

where the time varying coefficients $q_n(t)$ have yet to be determined. Equation (11) satisfies the boundary conditions given by Equation (4) for all integer values of n . When Equation (11) is substituted into Equation (2), and Equation (7) is used to eliminate the quantity $(EI Y_n^{IV} - TY_n'' + kY_n)$ from the result, it follows

$$\sum_{n=1}^{\infty} (\ddot{q}_n + \omega_n^2 q_n) Y_n = \frac{p}{\rho A} \quad (12)$$

where (') denotes differentiation with respect to time. Each side of Equation (12) is multiplied by $Y_m(x)$, $m=1,2,\dots$, and the results are then integrated over the range $0 \leq x \leq l$.

$$\begin{aligned} \int_0^l \sum_{n=1}^{\infty} (\ddot{q}_n + \omega_n^2 q_n) Y_n Y_m dx \\ = \frac{1}{\rho A} \int_0^l Y_m p dx \end{aligned} \quad (13)$$

The order of integration and summation are interchanged in Equation (13), assuming that q_n and its derivatives are "well behaved." When use is made of Equation (8) and the orthogonal conditions

$$\int_0^l Y_n Y_m dx = \begin{cases} 0 & \text{when } m \neq n \\ \frac{l}{2} & \text{when } m = n \end{cases} \quad (14)$$

the result is an ordinary, second order differential equation.

$$\ddot{q}_n + \omega_n^2 q_n = F_n(t) \quad (15)$$

where

$$F_n(t) = \frac{2}{l\rho A} \int_0^l p \sin \frac{n\pi x}{l} dx \quad (16)$$

Solutions to Equation (15) represent the responses of n forced harmonic oscillators, one for each mode shape $Y_n(x)$. The function $F_n(t)$ which excites each mode is the weighted integral of the applied pressure p over the length of the beam. The total solution, given by Equation (11), is then a linear sum of the response of each mode.

To obtain a unique solution to Equation (15), the initial values of $q_n(t_0)$ and $\dot{q}_n(t_0)$ must be specified at a time $t = t_0$. These initial values are related to the beam deflection through Equations (5) and (11).

$$y(x, t_0) = \sum_{n=1}^{\infty} q_n(t_0) \sin \frac{n\pi x}{l} = y_0(x) \quad (17a)$$

$$\frac{\partial y(x, t_0)}{\partial t} = \sum_{n=1}^{\infty} \dot{q}_n(t_0) \sin \frac{n\pi x}{l} = v_0(x) \quad (17b)$$

Thus, the initial values for Equation (15) are coefficients of a Fourier sine series, [37], given by

$$q_n(t_0) = \frac{2}{l} \int_0^l y_0(x) \sin \frac{n\pi x}{l} dx \quad (18a)$$

$$\dot{q}_n(t_0) = \frac{2}{l} \int_0^l v_0(x) \sin \frac{n\pi x}{l} dx \quad (18b)$$

The total solution to Equation (15) is most easily obtained by method of Laplace transforms, [38]. That is,

$$\begin{aligned} q_n(t) &= \frac{1}{\omega_n} \dot{q}_n(t_0) \sin \omega_n(t-t_0) \\ &\quad + q_n(t_0) \cos \omega_n(t-t_0) \\ &\quad + \frac{1}{\omega_n} \int_{t_0}^t F_n(\tau) \cdot \sin \omega_n(t-\tau) d\tau \end{aligned} \quad (19)$$

where the first two terms on the right represent the transient solution, and

the integral term is the particular solution. Thus, if $p = p(x, t)$ is known for the beam, and the initial beam deflection $y_0(x)$ and the initial vertical velocity $\dot{y}_0(x)$ are known for all $0 \leq x \leq l$, $F_n(t)$ can be found from Equation (16); $q_n(t_0)$ and $\dot{q}_n(t_0)$ can be found from Equations (18); $q_n(t)$ can be found from Equation (19); and finally, the deflections are found from Equation (11). This procedure will now be illustrated by two examples.

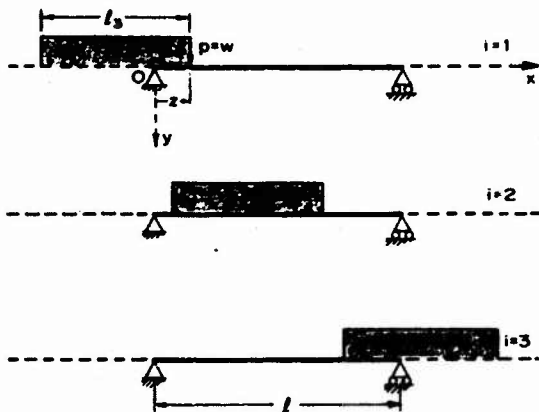


Figure 3. A single, moving patch of uniform pressure in the three loading intervals.

EXAMPLE A - BEAM RESPONSE TO A SINGLE, MOVING PATCH OF UNIFORM PRESSURE

Consider that a pressure patch of constant magnitude $p = w$, and of constant length l_3 , moves across the beam as shown in Figure 3. The position of the right end of this pressure patch, measured from point $x = 0$, is taken as a second degree polynomial in time, or

$$z = at + bt^2 \quad (20)$$

where a and b are constants. The velocity of the moving pressure is $a + 2bt$ and the acceleration is $2b$. Thus, the case of constant velocity is the case where $b = 0$. The case of constant acceleration is also included, when $b \neq 0$. The three intervals of pressure loading shown in Figure 3 are now classified.

In the entrance region, where the beam has not yet received the full length of the pressure patch, p is given by:

$$p = \begin{cases} w, & 0 \leq x \leq z \\ 0, & z \leq x \leq l \end{cases} \quad (21)$$

where $0 \leq z \leq l_3$. The time interval in region 1 is defined as t_1 , and is given by Equation (20), when $z = l_3$, or

$$t_1 = \begin{cases} \frac{l_3}{a}, & b = 0 \\ -\frac{a}{2b} + \frac{G}{2} \sqrt{\left(\frac{a}{b}\right)^2 + \frac{4l_3}{b}}, & \begin{cases} b > 0, G = 1 \\ b < 0, G = -1 \end{cases} \end{cases} \quad (22)$$

In the middle region, p is given by:

$$p = \begin{cases} 0, & 0 < x < (z - l_3) \\ w, & (z - l_3) \leq x \leq z \\ 0, & z < x \leq l \end{cases} \quad (23)$$

where $l_3 \leq z \leq l$. The time required for the right end of the pressure patch to reach the right beam support is given by Equation (20) for $z = l$, or

$$t_2 = \begin{cases} \frac{l}{a}, & b = 0 \\ -\frac{a}{2b} + \frac{G}{2} \sqrt{\left(\frac{a}{b}\right)^2 + \frac{4l}{b}}, & \begin{cases} b > 0, G = 1 \\ b < 0, G = -1 \end{cases} \end{cases} \quad (24)$$

In the exit region, p is given by:

$$p = \begin{cases} 0, & 0 < x < (z - l_3) \\ w, & (z - l_3) \leq x \leq l \end{cases} \quad (25)$$

where $l \leq z \leq (l + l_3)$. The time required for the whole pressure patch to exit is given by Equation (20) for $z = l + l_3$, or

$$t_j = \begin{cases} \frac{z + \ell_j}{c} \\ -\frac{a}{2F} + \frac{G}{2} \sqrt{\left(\frac{a}{G}\right)^2 + \frac{4(z + \ell_j)}{E}} \end{cases}, \quad b = 0 \quad (26)$$

The values of $F_{ni}(t)$, where $i = 1, 2, 3$ designates the interval, can now be calculated from Equation (16) using Equations (21), (23), and (25), respectively. The results are

$$F_{n1}(t) = \frac{2w}{\rho A n \pi} \left[1 - \cos \frac{n\pi}{\ell} z \right] \quad (27)$$

where $0 \leq t \leq t_1$;

$$F_{n2}(t) = \frac{2w}{\rho A n \pi} \left[\cos \frac{n\pi}{\ell} (z - \ell_1) - \cos \frac{n\pi}{\ell} z \right] \quad (28)$$

where $t_1 \leq t \leq t_2$;

$$F_{n3}(t) = \frac{2w}{\rho A n \pi} \left[\cos \frac{n\pi z}{\ell} - \cos n\pi \right] \quad (29)$$

where $t_2 \leq t \leq t_3$.

The values of $q_{ni}(t)$, designed in the same way as $F_{ni}(t)$, can now be calculated from Equation (19). In all three intervals,

$$q_{ni}(t) = \frac{1}{\omega_n} \dot{q}_{nj}(t_j) \sin \omega_n(t - t_j) + q_{nj}(t_j) \cos \omega_n(t - t_j) + \frac{1}{\omega_n} \int_{t_j}^t F_{ni}(\tau) \sin \omega_n(t - \tau) d\tau \quad (30)$$

where $j = i - 1$. For $i = 1$, the initial values $q_{n0}(t_0)$ and $\dot{q}_{n0}(t_0)$ are specified by Equations (18). For convenience, take $t_0 = 0$, the time at which the pressure patch begins its entrance at the left end of the beam. For $i = 2$ the initial values needed to calculate $q_{n2}(t)$ are found from the continuity conditions, where the beam deflection and velocity must match in each time region at $t = t_1$. These conditions are expressed by

$$\begin{aligned} q_{n2}(t_1) &= q_{n1}(t_1) \\ \dot{q}_{n2}(t_1) &= \dot{q}_{n1}(t_1) \end{aligned} \quad (31)$$

Likewise, the continuity conditions between time regions 2 and 3 must match at $t = t_2$, or

$$\begin{aligned} q_{n3}(t_2) &= q_{n2}(t_2) \\ \dot{q}_{n3}(t_2) &= \dot{q}_{n2}(t_2) \end{aligned} \quad (32)$$

The values of $\dot{q}_{ni}(t)$ of Equations (31) and (32) can be calculated explicitly from Equation (30) using Leibnitz's rule, (38). The result is

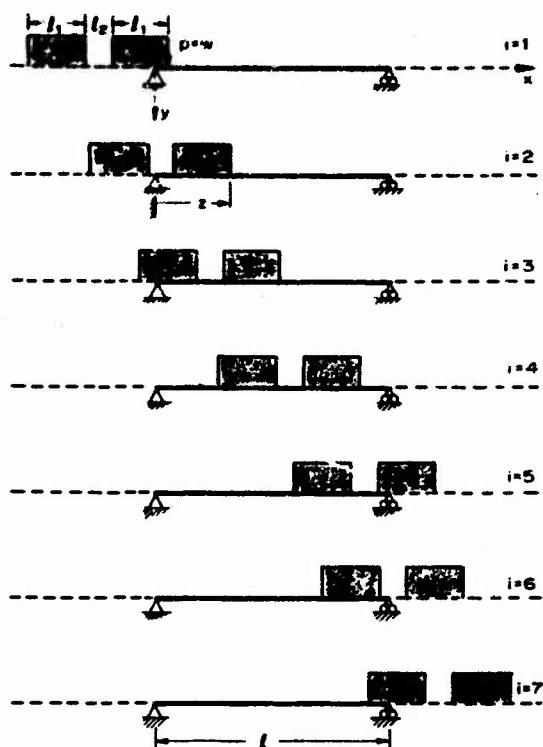
$$\begin{aligned} \dot{q}_{ni}(t) &= \dot{q}_{nj}(t_j) \cos \omega_n(t - t_j) \\ &\quad - \omega_n q_{nj}(t_j) \sin \omega_n(t - t_j) \\ &\quad + \int_{t_j}^t F_{ni}(\tau) \cos \omega_n(t - \tau) d\tau \end{aligned} \quad (33)$$

where $j = i - 1$. In Equations (30) and (33), the upper limit is a variable, and the lower limits are always constant, defined as $(0, t_1, t_2)$ for $i = 1, 2, 3$ respectively. Thus, $q_{ni}(t)$ is calculated from Equations (30) and (33) where the initial values for each successive value of i are based on the previously calculated values, at $(i - 1)$.

In the special case when the pressure patch moves at constant velocity, $b = 0$ in Equation (20), and the integrations of Equations (30) and (33) can be carried out explicitly using trigonometric identities, where $F_{ni}(t)$ is given by Equations (27) - (29). Numerical results will be illustrated presently. When $q_{ni}(t)$ is known, the dynamic deflections of the beam in each time region are given by Equation (11), or

$$y_i(x, t) = \sum_{n=1}^{\infty} q_{ni}(t) \sin \frac{n\pi x}{\ell} \quad (34)$$

where the series can generally be truncated after just a few terms because of its rapid convergence.



EXAMPLE B - BEAM RESPONSE TO DOUBLE MOVING PATCHES OF UNIT

Consider a double patch of pressure, each of magnitude $p = w$, each of length l_1 , and separated by a constant distance l_2 . Suppose that this ensemble moves across the beam as shown in Figure 4, where the total dimension, $2l_1 + l_2$, is less than the beam length, l . As for Example A, the position z of the right end of the ensemble is taken in the form of Equation (20), or

In this example, it is convenient for the purposes of analysis to describe the pressure distribution in seven different time intervals. The time t_i at the end of the i th interval, when the right end of the pressure ensemble is at the location $z = s_i$, is given by Equation (20), or

$$t_i = \begin{cases} \frac{s_i}{a} & , \quad b = 0 \\ -\frac{a}{2b} + \frac{G}{2} \sqrt{\left(\frac{a}{b}\right)^2 + \frac{4s_i}{b}} & \begin{cases} b > 0, G = 1 \\ b < 0, G = -1 \end{cases} \end{cases} \quad (25)$$

Figure 4. Double, moving patches of uniform pressure in the seven loading intervals.

TABLE 1. PRESSURE DISTRIBUTIONS FOR THE SEVEN INTERVALS OF EXAMPLE B

Interval, i	Maximum pressure front distance, s_i	Range of the pressure front distance, z	Value of pressure, p	Range of x
1	$s_1 = l_1$	$0 \leq z \leq l_1$	w	$0 \leq x \leq z$
			0	$z < x \leq l$
2	$s_2 = l_1 + l_2$	$s_1 \leq z \leq s_2$	0	$0 \leq x < z - s_1$
			w	$z - s_1 \leq x \leq z$
			0	$z < x \leq l$
3	$s_3 = 2l_1 + l_2$	$s_2 \leq z \leq s_3$	w	$0 \leq x \leq z - s_2$
			0	$z - s_2 < x < z - s_1$
			w	$z - s_1 \leq x \leq z$
4	$s_4 = l$	$s_3 \leq z \leq s_4$	0	$z < x \leq l$
			w	$0 \leq x < z - s_3$
			0	$z - s_3 \leq x \leq z - s_2$
			w	$z - s_2 < x < z - s_1$
			0	$z - s_1 \leq x \leq z$
			0	$z < x \leq l$

TABLE 1. continued

Interval, i	Maximum pressure front distance, s_i	Range of the pressure front distance, z	Value of pressure, p	Range of x
5	$s_5 = l + l_1$	$s_4 \leq z \leq s_5$	0	$0 \leq x < z - s_3$
			w	$z - s_3 \leq x \leq x - s_2$
			0	$z - s_2 < x < z - s_1$
			w	$z - s_1 \leq x \leq l$
6	$s_6 = l + l_1 + l_2$	$s_5 \leq z \leq s_6$	0	$0 \leq x < z - s_3$
			w	$z - s_3 \leq x \leq z - s_2$
			0	$z - s_2 < x \leq l$
7	$s_7 = l + 2l_1 + l_2$	$s_6 \leq z \leq s_7$	0	$0 \leq x < z - s_3$
			w	$z - s_3 \leq x \leq l$

The values of s_i for each i , and the values of p within those intervals consistent with Figure 4, are summarized in Table 1; the values of $F_{ni}(t)$ were calculated from Equation (16). The upper and lower limits on the integral in Equation (16) correspond to the extreme values of x of the inequalities given in Table 1. The results for $F_{ni}(t)$ are summarized in Table 2.

TABLE 2. INTEGRATIONS OF EQUATION (16) FOR EXAMPLE B, BASED ON THE PRESSURE DISTRIBUTIONS OF TABLE 1.

Interval, i	Values of $\left(\frac{\rho A n \pi}{2w}\right) \cdot F_{ni}(t)$, where $\lambda_n = \frac{n\pi}{l}$
1	$1 - \cos \lambda_n z$
2	$\cos \lambda_n (z - s_1) - \cos \lambda_n z$
3	$1 - \cos \lambda_n (z - s_2)$ $+ \cos \lambda_n (z - s_1) - \cos \lambda_n z$
4	$\cos \lambda_n (z - s_3) - \cos \lambda_n (z - s_2)$ $+ \cos \lambda_n (z - s_1) - \cos \lambda_n z$
5	$\cos \lambda_n (z - s_3) - \cos \lambda_n (z - s_2)$ $+ \cos \lambda_n (z - s_1) - \cos n\pi$
6	$\cos \lambda_n (z - s_3) - \cos \lambda_n (z - s_2)$
7	$\cos \lambda_n (z - s_3) - \cos n\pi$

The beam deflection response for this example is given by Equation (34) where $q_{ni}(t)$ is calculated from Equation (30). As in Example A, the initial values $q_{no}(t)$ and $\dot{q}_{no}(t)$ needed to calculate $q_{ni}(t)$ are found from Equation (18) where $y_0(x)$ and $v_0(x)$ are given. For the special case when the beam is initially in static equilibrium, $q_{no}(t) = \dot{q}_{no}(t) = 0$, as implied by Equations (18). Succeeding values of $q_{ni}(t)$ are based on the preceding initial value $q_{nj}(t)$ and its derivative $\dot{q}_{nj}(t)$ found from Equation (33), where $j = i - 1$. In this way, the conditions for continuity of the beam's deflection and its vertical velocity are preserved during the traverse time of the pressure ensemble. These continuity conditions, analogous to Equations (31) and (32) of Example A, are simply

$$q_{ni}(t_j) = q_{nj}(t_j) \quad (36a)$$

$$\dot{q}_{ni}(t_j) = \dot{q}_{nj}(t_j) \quad (36b)$$

where $i = 1, 2, \dots, 7$ and $j = i - 1$.

KINEMATICS

The vertical acceleration of a fixed point x on the beam at a given instant is $\partial^2 y / \partial t^2$. This is not the total vertical acceleration of an element of pressure crossing point x with velocity v . As shown in Appendix I, this total vertical acceleration is given by (37)

$$\frac{d^2 y}{dt^2} = \frac{\partial^2 y}{\partial t^2} + 2v \frac{\partial^2 y}{\partial x \partial t} + v^2 \frac{\partial^2 y}{\partial x^2} + \frac{\partial v}{\partial t} \frac{\partial y}{\partial x}$$

Thus, the vertical acceleration of a pressure element moving along a vibrating beam is equal to the vertical acceleration of the beam at the pressure point only in the limiting case of vanishing velocity of traverse. If the pressure point were on a relatively heavy air cushion vehicle, then a passenger on this vehicle would experience the total vertical acceleration given by Equation (37). Further implications of this observation will be discussed presently.

STATIC DEFLECTIONS

Suppose that the beam does not vibrate at all as a known pressure distribution traverses it. The resulting static beam deflection, $y_s(x, t)$, can be

calculated as a function of any pressure distribution by using energy methods. The methods and results of Langhaar [39] are extended to include the effects of the elastic foundation.

The static deflection is represented by the series

$$y_s = y_s(x, t) = \sum_{n=1}^{\infty} b_n(t) \sin \frac{n\pi x}{l} \quad (38)$$

which is of the same form as Equation (11) in the dynamic analysis, and also satisfies the boundary conditions given by Equation (4). The total energy, V , of the static system is expressed by:

$$V = \Omega_p + \Omega_T + U_B + U_k \quad (39)$$

where Ω_p and Ω_T are the potential energies of the pressure and end load, respectively; U_B and U_k are the strain energies of the beam and the elastic foundation, respectively. The first three of these energy terms have been evaluated by Langhaar [39], using the assumptions of classical beam theory and Equation (38). The results are:

$$\Omega_p = - \int_0^l p y_s dx \quad (40a)$$

$$= - \sum_{n=1}^{\infty} b_n \int_0^l p \sin \frac{n\pi x}{l} dx$$

$$\Omega_T = \frac{T}{2} \int_0^l (y_s')^2 dx = \frac{\pi^2 T}{4l} \sum_{n=1}^{\infty} n^2 b_n^2 \quad (40b)$$

$$U_B = \frac{1}{2} \int_0^l EI (y_s'')^2 dx = \frac{\pi^2 EI}{4l^3} \sum_{n=1}^{\infty} n^4 b_n^2 \quad (40c)$$

The "spring" energy per unit length of the linear elastic foundation is given by $ky_s^2/2$. This total energy, summed over the length of the beam, is evaluated using Equation (38)

$$U_k = \frac{1}{2} k \int_0^l y_s^2 dx = \frac{1}{2} k \frac{l}{2} \sum_{n=1}^{\infty} b_n^2 \quad (40d)$$

When Equations (40) are substituted into Equation (39), the generalized coordinates b_n can be evaluated by the principle of stationary potential energy. That is, the condition for the beam to be in static equilibrium is

$$\frac{\partial V}{\partial b_i} = 0 \quad (41)$$

where $n = 1, 2, \dots, i, \dots$. When this derivative is evaluated, and i is then replaced by n , the result is

$$b_n = \frac{\int_0^l p \sin \frac{n\pi x}{l} dx}{\left(\frac{\pi^4 EI}{2l^3} \right) n^4 + \frac{\pi^2 T}{2l} n^2 + \frac{kl}{2}} \quad (42)$$

The numerator of Equation (42) differs from Equation (16) only by a constant. Thus, b_n can be written in terms of $F_n(t)$ or

$$b_n = \frac{\rho A l^4 F_n(t)}{EI(\pi n)^4 + T(\pi n l)^2 + kl^4} \quad (43)$$

The results are summarized. In Example A, Equation (43) is used, where $F_n(t)$ is given by Equations (27) - (29), the time intervals by Equations (22), (24), and (26), and the position of the pressure in time by Equation (20). In Example B, the coefficients for the static deflections are also evaluated using Equations (38) and (43), with the corresponding values of $F_n(t)$ listed in Table 2 for each of the seven time intervals.

These results can be applied to the design of guideway systems for

tracked air cushioned vehicles, where these vehicles are represented by moving pressure loads. From the viewpoint of beam or guideway design, the maximum ratio of the dynamic to static deflection at the beam's center is an important design parameter. From the viewpoint of ride comfort for the passengers, the vertical acceleration of the moving pressure is an important design parameter. With the aid of a computer program, these two design parameters can be studied as a function of the beam variables: EI , ρA , l ; the beam constraints: T , k ; the vehicle weight and length parameters: w , l_v ; and the vehicle motion parameters: a , b . For the numerical examples tried, values for dynamic and static deflections and accelerations usually differed by less than 1% when results for $n = 4$ and $n = 6$ were compared. Wider discrepancies occurred in the immediate neighborhood of the end supports, a result which can be expected from such series solutions. For most engineering examples, it appears that the inclusion of six normal modes, or $n = 6$ adequately represents solutions to this problem.

constant over the whole vehicle length of 32 feet. Every span is assumed to be simply supported between piers. In this typical example:

$$\left. \begin{aligned} EI &= 2.52 \times 10^{11} \text{ lb-in}^2 \\ \rho A &= 0.188 \text{ lb-sec}^2/\text{in}^2 \end{aligned} \right\} \quad (44)$$

$$\left. \begin{aligned} w &= 65.1 \text{ lb/in.} \\ l_v &= 384 \text{ in (32 ft pressure length)} \\ l &= 900 \text{ in (75 ft span length)} \end{aligned} \right\} \quad (45)$$

SPAN FREQUENCIES

A study of guideway frequencies was first made using the example just cited as a reference case. For the 75 ft. span, for instance, if there are no end tensions ($T = 0$) and no foundation effects ($k = 0$), $\omega_1 = 14.11$ and $\omega_2 = 56.4$ radians/sec for the first ($n = 1$) and the second ($n = 2$) mode frequency, respectively. These results are shown in Figures 6 and 7 as the circled points,

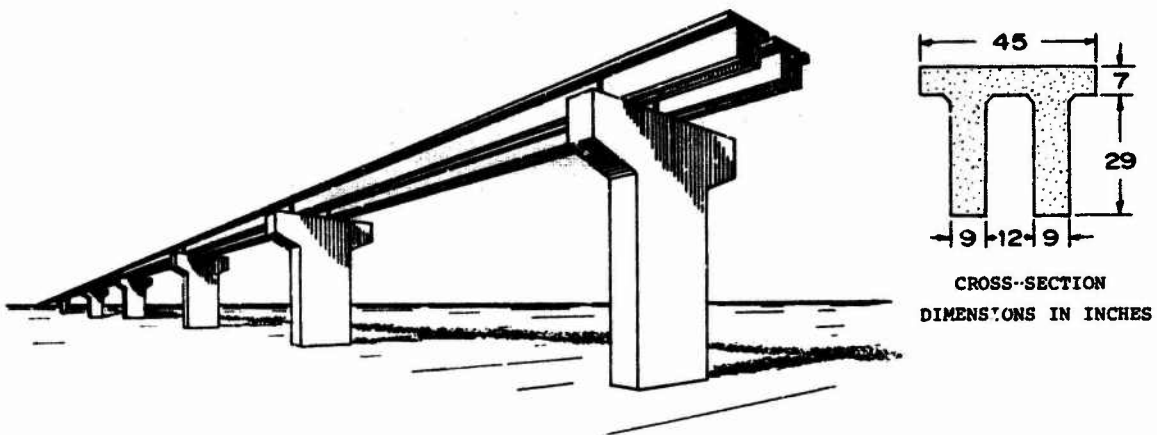


Figure 5. A typical reinforced concrete guideway for a tracked air cushion vehicle. Side guide rails not shown. Cross-section properties: $I = 63,000 \text{ in}^4$, $A = 837 \text{ in}^2$. For concrete: $\rho_g = 150 \text{ lb/ft}^3$; $E = 4 \times 10^6 \text{ psi}$.

NUMERICAL EXAMPLES

A typical guideway span of reinforced concrete is shown in Figure 5. Dimensions are shown for one of the two identical inverted "U" sections which together carry one 50,000 lb. air cushion vehicle. Side-rails, which are necessary for vehicle stability under wind loads, are not included. As a first approximation, it is assumed that the vehicle weight is equally distributed between the two parallel spans, and that the air cushion pressure is uniform

where $\rho A = 0.188$. These figures show that, while ω_n varies inversely as the square root of ρA , the span length has the dominant effect on the frequencies for a span of a given stiffness. Also, an increase in stiffness has more effect in increasing the mode frequencies for short spans than for long spans. Finally, end tensions as high as $T = 10^6 \text{ lbs.}$ have little effect on ω_n . However, if T is an increasing negative force, ω_1 decreases until T reaches the critical

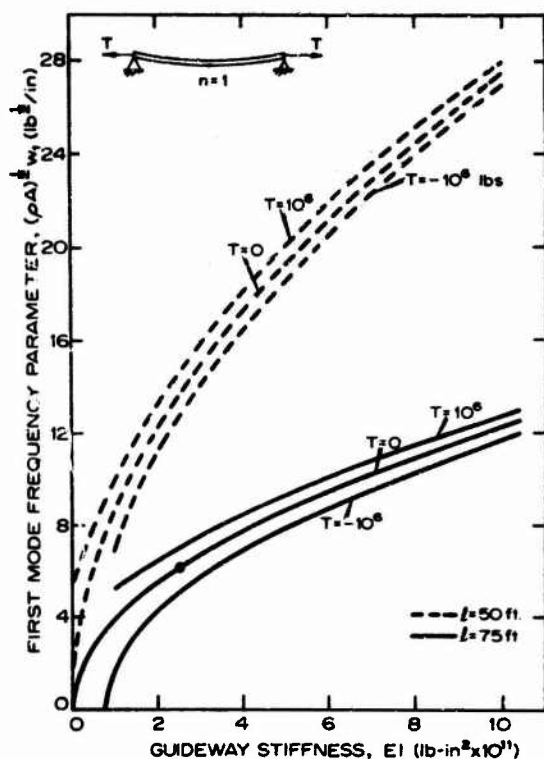


Figure 6. First mode frequency for a simply supported span without a foundation, showing effects of end tension, stiffness and span length.

Euler buckling load for the span. Then ω_1 is zero, and the span is unstable at all frequencies. This occurs for instance for $EI = 8.22 \times 10^{10}$ lb-in², $l = 75$ ft. and $T = -10^6$ lb., as shown in Figure 6.

If a given span rests on a soil foundation between piers, the beam frequencies are always increased. This is shown in Figure 8, where the soil is approximated as an elastic material. The value of $k = 5000$ lb/in² approximates a moderate value for a "strong" soil, as listed by Richart and Whitman [40]. The effects of end tensions on ω_n are negligible for k of this order of magnitude.

SPAN DEFLECTIONS

Static and dynamic deflections of two single spans with properties given by Equation (44) were calculated using the computer program. A 50 feet and a 75 feet span were considered, each subjected to a force $wl_1 = 25,000$ lbs. moving at constant velocities up to 500 mph. End tension and foundation effects were neglected in these calculations. For each span, two pressure patch

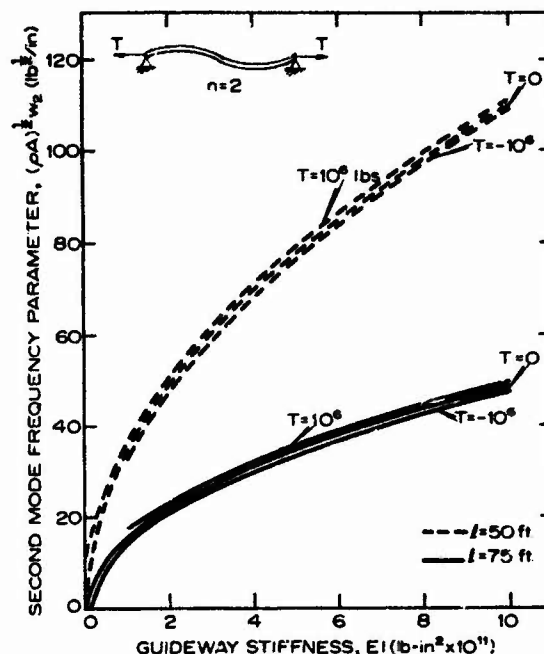


Figure 7. Second mode frequency for a simply supported span without a foundation, showing effects of end tension, stiffness and span length.

lengths were assumed: $l_1 = 384$ in. to simulate the passage of an air cushion vehicle, and $l_1 = 5$ in. to simulate the passage of a point force. In all of these cases, the maximum dynamic span deflections occurred at the midspan, or within 20 inches of it for the wider loading cases. Unlike the static deflections which reach their maximum values when the beams are symmetrically loaded about the midspans, the maximum dynamic deflections occurred as the pressure loads were unloading at the exit end. Timoshenko [11] observed this also for the point load case, which agrees favorably with the present case for $l_1 = 5$ in.

The dynamic deflection factors, or the ratio at midspan of the maximum dynamic deflections to maximum static deflections, were calculated at several constant velocities. These results are shown in Figure 9. For these spans and the two lengths of pressure loadings indicated, the dynamic deflection ratios reached peaks of about 1.8 at speeds between 100 and 250 mph. The interesting fact here is that this factor of 1.8 is almost independent of the length of the pressure loading, although the velocities at which these peaks occurred does change with l_1 . It is also noted that, if the pressure traverses fast enough the maximum dynamic deflection is actually less than the maximum static

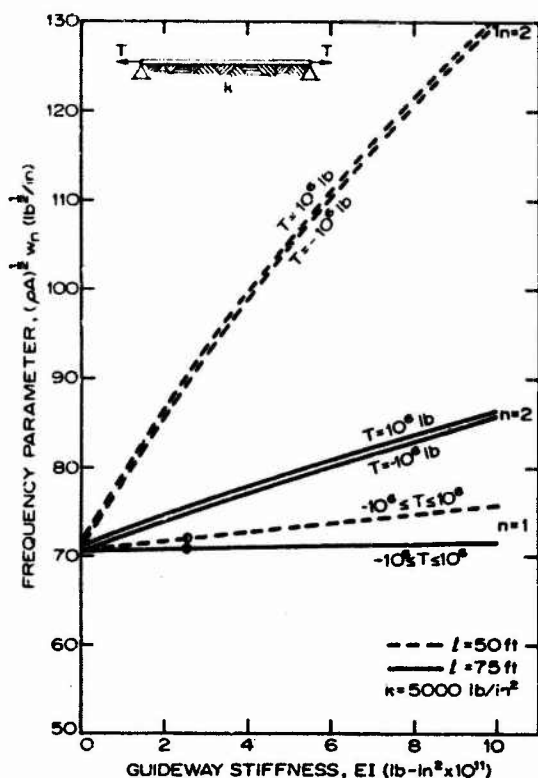


Figure 8. Lowest two mode frequencies for a simply supported span on a typically strong soil foundation, showing effects of end tension, stiffness, and span length.

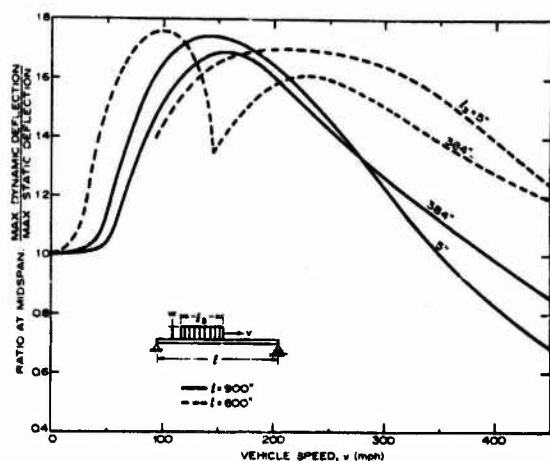


Figure 9. Dynamic deflections at mid-span for a single, constant pressure load moving at constant speed: $EI=2.52 \times 10^{11}$ lb-in², $\rho A=0.188$ lb sec²/in², $wl_3=25,000$ lbs, $T=k=0$.

deflection. This occurs for the 75 feet span, for instance, when v exceeds 400 mph.

The result that a pressure loading is capable of "outrunning" the static deflection capability of these spans is again illustrated by Figures 10 and 11. Here, the numerical results of the computer program for a pressure traverse across a single span were superimposed to simulate passage across identical, simple spans, all of which are initially at rest. The mean vertical displacements under a pressure load 384 in. in length are plotted as a function of the pressure front distance z shown in the inserted sketches on Figures 10 and 11. The mean vertical displacements \bar{y} are based on the arithmetic average of beam deflection at 20 evenly spaced points under the pressure. Values of \bar{y} are identical at $z=0$ and at $z=900$ in. This is because $z=0$ for the right span corresponds to $z=900$ for the identical left span shown in Figure 10. Thus, Figures 10 and 11 represent one cycle of mean deflection, which is repeated again every span length. In these Figures there is a definite trend toward smaller mean values of dynamic deflection under the air cushion vehicle at the higher constant speeds.

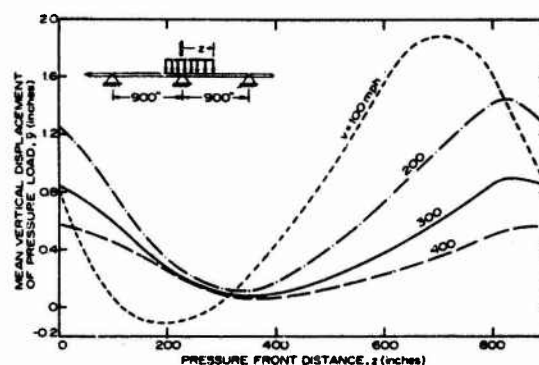


Figure 10. Mean vertical displacements of a single pressure load traversing identical, simple spans: $EI=2.52 \times 10^{11}$ lbs-in², $\rho A=0.188$ lb-sec²/in², $w=65.1$ lb/in, $l=900$ in, $l_3=384$ in., $T=k=0$.

LOAD ACCELERATIONS

The total acceleration d^2y/dt^2 of the pressure load at a given instant of time (or for a fixed z) varies along the length of the loading. Average values for this acceleration, $d^2\bar{y}/dt^2$, were calculated in the same way as for \bar{y} of Figures 10 and 11, where a pressure 384

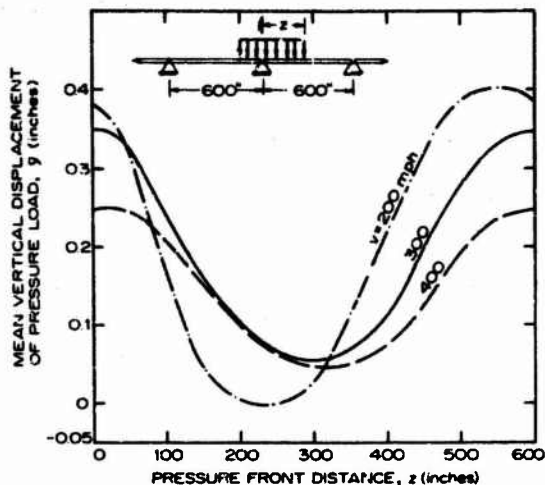


Figure 11. Mean vertical displacements of a single pressure load traversing identical simple spans: $EI=2.52 \times 10^{11}$ lbs-in², $\rho A=0.188$ lb-sec²/in², $w=65.1$ lb/in, $l=600$ in, $l_s=384$ in, $T=k=0$.

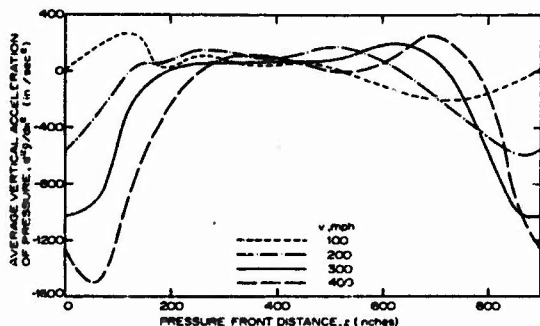


Figure 12. Mean vertical accelerations of a single pressure load traversing identical simple spans: $EI=2.52 \times 10^{11}$ lb-in², $\rho A=0.188$ lb-sec²/in², $w=65.1$ lb/in, $l=900$ in, $l_s=384$ in, $T=k=0$.

inches in length traverses identical spans at constant velocity. Figures 12 and 13 show how these average vertical accelerations vary with the pressure front distance measured from the end of one typical span. Again, these Figures represent one cycle of mean acceleration of the pressure which is repeated every span length.

Several observations can be made. First, at higher constant speeds, the mean vertical acceleration continues to increase. These increases always occur as the air cushion vehicle enters and exits a typical span. When the pressure

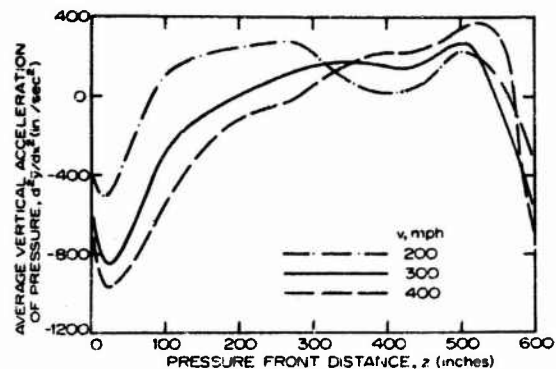


Figure 13. Mean vertical accelerations of a single pressure load traversing identical simple spans: $EI=2.52 \times 10^{11}$ lb/in², $\rho A=0.188$ lb-sec²/in², $w=65.1$ lb/in, $l=600$ in, $l_s=384$ in, $T=k=0$.

patch is near the midspan, vehicle speed has less effect on the mean vertical accelerations. In these Figures, the velocity is constant, so that the acceleration term in Equation (37) involving $\partial v / \partial t$ is zero. For values of v above 200 mph, numerical results show that the remaining three terms of Equation (37) which comprises d^2y/dt^2 are all of the same order of magnitude. Thus, the term $\partial^2 y / \partial t^2$, the vertical acceleration of the guideway alone, is not a good indication of the vertical acceleration of the moving vehicle.

When the results of Figures 12 and 13 are compared, it is concluded that, for the same vehicle speed, the mean accelerations can be reduced by decreasing the span length, where all of the other design variables remain fixed. The effect of a span length reduction is to increase ω_n , the span's natural frequency given by Equation (9).

CONCLUSIONS

Classical theory has been used to study the dynamic interactions of beams to segments of uniform, moving pressure. Uniform end tensions and elastic foundation effects were included in the Bernoulli-Euler beam model. Results show that for a given span and total load, the maximum dynamic span deflections for distributed and concentrated moving loads are nearly identical, although the velocity at which these deflections occur are different. Examples, utilizing anticipated TACV parameters,

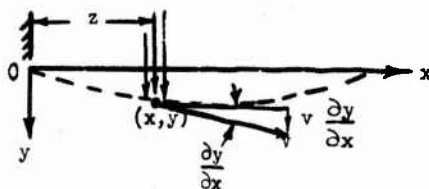
indicate that beyond certain velocities the mean value of the dynamic deflection under a pressure segment decreases with increasing speed. Although the vehicle may "outrun" the static span deflections, it can never outrun the vertical accelerations during traverse. These accelerations increased with increasing speed and approached 4 g's in the examples considered. In the case of a simply supported span, vertical accelerations can be decreased somewhat by decreasing span length and/or applying end tension. The effect of end tension on acceleration, however, is relatively small and probably not a practical method for improving ride. The high accelerations suggest the need for advanced vehicle suspensions or control systems to insure passenger safety and comfort.

It should be reiterated that these results are based on a simple mathematical model of the vehicle/guideway system. Additional work is needed for detailed analysis of multiple pressure patches, multiple spans, and trains of vehicles. Furthermore, the effects of vehicle mass, suspension systems and air cushion dynamics must be considered. As Bresse [33] first pointed out in 1859, the deflections of simple spans subjected to long flexible masses moving at constant velocity can become unbounded.

ACKNOWLEDGEMENTS

This research was accomplished during the Summer Faculty Fellowship Program sponsored by NASA and the American Society of Engineering Education. The writer wishes to acknowledge the contributions of David G. Stephens of the NASA Dynamic Loads Division who suggested this problem area and offered assistance in the formulation and interpretation of the results. The cooperation of Jean Mason in obtaining computer results is also greatly appreciated.

APPENDIX - KINEMATICS



The position of a massless element of pressure at point (x, y) is specified by $z = z(t)$ and the magnitude of its velocity by $z = v = v(t)$. The direction of v is always tangent to its trajectory, shown above by the dashed curves. The y-directed velocity of this pressure element is given by

$$\frac{dy}{dt} = \frac{\partial y}{\partial t} + v \frac{\partial y}{\partial x}$$

where the first term on the right is the component due to the moving trajectory (the vibrating beam). The second term is the y-component of the velocity v as shown above, where it is assumed that the slope of the trajectory, $\frac{\partial y}{\partial x}$, is always small compared to unity. When the "chain rules" are applied in the time differentiation of the total vertical velocity, the total y-directed acceleration is given by

$$\frac{d^2 y}{dt^2} = \frac{\partial^2 y}{\partial t^2} + 2v \frac{\partial^2 y}{\partial x \partial t} + v^2 \frac{\partial^2 y}{\partial x^2} + \frac{\partial v}{\partial t} \frac{\partial y}{\partial x}$$

The partial derivatives involving y on the right side of this equation are evaluated from Equation (34), where three of the coefficients of these derivatives depend on velocity v . For the special case in which the position z of an element of pressure is given in the form of Equation (20), $v = a + 2bt$ and $\partial v / \partial t = 2b$. In this derivation, the points z and x are coincident.

REFERENCES

1. Willis, R., "Report to the Commissioners . . . to Inquire into the Applications of Iron to Railway Bridges," London, 1849. See references 2 and 34, p. 197.
2. Stokes, G. G., "Discussion of the Differential Equation Relating to the Breaking of Railway Bridges," Mathematics Physics Papers, Vol. 2, 1849, p. 179.
3. Timoshenko, S. P., "On the Forced Vibration of Bridges," Philosophical Magazine, London, Vol. 43, 1922, p. 1018.
4. Kryloff, A. N., "Über die erzwungenen Schwingungen von gleichförmigen elastischen Stäben," Mathematische Annalen, Vol. 61, 1905, p. 211.
5. Jeffcott, H., "On the Vibration of Beams Under the Action of Moving Loads," Philosophical Magazine, Vol. 8, Series 7, 1929.
6. Inglis, G., A Mathematical Treatise of Vibrations in Railway Bridges. Oxford University Press, New York, 1934.
7. Schallenkamp, A., "Schwingungen von Trägern bei bewegten Lasten," Ingenieur-Archiv, Vol. 8, 1937, pp. 182-198.

8. Ayre, R. S.; Ford, G.; and Jacobsen, L. S., "Transverse Vibration of a Two-Span Beam Under Action of a Moving Constant Force," *Journal of Applied Mechanics*, ASME, Vol. 17, March 1950, pp. 1-12.
9. Ayre, R. S.; and Jacobsen, L. S., "Transverse Vibration of a Two-Span Beam Under the Action of a Moving Alternating Force," *Journal of Applied Mechanics*, ASME, Vol. 17, September 1950, pp. 283-290.
10. Ayre, R. S.; Jacobsen, L. S.; and Hsu, R. S., "Transverse Vibration of One and of Two-Span Beams Under the Action of Moving Mass Load," *Proceedings of the First U. S. National Congress of Applied Mechanics*, Illinois Institute of Technology, Chicago, Illinois, June 11-16, 1951, pp. 81-89.
11. Timoshenko, S.; and Young, D. H., *Vibration Problems in Engineering*. Third Edition, D. Van Nostrand, Inc., New York, N. Y., 1955.
12. Lowan, N., "On Transverse Oscillations of Beams Under the Action of Moving Variable Loads," *Philosophical Magazine*, Series 7, Vol. 19, 1935.
13. Ryazanova, M., "Vibrations in a Beam Under the Action of a Load Travelling Along It," *Dop. Akad. Nauk, Ursu.*, No. 2, 1958.
14. Schlack, A. L.; and Rashe, T. F., "Resonance of Beams Due to Cyclic Moving Loads," *Journal of the Engineering Mechanics Division*, ASCE, No. 6, Dec. 1966, pp. 175-184.
15. Romauldi, J. P., "The Dynamic Response of Floating Bridges to Transient Loads," Ph.D. Thesis, Carnegie Institute of Technology, 1954.
16. Vellozzi, J., "Vibration of Suspension Bridges Under Moving Loads," *Journal of the Structural Division*, ASCE, Vol. 94, August 1967, pp. 123-135.
17. Suer, H. S., "Dynamic Response of simple Span Highway Bridges to Moving Loads," Unpublished Doctor's Thesis, MIT Department of Civil and Sanitary Engineering, September 1955.
18. Stanisic, M. M.; and Hardin, J. C., "On the Response of Beams to an Arbitrary Number of Concentrated Moving Masses," *Journal of the Franklin Institute*, Vol. 287, No. 2, Feb. 1969, pp. 115-123.
19. Tan, C. P.; and Shore, S., "Dynamic Response of a Horizontally Curved Bridge," *Journal of the Structural Division*, ASCE, Vol. 95, March 1968.
20. Tan, C. P.; and Shore, S., "Response of a Curved Bridge to a Moving Load," *Journal of the Structural Division*, ASCE, Vol. 95, September 1968, pp. 2135-2151.
21. Ludwig, K., "Die Verformung Eines Beiderseits Unbegrenzten Elastisch Gebetten Geleises Durch Lasten Mit Konstanter Horizontalgeschwindigkeit," *Proceedings, Fifth International Congress of Mechanics*, 1938.
22. Kenny, J., "Steady-State Vibrations of a Beam on an Elastic Foundation for a Moving Load," *Journal of Applied Mechanics*, ASME, Vol. 76, 1954.
23. Matthews, P., "Vibrations of a Beam on an Elastic Foundation," *ZAMM*, Vol. 38, 1958.
24. Criner, H.; and McCann, G., "Rails on Elastic Foundations Under the Influence of High-Speed Travelling Loads," *Transactions*, ASME, Vol. 75, 1953.
25. Gesund, H.; and Young, D., "Dynamic Response of Beams to Moving Loads," *Publications, International Assn. for Bridge and Structural Engrg.*, 1961.
26. Saibel, E.; and Lee, W., "Vibrations of a Continuous Beam Under a constant Moving Force," *Journal of the Franklin Institute*, December 1952.
27. Crandall, S. H., "The Timoshenko Beam on an Elastic Foundation," *Proceedings of the Third Midwestern Conference on Solid Mechanics*, Ann Arbor, Michigan, 1957, pp. 146-159.
28. Florence, A. L., "Travelling Force on a Timoshenko Beam," *Journal of Applied Mechanics*, ASME, Vol. 32, No. 2, June 1965, pp. 351-358.
29. Achenbach, J. D.; and Sun, C. T., "Moving Load on a Flexibly Supported Timoshenko Beam," *International Journal of Solids and Structures*, Vol. 1, 1965, pp. 353-370.
30. Steele, C. R., "The Finite Beam with a Moving Load," *Journal of Applied Mechanics*, ASME, Vol. 34, No. 1, March 1967, pp. 111-118.

31. Steele, C. R., "Nonlinear Effects in the Problem of a Beam on a Foundation with a Moving Load," *International Journal of Solids and Structures*, Vol. 3, No. 4, July 1967, pp. 565-585.
32. Steele, C. R., "The Timoshenko Beam with a Moving Load," *Journal of Applied Mechanics*, ASME, Vol. 35, September 1968, pp. 481-488.
33. Bresse, F., *Cours de mecanique appliquee*. Paris, 1859, Vol. 1, Chapter VI. Reference cited by Panovko and Gubanov [34], p. 205.
34. Panovko, Y. G.; and Gubanov, I. I., *Stability and Oscillations of Elastic Systems*. (Translated from the Russian by C. V. Larrick) Consultants Bureau Enterprises, Inc., New York, N. Y., 1965, Chapter VII.
35. Chen, Y., *Vibrations, Theoretical Methods*. Addison-Wesley Co., Reading, Mass., 1966, Chapter 4.
36. Goldstein, S., *Classical Mechanics*. Addison-Wesley Co., Reading, Mass., 1959.
37. Hildebrand, F. B., *Advanced Calculus for Engineers*. Prentice-Hall, Inc., Englewood Cliffs, N. J., 1960, p. 242.
38. Moore, R. A., *Introduction to Differential Equations*. Allyn and Bacon, Inc., Boston, Mass., 1962, p. 134.
39. Langhaar, H. L., *Energy Methods in Applied Mechanics*. John Wiley and Sons, Inc., New York, 1962, pp. 44-48.
40. Richart, F. E.; and Whitman, R. V., "Design Procedures for Dynamically Loaded Foundations," *Journal of the Soil Mechanics and Foundations Division*, ASCE, Vol. 93, No. SM6, Nov. 1967.

DISCUSSION

Mr. Naylor (Defense Research Establishment, Suffield): Is it correct that at 400 mph those 3 g accelerations only last for approximately 10 milliseconds? If so, they would be hardly noticeable.

Mr. Wilson: That is correct. Probably with damping they might be reduced. For instance, at 300 mph, a 75 ft. span is passed in a second or less, so you are probably right. They do not last very long, and they only represent the average under the vehicle. One end might be higher than the other, and I have already averaged this and tried to make it as low as possible. However, they could be twice as large because of the distribution underneath the vehicle. I do not know how good this model is because it is the very first model of moving pressures of a finite length, over a beam of finite length, that anyone has ever attempted to analyze.

Mr. Michel (NASA Headquarters): Your analysis is for one span which I assume means that your initial condition had the vehicle traveling in a horizontal direction. When it leaves one span and enters the next one, the vehicle is no longer traveling in a horizontal direction. Have you performed a multi-span analysis?

Mr. Wilson: No. This model consists of many simple spans end to end, and the aver-

age accelerations represent those accelerations where part of the pressure wave is on the previous span and the other part of it is on the following span.

Mr. Addonizio (Gibbs & Cox): The ratio of the dynamic deflection to static deflection is unity at approximately 350 mph. Is your design based on the static condition for that particular case?

Mr. Wilson: It just happens for this particular problem that this is true. One could work some other problem and shift these curves so that some other velocity would yield a dynamic deflection factor higher than this. This is a particular sample problem. I know that this deflection is higher after the vehicle leaves the span. The results that I showed only applied to the vehicle when it traversed a span.

Voice: In that case they are not values to be used for design purposes?

Mr. Wilson: Recent calculations show that the maximum occurs while the vehicle is on the span. One never obtains a higher value than at one of the speeds as it accelerates to the maximum. For instance, if the vehicle accelerates from 0 to 400 mph, one would design for that speed in between those limits that yields the maximum dynamic deflection factor.

THE DESIGN OF A STRUCTURAL MEMBER ANALYSIS PROGRAM
FOR AN INTERACTIVE COMPUTER SYSTEM

Walter D. Pilkey *
University of Virginia
Charlottesville, Virginia

and

Richard Nielsen and Marvin Steier
COM/CODE Corporation *
Washington, D.C.

The design of a computer program system for determining the static, stability, and dynamic response of structural members is described. The programs are intended to be man-machine interactive with engineering user-oriented input languages and suitable for use on time-sharing, remote batch, or standard batch computers including certain limited capacity machines used by some small design firms. Such desirable design features as the capability to perform variation of parameter studies, to modify the problem statement as soon as a solution appears, and to couple the rapid analysis portion with optimization or sensitivity schemes are incorporated in the system.

INTRODUCTION

Typically a structural designer wishes to efficiently evaluate the relative merits of candidate design configurations. This is accomplished by coupling an analysis capability to a trial and error scheme or to the logic of formal optimization or sensitivity procedures. A new dimension to the design process is made available by the emerging development of rapid access computers. The philosophy underlying a computer code system for interactive machines is discussed here to illustrate the potential exploitation of this dimension. Particular attention is devoted to a system oriented to the engineer concerned with structural members or mechanical elements.

Although usually involving specific problems, there has been a steady increase in the use of the computer as a tool for the engineer. Among the many computer programs available today are few that are useful to the majority of engineers in any given discipline and fewer still that are readily accessible to the engineer associated with small concerns. This situation stems as much from the lack of generalized solutions to broad classes of problems as it does from the heretofore unavailability of universally accessible, large capacity, reliable computer systems. With contemporary improvement in analysis and design methodologies

and computer hardware technology we can anticipate rather astounding changes in the role the computer plays in the activities of the engineer. Not only will the mundane tasks of handbook engineering be expedited but a renaissance of the design process itself can be expected. Continued progress should signal a high degree of transparency of the computer for the practicing engineer in that he will be virtually unaware that a computer is being used to gain desired information. The discussion here concerns the design of structural member analysis computer programs which are developed with this theory of the future engineer in mind. Full advantage is taken of new structural analysis techniques and rapid access computers, in particular time-sharing systems.

A brief discourse on time-sharing computing is in order. Time-sharing is somewhat of a misnomer and is better called computer-sharing. It is a technique which takes advantage of the difference in speed between the electronics section of the computer, commonly known as the central processing unit, and the more mechanically dependent peripheral devices which serve as the input/output units. The central processor is literally thousands of times faster than the input/output terminals and therefore is capable of servicing more than one terminal if properly

programmed. In fact it is quite common for these computer-sharing systems to service about 50 terminals simultaneously. An individual at a terminal feels that he is using the computer exclusively.

These computer-sharing systems can be accessed from anywhere that a telephone connection can be made between the locations of the user and the computer. The terminal device is an ordinary 100 word per minute teletype unit which uses the normal voice grade telephone system as a communications network. The terminal unit is small enough to be placed on a desk, durable enough to be transported in the trunk of a car, and light enough to be carried in a suitcase by a man of average physical stature. Recent advances are leading to still lighter, smaller, and more reliable terminals. The user of this system simply makes an ordinary telephone call. He dials a standard length telephone number and is "answered" by a computer. He is connected to a communications device which is electronically interfaced with the computer. When the phone call is made and the connection established the computer sends a message to the terminal requesting the user to identify himself by typing a previously assigned identification number. If this is done in the prescribed manner the user may proceed to use the computer in whatever manner he desires.

ORGANIZATION OF THE PROGRAMS

The type of computer program system considered here is logically comprised of an extensive input routine, an analysis package, and an output code. The input package utilizes a user-oriented vocabulary (thesaurus) and numerical information to construct a file of raw data which describes the user's problem and his output specifications.

The analysis package accesses the raw data files, performs the required computations, and generates output files. COM/CODE Corporation has developed a computer program system (LINK) of the type described here, which executes analyses using a generalized line-solution technology. This analysis applies to bars, spring-mass systems, torsional bar systems, beams, rotating shafts, thin-walled beams, strings, arches, membranes, plates, grillages, thick shells, thin shells, and simple frameworks. Acceptable responses are static, stability, free and forced dynamics.

The output routine accesses all appropriate output files and prints solutions in the graphical or tabular format specified by the user. Its task completed, the output package returns the control to the input package to permit the user to modify the problem or introduce a new problem.

INPUT

The heart of an effective interactive re-

lationship between the designer and the computer is an input language which permits the user to describe his problem in his own terms and an input logic which assists the user in establishing a well-posed problem. This language and the concomitant logic should be such that the user need possess minimal knowledge of the mechanics of the time-sharing computer and no knowledge of the analysis routine. Should the user request a solution which is beyond the capability of the analysis, he should be so informed.

Input logic checks should monitor both the physics of the problem and the adequacy of the information given. Thus a kinematically unstable member should be noted, just as certain geometric and/or material properties should be prescribed for each section of the member and the sum of the lengths of the sections should equal the total length.

The input language itself should be constructed of alphanumerics since the engineer thinks in such terms, e.g., "a force of 100 lbs. is located at 10 ft. from the left end." The input compiler must recognize the engineer's vocabulary and upon sorting through the given data and checking the logic, place the input information in a form acceptable to the analysis package. The type of language appropriate to describe an analysis problem can be illustrated with the beam of Fig. 1. Suppose the first two natural frequencies are desired, then the complete input could be:

```
BEAM
FREE DYNAMICS
LENGTH=30,LEFT=PIN,RIGHT=FREE
E@0=30E6,I@0=.7854,SUPP@RT@25
MASS@0=.002300
CMASS@10=.05176@20=.05176@30=.05176
FREQUENCIES=2
G@
```

The ingredients of this problem description are almost self-evident. It is assumed that all distances are measured from the left end of the beam.

The desire to study the sensitivity of a response to a variation in a parameter can be indicated by the addition of a simple input statement. For example, if in the problem of Fig. 1 the effect on the frequencies of 10 increment changes of 0.5 in moment of inertia is sought, then the following command would be initiated:

```
VARY,I,0.5,1000
```

ANALYSIS

It is essential that a universal yet rapid

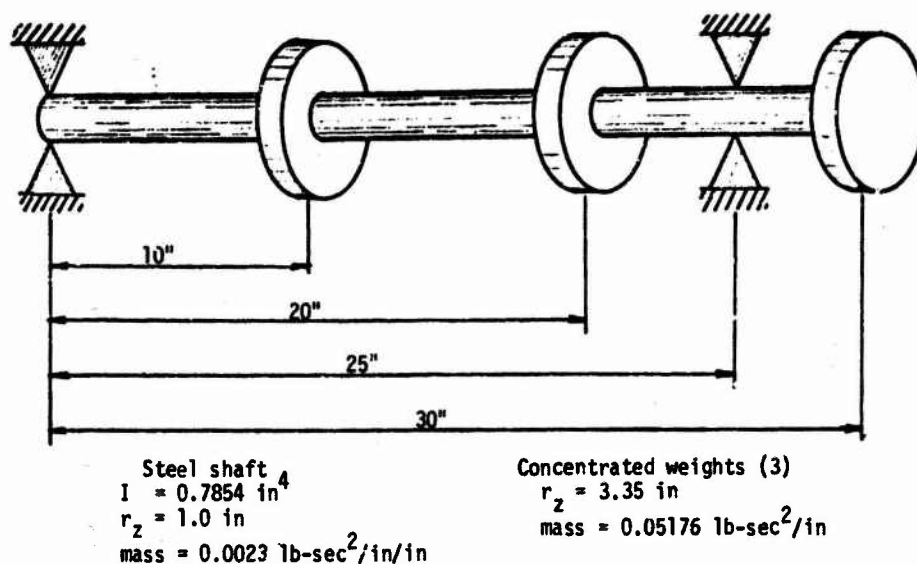


FIG. 1 STEEL SHAFT

analysis be available as the analysis portion of the program. In the case of the line-solution (initial parameter, transition, or transfer matrix) method [1], which is essentially a technique for converting a boundary value problem into an initial value problem, appropriate structural members or mechanical elements are those that exhibit either naturally or artificially a chain-like topology. The desired response data and necessary descriptive input information for this class of members are usually small; consequently, problems involving such members are ideal for treatment with computer systems with relatively slow input/output capabilities. The line-solution technique can be implemented on computer systems of moderate capacity and can be fully systematized in that all physical, geometric, material, and loading occurrences can be automatically taken into account.

OUTPUT

As long as a comprehensive analysis package is used, the output portion of the computer program is simply a data processing device which prints out the requested information in a useful, attractive format. Output options should include any or all of the displacements, slopes, moments, forces, or stresses printed or displayed in tabular or graphical form at specified increments along the member. Upon request the reactions and maximum values of variables should be given. Critical axial forces and frequencies should be available with or without mode shapes. The designer should be permitted to graphically observe the effect on the re-

sponse of a member of varying a parameter by requesting a plot of a particular response as a parameter varies over a specified increment, e.g., a plot of critical axial load vs. a range of values of a spring constant may be desired. Output for the problem of Fig. 1 could simply be:

FREE DYNAMICS PROBLEM

MODE	NAT FREQ
1	.78018E 03
2	.19665E 04

REPETITIVE ACCESS TO THE PROGRAM

A VARY option permits the designer to observe how a response is affected by a variation in parameters. Although this type of sensitivity study may be adequate to fulfill the designer's needs, frequently the trial and error designer wishes to analyze one design configuration at a time and adjust the configuration on the basis of the response of the first design. This can be accomplished in some cases by permitting the user to continue with a problem by supplementing the data already supplied and stored. For example, in the case of the beam of Fig. 1, we could continue to include additional effects with the sequence:

DO YOU WISH TO CONTINUE WITH THE SAME PROBLEM. TYPE YES OR NO.

programmed. In fact it is quite common for these computer-sharing systems to service about 50 terminals simultaneously. An individual at a terminal feels that he is using the computer exclusively.

These computer-sharing systems can be accessed from anywhere that a telephone connection can be made between the locations of the user and the computer. The terminal device is an ordinary 100 word per minute teletype unit which uses the normal voice grade telephone system as a communications network. The terminal unit is small enough to be placed on a desk, durable enough to be transported in the trunk of a car, and light enough to be carried in a suitcase by a man of average physical stature. Recent advances are leading to still lighter, smaller, and more reliable terminals. The user of this system simply makes an ordinary telephone call. He dials a standard length telephone number and is "answered" by a computer. He is connected to a communications device which is electronically interfaced with the computer. When the phone call is made and the connection established the computer sends a message to the terminal requesting the user to identify himself by typing a previously assigned identification number. If this is done in the prescribed manner the user may proceed to use the computer in whatever manner he desires.

ORGANIZATION OF THE PROGRAMS

The type of computer program system considered here is logically comprised of an extensive input routine, an analysis package, and an output code. The input package utilizes a user-oriented vocabulary (thesaurus) and numerical information to construct a file of raw data which describes the user's problem and his output specifications.

The analysis package accesses the raw data files, performs the required computations, and generates output files. COM/CODE Corporation has developed a computer program system (LINK) of the type described here, which executes analyses using a generalized finite-element technology. This analysis applies to bars, spring-mass systems, torsional bar systems, beams, rotating shafts, thin-walled beams, strings, arches, membranes, plates, grillages, thick shells, thin shells, and simple frameworks. Acceptable responses are static, stability, free and forced dynamics.

The output routine accesses all appropriate output files and prints solutions in the graphical or tabular format specified by the user. Its task completed, the output package returns the control to the input package to permit the user to modify the problem or introduce a new problem.

INPUT

The heart of an effective interactive re-

lationship between the designer and the computer is an input language which permits the user to describe his problem in his own terms and an input logic which assists the user in establishing a well-posed problem. This language and the concomitant logic should be such that the user need possess minimal knowledge of the mechanics of the time-sharing computer and no knowledge of the analysis routine. Should the user request a solution which is beyond the capability of the analysis, he should be so informed.

Input logic checks should monitor both the physics of the problem and the adequacy of the information given. Thus a kinematically unstable member should be noted, just as certain geometric and/or material properties should be prescribed for each section of the member and the sum of the lengths of the sections should equal the total length.

The input language itself should be constructed of alphanumeric characters since the engineer thinks in such terms, e.g., "a force of 100 lbs. is located at 10 ft. from the left end." The input compiler must recognize the engineer's vocabulary and upon sorting through the given data and checking the logic, place the input information in a form acceptable to the analysis package. The type of language appropriate to describe an analysis problem can be illustrated with the beam of Fig. 1. Suppose the first two natural frequencies are desired, then the complete input could be:

```
BEAM
FREE DYNAMICS
LENGTH=30,LEFT=PIN,RIGHT=FREE
E@0=30E6,I@0=.7854,SUPPORT@25
MASS@0=.002300
CMASS@10=.05176@20=.05176@30=.05176
FREQUENCIES=2
GO
```

The ingredients of this problem description are almost self-evident. It is assumed that all distances are measured from the left end of the beam.

The desire to study the sensitivity of a response to a variation in a parameter can be indicated by the addition of a simple input statement. For example, if in the problem of Fig. 1 the effect on the frequencies of 10 increment changes of 0.5 in moment of inertia is sought, then the following command would be initiated:

```
VARY,I,0.5,10@0
```

ANALYSIS

It is essential that a universal yet rapid

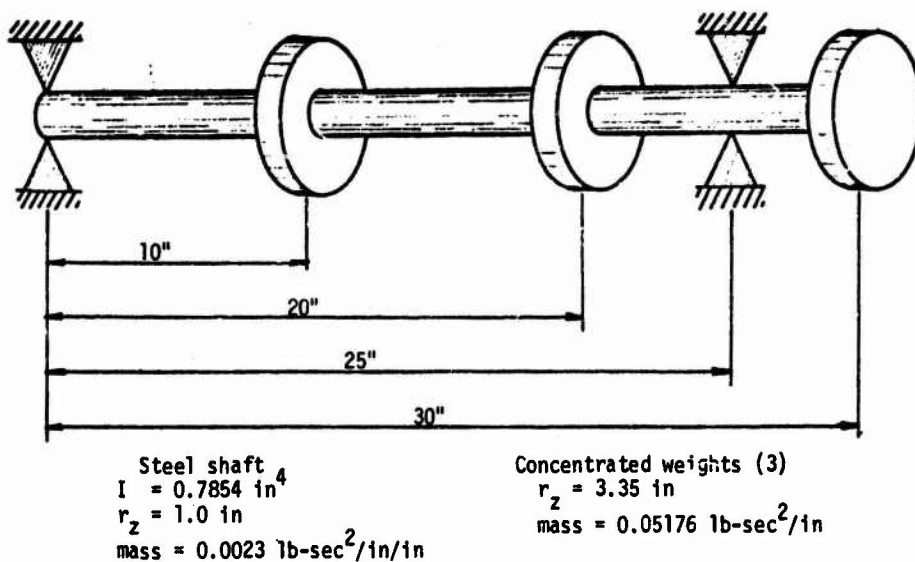


FIG. 1 STEEL SHAFT

analysis be available as the analysis portion of the program. In the case of the line-solution (initial parameter, transition, or transfer matrix) method [1], which is essentially a technique for converting a boundary value problem into an initial value problem, appropriate structural members or mechanical elements are those that exhibit either naturally or artificially a chain-like topology. The desired response data and necessary descriptive input information for this class of members are usually small; consequently, problems involving such members are ideal for treatment with computer systems with relatively slow input/output capabilities. The line-solution technique can be implemented on computer systems of moderate capacity and can be fully systematized in that all physical, geometric, material, and loading occurrences can be automatically taken into account.

OUTPUT

As long as a comprehensive analysis package is used, the output portion of the computer program is simply a data processing device which prints out the requested information in a useful, attractive format. Output options should include any or all of the displacements, slopes, moments, forces, or stresses printed or displayed in tabular or graphical form at specified increments along the member. Upon request the reactions and maximum values of variables should be given. Critical axial forces and frequencies should be available with or without mode shapes. The designer should be permitted to graphically observe the effect on the re-

sponse of a member of varying a parameter by requesting a plot of a particular response as a parameter varies over a specified increment, e.g., a plot of critical axial load vs. a range of values of a spring constant may be desired. Output for the problem of Fig. 1 could simply be:

FREE DYNAMICS PROBLEM

	NAT
MODE	FREQ
1	.78018E 03
2	.19665E 04

REPETITIVE ACCESS TO THE PROGRAM

A VARY option permits the designer to observe how a response is affected by a variation in parameters. Although this type of sensitivity study may be adequate to fulfill the designer's needs, frequently the trial and error designer wishes to analyze one design configuration at a time and adjust the configuration on the basis of the response of the first design. This can be accomplished in some cases by permitting the user to continue with a problem by supplementing the data already supplied and stored. For example, in the case of the beam of Fig. 1, we could continue to include additional effects with the sequence:

DO YOU WISH TO CONTINUE WITH THE SAME PROBLEM. TYPE YES OR NO.

YES

RINERTIA@0=1.0

CR@TARY@10=3.35@20=3.35@30=3.35

G@

S@LUT@NS

FREE DYNAMICS PR@BLEM

MODE	NAT FREQ
1	.71725E 03
2	.16622E 04

DO YOU WISH TO CONTINUE WITH THE SAME
PR@BLEM. TYPE YES OR N@.

YES

FORWARD WHIRL

G@

S@LUT@NS

FREE DYNAMICS PR@BLEM

MODE	NAT FREQ
1	.85265E 03
2	.24005E 04

A MODIFY command can be included to permit the user to reenter the program upon the completion of a solution to change the magnitude or location of any geometrical or material parameter or occurrence. No other input or output alteration need be made; the response is automatically computed for the new configuration. Since a common modification is to remove some force or support, a valuable command is that of DELETE, which will effectively remove a prescribed variable.

Frequently a design or analysis problem is not completed at one sitting and the user would like to begin again where he left off, perhaps the previous day. This desire can be taken into account by storing input data until the next terminal connection. A RED@ command given by the user would provide the option of activating the previous data. Without this instruction, it would be assumed that the problem at hand is new and all old data would be cleared from the files.

A truly viable system should permit the rapid analysis program to be used in conjunction with automated optimization and sensitivity schemes. That is, there should be the option of letting the logic of an optimization or sensitivity computer program determine and regulate modifications in parameters. Preferably this should be accomplished so that only a portion

of the response computation need be repeated at each iteration. If this is not feasible, then as a minimum the relatively inefficient regeneration of a new input data file and the logic associated with placing this data in the form acceptable to the analysis package must be avoided at each iteration. This latter goal is achieved simply by circumventing the input package after the first analysis.

SUMMARY AND CONCLUSIONS

A possible logic behind the development of a design engineer oriented computer program system for the analysis of structural members has been explained. It was intended to take advantage of contemporary and near-future computer hardware by providing the engineer with an accessible, versatile, easy to use design and analysis tool. Because of the mobility of input terminals, this system is best implemented on computers with true time-sharing or remote batch, options. However, the type of input compiler required to accept user-oriented input can be developed for pure batch computers. In such cases the degree of interactivity between the user and the machine is usually severely restricted relative to the time-sharing version.

REFERENCE

1. W. D. Pilkey and R. Nielsen, "Line-Solution Technology as a General Engineering Approach to the Static, Stability, and Dynamic Response of Structural Members and Mechanical Elements," Shock and Vibration Bull., Vol. 38, Pt. 2, pp 157-168, Aug 1968

DYNAMIC RESPONSE OF A SINGLE-DEGREE-OF-FREEDOM ELASTIC-PLASTIC SYSTEM SUBJECTED TO A HALF SINE PULSE

Martin Wohltmann
Structures and Mechanics Department
Martin Marietta Corporation
Orlando, Florida

The dynamic response of a single-degree-of-freedom system subjected to a half sine pulse, where the resistance function is elastic-plastic, has been analyzed. Maximum displacement, time to maximum displacement, and work done are the response quantities computed. Results are presented in design charts in non dimensional form as a function of two parametric ratios. A numerical example is included.

INTRODUCTION

Much analytical work has been done in determining the dynamic response of a single-degree-of-freedom(SDOF) system subjected to various types of pulse loadings where the restoring force or resistance is one of the following:

- 1 Linear with displacement (elastic)
- 2 Constant with displacement (rigid-plastic)
- 3 Linear with displacement followed by constant with displacement (elastic-plastic)
- 4 Nonlinear with displacement.

Figure 1 illustrates these resistance functions. The analysis most often presented in textbooks and handbooks is the one involving linear elasticity (Figure 1a). Reference 1 presents a treatment of systems involving the first three categories, subjected to rectangular and triangular pulse loadings. Category 2 (rigid-plastic) was extended to include response to sawtooth and parabolic pulse loadings, the results of which were presented in reference 2. Reference 3 extends category 3 to include response to a sawtooth pulse. The present work analyzes the category 3 (elastic-plastic) SDOF system subjected to a half sine pulse loading.

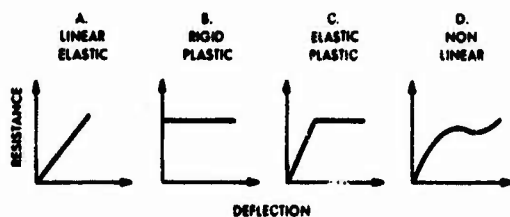


FIGURE 1. RESISTANCE FUNCTIONS

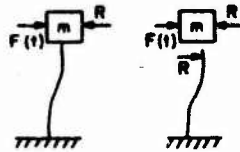
MATHEMATICAL FORMULATION

Symbols.

a,b	constants of integration
B	amplitude of loading pulse (lb)
A,C	constants
$A_1, A_2,$ $B_1, B_2,$ B_3	equal to various mathematical expressions
K	stiffness (lbs/in)
R	resistance (lb)
R_m	maximum resistance (lb)
M	mass (lb-sec ² /in)
f(t)	forcing function (lb)
W	weight (lb)
X	displacement (in)
X_T	displacement at $t = T$
X_e	displacement at $t = t_e$ (peak elastic displacement)
X_m	maximum displacement (in)
t	time (sec)
t_e	time to elastic displacement (sec)
t_m	time to maximum displacement (sec)
T	pulsewidth (sec)
T_N	system natural period (sec)
W_m	maximum work done by loading pulse (in-lb)
W_p	maximum possible work done by loading pulse (in-lb)
H	impulse
.	first derivative with respect to time
..	second derivative with respect to time

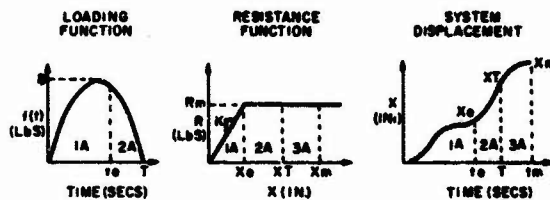
The system analyzed is illustrated below.

SYSTEM



There are two distinct cases to be solved. Case I is for the condition where the time (t_e) to reach the end of the elastic deflection (X_e) occurs before the end of the loading pulse (T) and Case II where t_e is greater than T . The equations of motions and the regions in which they are applicable for each of the cases are:

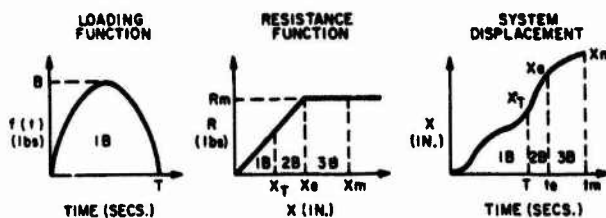
$$\text{Case I } \left(\frac{t_e}{T} < 1.0 \right)$$



X_m = maximum displacement
 X_e = maximum elastic displacement
 t_e = time to maximum elastic displacement
 t_m = time to maximum displacement

Region	Equation of Motion	
1A	$M\ddot{X} = f(t) - KX$	$0 < X < X_e$ $0 < t < t_e$
2A	$M\ddot{X} = f(t) - R_m$	$X_e < X < X_T$ $t_e < t < T$
3A	$M\ddot{X} = -R_m$	$X_T < X < X_m$ $T < t < t_m$

$$\text{Case II } \left(\frac{t_e}{T} > 1.0 \right)$$



Region	Equations of Motion	
1B	$M\ddot{X} = f(t) - KX$	$0 < X < X_T$ $0 < t < t_e$
2B	$M\ddot{X} = -KX$	$X_T < X < X_e$ $T < t < t_e$
3B	$M\ddot{X} = -R_m$	$X_e < X < X_m$ $t_e < t < t_m$

Case I Solution

The equation of motion for region 1A is:

$$M\ddot{X} = f(t) - KX \quad (1)$$

with $f(t) = B \sin(\pi \frac{t}{T})$ equation (1) may be written as:

$$M\ddot{X} + KX = B \sin(\pi \frac{t}{T}) \quad (2)$$

The forced solution of equation (2) is:

$$X(t) = \frac{B/K}{\left[1 - \frac{1}{4} \left(\frac{TN}{T} \right)^2 \right]} \sin(\pi \frac{t}{T}) \quad (3)$$

while the complementary solution is:

$$X(t) = A \sin\left(\frac{2\pi}{TN} t\right) + C \cos\left(\frac{2\pi}{TN} t\right) \quad (4)$$

where A and C are constants determined from initial conditions.

The general solution is then:

$$X(t) = A \sin\left(\frac{2\pi}{TN} t\right) + C \cos\left(\frac{2\pi}{TN} t\right) + \frac{B/K}{\left[1 - \frac{1}{4} \left(\frac{TN}{T} \right)^2 \right]} \sin(\pi \frac{t}{T}) \quad (5)$$

Applying the initial conditions $X = 0$ and $\dot{X} = 0$ at $t = 0$, the constants are:

$$C = 0$$

and

$$A = \frac{-B/K}{2 \left(\frac{T}{TN} \right) \left[1 - \frac{1}{4} \left(\frac{TN}{T} \right)^2 \right]}$$

Thus region 1A solution is:

$$X(t) = \frac{B/K}{\left[1 - \frac{1}{4} \left(\frac{TN}{T} \right)^2 \right]} \left\{ \sin(\pi \frac{t}{T}) - \frac{1}{2} \left(\frac{TN}{T} \right) \sin\left[\frac{2\pi T}{TN} \left(\frac{t}{T}\right)\right] \right\} \quad (6)$$

which may be written in nondimensional form as:

$$\frac{X(t)}{B/K} = \frac{1}{\left[1 - \frac{1}{4} \left(\frac{TN}{T}\right)^2\right]} \left\{ \sin\left(\pi \frac{t}{T}\right) - \frac{1}{2} \left(\frac{TN}{T}\right) \sin\left[\left(\frac{2\pi T}{TN}\right) \left(\frac{t}{T}\right)\right] \right\} \quad (7)$$

The velocity for region 1A is:

$$\dot{X}(t) = \frac{(B/KT)\pi}{\left[1 - \frac{1}{4} \left(\frac{TN}{T}\right)^2\right]} \left\{ \cos\left(\pi \frac{t}{T}\right) - \cos\left[\left(\frac{2\pi T}{TN}\right) \left(\frac{t}{T}\right)\right] \right\} \quad (8)$$

or in nondimensional form:

$$\frac{\dot{X}(t)}{(B/KT)} = \frac{\pi}{\left[1 - \frac{1}{4} \left(\frac{TN}{T}\right)^2\right]} \left\{ \cos\left(\pi \frac{t}{T}\right) - \cos\left[\left(\frac{2\pi T}{TN}\right) \left(\frac{t}{T}\right)\right] \right\} \quad (9)$$

The next step is to determine the displacement and velocity, when the displacement reaches the elastic displacement (X_e). These quantities are the initial conditions for region 2A.

Referring to the resistance function shown in an earlier illustration, the elastic displacement is:

$$X_e = \frac{R_m}{K} \equiv \left(\frac{R_m}{B}\right) \left(\frac{B}{K}\right) \quad (10)$$

Substituting equation (10) into equation (6), we have:

$$\left(\frac{R_m}{B}\right) \left[1 - \frac{1}{4} \left(\frac{TN}{T}\right)^2\right] = \sin\left(\pi \frac{t_e}{T}\right) - \frac{1}{2} \left(\frac{TN}{T}\right) \sin\left[\left(\frac{2\pi T}{TN}\right) \left(\frac{t_e}{T}\right)\right] \quad (11)$$

Equation (11) was solved for (t_e/T), for various combinations of the parameters: (R_m/B) and ($2\pi T/TN$) with the aid of the IBM 1130 computer. Results are plotted in Figure 6 and tabulated in Table III.

In region 2A the loading pulse has not been completed ($t_e \leq t \leq T$), and the resistance is constant ($X > X_e$). The equation of motion is:

$$M\ddot{X} = f(t) - R_m \quad (12)$$

with

$$f(t) = B \sin\left(\pi \frac{t}{T}\right)$$

$$M\ddot{X} = B \sin\left(\pi \frac{t}{T}\right) - R_m \quad (13)$$

or

$$\ddot{X} = \frac{B}{M} \sin\left(\pi \frac{t}{T}\right) - \frac{R_m}{M} \quad (14)$$

Integrating equation (14) twice gives:

$$\dot{X} = -\left(\frac{BT}{M\pi}\right) \cos\left(\pi \frac{t}{T}\right) - \frac{R_m}{M} t + a \quad (15)$$

$$X = -\frac{B}{M} \left(\frac{T}{\pi}\right)^2 \sin\left(\pi \frac{t}{T}\right) - \frac{R_m}{2M} t^2 + at + b \quad (16)$$

The initial conditions for region 2A are obtained from the end conditions in region 1A. Substituting $t = t_e$ into equations (6) and (8), the initial displacement and velocity are:

$$\begin{aligned} X(t_e) &= \frac{B/K}{\left[1 - \frac{1}{4} \left(\frac{TN}{T}\right)^2\right]} \left\{ \sin\left(\pi \frac{t_e}{T}\right) - \frac{1}{2} \left(\frac{TN}{T}\right) \sin\left[\left(\frac{2\pi T}{TN}\right) \left(\frac{t_e}{T}\right)\right] \right\} \\ &= \left(\frac{R_m}{B}\right) \left(\frac{B}{K}\right) \equiv A_1 \left(\frac{B}{K}\right) \end{aligned} \quad (17)$$

$$\begin{aligned} \dot{X}(t_e) &= \left(\frac{B}{KT}\right) \frac{\pi}{\left[1 - \frac{1}{4} \left(\frac{TN}{T}\right)^2\right]} \left\{ \cos\left(\pi \frac{t_e}{T}\right) - \cos\left[\left(\frac{2\pi T}{TN}\right) \left(\frac{t_e}{T}\right)\right] \right\} \\ &\equiv B_1 \left(\frac{B}{KT}\right) \end{aligned} \quad (18)$$

Setting the LHS of equations (15) and (16) equal to equations (18) and (17), respectively, and setting $t = t_e$ in the RHS of (15) and (16), gives:

$$B_1 \left(\frac{B}{KT}\right) = -\left(\frac{BT}{M\pi}\right) \cos\left(\pi \frac{t_e}{T}\right) - \frac{R_m}{M} t_e + a \quad (19)$$

$$\begin{aligned} A_1 \left(\frac{B}{K}\right) &= \frac{R_m}{B} \left(\frac{B}{K}\right) = -\frac{B}{M} \left(\frac{T}{\pi}\right)^2 \sin\left(\pi \frac{t_e}{T}\right) \\ &\quad - \frac{R_m}{2M} t_e^2 + at_e + b \end{aligned} \quad (20)$$

Solving for a and b (the integration constants) in equations (19) and (20) yields:

$$a = B_1 \left(\frac{B}{KT}\right) + \frac{B}{M} \left(\frac{T}{\pi}\right) \cos\left(\pi \frac{t_e}{T}\right) + \frac{R_m}{M} t_e \quad (21)$$

$$b = A_1 \left(\frac{B}{K} \right) + \frac{B}{M} \left(\frac{T}{\pi} \right)^2 \sin \left(\pi \frac{t_e}{T} \right) + \frac{R_m}{M} t_e^2$$

$$- B_1 \left(\frac{B}{K} \right) \left(\frac{t_e}{T} \right) - \frac{B}{M} \left(\frac{T}{\pi} \right) t_e \cos \left(\pi \frac{t_e}{T} \right) - \frac{R_m}{M} t_e^2. \quad (22)$$

Substituting equations (21) and (22) into equations (15) and (16), and after some rearrangement, the displacement and velocity in region 2A become:

$$X(t) = \left(\frac{B}{K} \right) \left\{ A_1 + B_1 \left(\frac{t}{T} - \frac{t_e}{T} \right) - \frac{1}{2} \left(\frac{R_m}{B} \right) \left(\frac{2\pi T}{TN} \right)^2 \left[\left(\frac{t}{T} - \frac{t_e}{T} \right)^2 - 4 \left(\frac{T}{TN} \right)^2 \left[\sin \left(\pi \frac{t}{T} \right) - \sin \left(\pi \frac{t_e}{T} \right) \right] + 4\pi \left(\frac{T}{TN} \right)^2 \left[\frac{t}{T} - \frac{t_e}{T} \right] \cos \left(\pi \frac{t_e}{T} \right) \right\} \quad (23)$$

$$\dot{X}(t) = \left(\frac{B}{KT} \right) \left\{ B_1 - 4\pi \left(\frac{T}{TN} \right)^2 \left[\cos \left(\pi \frac{t}{T} \right) - \cos \left(\pi \frac{t_e}{T} \right) \right] - \left(\frac{R_m}{B} \right) \left(\frac{2\pi T}{TN} \right)^2 \left[\frac{t}{T} - \frac{t_e}{T} \right] \right\}. \quad (24)$$

The initial conditions for region 3A are obtained from the end conditions in region 2A. Substituting $t = T$ into equations (23) and (24) gives:

$$X(T) = \left(\frac{B}{K} \right) \left\{ A_1 + B_1 \left(1 - \frac{t_e}{T} \right) - \frac{1}{2} \left(\frac{R_m}{B} \right) \left(\frac{2\pi T}{TN} \right)^2 \left[1 - \frac{t_e}{T} \right]^2 + 4 \left(\frac{T}{TN} \right)^2 \sin \left(\pi \frac{t_e}{T} \right) + 4\pi \left(\frac{T}{TN} \right)^2 \left[1 - \frac{t_e}{T} \right] \cos \left(\pi \frac{t_e}{T} \right) \right\}$$

$$\equiv A_2 \left(\frac{B}{K} \right) \quad (25)$$

$$\dot{X}(t) = \left(\frac{B}{KT} \right) \left\{ B_1 + 4\pi \left(\frac{T}{TN} \right)^2 \left[1 + \cos \left(\pi \frac{t_e}{T} \right) \right] - \left(\frac{R_m}{B} \right) \left(\frac{2\pi T}{TN} \right)^2 \left[1 - \frac{t_e}{T} \right] \right\} \equiv B_2 \left(\frac{B}{KT} \right) \quad (26)$$

In region 3A the equation of motion is:

$$M\ddot{X} = -R_m \quad (27)$$

or

$$\ddot{X} = -\frac{R_m}{M} \quad (28)$$

Integrating equation (28) twice gives:

$$\dot{X} = -\frac{R_m}{M} t + a \quad (29)$$

$$X = -\frac{R_m}{M} t^2 + at + b. \quad (30)$$

Making use of the initial conditions at $t = T$ from equations (25) and (26) and setting $t = T$ in (29) and (30), we have:

$$X(T) = A_2 \left(\frac{B}{K} \right) = -\frac{R_m}{2M} T^2 + aT + b \quad (31)$$

$$\dot{X}(T) = B_2 \left(\frac{B}{KT} \right) = -\frac{R_m}{M} T + a. \quad (32)$$

Solving for a and b in equations (31) and (32) gives:

$$a = B_2 \left(\frac{B}{KT} \right) + \frac{R_m}{M} T \quad (33)$$

$$b = A_2 \left(\frac{B}{K} \right) - \frac{R_m}{2M} T^2 - B_2 \left(\frac{B}{K} \right). \quad (34)$$

Substituting equations (33) and (34) into (29) and (30), the displacement and velocity in region 3A are:

$$X(t) = \left(\frac{B}{K} \right) \left\{ A_2 - B_2 \left[1 - \frac{t}{T} \right] - \frac{1}{2} \left(\frac{R_m}{B} \right) \left(\frac{2\pi T}{TN} \right)^2 \left[\frac{t}{T} - 1 \right]^2 \right\} \quad (35)$$

$$\dot{X}(t) = \left(\frac{B}{KT} \right) \left\{ B_2 + \left(\frac{R_m}{B} \right) \left(\frac{2\pi T}{TN} \right)^2 \left[1 - \frac{t}{T} \right] \right\}. \quad (36)$$

The time to maximum displacement is found by setting equation (36) equal to zero and $t = t_m$:

$$\dot{X}(t_m) = 0 = \left(\frac{B}{KT} \right) \left\{ B_2 + \left(\frac{R_m}{B} \right) \left(\frac{2\pi T}{TN} \right)^2 \left[1 - \frac{t_m}{T} \right] \right\} \quad (37)$$

or

$$B_2 + \left(\frac{R_m}{B} \right) \left(\frac{2\pi T}{TN} \right)^2 \left[1 - \frac{t_m}{T} \right] = 0 \quad (38)$$

Thus time to maximum displacement is:

$$\frac{t_m}{T} = 1 + \frac{B_2}{\left(\frac{R_m}{B} \right) \left(\frac{2\pi T}{TN} \right)^2} \quad (39)$$

Maximum displacement is obtained by substituting equation (39) into equation (35). After some rearrangement the maximum displacement is:

$$X_m = \left(\frac{B}{K}\right) \left\{ A_2 + \frac{1}{2} \left(\frac{R_m}{B} \right) \left(\frac{2\pi T}{TN} \right)^2 \right. \\ \left. \equiv B_3 \left(\frac{B}{K} \right) \right\} \quad (40)$$

For design purposes it is convenient to work with the ratio of the maximum displacement (X_m) to the peak elastic displacement (X_e). With:

$$X_e = \left(\frac{R_m}{B} \right) \left(\frac{B}{K} \right) \quad (41)$$

this ratio becomes:

$$\frac{X_m}{X_e} = \frac{B_3}{R_m/B} \quad (42)$$

An IBM 1130 program was written to compute values A_2 , B_1 , B_2 , and B_3 and thus evaluate the ratio X_m/X_e and t_m/T as a function of the parameters (R_m/B) and (T/TN).

The maximum work done by the pulse on the mass is given by the expression:

$$W_m = \int_0^{X(T)} f(t) dx \quad (43)$$

which may be written as:

$$W_m = \int_0^T f(t) (\dot{X}) dt \quad (44)$$

For regions 1A and 2A equation (44) becomes:

$$W_m = \int_0^{t_e} f(t) (\dot{X}) dt + \int_{t_e}^T f(t) (\dot{X}) dt \quad (45)$$

With $f(t) = B \sin(\pi \frac{t}{T})$ and substituting equations (8) and (24) into equation (45) gives:

$$W_m = \int_0^{t_e} B \sin\left(\pi \frac{t}{T}\right) \left\{ \frac{B/KT}{1 - \frac{1}{4} \left(\frac{TN}{T} \right)^2} \left[\cos\left(\pi \frac{t}{T}\right) - \cos\left(\frac{2\pi T}{TN} \frac{t}{T}\right) \right] \right. \\ \left. + \int_{t_e}^T B \sin\left(\pi \frac{t}{T}\right) \left(\frac{B}{KT} \right) \left[B_1 - 4\pi \left(\frac{T}{TN} \right)^2 \left[\cos\left(\pi \frac{t}{T}\right) - \cos\left(\pi \frac{t_e}{T}\right) \right] \right. \right. \\ \left. \left. - \cos\left(\pi \frac{t_e}{T}\right) \right] \cdot \left(\frac{R_m}{B} \right) \left(\frac{2\pi T}{TN} \right)^2 \left[\frac{t}{T} - \frac{t_e}{T} \right] \right\} dt \quad (46)$$

Integration of equation (46) provides:

$$W_m = \frac{B^2}{2K} \left[\frac{1}{1 - \frac{1}{4} \left(\frac{TN}{T} \right)^2} \left\{ \sin^2\left(\pi \frac{t_e}{T}\right) + \cos\left[\pi \left(1 - 2 \frac{T}{TN}\right) \frac{t_e}{T}\right] \frac{t_e}{T} + \cos\left[\pi \left(1 + 2 \frac{T}{TN}\right) \frac{t_e}{T}\right] \frac{t_e}{T} \right\} \right. \\ \left. - \frac{1}{\left(1 - 2 \frac{T}{TN}\right)} - \frac{1}{\left(1 + 2 \frac{T}{TN}\right)} \right] \left(\frac{B^2}{K\pi} \right) \left\{ \left[B_1 + 4\pi \left(\frac{T}{TN} \right)^2 \cos\left(\pi \frac{t_e}{T}\right) + \left(\frac{R_m}{B} \right) \left(\frac{2\pi T}{TN} \right)^2 \right. \right. \\ \left. \left. \left(\frac{t_e}{T} \right) \left[1 + \cos\left(\pi \frac{t_e}{T}\right) \right] + 2\pi \left(\frac{T}{TN} \right)^2 \sin^2\left(\pi \frac{t_e}{T}\right) \right] \right. \\ \left. \left. - \left(\frac{R_m}{B} \right) \left(\frac{2\pi T}{TN} \right)^2 \left[1 - \frac{1}{\pi} \sin\left(\pi \frac{t_e}{T}\right) + \left(\frac{t_e}{T} \right) \cos\left(\pi \frac{t_e}{T}\right) \right] \right\} \quad (47)$$

As shown in reference 1 the maximum possible work done by the pulse occurs when the resistance is zero and is given by:

$$W_p = \frac{H^2}{2M} \quad (48)$$

The impulse H is obtained as follows:

$$H = \int_0^T f(t) dt = \int_0^T A \sin\left(\pi \frac{t}{T}\right) dt = \frac{2}{\pi} Bt \quad (49)$$

Substituting equation (49) into equation (48) and after some manipulation, the maximum possible work done becomes:

$$W_p = 8 \left(\frac{B}{K} \right) \left(\frac{T}{TN} \right)^2 \quad (50)$$

It is convenient to divide equation (47) by (50) to form the nondimensional work done ratio:

$$\begin{aligned} \frac{W_m}{W_p} = & \frac{1}{8} \left(\frac{TN}{T} \right)^2 \left[\frac{1}{1 - \frac{1}{4} \left(\frac{TN}{T} \right)^2} \right] \left\{ \sin^2 \left(\pi \frac{t_c}{T} \right) \right. \\ & + \frac{\cos \left[\pi \left(1 - 2 \frac{T}{TN} \right) \frac{t_c}{T} \right]}{\left(1 - 2 \frac{T}{TN} \right)} + \frac{\cos \left[\pi \left(1 + 2 \frac{T}{TN} \right) \frac{t_c}{T} \right]}{\left(1 + 2 \frac{T}{TN} \right)} \\ & \left. - \frac{1}{\left(1 - 2 \frac{T}{TN} \right)} - \frac{1}{\left(1 + 2 \frac{T}{TN} \right)} \right\} \\ & + \frac{1}{8\pi} \left(\frac{TN}{T} \right)^2 \left\{ \left[B_1 + 4\pi \left(\frac{T}{TN} \right)^2 \cos \pi \left(\frac{t_c}{T} \right) \right] \right. \\ & + \left(\frac{R_m}{B} \right) \left(\frac{2\pi T}{TN} \right)^2 \left(\frac{t_c}{T} \right) \times \left[1 + \cos \left(\pi \frac{t_c}{T} \right) \right] \\ & + 2\pi \left(\frac{T}{TN} \right)^2 \sin^2 \left(\pi \frac{t_c}{T} \right) - \left(\frac{R_m}{B} \right) \left(\frac{2\pi T}{TN} \right)^2 \\ & \left. \left[1 - \frac{1}{\pi} \sin \left(\pi \frac{t_c}{T} \right) + \left(\frac{t_c}{T} \right) \cos \left(\pi \frac{t_c}{T} \right) \right] \right\} \quad (51) \end{aligned}$$

This concludes the Case I analysis. The pertinent mathematical relations are summarized in Table I. Maximum displacement, time to maximum displacement, time to elastic peak displacement, and the work done ratios are presented in Figures 2, 3, 4, and 6 as functions of the parameters (R_m/B) and T/TN . A portion of the computer program output from which the figures were drawn is presented in Table III.

CASE II SOLUTION

The equations of motion and its solution for region 1B are the same as region 1A. Proceeding to region 2B, the equation of motion is:

$$M\ddot{X} + KX = 0 \quad (52)$$

for which the solution is:

$$X(t) = A \sin \left(\frac{2\pi}{TN} t \right) + C \cos \left(\frac{2\pi}{TN} t \right) \quad (53)$$

The velocity in region 2B is obtained by taking the derivative of equation (53):

$$\dot{X}(t) = A \left(\frac{2\pi}{TN} \right) \cos \left(\frac{2\pi}{TN} t \right) - C \left(\frac{2\pi}{TN} \right) \sin \left(\frac{2\pi}{TN} t \right) \quad (54)$$

The initial conditions for region 2B are taken from the end conditions of region 1B by setting $t = T$ in equations (6) and (8), namely:

$$X(T) = - \left(\frac{B}{K} \right) \left[\frac{\frac{1}{2} \left(\frac{TN}{T} \right)}{1 - \frac{1}{4} \left(\frac{TN}{T} \right)^2} \right] \sin \left(\frac{2\pi T}{TN} \right) \equiv A_1 (B/K) \quad (55)$$

$$\dot{X}(T) = \left(\frac{B}{KT} \right) \left[\frac{\pi}{1 - \frac{1}{4} \left(\frac{TN}{T} \right)^2} \right] \left\{ 1 + \cos \left(\frac{2\pi T}{TN} \right) \right\} \equiv B_1 \left(\frac{B}{KT} \right) \quad (56)$$

Setting equations (55) and (56) equal to LHS of equations (53) and (54), respectively, again setting $t = T$ on the RHS, the equations for calculating the integration constants A and C are obtained:

$$A_1 \left(\frac{B}{K} \right) = A \sin \left(\frac{2\pi T}{TN} \right) + C \cos \left(\frac{2\pi T}{TN} \right) \quad (57)$$

$$B_1 \left(\frac{B}{KT} \right) = A \left(\frac{2\pi}{TN} \right) \cos \left(\frac{2\pi T}{TN} \right) - C \left(\frac{2\pi}{TN} \right) \sin \left(\frac{2\pi T}{TN} \right) \quad (58)$$

Solution for A and C in equations (57) and (58) provide:

$$A = - \left(\frac{B}{K} \right) \left[\frac{\frac{1}{2} \left(\frac{TN}{T} \right)}{1 - \frac{1}{4} \left(\frac{TN}{T} \right)^2} \right] \left\{ 1 + \cos \left(\frac{2\pi T}{TN} \right) \right\} \quad (59)$$

and

$$C = \left(\frac{B}{K} \right) \left[\frac{\frac{1}{2} \left(\frac{TN}{T} \right)}{1 - \frac{1}{4} \left(\frac{TN}{T} \right)^2} \right] \sin \left(\frac{2\pi T}{TN} \right) \quad (60)$$

Substituting equations (59) and (60) into equations (53) and (54), the displacement and velocity in region 2B become:

$$\begin{aligned} X(t) = & \left(\frac{B}{K} \right) \left[\frac{\frac{1}{2} \left(\frac{TN}{T} \right)}{1 - \frac{1}{4} \left(\frac{TN}{T} \right)^2} \right] \left\{ \sin \left(\frac{2\pi T}{TN} \right) \cos \left[\left(\frac{2\pi T}{TN} \right) \left(\frac{t}{T} \right) \right] \right. \\ & \left. - \cos \left(\frac{2\pi T}{TN} \right) \sin \left[\frac{2\pi T}{TN} \left(\frac{t}{T} \right) \right] - \sin \left(\frac{2\pi T}{TN} \right) \right. \\ & \left. \left(\frac{t}{T} \right) \right\} \quad (61) \\ \dot{X}(t) = & \left(\frac{B}{KT} \right) \left[\frac{\pi}{1 - \frac{1}{4} \left(\frac{TN}{T} \right)^2} \right] \left\{ \cos \left[\left(\frac{2\pi T}{TN} \right) \left(\frac{t}{T} \right) \right] \right. \end{aligned}$$

$$+ \cos\left(\frac{2\pi T}{TN}\right) \cos\left[\left(\frac{2\pi T}{TN}\right)\left(\frac{t}{T}\right)\right] + \sin\left(\frac{2\pi T}{TN}\right) \sin\left[\left(\frac{2\pi T}{TN}\right)\left(\frac{t}{T}\right)\right] \Bigg\} \quad (62)$$

The next step is to determine the time (t_e) to reach the peak elastic deflection (X_e). This is accomplished by setting $t = t_e$ in equation (61) and equating this to equation (10) as follows:

$$\left(\frac{R_m}{B}\right) \frac{1}{2} \left(\frac{TN}{T}\right) \left\{ \sin\left(\frac{2\pi T}{TN}\right) \cos\left[\left(\frac{2\pi T}{TN}\right)\left(\frac{t_e}{T}\right)\right] - \cos\left(\frac{2\pi T}{TN}\right) \sin\left[\left(\frac{2\pi T}{TN}\right)\left(\frac{t_e}{T}\right)\right] \right\} \quad (63)$$

Equation (63) has been solved for $t_e/T > 1.0$ on the IBM 1130 computer for various values of the parameters $\left(\frac{R_m}{B}\right)$ and $\left(\frac{T}{TN}\right)$.

The displacement and velocity in region 3B are the same as in region 3A, namely:

$$X(t) = -\frac{R_m}{2M} t^2 + at + b \quad (64)$$

$$\dot{X}(t) = -\frac{R_m}{M} t + a \quad (65)$$

Integration constants a and b are determined from the initial conditions in region 3B or end conditions in region 2B. These end conditions are obtained by setting $t = t_e$ in equations (61) and (62) and for convenience setting the results in braces as follows:

$$X(t_e) = \left\{ A_1 \right\} \left(\frac{B}{K} \right) \quad (66)$$

and

$$\dot{X}(t_e) = \left\{ B_2 \right\} \left(\frac{B}{KT} \right) \quad (67)$$

Setting $t = t_e$ in equations (64) and (65) and equating these to equations (66) and (67), respectively, we have:

$$\left\{ A_2 \right\} \left(\frac{B}{K} \right) = -\frac{R_m}{2M} t_e^2 + a t_e + b \quad (68)$$

$$\left\{ B_2 \right\} \left(\frac{B}{KT} \right) = -\frac{R_m}{M} t_e + a \quad (69)$$

Solution for a and b in equations (68) and (69) provides:

$$a = B_2 \left(\frac{B}{KT} \right) + \frac{R_m}{M} t_e = B_2 \left(\frac{B}{KT} \right) + \left(\frac{R_m}{B} \right) \left(\frac{B}{K} \right) \left(\frac{2\pi T}{TN} \right)^2 \left(\frac{t_e}{T} \right) \quad (70)$$

and

$$b = A_2 \left(\frac{B}{K} \right) - B_2 \left(\frac{t_e}{T} \right) \left(\frac{B}{K} \right) - \frac{1}{2} \left(\frac{R_m}{B} \right) \left(\frac{2\pi T}{TN} \right)^2 \left(\frac{t_e}{T} \right)^2 \left(\frac{B}{K} \right) \quad (71)$$

Substituting equations (70) and (71) into equations (64) and (65) the displacement and velocity in region 3B become, after some rearrangement:

$$X(t) = \left(\frac{B}{K} \right) \left\{ A_2 + B_2 \left[\frac{t}{T} - \frac{t_e}{T} \right] - \frac{1}{2} \left(\frac{R_m}{B} \right) \left(\frac{2\pi T}{TN} \right)^2 \left[\frac{t}{T} - \frac{t_e}{T} \right]^2 \right\} \quad (72)$$

and

$$\dot{X}(t) = \left(\frac{B}{KT} \right) \left\{ B_2 + \left(\frac{R_m}{B} \right) \left(\frac{2\pi T}{TN} \right)^2 \left[\frac{t_e}{T} - \frac{t}{T} \right] \right\} \quad (73)$$

The time to reach maximum displacement is obtained by setting $t = t_m$ and equation (73) equal to zero:

$$\dot{X}(t_m) = 0 = \left(\frac{B}{KT} \right) \left\{ B_2 + \left(\frac{R_m}{B} \right) \left(\frac{2\pi T}{TN} \right)^2 \left[\frac{t_e}{T} - \frac{t_m}{T} \right] \right\} \quad (74)$$

Solving for t_m/T in equation (74) gives:

$$\left(\frac{t_m}{T} \right) = \left(\frac{t_e}{T} \right) + \frac{B_2}{\left(\frac{R_m}{B} \right) \left(\frac{2\pi T}{TN} \right)^2} \quad (75)$$

Setting $t = t_m$ in equation (72), the maximum displacement is obtained:

$$X_m = \left(\frac{B}{K} \right) \left\{ A_2 + B_2 \left[\frac{t_m}{T} - \frac{t_e}{T} \right] - \frac{1}{2} \left(\frac{R_m}{B} \right) \left(\frac{2\pi T}{TN} \right)^2 \left[\frac{t_m}{T} - \frac{t_e}{T} \right]^2 \right\} \equiv B_3 \left(\frac{B}{K} \right) \quad (76)$$

Again, for design purposes, it is convenient to work with the ratio of the maximum displacement (X_m) to the peak elastic deflection (X_e). With:

$$X_e = \left(\frac{R_m}{B}\right) \left(\frac{B}{K}\right) \quad (77)$$

this ratio becomes:

$$\frac{X_m}{X_e} = \frac{B_3}{\left(\frac{R_m}{B}\right)} \quad (78)$$

An IBM 1130 computer program was written to compute values of A_2 , B_2 , and B_3 and thus evaluate the ratios (X_m/X_e) and (t_m/T) as a function of the parameters (R_m/B) and (T/TN) .

The maximum work done by the pulse, acting on the mass, is given by the expression:

$$W_m = \int_0^T f(t) (\dot{X}) dt, \quad (79)$$

With $f(t) = B \sin(\pi t/T)$ and the velocity being given by equation (8) (region 1A/1B velocity), equation (79) becomes

$$W_m = \int_0^T \left[B \sin\left(\pi \frac{t}{T}\right) \right] \frac{\left(\frac{B}{KT}\right) \pi}{\left[1 - \frac{1}{4} \left(\frac{TN}{T}\right)^2\right]} \left\{ \cos\left(\pi \frac{t}{T}\right) - \cos\left[\left(\frac{2\pi T}{TN}\right) \left(\frac{t}{T}\right)\right] \right\} dt. \quad (80)$$

Integration of equation (80) gives:

$$W_m = \frac{-\left(\frac{B^2}{K}\right)}{\left[1 - \frac{1}{4} \left(\frac{TN}{T}\right)^2\right] \left[1 - 4 \left(\frac{T}{TN}\right)^2\right]} \left[1 + \cos\left(\frac{2\pi T}{TN}\right)\right]. \quad (81)$$

With the use of equation (50) the work done ratio becomes:

$$\frac{W_m}{W_p} = \frac{1 + \cos\left(\frac{2\pi T}{TN}\right)}{32 \left(\frac{T}{TN}\right)^4 - 16 \left(\frac{T}{TN}\right)^2 + 2.0}. \quad (82)$$

This concludes the Case II analysis. Pertinent mathematical relations are summarized in Table II. Displacement, time, and work ratios are included in Figures 2, 3, 4, and 6. A partial listing of the computer output is presented in Table III.

NUMERICAL EXAMPLE

It is desired to find the maximum displacement, time to maximum displacement, and maximum work done on the system enumerated below.

A half sine pulse of amplitude 14,375 pounds and width 0.006 second acts on a weight of 150 pounds. The weight is supported on crushable honeycomb, the characteristics of which are illustrated in Figure 5. Maximum resistance is 10,060 pounds, the stiffness (K) is 520,000 lb/in, and the elastic deflection (X_e) is 0.01935 inch.

Parameters given are:

$$R_m = 10,060 \text{ pounds}$$

$$B = 14,375 \text{ pounds}$$

$$W = 150 \text{ pounds}$$

$$T = 0.006 \text{ s}$$

$$K = 520,000 \text{ lb/in}$$

$$X_e = 0.01935 \text{ inch}$$

The natural period (TN) is:

$$TN = 2\pi \sqrt{\frac{W}{gK}}$$

$$TN = 6.28 \sqrt{\frac{150 \text{ lb}}{386 \text{ in/s}^2 \times 5.2 \times 10^5 \text{ lb/in}}}$$

$$TN = 0.0054 \text{ second}$$

Computed quantities are as follows:

$$\frac{R_m}{B} = 0.7$$

$$\frac{T}{TN} = 1.11$$

$$\frac{B}{K} = 0.027605 \text{ inch}$$

From figures 2, 3, and 4 the following ratios are obtained:

$$\frac{X_m}{X_e} = 8.6 \quad \frac{t_m}{T} = 1.15 \quad \frac{W_m}{W_p} = 0.405$$

Thus the maximum displacement is:

$$X_m = 8.6 (X_e) = 8.6 (0.01935 \text{ in}) = 0.16641 \text{ in}$$

and time to maximum displacement is:

$$t_m = 1.15 (T) = 1.15 (0.006 \text{ s}) = 0.0069 \text{ s}$$

To compute work done, the maximum possible work (W_p) is:

$$W_p = 8 \left(\frac{B^2}{K}\right) \left(\frac{T}{TN}\right)^2$$

$$W_p = \frac{8 \times (14,375 \times 10^4 \text{ lb})^2 (1.11)^2}{5.2 \times 10^5 \text{ lb/in}}$$

$$W_p = 3917 \text{ in-lb.}$$

Thus maximum work done is:

$$W_m = 0.405 (W_p) = 0.405 (3917 \text{ in-lb})$$

$$W_m = 1586 \text{ in-lb.}$$

A time history of the displacement is given in figure 7. The value of t_e/T is obtained from figure 6 and is 0.34. Thus $t_e = 0.34 (T) = 0.34 (0.006s) = 0.00204s$.

Asymptotes for Work Done Ratio

As $T/TN \rightarrow \infty$ or $TN/T \rightarrow 0$ equation (51), the work done ratio, for $t_e/T \leq 1.0$ reduces to the following:

$$\begin{aligned} \frac{W_m}{W_p} = & \left[\frac{1}{2} \cos\left(\pi \frac{t_e}{T}\right) + \left(\frac{\pi}{2}\right) \left(\frac{R_m}{B}\right) \left(\frac{t_e}{T}\right) \right] \left[1 + \cos\left(\pi \frac{t_e}{T}\right) \right] \\ & + \frac{1}{4} \sin^2\left(\pi \frac{t_e}{T}\right) - \left[\left(\frac{\pi}{2}\right) \left(\frac{R_m}{B}\right) \right] 1 - \frac{1}{\pi} \sin\left(\pi \frac{t_e}{T}\right) \\ & + \frac{t_e}{T} \cos\left(\pi \frac{t_e}{T}\right) \end{aligned} \quad (83)$$

In addition, from equation (11) as $T/TN \rightarrow \infty$

$$\sin\left(\pi \frac{t_e}{T}\right) = \frac{R_m}{B} \quad (84)$$

Thus

$$\cos\left(\pi \frac{t_e}{T}\right) = \sqrt{1 - \left(\frac{R_m}{B}\right)^2} \quad (85)$$

Substituting equations (84) and (85) into equation (83) the work done ratio for large values of T/TN becomes:

$$\begin{aligned} \frac{W_m}{W_p} = & \left(\frac{\pi}{2}\right) \left(\frac{R_m}{B}\right) \left(\frac{t_e}{T} - 1.0\right) + \frac{1}{2} + \frac{1}{4} \left(\frac{R_m}{B}\right)^2 \\ & + \frac{1}{2} \sqrt{1 - \left(\frac{R_m}{B}\right)^2} \end{aligned} \quad (86)$$

The work done asymptotes computed from equation (86) are plotted in Figure 4. It can be seen that for T/TN values > 4.0 , the work done ratio is essentially independent of the T/TN ratio.

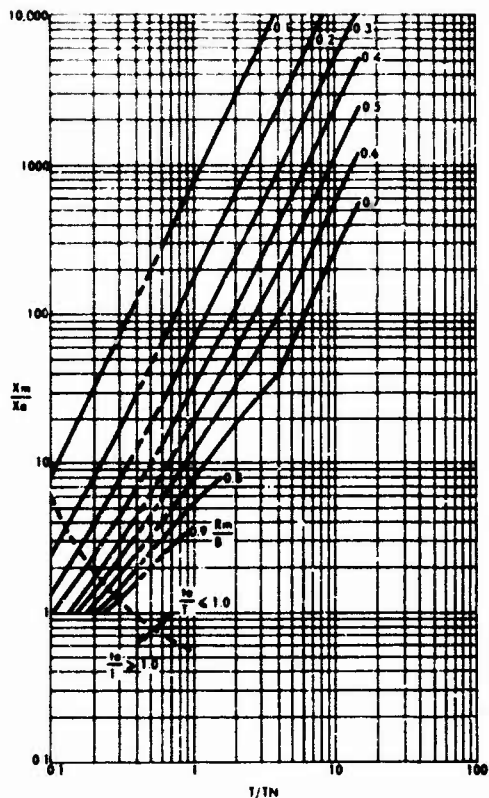


FIGURE 2. MAXIMUM DISPLACEMENT TO ELASTIC DISPLACEMENT RATIO

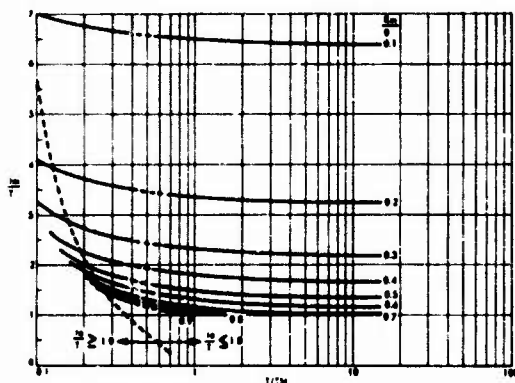


FIGURE 3. RATIO OF TIME TO MAXIMUM DISPLACEMENT TO PULSE WIDTH

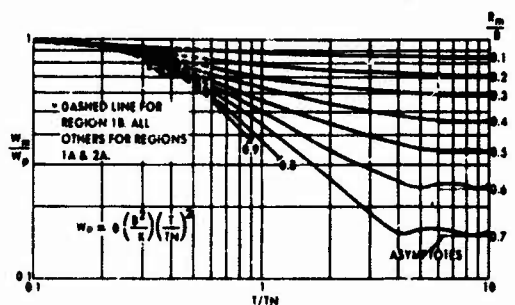


FIGURE 4. RATIO OF MAXIMUM WORK DONE TO MAXIMUM WORK POSSIBLE

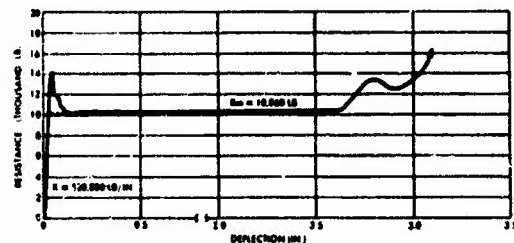


FIGURE 5. RESISTANCE-DEFLECTION FOR A PARTICULAR CRUSHABLE HONEYCOMB STRUCTURE

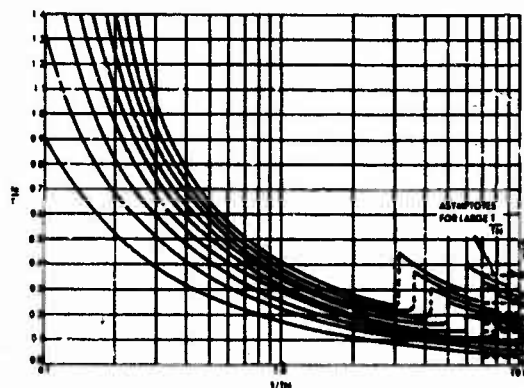


FIGURE 6. $\frac{T_0}{T}$ VERSUS $\frac{T}{T_N}$ FOR VARIOUS $\frac{R_m}{B}$

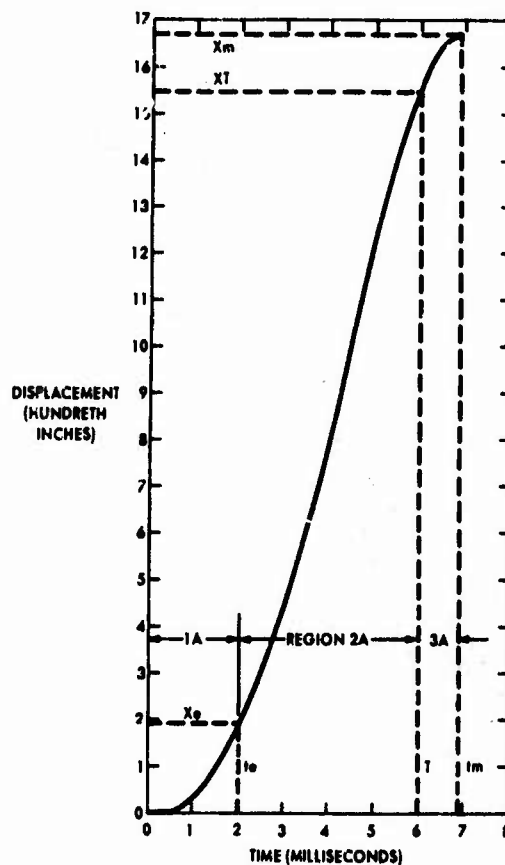
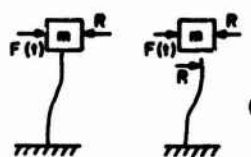
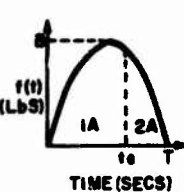
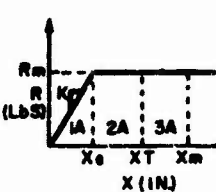
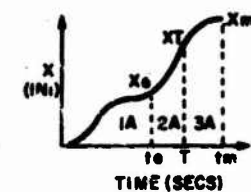


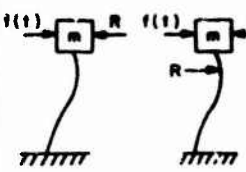
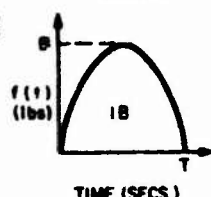
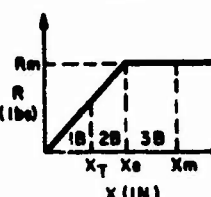
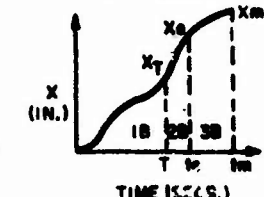
FIGURE 7. TIME HISTORY OF DISPLACEMENT FOR PROBLEM GIVEN IN NUMERICAL EXAMPLE

TABLE I. SUMMARY OF EQUATIONS FOR REGIONS 1A, 2A, 3A

SYSTEM		LOADING FUNCTION	RESISTANCE FUNCTION	SYSTEM DISPLACEMENT
				
X_m = MAXIMUM DISPLACEMENT X_0 = MAXIMUM ELASTIC DISPLACEMENT			t_0 = TIME TO MAXIMUM ELASTIC DISPLACEMENT t_m = TIME TO MAXIMUM DISPLACEMENT	
DISPLACEMENT (1A)	$\frac{X(t)}{(B/K)} = \left[\frac{1}{1 - 1/4 \left(\frac{TN}{T} \right)^2} \right] \left\{ \sin \left(\pi \frac{t}{T} \right) - 1/2 \left(\frac{TN}{T} \right) \sin \left[\left(\frac{2\pi T}{TN} \right) \left(\frac{t}{T} \right) \right] \right\}$			
VELOCITY (1A)	$\frac{\dot{X}(t)}{(B/KT)} = \left[\frac{\pi}{1 - 1/4 \left(\frac{TN}{T} \right)^2} \right] \left\{ \cos \left(\pi \frac{t}{T} \right) - \cos \left[\left(\frac{2\pi T}{TN} \right) \left(\frac{t}{T} \right) \right] \right\}$			
TIME TO ELASTIC DEFLECTION	$\sin \left(\pi \frac{t_0}{T} \right) - 1/2 \left(\frac{TN}{T} \right) \sin \left[\left(\frac{2\pi T}{TN} \right) \left(\frac{t_0}{T} \right) \right] - \left(\frac{R_m}{B} \right) \left[1 - 1/4 \left(\frac{TN}{T} \right)^2 \right] = 0$			
DISPLACEMENT (2A)	$\begin{aligned} \frac{X(t)}{(B/K)} = & A_1^* + B_1^* \left(\frac{t}{T} - \frac{t_0}{T} \right) - 1/2 \left(\frac{R_m}{B} \right) \left(\frac{2\pi T}{TN} \right)^2 \left[\left(\frac{t}{T} \right) - \left(\frac{t_0}{T} \right) \right]^2 \\ & - 4 \left(\frac{T}{TN} \right)^2 \left[\sin \left(\pi \frac{t}{T} \right) - \sin \left(\pi \frac{t_0}{T} \right) \right] + 4\pi \left(\frac{T}{TN} \right)^2 \left[\left(\frac{t}{T} \right) - \left(\frac{t_0}{T} \right) \right] \cos \left(\pi \frac{t_0}{T} \right) \end{aligned}$			
VELOCITY (2A)	$\frac{\dot{X}(t)}{(B/KT)} = B_1^* - 4\pi \left(\frac{T}{TN} \right)^2 \left[\cos \left(\pi \frac{t}{T} \right) - \cos \left(\pi \frac{t_0}{T} \right) \right] - \left(\frac{R_m}{B} \right) \left(\frac{2\pi T}{TN} \right)^2 \left[\left(\frac{t}{T} \right) - \left(\frac{t_0}{T} \right) \right]$			
DISPLACEMENT (3A)	$\frac{X(t)}{(B/K)} = A_2^* - B_2^* \left[1 - \frac{t}{T} \right] - 1/2 \left(\frac{R_m}{B} \right) \left(\frac{2\pi T}{TN} \right)^2 \left[1 - \frac{t}{T} \right]^2$			
VELOCITY (3A)	$\frac{\dot{X}(t)}{(B/KT)} = B_2^* + \left(\frac{R_m}{B} \right) \left(\frac{2\pi T}{TN} \right)^2 \left[1 - \frac{t}{T} \right]$			
TIME TO MAXIMUM DEFLECTION	$\frac{t_m}{T} = 1 + \frac{B_2^*}{\left(\frac{R_m}{B} \right) \left(\frac{2\pi T}{TN} \right)^2}$			
MAXIMUM DISPLACEMENT	$\frac{X_m}{(B/KT)} = A_2^* + 1/2 \frac{(B_2^*)^2}{\left(\frac{R_m}{B} \right) \left(\frac{2\pi T}{TN} \right)^2} = B_3^*$			
DISPLACEMENT RATIO	$\frac{X_m}{X_0} = \frac{B_3^*}{R_m/B}$			
WORK RATIO $W_p = B \left(\frac{B^2}{K} \right) \left(\frac{T}{TN} \right)^2$	$\begin{aligned} \frac{W_m}{W_p} = & 1/16 \left(\frac{TN}{T} \right)^2 \left[\frac{1}{1 - 1/4 \left(\frac{TN}{T} \right)^2} \right] \left\{ \sin^2 \left(\pi \frac{t_0}{T} \right) + \frac{\cos \left[\pi \left(1 - 2 \frac{t_0}{TN} \right) \right] \frac{t_0}{T}}{\left(1 - 2 \frac{t_0}{TN} \right)} + \frac{\cos \left[\pi \left(1 + 2 \frac{t_0}{TN} \right) \right] \frac{t_0}{T}}{\left(1 + 2 \frac{t_0}{TN} \right)} \right. \\ & \left. - \frac{1}{\left(1 - 2 \frac{t_0}{TN} \right)} - \frac{1}{\left(1 + 2 \frac{t_0}{TN} \right)} \right\} + \frac{1}{8\pi} \left(\frac{TN}{T} \right)^2 \left\{ \left[B_1^* + 4\pi \left(\frac{T}{TN} \right)^2 \cos \left(\pi \frac{t_0}{T} \right) + \left(\frac{R_m}{B} \right) \left(\frac{2\pi T}{TN} \right)^2 \left(\frac{t_0}{T} \right) \right] \times \right. \\ & \left. \left[1 + \cos \left(\pi \frac{t_0}{T} \right) \right] + 2\pi \left(\frac{T}{TN} \right)^2 \sin^2 \left(\pi \frac{t_0}{T} \right) - \left(\frac{R_m}{B} \right) \left(\frac{2\pi T}{TN} \right)^2 \left[1 - \frac{1}{\pi} \sin \left(\pi \frac{t_0}{T} \right) \right. \right. \right. \\ & \left. \left. + \left(\frac{t_0}{T} \right) \cos \left(\pi \frac{t_0}{T} \right) \right] \right\} \end{aligned}$			

* THESE QUANTITIES ARE END CONDITIONS FROM PREVIOUS REGIONS

TABLE II SUMMARY OF EQUATIONS FOR REGIONS 1B, 2B, 3B

SYSTEM		LOADING FUNCTION	RESISTANCE FUNCTION	SYSTEM DISPLACEMENT
				
x_m = MAXIMUM DISPLACEMENT x_e = MAXIMUM ELASTIC DISPLACEMENT			t_e = TIME TO MAXIMUM ELASTIC DISPLACEMENT t_m = TIME TO MAXIMUM DISPLACEMENT	
DISPLACEMENT (1B)	$\frac{x(t)}{(B/K)} = \frac{1}{[1 - 1/4 (\frac{TN}{T})^2]} \left\{ \sin \left(\pi \frac{t}{T} \right) - 1/2 \left(\frac{TN}{T} \right) \sin \left[\left(\frac{2\pi T}{TN} \right) \left(\frac{t}{T} \right) \right] \right\}$			
VELOCITY (1B)	$\frac{\dot{x}(t)}{(B/KT)} = \frac{\pi}{[1 - 1/4 (\frac{TN}{T})^2]} \left\{ \cos \left(\pi \frac{t}{T} \right) - \cos \left[\left(\frac{2\pi T}{TN} \right) \left(\frac{t}{T} \right) \right] \right\}$			
DISPLACEMENT (2B)	$\frac{x(t)}{(B/K)} = \frac{1/2 (\frac{TN}{T})}{[1 - 1/4 (\frac{TN}{T})^2]} \left\{ \sin \left(\frac{2\pi T}{TN} \right) \cos \left[\left(\frac{2\pi T}{TN} \right) \left(\frac{t}{T} \right) \right] - \cos \left(\frac{2\pi T}{TN} \right) \sin \left[\left(\frac{2\pi T}{TN} \right) \left(\frac{t}{T} \right) \right] - \sin \left[\left(\frac{2\pi T}{TN} \right) \left(\frac{t}{T} \right) \right] \right\}$			
VELOCITY (2B)	$\frac{\dot{x}(t)}{(B/KT)} = \frac{\pi}{[1 - 1/4 (\frac{TN}{T})^2]} \left\{ -\cos \left[\left(\frac{2\pi T}{TN} \right) \left(\frac{t}{T} \right) \right] - \cos \left(\frac{2\pi T}{TN} \right) \cos \left[\left(\frac{2\pi T}{TN} \right) \left(\frac{t}{T} \right) \right] - \sin \left(\frac{2\pi T}{TN} \right) \sin \left[\left(\frac{2\pi T}{TN} \right) \left(\frac{t}{T} \right) \right] \right\}$			
TIME TO ELASTIC DEFLECTION	$\sin \left[\left(\frac{2\pi T}{TN} \right) \left(1 - \frac{t_e}{T} \right) \right] - \sin \left[\left(\frac{2\pi T}{TN} \right) \left(\frac{t_e}{T} \right) \right] - \left(\frac{R_m}{B} \right) \left[2 \left(\frac{T}{TN} \right) - 1/2 \left(\frac{TN}{T} \right) \right] = 0$			
DISPLACEMENT (3B)	$\frac{x(t)}{(B/K)} = A_2^* + B_2^* \left[\frac{t}{T} - \frac{t_e}{T} \right] - 1/2 \left(\frac{R_m}{B} \right) \left(\frac{2\pi T}{TN} \right)^2 \left[\frac{t}{T} - \frac{t_e}{T} \right]^2$			
VELOCITY (3B)	$\frac{\dot{x}(t)}{(B/KT)} = B_2^* + \left(\frac{R_m}{B} \right) \left(\frac{2\pi T}{TN} \right)^2 \left[\frac{t_e}{T} - \frac{t}{T} \right]$			
TIME TO MAXIMUM DEFLECTION	$\frac{t_m}{T} = \frac{t_e}{T} + \frac{B_2^*}{\left(\frac{R_m}{B} \right) \left(\frac{2\pi T}{TN} \right)^2}$			
MAXIMUM DEFLECTION	$\frac{x_m}{(B/K)} = A_2^* + B_2^* \left[\frac{t_m}{T} - \frac{t_e}{T} \right] - 1/2 \left(\frac{R_m}{B} \right) \left(\frac{2\pi T}{TN} \right)^2 \left[\frac{t_m}{T} - \frac{t_e}{T} \right]^2 + B_3^*$			
DISPLACEMENT RATIO	$\frac{x_m}{x_e} = \frac{B_3^*}{(R_m/B)}$			
WORK RATIO	$W_D = 8 \left(\frac{B^2}{K} \right) \left(\frac{T}{TN} \right)^2 \quad \frac{W_m}{W_D} = \frac{1 + \cos \left(\frac{2\pi T}{TN} \right)}{32 (T/TN)^4 - 16 (T/TN)^2 + 2.0}$			

* THESE QUANTITIES ARE END CONDITIONS FROM PREVIOUS REGIONS

TABLE III

Partial Listing of Computer Program Output

$\frac{R_m}{B}$	$\frac{T}{TN}$	$\frac{t_e}{T}$	$\frac{t_m}{T}$	$\frac{X_m}{X_e}$	$\frac{W_m}{W_p}$
0.1	0.1	0.905293	7.009	8.352	0.981
	0.3	0.390669	6.656	67.2	0.927
	0.6	0.243532	6.547	259.0	0.898
	1	0.173396	6.495	706.0	0.883
	2	0.110252	6.448	2774.0	0.868
	4	0.070836	6.418	10999.0	0.859
	6	0.055088	6.406	24640.0	—
	8	0.046324	6.400	43698.0	—
	10	0.040673	6.395	68169.0	0.852
	15	0.032593	6.389	153024.0	0.850
0.2	0.1	1.341987	4.064	2.463	0.98
	0.3	0.503876	3.553	16.51	—
	0.6	0.311654	3.414	59.78	0.823
	1	0.222016	3.347	157.0	0.786
	2	0.142108	3.288	601.0	0.751
	4	0.092785	3.250	2330.0	0.728
	6	0.073491	3.236	5175.0	—
	8	0.063163	3.227	9135.0	—
	10	0.057016	3.222	14208.0	0.710
	15	0.053929	3.215	31774.0	0.706
0.3	0.1	1.866806	3.240	1.372	0.98
	0.3	0.589658	2.552	7.44	0.868
	0.6	0.361826	2.388	24.91	0.763
	1	0.257880	2.312	62.84	0.701
	2	0.166143	2.243	228.0	0.641
	4.2	0.107521	2.199	942.0	0.600
	6	0.089703	2.184	1879.0	0.587
	8	0.080395	2.175	3294.0	0.579
	10	0.081562	2.170	5105.0	0.574
	12	0.109634	2.172	7367.0	0.576
0.4	0.2	0.934092	2.244	2.355	0.928
	0.3	0.663530	2.071	4.349	0.855
	0.6	0.403669	1.887	13.33	0.713
	1.0	0.287824	1.802	31.75	0.625
	2.0	0.186713	1.727	108.0	0.538
	4.0	0.126832	1.680	386.0	0.482
	6.0	0.107507	1.663	830.0	0.461
	8.0	0.151984	1.657	1450.0	0.453
	10.0	0.140482	1.659	2281.0	0.456
	15.0	0.119835	1.656	5090.0	0.452

TABLE III (Cont)

$\frac{R_m}{B}$	$\frac{T}{TN}$	$\frac{t_e}{T}$	$\frac{t_m}{T}$	$\frac{X_m}{X_e}$	$\frac{W_m}{W_p}$
0.5	0.25	0.852619	1.874	2.278	0.889
	0.4	0.586849	1.700	4.469	0.775
	0.6	0.440696	1.594	8.224	0.670
	1.0	0.313240	1.502	18.28	0.556
	2.0	0.205442	1.426	56.94	0.441
	4.2	0.140838	1.369	205.0	0.363
	6.2	0.194845	1.355	421.0	0.342
	8.0	0.177311	1.359	711.0	0.347
	9.8	0.159286	1.357	1062.0	0.345
	12.0	0.178083	1.354	1571.0	0.341
0.6	0.25	0.938933	1.711	1.735	0.888
	0.4	0.634421	1.517	3.206	0.761
	0.6	0.474657	1.405	5.579	0.635
	1.0	0.338702	1.306	11.45	0.493
	2.0	0.223195	1.219	31.49	0.349
	4.0	0.162691	1.168	91.9	0.257
	6.0	0.228157	1.164	199.0	0.248
	7.0	0.209535	1.165	272.0	0.249
	8.0	0.194935	1.162	352.0	0.247
	9.4	0.183723	1.160	475.0	0.242
0.7	0.3	0.862110	1.510	1.740	0.844
	0.4	0.680001	1.394	2.462	0.751
	0.6	0.506599	1.274	4.055	0.605
	0.8	0.417464	1.210	5.783	0.506
	1.0	0.361623	1.170	7.606	0.435
	2.0	0.240561	1.078	17.57	0.261
	4.4	0.294923	1.028	49.8	0.156
	6.0	0.247700	1.032	96.0	0.163
	8.4	0.272495	1.027	176.0	0.153
	10.0	0.248348	1.028	254.0	0.155
0.8	0.3	0.930517	1.434	1.449	0.844
	0.4	0.724744	1.307	1.989	0.745
	0.7	0.483483	1.142	3.667	0.517
	0.8	0.442506	1.113	4.219	0.465
	0.9	0.410052	1.089	4.758	0.421
	1.0	0.383618	1.070	5.284	0.383
	1.2	0.343004	1.040	6.285	0.321
0.9	0.4	0.769718	1.245	1.670	0.741
	0.6	0.567113	1.110	2.486	0.559
	0.7	0.510087	1.070	2.861	0.488
	0.8	0.466849	1.040	3.209	0.429
	0.9	0.432749	1.015	3.516	0.378

SUMMARY

The enclosed charts (figures 2 through 4) permit rapid calculation of maximum displacements, time to maximum displacements, and work done on SDOF systems subjected to a half sine pulse when the resistive force may be classed as elastic-plastic.

Figure 6 and Table III present values of t_c/T for various values of (R_m/B) and (T/TN) . These values are necessary to compute displacement time histories.

REFERENCES

1. U.S. Army Corps of Engineers, "Design of Structures to Resist the Effects of Atomic Weapons," Manual EM 1110-345-415, 15 March 1957
2. M. Wohltmann and John D. Calowell, "Dynamic Response of a Single Degree of Freedom, Completely Plastic System Subjected to Sawtooth and Parabolic Impulses," IES Proceedings of the 14th Annual Technical Meeting and Exposition, 28 April 1968
3. M. Wohltmann, "Dynamic Response of a Single-Degree-of-Freedom Elastic-Plastic System Subjected to a Sawtooth Pulse," Shock and Vibration Bulletin No. 39, Part 5, p. 1, December 1968

PROPAGATION OF YIELDING IN A BILINEAR HYSTERETIC BEAM
AND DISTRIBUTED FOUNDATION UNDER DYNAMIC PULSE LOADING

John R. Mays
University of Colorado
Denver, Colorado

Effects of system parameter variation on propagation of yielding in both a finite beam and in its supporting distributed foundation when loaded by a dynamic pulse are presented.

INTRODUCTION

This paper presents the study of propagation of yielding in a finite beam and a distributed foundation subjected to a transverse force pulse applied at the center of the beam. The pulse shape is a sine function of time having half-cycle duration. The beam and foundation have separate yielding bilinear hysteretic force-deformation characteristics. The effects of varying stiffnesses, applied force, yield values, pulse duration, and system frequency are presented. A finite difference technique is used to solve the nonlinear differential equations.

Propagation of yielding in the system is shown by space-time plots. The effects of parameter variation is pictured by use of families of curves, and results are shown in dimensionless form.

PROBLEM STATEMENT AND ANALYSIS

A yielding beam of uniform properties supported by a yielding foundation of uniform properties is shown in Fig. 1. The symmetric beam of length l and mass μl is loaded at its center

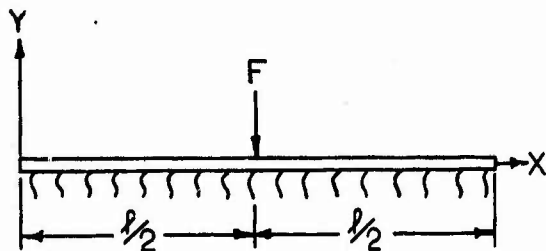


Fig. 1 - Yielding beam on yielding support

by a sinusoidal shock load of amplitude F_1 , duration t_1 , and circular frequency ω . See Fig. 2.

The moment-curvature function for a yielding beam has been approximated by the bilinear hysteretic function shown in Fig. 3. A positive hinge will be considered to have formed at a section along the beam when the values of moment (M) and curvature (K) at that section correspond to a point on the line AB. Values of moment and curvature corresponding to points along CD indicate the presence of a negative hinge. No yielding is present at a section when the $M - K$ coordinate lies along a line with slope k_1 .

A similar bilinear hysteretic function (Fig. 4) describes the yielding properties of the distributed foundation. Again positive yielding is denoted by values of foundation reaction (R) and beam displacement (y) corresponding to a point along the line AB. Similarly, negative yielding relates to line CD, and no yielding is considered present along any line of slope q_1 .

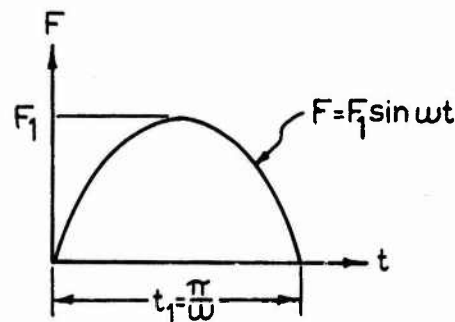


Fig. 2 - Force pulse

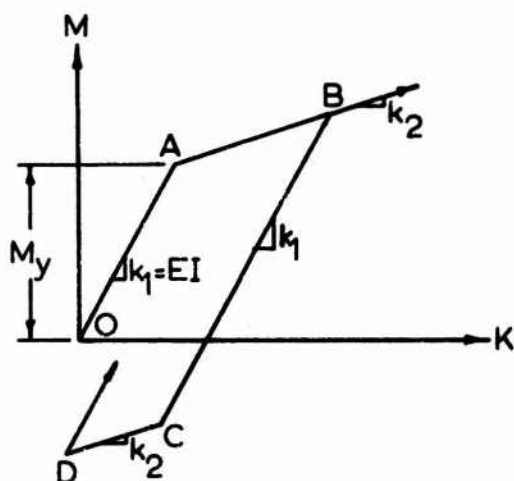


Fig. 3 - Beam moment-curvature relation

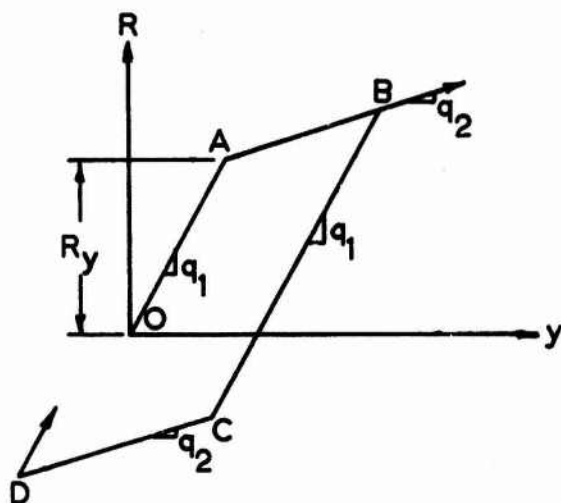


Fig. 4 - Foundation reaction - displacement relation

A value of zero for the ratio k_2/k_1 or q_2/q_1 indicates the elastic-perfectly plastic condition. When both the ratios k_2/k_1 and q_2/q_1 become unity, the system degenerates into the limiting linear case of an elastic beam supported by an elastic foundation. The fundamental period T_1 for this system is found to be [1],

$$T_1 = \frac{2\pi}{\sqrt{q_1/\mu}} \quad (1)$$

The centrally located concentrated static load necessary to cause the bending moment at mid-span to equal M_y will be referred to as F_{My} . In similar notation, F_{Ry} is the value of static load which will cause the reaction intensity at the center of the foundation to equal R_y .

The second order partial differential equation for this system can be written:

$$\frac{\partial^2 y}{\partial t^2} = -\frac{1}{\mu} \left(\frac{\partial^2 M}{\partial x^2} + R + f \right), \quad (2)$$

where the concentrated load has been replaced by a distributed load of intensity f .

The differential equation was cast into dimensionless form by defining nondimensional time τ and nondimensional displacement Z as:

$$\tau = t/t_1 \quad (3)$$

$$Z = \frac{y}{F_{1/q_1} l} \quad (4)$$

The resulting nondimensional nonlinear partial differential equation was solved numerically by dividing the system into thirty-three equal length elements and employing a finite difference technique. The computer program contained a subroutine for each of the hysteretic functions. These routines were capable of detecting the state of yield in both the beam and foundation at each of the nodes and for each interval of time.

The solution of Z vs τ [2] and the resulting yield propagation depends upon six dimensionless parameters. These are listed in Table 1 along with the symbol by which each will be represented.

TABLE 1

DEFINITION OF SYSTEM PARAMETERS			
RATIO	SYMBOL	TERMINOLOGY	STANDARD VALUE
k_2/k_1	α	Beam Stiffness Ratio	0.5
q_2/q_1	β	Foundation Stiffness Ratio	0.75
F_1/F_{Ry}	γ_R	Yield Reaction Ratio	1.5
F_1/F_{My}	γ_M	Yield Moment Ratio	3.0
$\frac{q_1 l^3}{EI}$	S	Component Stiffness Ratio	1000
t_1/T_1	γ	Pulse Duration Ratio	0.75

PRESENTATION OF RESULTS

Space-time plots are presented to indicate propagation of yielding throughout the system (figs. 5 through 11). Because the system is symmetric, complete information for space propagation can be shown by indicating beam yield from the center line to the left end of the beam and indicating foundation yield from the system centerline to the right end. Regions of positive hinges in the beam (concave upward) are noted by the symbol P, negative beam hinge by N, positive foundation yielding (upward) by +, and negative foundation yielding by -.

A set of standard values for the six system parameters have been assumed on the basis of a typical beam-foundation system and are tabulated in Table 1. Figure 5 presents yield propagation in space and time for this "standard case." Damping due to hysteresis energy loss is clearly shown. No yielding in the beam occurs after a time of five times the pulse duration ($\tau = 5$). The entire system has again become linear before a time τ equal to fourteen.

In order to show the effect of parameter variation, families of space-time yielding regions are shown in Figs. 6 through 11. In each of these figures, the family parameter has been taken as one of the system's parameters. In all figures the "standard case" is shown so that comparison between figures is possible.

CONCLUSIONS

The yield propagation in both the beam and foundation indicate consistent variation as the parameters are altered. The qualitative behavior of yield spreading can be understood by observing that the mathematical model of the system requires that a point in the foundation acting alone does not effect the state of its neighboring point. Therefore, propagation of force in the system from the load outward is accomplished chiefly by the load carrying capability of the beam. It then follows that increased propagation in space of yielding in the beam and in the foundation will be a direct function of the stiffness of the beam relative to the stiffness of the foundation. Increased relative stiffness and therefore increased propagation of yielding should be accomplished by an increase in α or Y_R and a decrease in Y_M , β , or S . The one apparent anomaly, found in Fig. 7, i.e., a decrease in Y_M causing a noticeable decrease in yield propagation can be justified easily by observing that a decrease in Y_M is indicative of increased M_y , causing fewer local hinges in the beam.

The effect of varying γ is to alter the system modes which are excited. The case of $\gamma = 0.2$ has clearly excited the third mode.

This study is part of a series of related studies of the response of nonlinear structural components to transient loadings [2, 3, 4, 5,

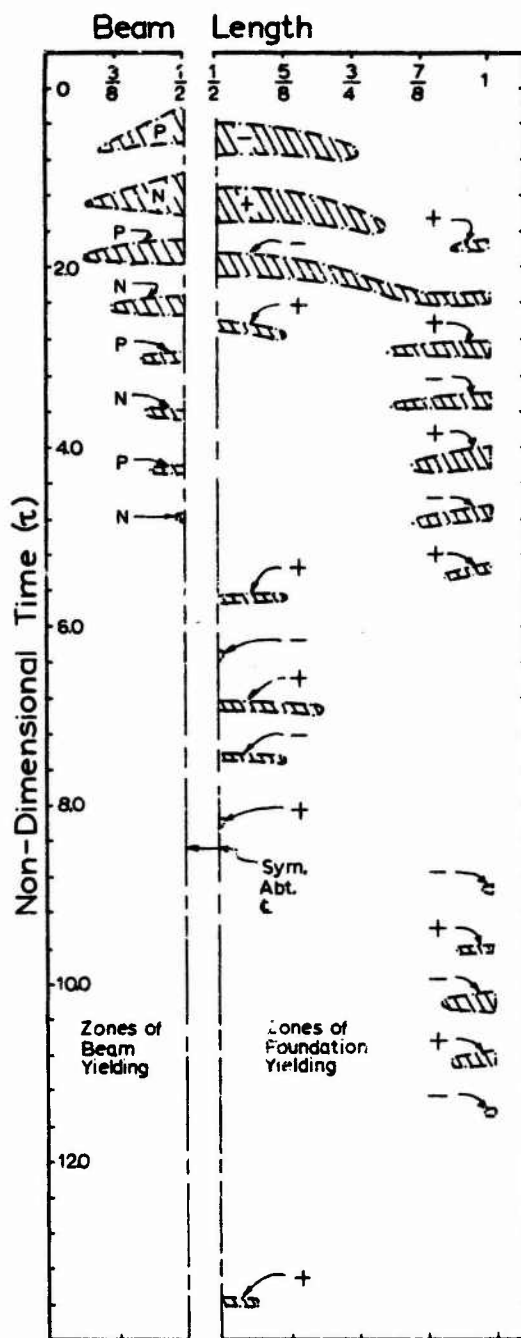
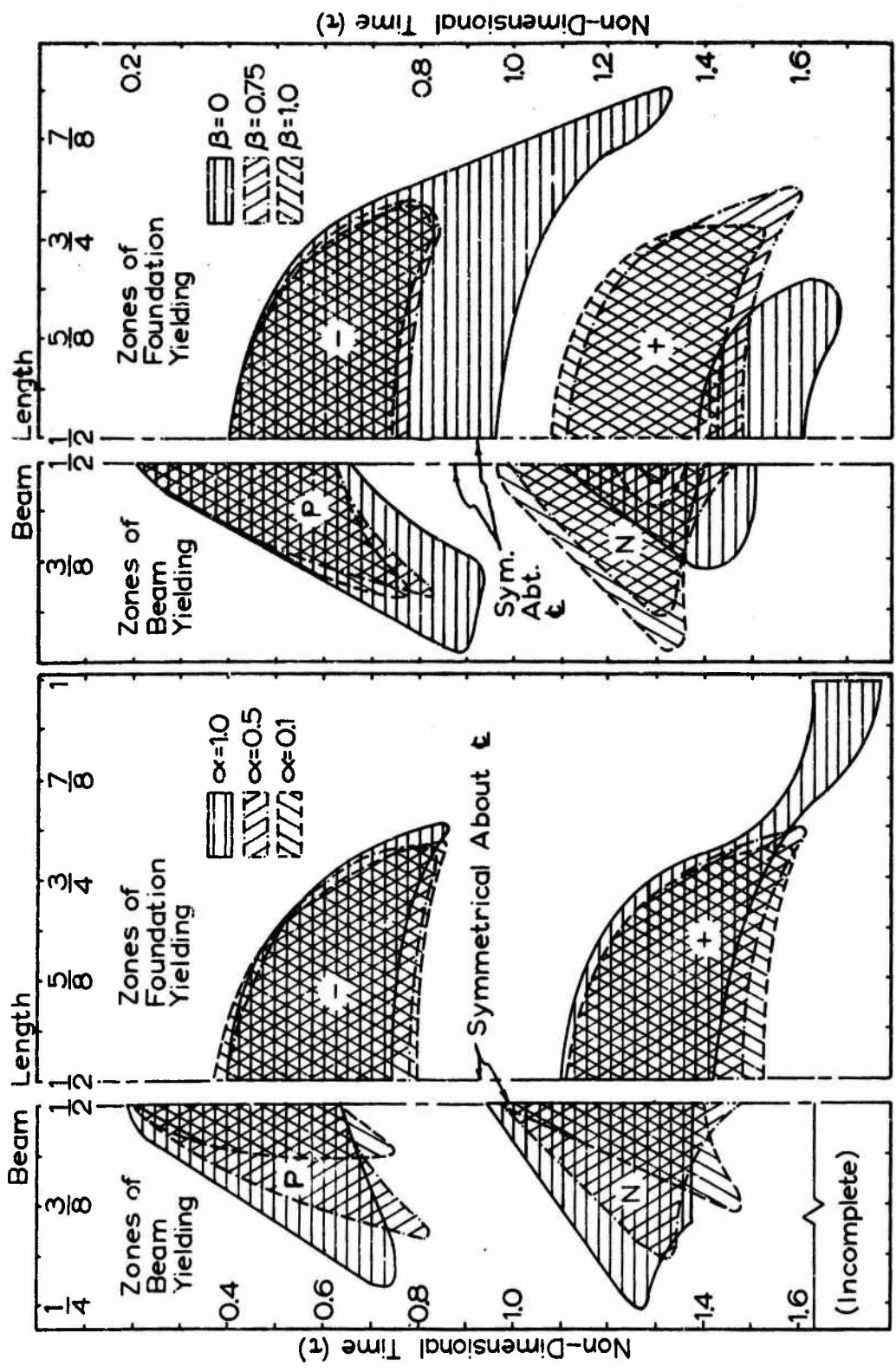


Fig. 5 - Space-time zones of yielding
Standard parameter values
 $\alpha = 0.5$, $\beta = 0.75$, $Y_R = 1.5$,
 $Y_M = 3.0$, $S = 1000$, $\gamma = 0.75$



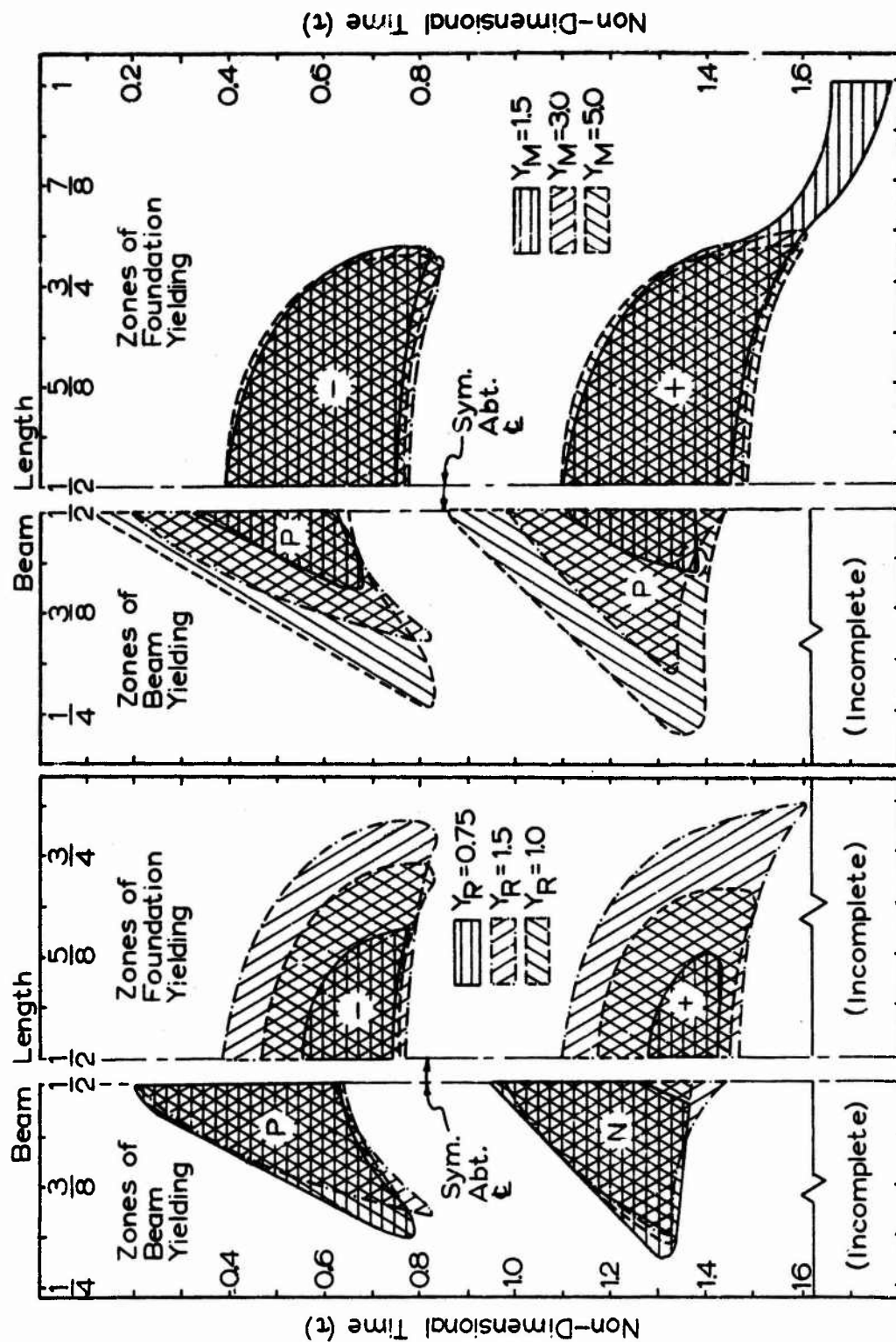


Fig. 8 - Space-time zones of yielding
Effect of varying Yield Reaction Ratio
 $\alpha = 0.5$, $\beta = 0.75$, $Y_M = 3.0$, $S = 1000$, $\gamma = 0.75$

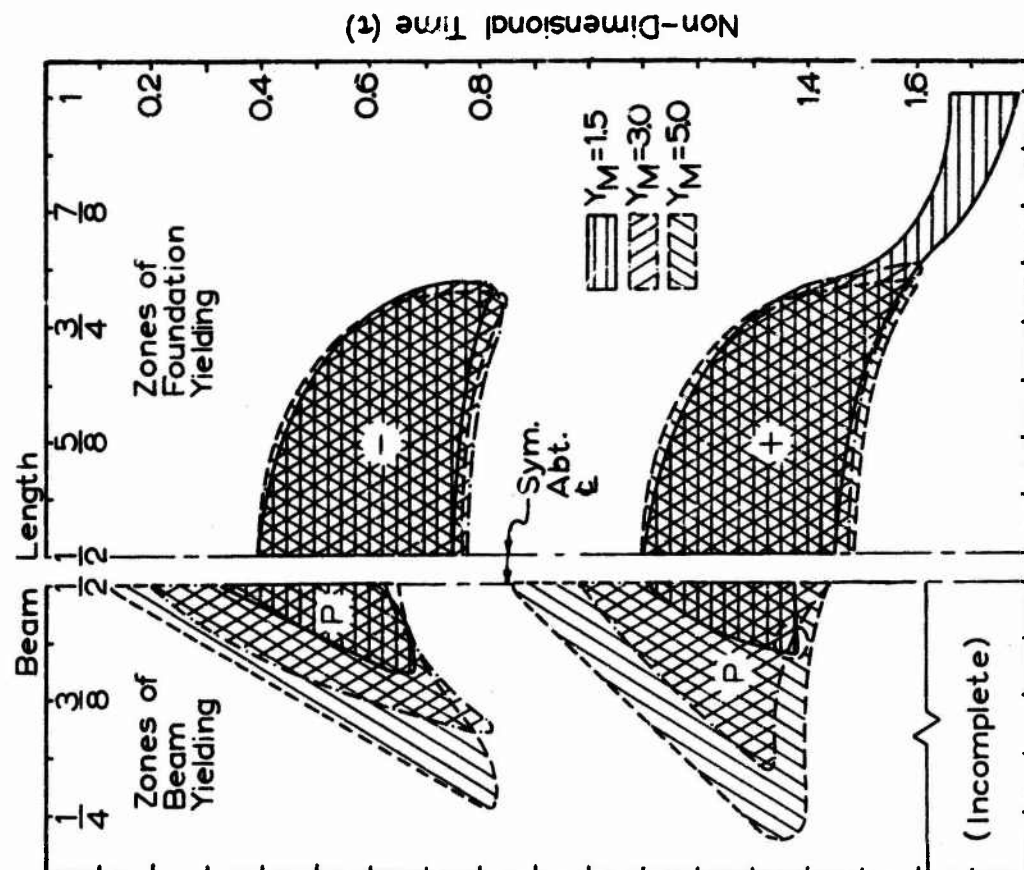


Fig. 9 - Space-time zones of yielding
Effect of varying Yield Moment Ratio
 $\alpha = 0.5$, $\beta = 0.75$, $Y_R = 1.5$, $S = 1000$, $\gamma = 0.75$

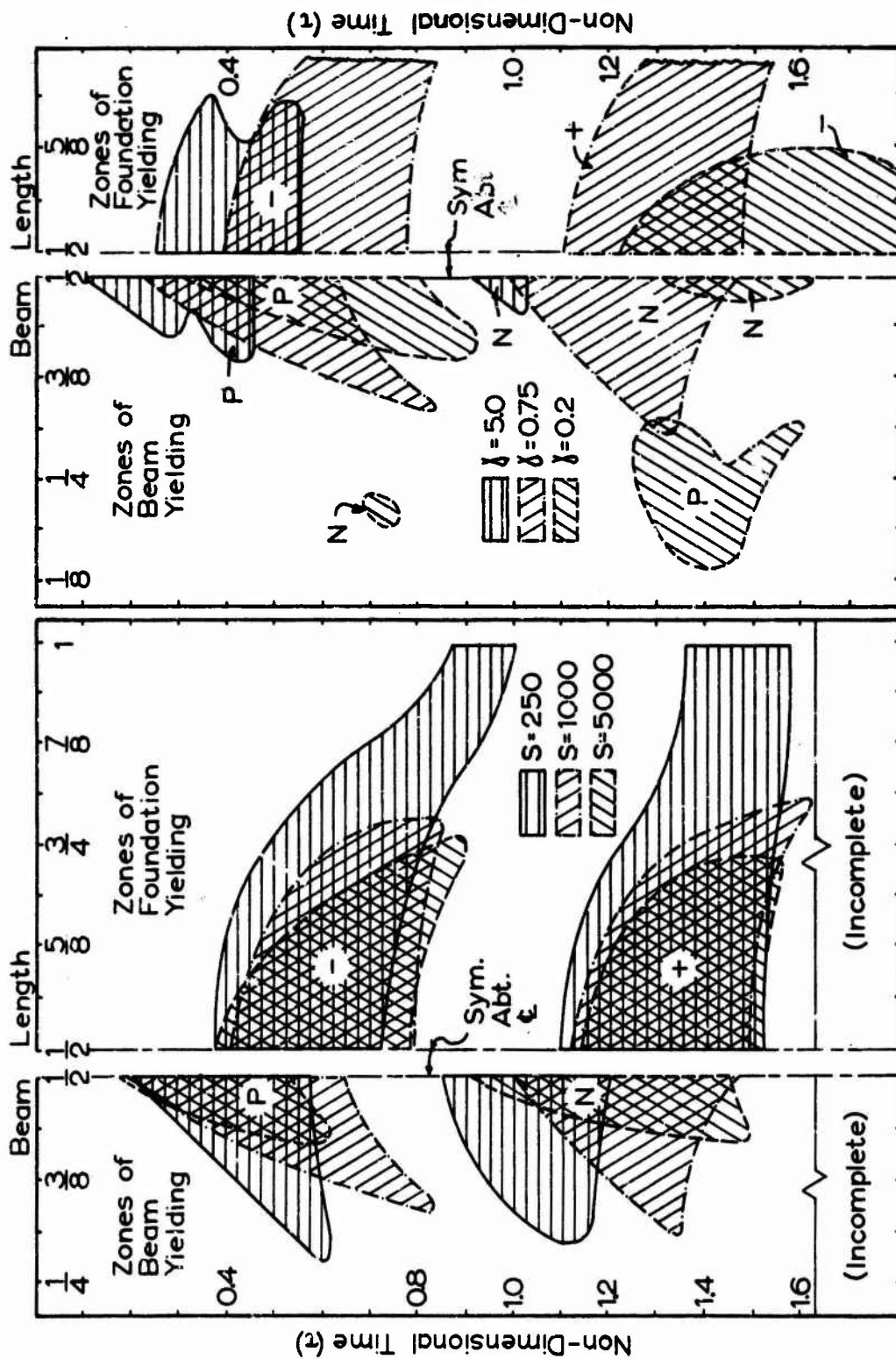


Fig. 10 - Space-time zones of yielding
Effect of varying Component Stiffness Ratio
 $\alpha = 0.5$, $\beta = 0.75$, $Y_R = 1.5$, $Y_M = 3.0$, $Y = 0.75$

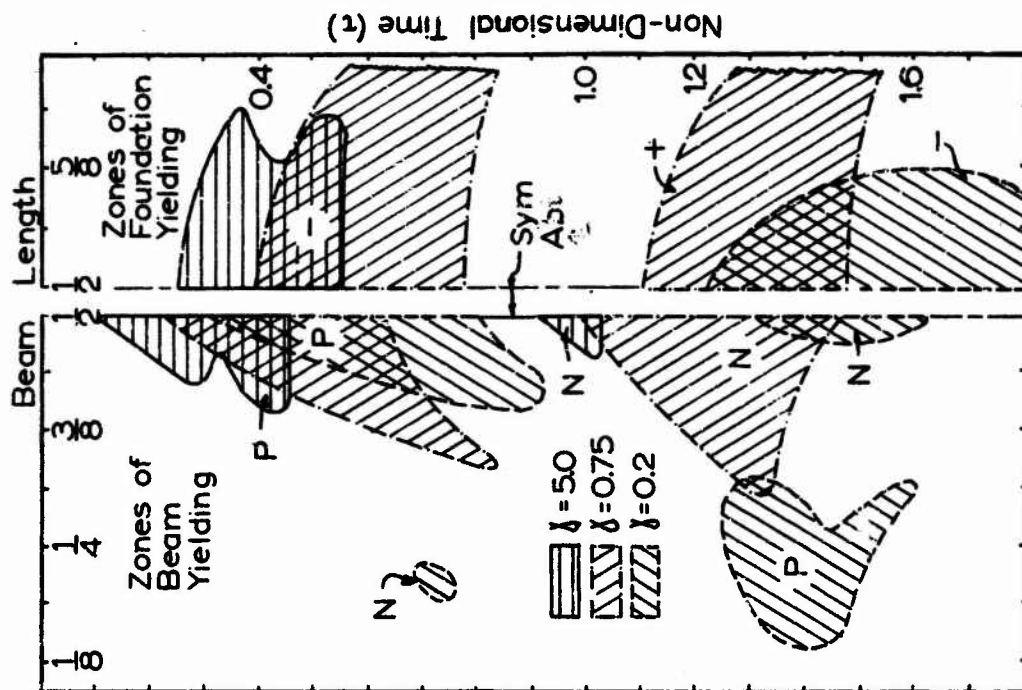


Fig. 11 - Space-time zones of yielding
Effect of varying Pulse Duration Ratio
 $\alpha = 0.5$, $\beta = 0.75$, $Y_R = 1.5$, $Y_M = 3.0$, $S = 1000$

6]. The results contribute to the general understanding of the inelastic behavior of beam-foundation problems.

ACKNOWLEDGEMENT

This research was completed under Research Initiation Grant GK 4813 from the National Science Foundation.

NOTATION

EI = flexural rigidity of the beam
 F = force magnitude of the one-half-cycle sinusoidal shock pulse $F = F_1 \sin \omega t$
 F_1 = amplitude of F
 F_{My} = static load at the center of the limiting elastic beam-foundation system necessary to produce maximum bending moment equal to M_y
 F_{Ry} = static load at the center of the limiting elastic beam-foundation system necessary to produce maximum foundation reaction intensity equal to R_y
 f = intensity of the distributed load on the beam
 K = curvature of the beam
 k_1, k_2 = slopes of the bilinear hysteretic moment-curvature function for the beam
 l = length of the beam
 M = bending moment in the beam
 M_y = bending moment at the yield point in the moment-curvature function
 N = symbol used on space-time plots to indicate regions of negative yielding
 P = symbol used on space-time plots to indicate regions of positive yielding in the beam
 q_1, q_2 = slopes of the bilinear hysteretic force intensity-displacement function for the foundation
 R = intensity of the foundation reaction

R_y = foundation intensity at the yield point in the foundation force-intensity displacement function

S = nondimensional component stiffness ratio, i.e., ratio of foundation stiffness to beam stiffness

$$S = \frac{q_1 l^3}{EI/l^3}$$

T_1 = fundamental natural period of the limiting linear case of an elastic beam on an elastic foundation

t = time

t_1 = pulse duration for the one-half cycle sinusoidal shock-load, $t_1 = \pi/\omega$

x = coordinate along the beam measured from the left end

Y_M = nondimensional yield moment ratio for the beam, F_1/F_{My}

Y_R = nondimensional yield reaction ratio for the foundation, F_1/F_{Ry}

y = deflection coordinate for the beam

Z = nondimensional deflection coordinate for the beam, $Z = \frac{y}{F_1/q_1 l^2}$

α = nondimensional beam stiffness ratio k_2/k_1

β = nondimensional foundation stiffness ratio q_2/q_1

γ = nondimensional ratio of pulse period to limiting beam fundamental period, $\gamma = t_1/T_1$

τ = nondimensional time, $\tau = t/t_1$

μ = mass per unit length of beam

ω = circular frequency of the sinusoidal load F , $\omega = \pi/t_1$

$+$ = symbol used on space-time plots to indicate regions of positive yielding in the foundation

$-$ = symbol used on space-time plots to indicate regions of negative yielding in the foundation

REFERENCES

1. J. R. Mays, "Shock Load Response of a Beam on a Distributed Foundation with Yielding, Bilinear, Hysteretic Action," Thesis presented to the University of Colorado, Denver, Colo. pp. 31-35, August 1967
2. J. R. Mays and R. S. Ayre, "Shock Load Response of a Beam on a Distributed Foundation with Yielding, Bilinear, Hysteretic Action in Either Member," Proceedings, 10th Midwestern Mechanics Conference, pp. 681-701, August 1967
3. A. B. Schultz, "Nonlinear Response of a Beam to Shock Pulse," Franklin Institute Journal, Vol. 276, No. 5, pp. 385-393, 1963
4. T. R. Tauchert and R. S. Ayre, "Shock Response of a Simple Beam on Nonlinear Supports," Journal of the Engineering Mechanics Division, A.S.C.E., Vol. 91, No. EM6, pp. 91-109, 1965
5. T. R. Tauchert and R. S. Ayre, "Shock-Resistant Design of Simple Beams on Yielding, Nonlinear Supports," International Journal of Mechanical Sciences, Pergamon Press Ltd., Vol. 8, pp. 479-490, 1966
6. B. E. Burton, "Shock Response of an Elasto-Inelastic Beam on Elasto-Inelastic Supports," Thesis presented to the University of Colorado, July 1968

PLASTIC MODELS FOR DYNAMIC STRUCTURAL ANALYSIS

W. A. Elliott
Chevrolet Division, General Motors Corporation
Detroit, Michigan

Scaled plastic models can be used to predict the dynamic response of complex structures, particularly critical frequencies and mode shapes. The basic advantage in model design analysis is the flexibility in altering initial concepts at early stages of design which can be accomplished quickly, simply and at lower costs than would probably be encountered if the structure was fabricated in the prototype material. This paper presents the use of plastic models as a design tool for stamped, welded steel automotive structures and subsequent engineering tests.

INTRODUCTION

The use of plastic models for structural analysis was developed by engineers at the Westinghouse Research Laboratories in the early 1950's for use in the design of large turbo-electric installations. In the late '50's, plastic models were first used for static testing of automotive vehicle structures and components by Chrysler Corporation (1)*.

Chevrolet has utilized the technique by static testing in early design stages for several years with good success in predicting high stress areas and buckling modes. Until recently, however, the use of plastic models for dynamic testing was infeasible because of the variation in the dynamic mechanical properties of plastic compared to prototype metals. Characteristics such as viscoelasticity, structural damping, and fabricating techniques make correlation between plastic models and steel prototypes difficult.

By using established theory to develop the requirements of dimensional analysis, suitable scaling factors for the investigation of vibrational characteristics of model structures can be demonstrated. Because examination of complex structural characteristics by computer mathematical models is tedious and time consuming, the plastic model lends itself well to automotive testing and elastic range.

Experience indicates that there is insufficient knowledge of internal structural damping and coulomb damping to adequately correlate analytical systems at early stages of design. In addition, full-scale experimental techniques are undesirable due to high fabrication cost of pretest and prototype structures which limit the number of design proposals that can be tested within a given time frame.

*See bibliography.

With increased customer sensitivity to unpleasant ride conditions, vibrational testing has become essential in proper vehicle development. Chevrolet has advanced the use of plastic models in dynamic testing to the point where reliable data can be experimentally obtained and accurately correlated with steel prototypes through the careful manipulation of the mechanical and dynamic properties of plastic, fiberglass, steel, and aluminum.

THEORETICAL BACKGROUND

Using Buckingham's Pi Theory, a set of dimensionless ratios shown in Fig. 1 can be determined to establish a relationship between the model and prototype

$$\begin{array}{lll} (PI)_1 = \frac{xK}{F} & (PI)_4 = \frac{gKr^2}{F} & (PI)_{10} = \frac{C}{xK} \\ (PI)_2 = \frac{LK}{F} & (PI)_5 = \frac{EF}{K^2} & (PI)_{11} = \frac{AK^2}{F^2} \\ (PI)_3 = \frac{F^2 \rho}{K^3} & (PI)_6 = \frac{xK^4}{F^4} & (PI)_{12} = \frac{F\theta}{K^2} \end{array}$$

WHERE

x = DEFLECTION DUE TO LOADING IN
L = CHARACTERISTIC LENGTH OF THE MODEL
IN GEOMETRIC DIMENSION IN
ρ = DENSITY OF THE MATERIALS, #/IN³
g = ACCELERATION OF GRAVITY, IN/SEC²
E = MODULUS OF ELASTICITY, #/IN²
I = AREA MOMENT OF INERTIA IN⁴
K = SPRING RATE, #/IN

T = TIME, SEC
F = FORCE, #
C = DAMPING, # SEC/IN
A = AREA, IN²
θ = STRESS, #/IN²
ϕ = STRAIN IN/IN
ν = POISSON'S RATIO

Fig. 1 — Dimensionless ratios

This can be developed into the following equation that relates the basic vibrational characteristics between the model and prototype.

$$f_m = f_p \frac{l_p}{l_m} \sqrt{\frac{E_m}{(1-\nu_m^2)} \rho_p} \sqrt{\frac{E_p}{(1-\nu_p^2)} \rho_m}$$

Where:

- m = Model subscript
- p = Prototype subscript
- l = Length
- E = Modulus
- ν = Poisson's Ratio
- f = Frequency

By determining the dynamic mechanical properties of the materials involved within the environmental and frequency domain, the natural frequency and mode shape of the prototype can be predicted from the model by incorporating those values into the basic equation.

In order to correlate the essential first and second bending and torsional frequencies of plastic model vehicle structures and steel prototypes, the dynamic properties of the material must be determined, with shear and bending modulus being the most critical.

Planished polyvinylchloride-acetate (PVC-A) or clear, rigid vinyl was chosen as the model material for the following reasons:

1. Transparent
2. Poisson's Ratio approximates that of steel over the frequency range of interest, 0-150 HZ. (Hertz)
3. Isotropic in X-Y Plane.
4. Can be fabricated by simulated spot and seam welding.
5. Has been used extensively in static testing.

The basic disadvantage of this material is its pronounced viscoelastic properties that are demonstrated by Voigt Models which can be used to illustrate their effects on the dynamic correlation of the plastic and steel.

The stress-strain behavior of viscoelastic material can be represented by one of four basic models or a combination shown in Fig. 2.

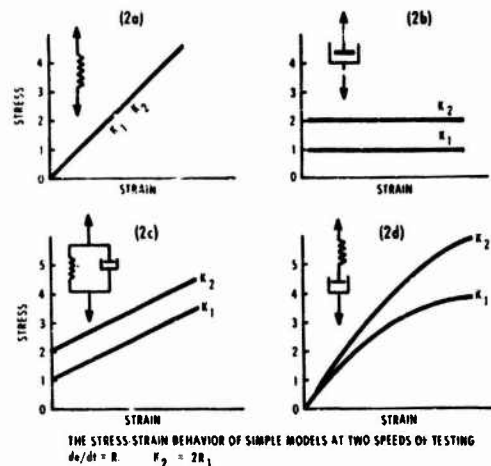


Fig. 2 - The stress-strain behavior of simple models

A purely elastic material may be modeled by a spring shown in (2a), while a viscous substance is represented by a damper in (2b). A viscoelastic material is modeled by a spring damper in parallel or series or a combination that will reproduce its specific strain rates shown in (2c) and (2d).

PVC-A, unlike steel, is represented by a spring constant E, structural damping C, and a series of parallel spring-dampers, while steel has very little damping as shown in Fig. 3.

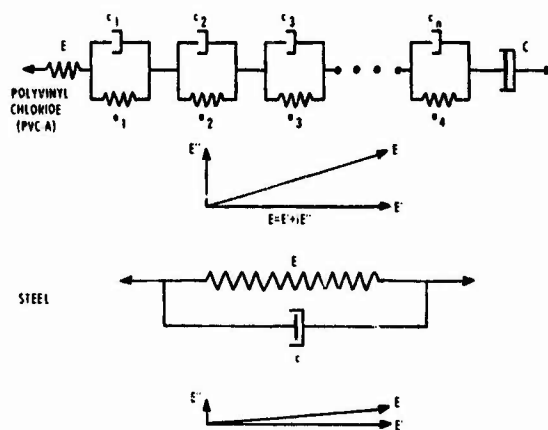


Fig. 3 - Approximate viscoelastic models for PVC and steel

Each of these components are temperature sensitive in that they are either mobile or are frozen into an inactive state. At very low temperatures, the model consists entirely of E and may be considered a purely elastic body, while at high temperatures, the parameter C is dominant and the model demonstrates varying degrees of viscoelasticity, which causes variation in its physical properties. Thus, the internal damping of the plastic makes the model frequency sensitive and is an important consideration in the dimensional analysis.

Hence, Young's modulus must be considered a complex value; a real part produced by material elasticity and an imaginary part created by the mechanical loss due to damping, both of which are affected by temperature and frequency. The vector representation is included in Fig. 3:

where: E' = real part of complex modulus.
 E'' = imaginary part of complex modulus.

The ratio of the imaginary to real part of complex modulus is defined as the mathematical loss dissipation factor E''/E' and is a term that relates the effects of temperature and frequency on damping. E'' is considered a function of that energy dissipated per cycle.

Similarly, the characteristics of the shear properties and Poisson's ratio are described by a complex value and must be investigated for their reaction to dynamic excitation and ambient conditions.

Using the vibrating reed test (2, 3)* shown schematically in Fig. 4, the effects of frequency and temperature are determined from the frequency response curve illustrated in Fig. 5.

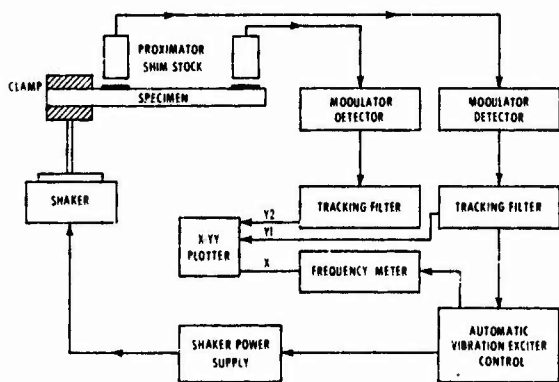


Fig. 4 - Schematic diagram of vibrating reed test apparatus

*See bibliography.

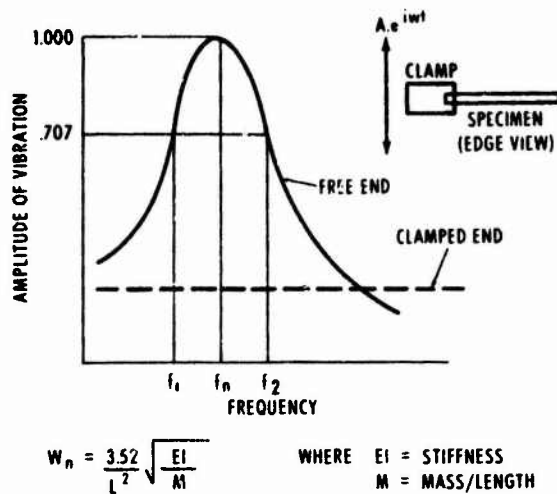


Fig. 5 - Free and clamped end amplitude response vibrating reed test

This figure shows the response curve and equations from which the dynamic properties are calculated and plotted in Fig. 6.

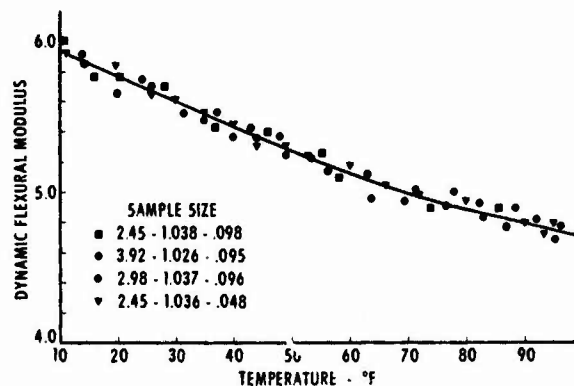


Fig. 6 - Temperature vs. dynamic module, PVC-A

The sensitivity of dynamic modulus to temperature in normal ambient conditions is shown by this descending curve.

Fig. 7 illustrates the temperature versus dissipation factor between 20 to 100°F and varies among the four samples with different lengths, widths, and thicknesses.

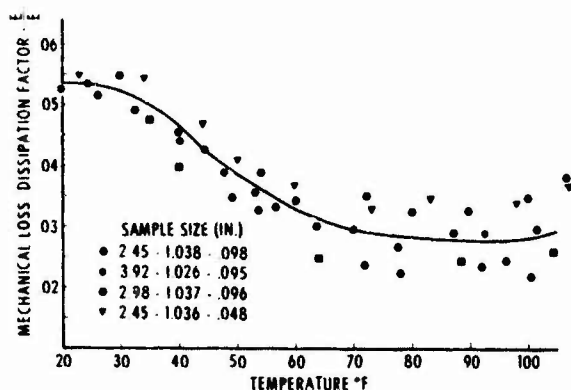


Fig. 7 - Temperature vs. dissipation factor, PVC-A

The effect of frequency on dynamic modulus and dissipation factor is illustrated in Figs. 8 and 9.

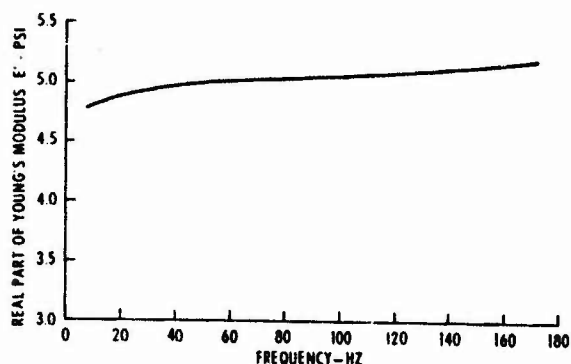


Fig. 8 - Real part of the complex Young's modulus

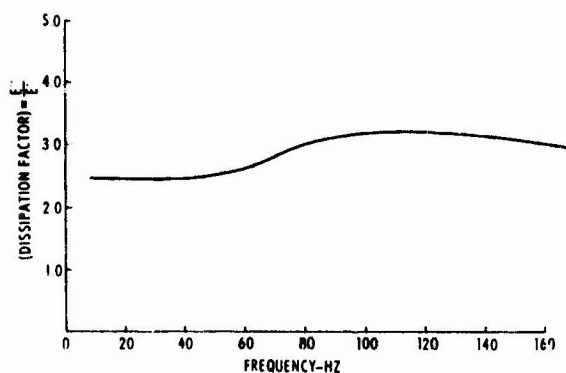


Fig. 9 - Dissipation factor of Young's modulus

Dynamic Poisson's ratio is obtained with similar methods shown schematically in Fig. 10. Using a strain gage rosette, samples of varying dimensions were examined and plotted using instrumentation similar to the vibrating reed test.

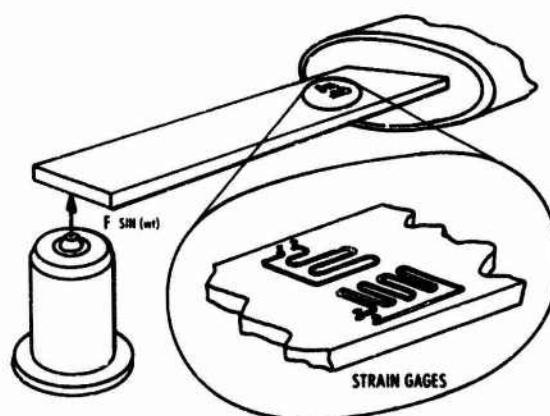


Fig. 10 - Schematic dynamic Poisson's ratio test

Shown in Fig. 11 is the variation of Poisson's ratio with frequency.

By applying the appropriate values to the basic equation in the proper frequency and temperature domain, a constant that relates the natural frequency between the model and prototype is established.

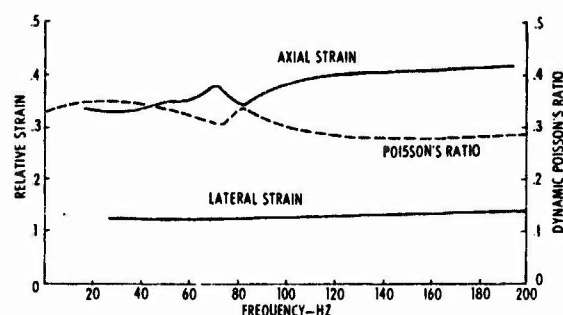


Fig. 11 - Dynamic Poisson's ratio

MODEL – PROTOTYPE COMPARISON

In constructing the plastic model vehicle structure, 3/8 scale was chosen because of its relatively small size without loss of too much detail.

The actual full scale prototype layout drawings were reduced to 3/8 scale by a photographic process. From these drawings, wooden patterns were made which were used to vacuum form and fabricate plastic parts. Shown in Fig. 12 are the front end component parts consisting of the stub frame, fenders and scaled body mounts of a plastic model.

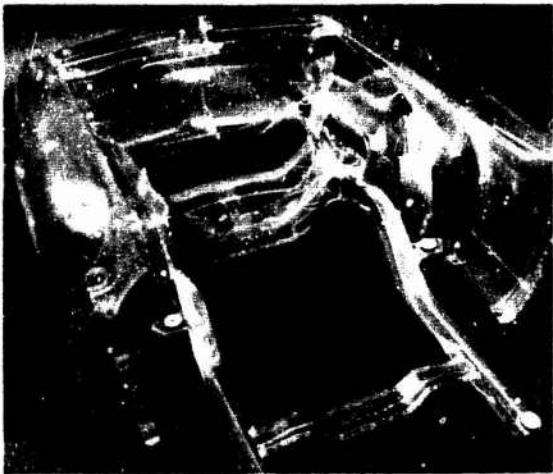


Fig. 12 – Plastic model, front end construction

Fig. 13 is the body-in-white plastic model showing rear structural detail.

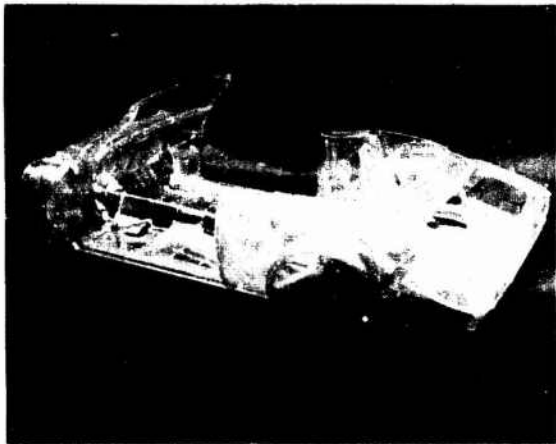


Fig. 13 – Body construction

The plastic model also underwent dynamic testing on electrodynamic shakers as shown in Fig. 14.

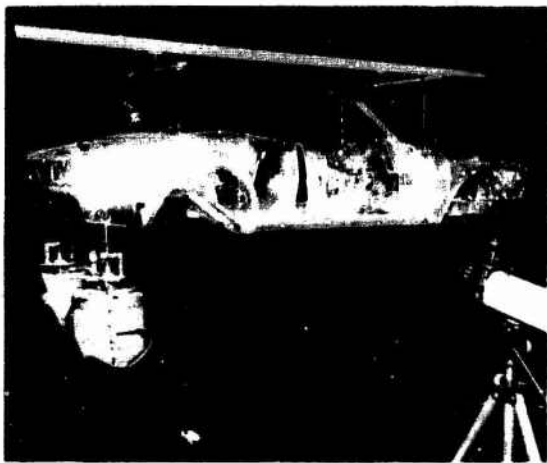


Fig. 14 – Dynamic test of plastic model

By utilizing an optical tracker for dynamic displacement measurements, a phase coherent signal is used to plot the frequency response and mode shape of the vehicle utilizing electronic conditioning equipment shown in Fig. 15.

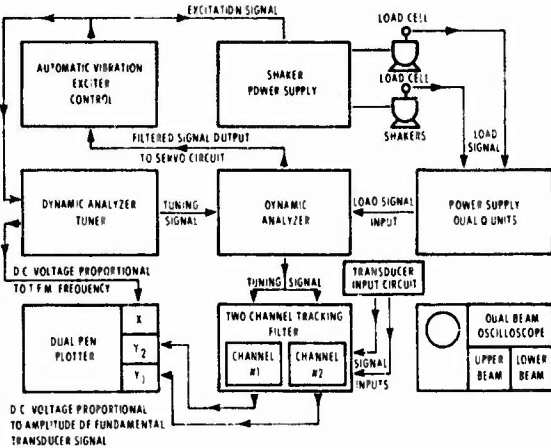


Fig. 15 – General purpose instrumentation console, schematic

Similar tests were conducted on the steel prototype as shown in Fig. 16.



Fig. 16 - Dynamic test of metal prototype

Fig. 17 shows a representative bending response of the model in terms of peak to peak displacement while Fig. 18 illustrates a similar prototype response in terms of acceleration.

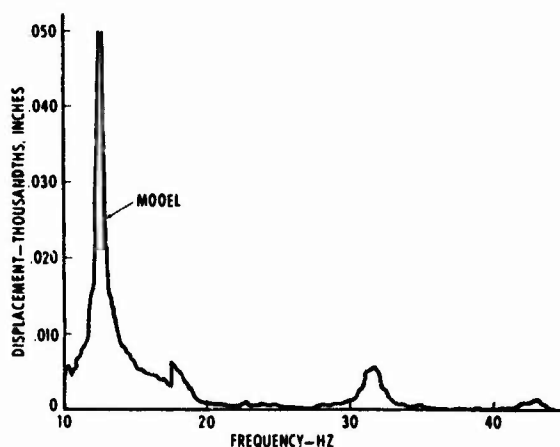


Fig. 17 - Bending frequency responses (model)

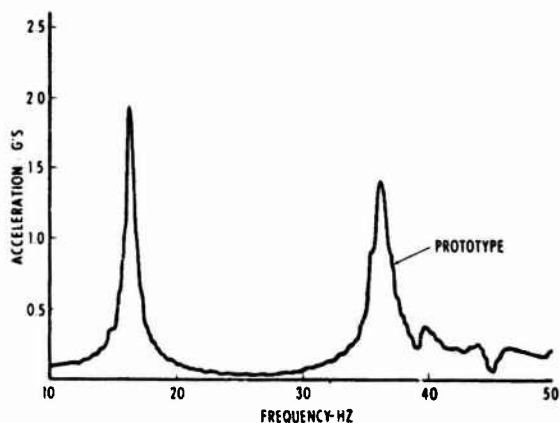


Fig. 18 - Bending frequency responses (prototype)

Figs. 19 and 20 illustrate the comparative torsional responses.

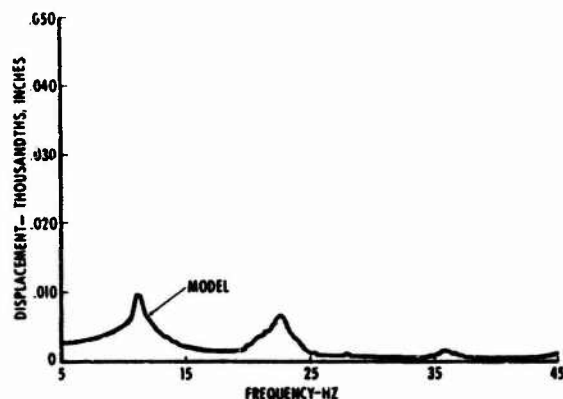


Fig. 19 - Torsional frequency responses (model)

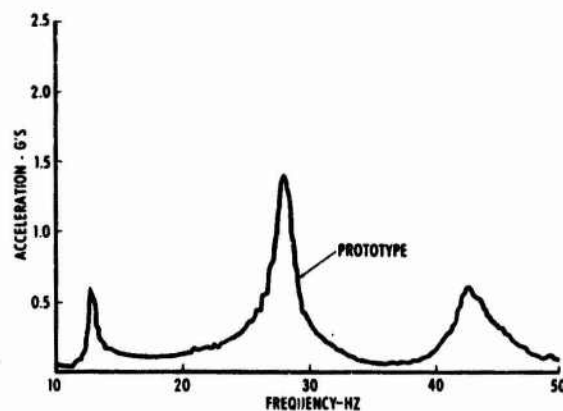


Fig. 20 - Torsional frequency responses (prototype)

Fig. 21 shows the first bending mode shapes with inputs applied to the rear of the structure as demonstrated in Figures 14 and 16. This particular mode shape shows

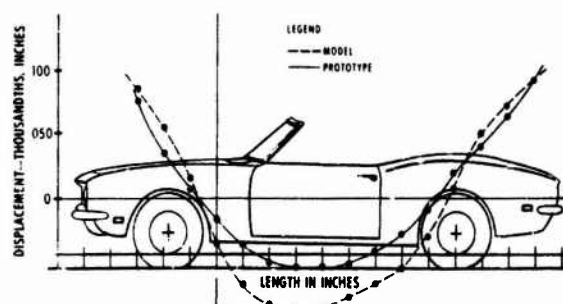


Fig. 21 - Model prototype first bending mode shape

absolute values, however, the normalized curves are very similar including the proximity of the nodal points. Figs. 22 and 23 show similar mode shape comparisons for second mode bending and first mode torsion. In addition, prototype excitation frequencies are within 10% of the model frequencies.

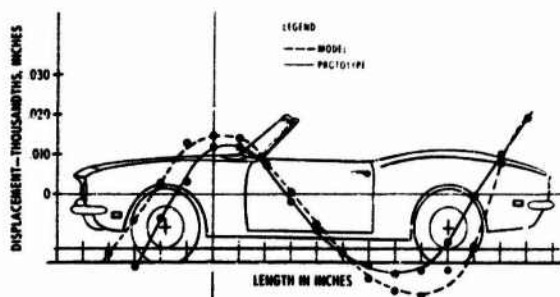


Fig. 22 – Model prototype second bending mode shape

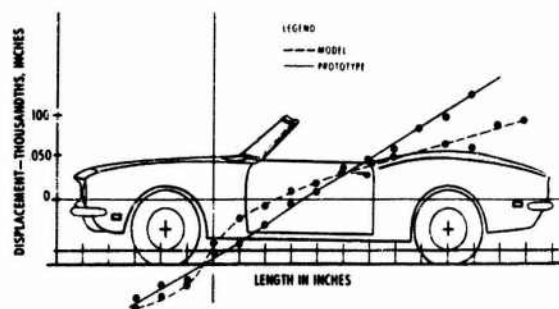


Fig. 23 – Model prototype first torsional mode shape

BIBLIOGRAPHY

1. Penn and Pickford, "Predicting Metal Stresses from Plastic Models," Industrial Models and Patterns, November, 1962.
2. Nielsen, "Mechanical Properties of Polymers," Reinhold Publishing Corporation, London, 1962.

CONCLUSION

Data indicates that correlation of natural frequencies and model shapes is well within experimental error and that most vehicle dynamic studies can be easily investigated through the use of these models. Power spectral density analysis of random road inputs has been successfully related to the plastic model. This allows a great deal of development work to be accomplished on the vehicle before the first prototype is available.

The use of plastic models is being extended by Chevrolet Engineering to dynamic stress studies, engine mounting systems, analysis of the effect of glass on structures, acoustical studies, and fluid flow evaluation, to mention a few.

In addition, the use of holography and fatigue testing have been found feasible in expanding the utilization of modeling techniques. By running parallel design programs with analytical programs, a closed loop design system shown in Fig. 24 can easily reduce design time. In short, the use of

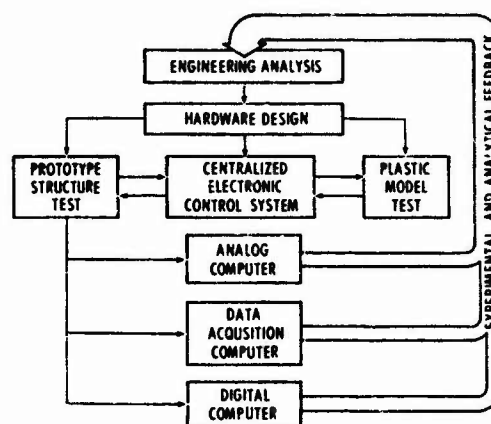


Fig. 24 – Vehicle design sequence

plastic models is limited only by the ingenuity of the project engineer and his ability to manipulate the dimensionless ratios and apply them to the model in a manner that will simulate actual conditions.

3. Nolle, "Methods for Measuring Dynamic Mechanical Properties of Rubber-Like Materials," Journal of Applied Physics, Vol. 19, Pages 753-774, August, 1948.
4. Langhaar, "Dimensional Analysis and Theory of Models," John Wiley & Sons, New York, 1951.

DISCUSSION

Mr. Fritz (General Electric Co.): What is the cost of that plastic model that you showed us? Also, what is the criterion of acceptability for the vibration limits?

Mr. Elliott: The cost of this particular model, because of the care we took in duplicating the prototype, was approximately \$100,000. The problem there is the detail that is required. We cut that down to \$25,000 in the past year, eliminating things which we think are unnecessary. Concerning acceptability criteria, we do not really know until we get a car on the road. There are so many opinions involved in this that management has difficulty deciding what is acceptable and what is not. For instance, the people who like Corvettes like a hard ride, no roll, and like to lay a patch 100 feet. With another fellow who buys a Cadillac, it is entirely different.

Mr. Verga (Hazeltine Corp.): My question is very much in line with the last one. I was thinking in terms of what is an optimum response? If you cannot tell us what is an

acceptable response, can you tell us what is unacceptable?

Mr. Elliott: We know, for instance, that strength-to-weight ratio in our case is very important. We have to compromise because of the ride motions of the suspension, so we simply designed the car to separate and increase the mechanical impedance between the suspension and the body. We want all these things separated and the amplitudes as low as possible. I think the Air Force has published considerable data on what is acceptable response and what is not. We tried to use some of this data. If that answers your question.

Mr. Simon (General Electric Co.): What is the design life of an automobile?

Mr. Elliott: The design life of an automobile? I prefer not to answer that. It is very strange. I am originally from Virginia. I come down here and see 1950 automobiles running around. I live in Detroit and have not seen a 1950 automobile in 10 years.

FATIGUE DESIGN OF ELECTRONIC EQUIPMENT

LaVerne Root
Collins Radio Company
Cedar Rapids, Iowa

This paper reviews portions of fatigue theory applicable to design of electronic equipment. The basic approach to fatigue design should include: (1) definition of loads, (2) detailed stress analysis, and (3) consideration of statistical variations in loads and material properties.

Several aspects of detailed design are discussed to assist designer in obtaining a suitable fatigue design. Testing and experimental techniques are the designer's primary tools.

INTRODUCTION

The trend in the mechanical design of electronic equipment is toward lighter equipment while the environmental stresses have remained constant or have increased. In the case of the dynamic environments, the probability of fatigue failures has been increased by the requirements for lighter weight and more highly stressed equipment structures.

The purpose of this paper is to review some of the techniques which the mechanical designer can use in improving the fatigue design of electronic equipment. Fatigue design techniques are well documented in the literature [1, 2]. However, it is necessary to adapt published results to the specialized problems of the electronic equipment designer, since much of published information deals with flight vehicle fatigue problems.

It should be recognized that fatigue design is inherently more difficult than design for static loads. Fatigue failures usually originate at stress risers and are therefore dependent on localized stress conditions. Since fatigue stresses are usually too low to cause local yielding and the associated redistribution of stresses, it is necessary to perform a

detailed stress analysis which accounts for both the gross stress pattern and the high localized stresses due to the stress concentrations. In contrast, static stress analysis only requires the definition of the gross stress field with high localized stresses being redistributed by local yielding.

DESIGN PHILOSOPHY

Three basic steps are involved in any fatigue design. These are: (1) load definition, (2) detailed stress analysis, and (3) consideration of statistical variability in loads and material properties. If these basic steps are given adequate attention, the detailed design becomes relatively straightforward.

Load definition for fatigue design must be quite detailed. Fatigue damage is strongly dependent on the following parameters of the load history: (1) oscillatory components of load, (2) static components of load, and (3) order of application of various loads. The damage is dependent to a lesser degree on: (1) frequency of oscillatory loads and (2) rest periods between loads. Again, this strongly contrasts to the load definition required for static design, where the peak amplitude is usually the only parameter of interest.

Since it is generally impractical to define fatigue loads to the degree suggested above, the order of load application, frequency, and rest periods are usually neglected. This allows loads to be defined by the static components of load and probability distribution functions for the amplitudes of the oscillatory components.

Design loads for electronic equipment consist of two types: (1) complex loading due to transportation, handling, and usage and (2) relatively simple loading representing various required laboratory vibration tests. In general, the designer will base his design on the laboratory tests since these tests are supposed to be representative of field usage and the simpler loading is much easier to handle in the design analysis. In addition, the loads representing laboratory tests have a very small statistical variation (standard deviation about one-sixth of the tolerance range) which further simplifies the design analysis.

In a number of cases, no laboratory tests are required, so the designer must consider the more complex loading representing the usage. Two examples of such systems are equipment to be qualified at Munson Road and one of a kind systems which require a minimal qualification program. The loading should be defined in sufficient detail so that static loads, oscillatory loads, and statistical variation of loads can be defined.

The second step of the basic fatigue design consists of performing a detailed stress analysis of the equipment. Since fatigue failure is strongly dependent on localized stresses, the strength of materials type analysis used for static loading is insufficient except for the simplest of structures. Plate and shell theory and elasticity and experimental stress analysis are required for analysis of the typical electronic equipment. Theoretical analysis will in most cases require the use of the digital computer to carry out the numerical computations. The theoretical analysis is useful during preliminary design to tentatively size structural components.

Experimental stress techniques are useful during later stages of design. Measured stresses on hardware built to fabrication drawings are more accurate than computed stresses. The use of models [3] during early phases of design allows optimization of the structure and verification of dynamic response calculations. Plexiglas models of quite complex equipment are easily fabricated in the laboratory and are relatively easy to modify as tests proceed. Stress coat can be used with the plexiglas models to obtain the complete stress field and to determine locations for strain gauges.

Stress coat may also be useful on the actual hardware to verify conclusions based on the plastic models. The final fatigue analysis should be based on strain gauge readings since stress coat readings are of limited accuracy.

The final step in the basic fatigue design consists of considering the statistical variation in the loads and material properties. Each equipment of a given type will be subjected to a different load history due

to differences in history of transportation and usage. In addition, differences between "identical" flight vehicles alters loading for identical transportation and usage histories. Compiling the various possible load histories will lead to a probability distribution function (pdf) of loads, which may be represented by a typical (mean) load history and a measure of the scatter (standard deviation) between the load histories.

In a similar manner the pdf of material properties must be obtained. The material properties in the form of S-N curves represent a median life failure curve; that is, fifty percent of specimens would be expected to fail at lives less than that given by the S-N curve. Typically the scatter in fatigue lives at a given stress may be 10 to 1. As in the case of loads, the fatigue lives may be represented by a mean life and a standard deviation.

Alternately we may look at scatter in stresses for a given life. Again we can define a mean stress and a standard deviation. This viewpoint is more useful in our fatigue design. The design problem now reduces to selecting a material whose pdf of strength has some small but acceptable overlap with the pdf of loads. Figure 1 shows typical pdf of load and strength.

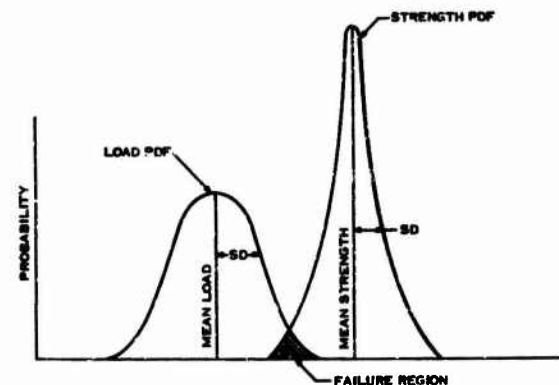


Figure 1. Typical Probability Distribution Functions for Load and Strength.

As can be seen from the figure, the failure region can be reduced by: (1) reducing mean load while holding mean strength and standard deviations constant, (2) reducing load standard deviation while holding mean load, mean strength, and strength standard deviation constant, (3) increasing mean strength while holding mean load and standard deviations constant, (4) reducing strength standard deviation while holding mean load, mean strength, and load standard deviation constant, and (5) changes in two or more parameters simultaneously. The electronics designer seldom has any control over the load pdf so he must work with the strength pdf.

The selection of the safety factor determines the spacing between the mean load and mean strength, while process controls and tolerance ranges are primary variables in the control of the standard

deviation of strength. In actual practice the designer will have only limited knowledge of the pdf of strength and load; but an understanding of the principles involved will allow the designer to properly use his engineering judgment.

Once the basic steps in the fatigue design are complete, the detailed design becomes relatively straightforward.

DETAILED DESIGN

The most important phase of detailed design is the reduction of stress risers. Fatigue cracks start at high localized stresses which are usually associated with stress risers; such as, abrupt changes of dimension, holes, notches, machining marks, dents and scratches introduced by mishandling, poor attachments, and change of modulus. Many of the stress risers are necessary features of the design, but the designer can reduce stress concentration factors by using generous radii and gradual transitions in dimensional changes. Shifting the location of stress riser to lower tensile stress region or to compressive stress region will extend fatigue life.

The fatigue notch factor (K_f) is related to the static stress concentration factor (K_t) and the notch sensitivity factor (q).

$$K_f = q(K_t - 1) + 1$$

The notch sensitivity is nearly zero for large K_t and approaches unity as K_t decreases. Figure 2 is a typical plot of q versus notch radius. The published q curves for various materials can be used with K_t curves for various geometries to estimate K_f . A conservative estimate for K_f would be to use K_t .

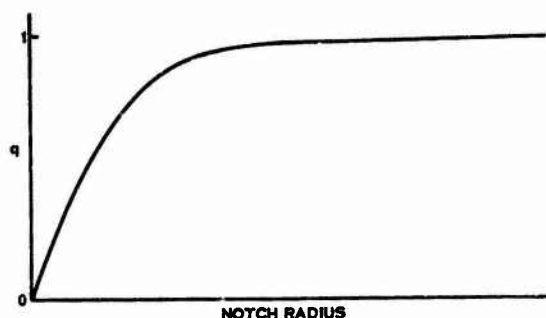


Figure 2. Typical Plot of q Versus Notch Radius.

Another area which must be considered is the effect of a mean stress superimposed on the alternating stresses. Increasing the mean stress (except mean tension or mean simple shear) for given alternating stress will reduce the fatigue life. In the cases of tension or simple shear, the fatigue life is unaffected by the mean stress. Most electronic equipment has a zero mean stress. Two possible exceptions would be structures with residual stresses or preloaded devices within equipment.

The fatigue data for superimposed mean stress may be presented in many ways. Two common ways are: (1) a family of S-N curves at various mean stresses and (2) the modified Goodman (constant life) diagram which is the more useful diagram. Figure 3 presents a typical modified Goodman diagram from MIL-HDBK-5. It should be noted that MIL-HDBK-5 is an excellent source of both fatigue and static mechanical properties for materials used in aerospace structures.

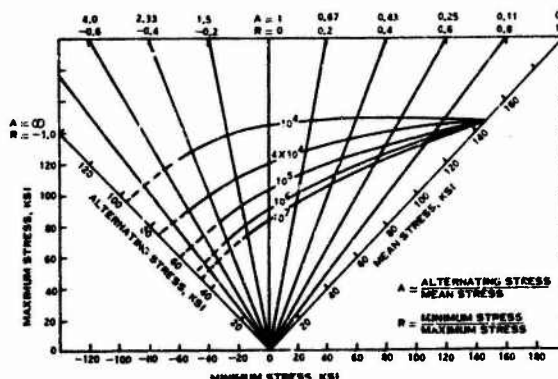


Figure 3. Typical Modified Goodman Diagram.

The mean stress effect applies to residual stresses since structure cannot recognize whether mean stress is due to applied load or residual stress. The designer must guard against high tensile residual stresses being introduced at critical areas. Residual stresses can be introduced during heat treating and fabrication operations.

The designer can intentionally introduce compressive stresses at critical regions to increase fatigue life. This might be done by shot peening the surface to obtain a compressive surface layer or intentionally overstressing in bending where expected loadings are not completely reversed.

The fatigue life of a part can be changed drastically by the simultaneous application of the fatigue loading and one of the other environments. Corrosive environments greatly accelerate fatigue failure. The fatigue strength is reduced by elevated temperature and creep can become a problem if the elevated temperature is combined with a static load. Reduced temperatures increase the fatigue life of all metals.

Fatigue design for complex load histories requires the designer to use one of the fatigue damage accumulation hypotheses. Kaechele [4], and Crichlow [5], et al review a number of these hypotheses and conclude that the Palmgren-Miner hypothesis [6, 7] is the most correct in an average sense. The hypothesis as formulated by Miner is given as

$D = \sum \frac{n_i}{N_i}$ where n_i is the applied cycles, N_i is the cycles to failure from the S-N curve, and D is computed damage. Failure is assumed to occur when the computed damage is equal to unity.

Numerous studies have shown that computed damage can be greatly different from unity at failure. If a high stress block (many cycles at constant amplitude) is followed by a low stress block the computed damage tends to be less than unity. Conversely, if a low stress block is followed by a high stress block the computed damage tends to be greater than unity. In the extreme case (coaxing) where many small blocks of stresses are applied, with the stress amplitude of each block slightly higher than the preceding block, the computed damage can exceed 100. If the stress blocks are well mixed without any ordering by amplitude, the computed damage normally lies in the range 0.3 to 3. This allows the designer to select a computed damage less than one to obtain conservative estimates of mean lives.

TESTING

The designer should recognize that analytically predicted fatigue lives are open to question due to many simplifying assumptions required in any practical fatigue analysis. Therefore, testing plays a primary role in fatigue design.

Testing under representative load spectrums allows accurate determination of failure locations and the associated stresses. Alternate design details can be evaluated under actual or closely simulated load spectrums. A considerable improvement in detailed design can be expected from properly designed tests.

Measured stresses, failure locations, lives, and dynamic responses can be used to improve analysis procedures and to evaluate effects of the various simplifying assumptions required in the analysis.

CURRENT RESEARCH

Much of the current research is aimed primarily at understanding basic fatigue phenomena and is of little direct interest to the designer. An additional large block of research involves ad hoc testing of specific equipment and the studies of crack propagation in airframe materials and assemblies. A few areas with more potential for electronic equipment design application include: (1) prediction of fatigue curves from static properties, (2) fatigue damage accumulation hypothesis based on theoretical knowledge of fatigue rather than empirical observations, and (3) theoretical explanations of the effects of mean stress and alternating stress on fatigue life.

The prediction of S-N curves from the static properties is useful in estimating fatigue curves for new materials and for extrapolating the S-N curve outside the range of measured data. Manson [8] presents two such techniques giving curves asymptotic to the log strain versus log life at both short and long lives.

The first technique (4-point correlation method) is shown in figure 4,

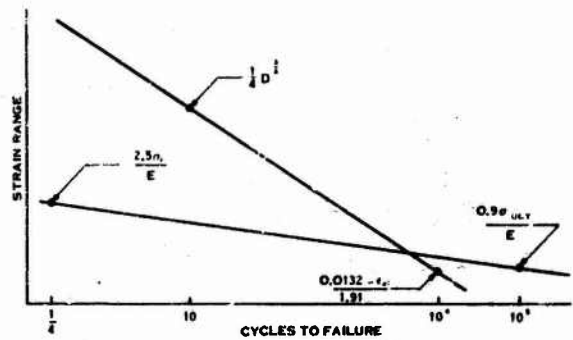


Figure 4. Asymptotic Curves for 4-Point Correlation Method.

where $D = \frac{1}{1 - RA}$, RA is reduction in area in percent, E is Young's modulus, σ_f is true fracture stress, ϵ_{el} is elastic strain range at 10^4 cycles, and σ_{ult} is ultimate tensile strength. The second technique (universal slope method) is shown in figure 5.

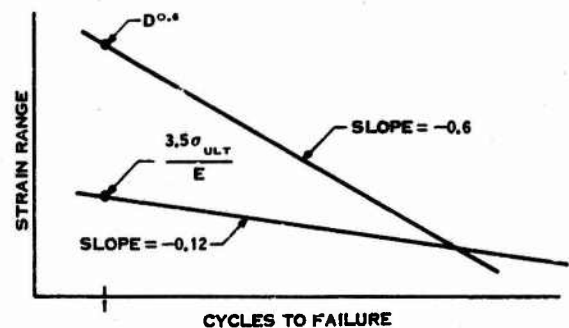


Figure 5. Asymptotic Curves for Universal Slope Method.

The two techniques give comparable results for 28 out of 29 materials reported in Manson's paper.

Most of the fatigue damage accumulation hypotheses are based on empirical observations and as such make no attempt to relate fatigue damage to the microstructural phenomena. Valluri's [9] hypothesis is one of the exceptions as it is based on dislocation theory and strain hardening theory. Unfortunately this more complex hypothesis yields no better predictions than the more familiar Palmgren-Miner hypothesis.

CONCLUSIONS

Fatigue design of electronics is more difficult than static design. The load history must be defined in much greater detail and stress analysis must account for localized stresses. Since fatigue failures originate at high localized stresses, the detailed design becomes much more important.

Testing and experimental stress analysis are the designer's most powerful tools in increasing fatigue lives of electronic equipment. Analytic techniques can be used in arriving at initial design but complexity of electronic equipment precludes complete reliance on analysis.

Many of the techniques suggested for the design of electronic equipment are the same ones used by the designer of aerospace structures. In some cases it is necessary to modify techniques to account for basic differences between the electronic equipment and aerospace structures. A final idea that might be taken from the fatigue design of aerospace structures is the cataloging of design details which have a demonstrated superiority in fatigue. These design details can be applied to future designs.

ACKNOWLEDGMENTS

The review of fatigue design techniques has been sponsored by Collins Radio Company as a part of a continuing program to improve the environmental design of its products.

REFERENCES

- (1) G. Sines and J. L. Waisman, editors, *Metal Fatigue*, McGraw-Hill, New York, 1959.
- (2) A. F. Madayag, editor, *Metal Fatigue: Theory and Design*, John Wiley & Sons, New York, 1969.
- (3) A. Henry, L. Sackett and J. Risney, "Experimental Stress Analysis Methods," Collins Radio Company Working Paper 3261, October 1968.
- (4) L. Kaechele, "Review and Analysis of Cumulative-Fatigue-Damage Theories," RM-3650-PR, August 1963.
- (5) W. Crichlow, A. McCulloch, L. Young, and M. Melcon, "An Engineering Evaluation of Methods for Prediction of Fatigue Life in Airframe Structures," ASD-TR-61-434, March 1962.
- (6) A. Palmgren, "Die Lebensdauer Von Kugellagern," *Zeitschrift des Vereines Deutscher Ingenieure*, 1924.
- (7) M. Miner, "Cumulative Damage in Fatigue," *Journal of Applied Mechanics*, 1945.
- (8) S. Manson, "Fatigue: A Complex Subject - Some Simple Approximations," *Experimental Mechanics*, Vol. 5, No. 7, pp. 193-226, July 1965.
- (9) S. Valluri, "A Unified Engineering Theory of High Stress Level Fatigue," *Aerospace Engineering*, Vol. 20, No. 10, October 1961.

DISCUSSION

Mr. Stein (Arizona State Univ.): This is in the nature of a question and a comment, perhaps for both of the first speakers, because they both advocate and use strain gages on plastic materials. This is an operation fraught with a considerable amount of danger because of the selfheating effects, that is, strain gages on poor heat conductors. I wondered if you might have some comments on this? Also, you have a statement that you feel that strain gages are more accurate than stress coat for fatigue design. If there were more time I would like

to discuss this with you but perhaps you have some comments on that statement.

Mr. Root: On the first one, we are aware of the problems. I am not sure that I can say much more than that. We use care in using the strain gages on plastic. And the second, we use stress coat strictly under noncontrolled laboratory ambient conditions, so we use it only as a qualitative tool. We use it more for deciding locations for strain gages rather than to attempt to get quantitative measurements.

MODEL STUDIES TO DETERMINE LOW-FREQUENCY NOISE REDUCTION OF SPACECRAFT

Arnold W. Mueller
NASA Langley Research Center
Hampton, Virginia

A specially designed model has been used to study the low-frequency (below 50 Hz) noise reduction of large spacecraft. The model was constructed of a thin-walled double shell and was a full-scale representation of the Apollo Command Module class of spacecraft. The noise reduction contributions of component structures were measured and compared with predicted values based on a quasi-static pressure theory. The measured results were found to be in general agreement with the predicted noise reduction values.

INTRODUCTION

The intense noise to which a large spacecraft is exposed during launch is of concern because it may, in some cases, create a detrimental inside environment for the crew and equipment. Figure 1 indicates the nature of the outside acoustic environment of a spacecraft such as the Apollo Command Module due to the noise of the rocket engines (from unpublished

engulf it. The effects of such intense low-frequency components on the spacecraft structure and the associated transmission of noise into the spacecraft are of particular concern. Conventional methods of predicting noise reduction at higher frequencies are not pertinent in this low-frequency range. The material of this paper relates to a research program designed specifically to explore the problem of predicting noise reduction at low frequencies.

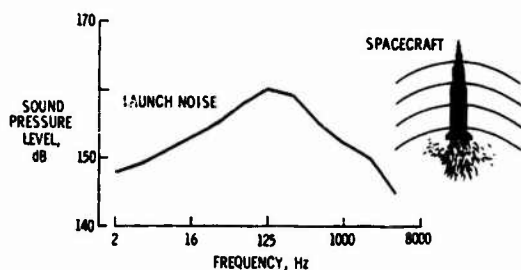


Fig. 1 - Measured one-third octave band noise spectrum near a large manned spacecraft during launch

data). The spectrum is seen to peak at about 100 Hz and to include intense noise components at frequencies down to a few hertz. Some of the wavelengths are thus long compared to the dimensions of the spacecraft and completely

The NASA has had a program to investigate the low-frequency noise reduction of large spacecraft structures of the Apollo Command Module type. This investigation included a theoretical study based on static pressure vessel principles by Dr. Richard H. Lyon, et al., of Bolt Beranek and Newman, Inc., and an associated model study in the Langley low-frequency noise facility. The basis for the above model design is described in Refs. [1] and [2]. This paper contains results of the model tests at Langley along with calculations using the theoretical methods developed by Dr. Lyon. Validations are given for both the low-frequency noise reduction theory and the modeling technique.

NOISE TRANSMISSION CONCEPTS

Some factors in noise reduction are identified for purposes of review in Fig. 2. Although the data of Fig. 2 apply directly to flat panels,

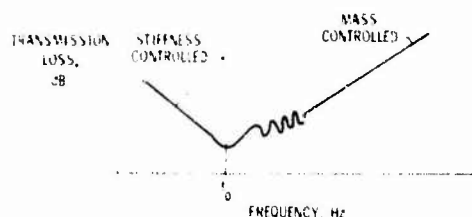


Fig. 2 - Schematic representation of transmission loss for a flat panel

the concepts involved are valid for spacecraft which have surfaces of complex curvature. Shown is a transmission loss curve which included both stiffness controlled and mass controlled segments. The stiffness controlled region covers the frequency range below the first natural vibration frequency, whereas the mass controlled region includes the higher frequencies. Because of the size and shape of manned spacecraft and their types of construction, the stiffness controlled region is important relative to noise transmission for a substantial portion of the spectrum of Fig. 1. This was the motivation for a research program involving a theoretical method for the prediction of low-frequency noise reduction and an experimental program involving a unique acoustic model of the Apollo spacecraft.

The theoretical method of Refs. [1] and [2] is based on the concept that below the fundamental structural and acoustic resonances of a spacecraft, the low-frequency acoustic waves, acting as a quasi-static pressure, would slowly squeeze the structure which responds as an elastic pressure vessel. Thus, in the theory, mechanical and acoustical compliances of the structure and its enclosed volume are considered as significant factors in its response. Other phenomena such as structural damping, modal responses, and the acoustic characteristics of the interior are not accounted for in the quasi-static theory.

Figure 3 presents some of the basic equations which are used in the prediction of low-frequency noise reduction. A slowly varying or quasi-static external pressure P_e applied to an airtight elastic container of volume V_i and at an internal pressure P_i will cause a change in the internal volume by an amount

$$\Delta V_i = \Delta P_i \left(\frac{V_i}{P_i} \right) = \Delta P_i C_a \quad (1)$$

where C_a is defined as the acoustic compliance of the enclosed volume. For an elastic shell, the volume change is given by

$$\Delta V_i = C_s (\Delta P_e - \Delta P_i) \quad (2)$$

where C_s is defined as the overall compliance of the shell. The overall shell compliance is equal to the arithmetic sum of the compliances of each of the shell components.

NOISE REDUCTION = $20 \log_{10} \left(\frac{C_a + C_s}{C_s} \right)$

WHERE: $C_a = \frac{\Delta V_i}{\Delta P_i}$

$C_s = \frac{\Delta V_i}{\Delta P_e - \Delta P_i}$

AND: P_e IS A QUASI-STATIC PRESSURE

Fig. 3 - Basic equations used to predict low-frequency noise reduction values for spacecraft

Therefore, combining Eqs. (1) and (2) we obtain

$$\frac{\Delta P_e}{\Delta P_i} = \frac{C_s + C_a}{C_s}$$

where $\frac{\Delta P_e}{\Delta P_i}$ gives the pressure or noise reduction. In terms of dB this is

$$\begin{aligned} NR &= 20 \log_{10} \frac{\Delta P_e}{\Delta P_i} \\ &= 20 \log_{10} \left(\frac{C_s + C_a}{C_s} \right) \end{aligned} \quad (3)$$

MODEL EXPERIMENTS

In order to validate the low-frequency noise reduction concepts and the modeling techniques described in Refs. [1] and [2],

a model of the Apollo spacecraft was fabricated for tests in the low-frequency noise facility at Langley. Figure 4 contains schematic representations of the model, in three different test configurations. It consists of three main elements indicated in the figure. These are: an inner shell, an outer shell, and a filler material between the two. Overall dimensions of

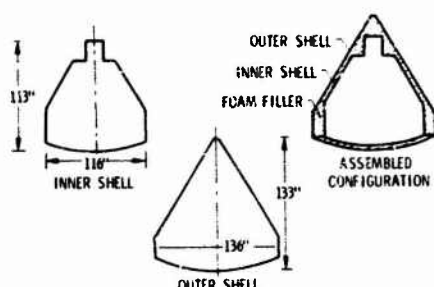


Fig. 4 - Sketches of model test configurations used for low-frequency noise reduction studies

the model are the same as those of the Apollo Command Module, the height and diameter being approximately 11 feet. Thicknesses of the model vary from 0.002 inch for the inner shell cylinder to 0.750 inch for the cylinder cap plate. The truncated cone of the outer shell was 0.051 inch thick. The inner shell was rigidly connected to the outer shell, at 12 points around its base perimeter.

The model was designed to simulate the acoustical and structural compliances of the spacecraft in the low-frequency range. This involved a 1:1 scaling of the overall interior dimensions whereas the shell material thicknesses were scaled according to either membrane or flexural considerations, depending on the geometry of the particular components. The designs of the curved surfaces were dominated by membrane considerations. The designs of the flat surfaces, on the other hand, were dominated by flexural considerations. This accounts for the wide range of material thicknesses of the model.

Because of the manner in which the model is designed, it should represent the noise reduction behavior of the Apollo spacecraft at low frequencies but does not necessarily represent it at the higher frequencies where structural vibration modes occur.

Figure 5 is a photograph of the model in test position at the low-frequency noise facility.

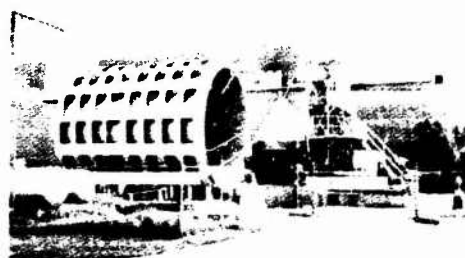


Fig. 5 - Model in test position at the low-frequency noise facility

The test chamber of this facility is 22 feet in length and 24 feet in diameter. The facility has a hydraulically operated piston which moves a 14-foot-diameter honeycomb speaker cone sinusoidally in the frequency range 1 Hz to 50 Hz. The end wall as seen in Fig. 5 is free to move and may be positioned within the test chamber to tune it over its operating frequency range. For the data presented in this paper, the facility was operated between the frequencies of 2.5 Hz to 50 Hz and sound pressure levels were measured on the inside and on the outside of the model. The arithmetic differences between these two levels were used to give the measured noise reduction values of Figs. 6 through 8.

RESULTS AND DISCUSSIONS

Figure 6 presents a comparison of the predicted and measured noise reduction data, over the frequency range of 2.5 Hz to 50 Hz, for the inner shell. The predicted value of 17.2 dB was calculated from Eq. (3) using the appropriate compliance values. It can be seen that the predicted and measured data are in good agreement at low frequencies. In the range of frequencies of the plate and shell vibrations, however, marked discrepancies occur. These discrepancies are believed to be due to dynamic response considerations.

The measured noise reductions for the outer shell are compared to the predicted value of 49.4 dB in Fig. 7. The measurements generally follow the trend of the theory up to the frequency range in which dynamic

responses may be important. The measured noise reduction values are generally lower than the predicted value. These lower values may be due to local inhomogeneities of the shell structure and imperfect pressure seals at the joints.

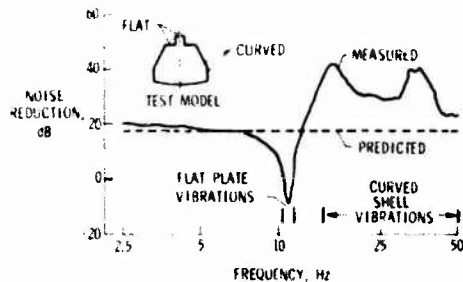


Fig. 6 - Comparison of measured and predicted noise reductions for inner shell

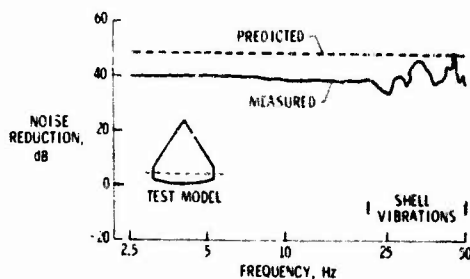


Fig. 7 - Comparison of measured and predicted noise reduction for outer shell

Similar data for the fully assembled model are given in Fig. 8. Figure 8(a) contains results for both the inner and outer shells in combination. The trends of these measured data are similar to those of Figs. 6 and 7 and the noise reduction values are generally lower than the predicted value. Figure 8(b) contains results for the inner and outer shells in combination with a foam-type filler material to block the intervening air volume. These latter results indicate greater noise reductions than for Fig. 8(a) and a better agreement with

predicted value. The foam material minimized the amplitudes of the air cavity acoustic resonances between the shells and the shells' vibration responses. It is believed that this filler material also provided some local stiffening.

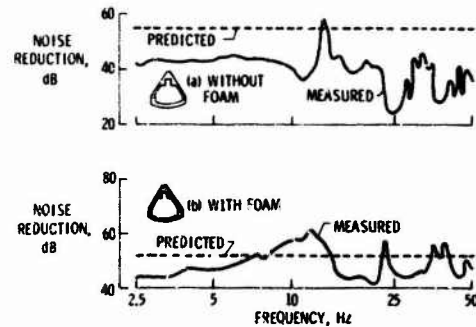


Fig. 8 - Comparison of measured and predicted noise reductions of assembled model with and without foam filler material

CONCLUDING REMARKS

A specially designed model has been used to study the low-frequency noise reduction of large spacecraft of double shell construction. In this study, the noise reduction contributions of component structures were measured and were compared with the predicted values based on quasi-static pressure theory. The results indicate general agreement in the noise reduction values and in the trends of the data for the frequency range where dynamic responses are not significant.

REFERENCES

- [1] Lyon, R. H.; Dietrich, C. W.; Ungar, E. E.; Pyle, R. W., Jr.; and Apfel, R. E.: "Low-Frequency Noise Reduction of Spacecraft Structures." NASA CR-589, September 1966.
- [2] Lyon, Richard H.; Apfel, Robert E.; and Dietrich, Charles W.: "Modeling of Spacecraft for Low-Frequency Noise Reduction." The Shock and Vibration Bulletin, Bulletin 35, Part 5, pp. 235-242, February 1966.

DISCUSSION

Mr. Verga (Hazeltine Corp.): You said that the noise at the spacecraft is mainly due to blastoff and then you proceeded to try to eliminate or minimize the low frequency noise. What is the purpose of wanting to do that if the noise is limited to blastoff? Ear muffs or something mechanical like that perhaps could solve the problem.

Mr. Mueller: Ear devices really would not solve the problems. We are in a low frequency range from 2 Hz to around 50 Hz or so, where ear muffs or ear attenuators of some sort give very little protection. They are effective only at higher frequencies. The equipment would respond at these low frequencies if there were a sufficient sound pressure level within the capsule. It is possible to have sound pressure levels at these low frequencies in that your body cavity or eyes would jump or vibrate and create difficulty in either breathing or communication.

Mr. Dorland (NASA Manned Spacecraft Ctr.): Did you make any attempt to correlate any of the results of your study with any flight data which may have become available over the last half dozen flights?

Mr. Mueller: Yes. I contacted some people at Houston. What I learned was that there were very meager data taken within the spacecraft on the noise or sound pressure levels in the low frequency range. I did find, as I indicated, some data from around 20 Hz and higher. In that instance we find that the spacecraft does, in fact, attenuate the noises at 20 Hz to 50 Hz pretty well in agreement with the theory. If you have any additional data which might be of some interest to me, I would like to have it.

Mr. Dorland: I do not know what you were able to find. I am only grossly familiar with the flight measurement program so I do not know what they might have produced for you. I have another comment. I noticed by looking at the dimensions of your model that it is a little differently scaled than the actual command module. Is this done for some specific purpose?

Mr. Mueller: No. I was out in California and obtained the dimensions from the people at North American, Downey, and these are the dimensions which they gave me. If there is a difference, I cannot explain why.

Mr. Edge (NASA Langley Research Ctr.): I might comment with regard to dimensions. The fact was that some compromises were made to economize, to just reduce the cost of fabrication.

Mr. Ungar (Bolt Beranek & Newman): As you probably recall, we did some measurements on a very small model. As I recall, we had a hard time coming up with models that behave like the theory, mainly because any small crinkle in the surface would destroy the stiffness and reduce the noise reduction. I am not surprised to see that your noise reduction was not quite up to predictions because you may well have had crinkles in the skin.

Mr. Mueller: We feel very proud, actually, of the measurements. We think that the measurements tended to confirm very well the calculations or methods for which you people were responsible.

Mr. Forkois (Naval Research Lab.): Were you satisfied with your simulation? It seems to me that the missile itself was in a free field and then you generated a pressure wave with a reflecting wall. Was there good correlation between your test and the actual flight conditions?

Mr. Mueller: Certainly we did not run a statistical correlation on that. For the particular cases which we had, we do feel that we pretty well simulated the pressure field. You are right, we did have a reflecting wall and we did have some varying sound pressure levels around the spacecraft. This, in turn, I feel did add to the reduced values of the measured data as compared to the theory. It was probably the best we could do at the time, and we think that our test is pretty good.

COMBUSTION INSTABILITY TESTS OF THE SATURN IB FIRST STAGE

W. S. Parker
Chrysler Corporation
New Orleans, Louisiana

A series of combustion instability tests were conducted on the S-IB Stage (booster stage) of the Saturn IB launch vehicle. During these tests, the liquid rocket engines were intentionally driven into combustion instability for short periods to determine if there was any tendency of the stage structure and propellant feedlines to couple with and sustain the pressure and structural oscillation resulting from the temporarily induced unstable combustion. Data recorded during the instability periods showed no excitation of the natural frequency of the stage or the rocket engines and no evidence of coupling or reinforcing of the vibrations from the instability. The tests increased the confidence in the stage design and suggested a criterion for the stability rating of manned mission launch vehicles.

INTRODUCTION

A series of engine combustion instability tests were conducted by Chrysler Corporation Space Division on the S-IB Stage of the Saturn IB launch vehicle stage number S-IB-11. The tests were under the technical direction of National Aeronautics and Space Administration at the Marshall Space Flight Center (MSFC) in Huntsville, Alabama. They were made to determine the influence of the stage structure and the propellant feed systems on engine combustion stability when the engines were driven unstable. These tests were significant because they marked the first time that a stage was subjected to such combustion instability. The benefits to be derived from the tests included increased confidence in the flight reliability of the stage and an improved math model of the stage; the possibility of incurring damage to the stage as a result of the tests was considered minimal.

BACKGROUND

The S-IB Stage is a multitank, multiengine booster. Eight H-1 model engines, rated at 205,000 pounds thrust each, are positioned at the base of the stage as shown in figure 1. The four inboard engines (5, 6, 7, and 8) and

the four outboard engines (1, 2, 3, and 4) are the same except the outboard engines can be gimbaled for thrust vector control (not a consideration in these tests); and the routing of the propellant feedlines differs slightly.

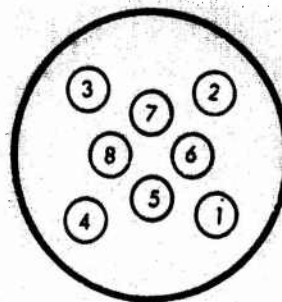


Fig. 1 - Engine position (from aft)

The engine is turbopump fed with liquid oxygen (LOX) and kerosene type RP-1 fuel. These propellants are mixed and atomized before burning in the thrust chamber. Figure 2 provides a schematic representation of the thrust chamber.

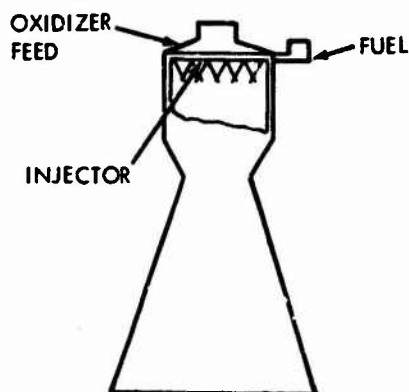


Fig. 2 - Thrust chamber

The injector is the focal point of the combustion process. Early injectors had a flat face design but as thrust up-ratings of the engine occurred, combustion instability was occasionally encountered. The injector design was, therefore, modified to reduce the likelihood of such instability occurring. At the same time, it tended to dampen any instability pressure oscillations if instability should occur. The modification consisted of adding 3-inch-long copper baffles, or vanes, to the face of the injector. (See figure 3.) The six radial and one cylindrical baffle divides the combustion zone into small compartments and discourage tangential and radial modes of instability.

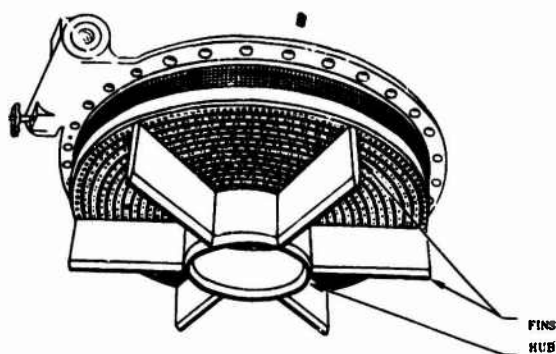


Fig. 3 - Baffled injector

During the normal production sample testing of the injector by the engine contractor (Rocketdyne), isolated cases of self-triggered, sustained instability were encountered. The initiation and sustention of the potentially damaging instability was thought to result from a sympathetic coupling of the engine test stand structure and propellant system with the instability frequency. This cause was confirmed by 41 tests that were conducted during which the engine was purposely driven into instability by detonating a 50 grain bomb placed several inches below the injector face. See figure 4 for a picture of the bomb. The bomb was detonated by the heat of combustion about 2 to 3 seconds after engine start.

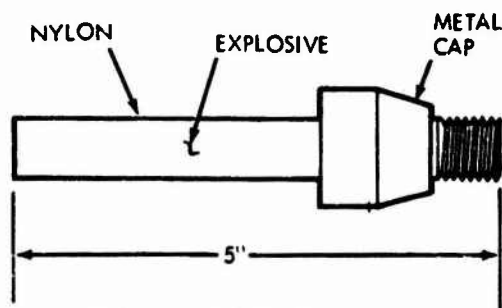


Fig. 4 - Explosive device

Because of the complexities and uncertainties of the structural dynamics in an analytical solution of the problem, it was decided that similar tests should be conducted during a full scale flight stage test to determine the characteristics of the engine-stage combination when the engine is driven into an unstable combustion condition.

STAGE DESCRIPTION

The S-IB Stage consists of nine propellant tanks and eight engines. Four Lox tanks and four fuel tanks are arranged alternately around a center Lox tank. The four outer Lox tanks are 70 inches in diameter and are interconnected at the bottom through sumps with the 105-inch diameter center tank sump. The four fuel tanks are also interconnected at the bottom through a similar manifold arrangement. Figure 5 depicts the tank interconnecting system. The eight engines are arranged in a manner shown earlier in figure 1.

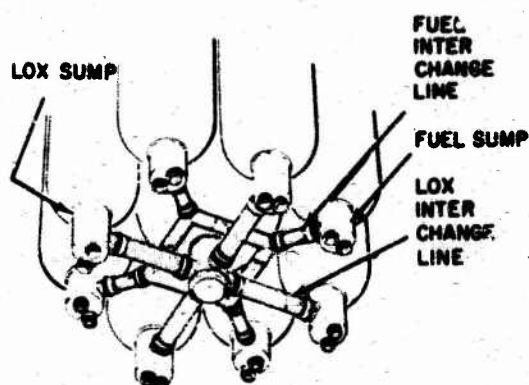


Fig. 5 - Propellant Tank interchange system

The nine propellant tanks are mounted between a lower radial structure called the thrust structure and an upper radial structure called the spider beam. The five Lox tanks transmit the thrust loads between the thrust structure and the spider beam. Because of the unequal expansion and contraction extremes between the cryogenic Lox tanks and the fuel tanks, the fuel tanks are attached to the spider beam through sliding pins which precludes the use of these tanks as vertical load bearing members.

The four outer Lox and four fuel tanks supply the engines with propellant from sumps at the tank bottoms. Each outer tank furnishes Lox or fuel directly to one inboard and one outboard engine. The center Lox tank feeds all engines indirectly through the interconnection system. Figure 6 shows the feedlines for only one propellant, but is typical of both. During operation, near equal propellant levels are maintained between each Lox tank and between each fuel tank. The interchange between tanks at the bottom also furnishes a path for pressure disturbances to travel from engine to engine. Besides the objective of determining the structural-propellant system-engine vibration frequency relationship, it was also desirable to see if a pressure disturbance, as would be caused by a burst of instability, could propagate to another engine through the feed system.

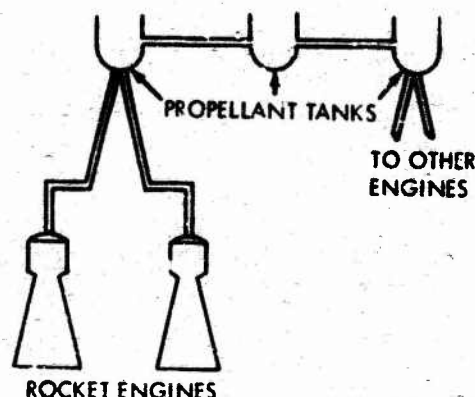


Fig. 6 - Engine, feedline, and tank relationship

TEST PLAN

The tests were conducted on stage number S-IB-11 in the static test tower at the Marshall Space Flight Center in Huntsville, Alabama. The plan called for two engines to be bombed. The engines in positions 1 and 7 were selected. These were chosen because 1) they represent both an inboard and an outboard engine configuration and 2) have the maximum physical separation; 3) they are not fed from the same propellant tanks; and, since the S-IB uses a staggered pairs engine start sequence, 4) they have the greatest time separation in the staggered engine startup sequence. As a precaution, and to facilitate the special measurements and the explosive device installation, test engines replaced the two production engines normally in positions 1 and 7; however, this substitution in no way compromised any of the data or test program conclusions.

The plan further called for tests of approximately 15 seconds duration with a normal start sequence. Steady-state operation is realized in approximately 3 seconds so the 15 second duration gave adequate test time without adding excessive running time to the stage components. The propellant loads predicted for flight were loaded to obtain normal stage fluid dynamic response.

The explosive device used to create the instability comprises a 50-grain mixture of PETN, composition C, and Plast-T-Cap all encased in a nylon tube. A threaded metal cap at the top of the explosive device screws into the face of the specially modified thrust chamber injector. The same bomb design was used

as was employed in the single engine tests (mentioned earlier) when the coupling phenomenon was initially discovered. This assured comparable initiation of combustion instability. Detonation of the device is simple and requires no external controls or electrical connections. When the heat of combustion becomes great enough to melt the nylon encapsulating the explosive mixture, detonation occurs. The detonation time proved very repeatable, varying between 2.4 and 2.8 seconds after ignition signal.

Previous single engine bomb tests showed thrust increases of as much as 100 percent above the nominal 205,000 pound level of the H-1 engine. A computer analysis of the thrust structure response to the shock was made before the test series. This analysis indicated some fasteners in the inboard engine thrust beams would be subject to failure from this overthrust. Accordingly, the fasteners were replaced with larger, stronger ones before the test series started. As with the other changes, the stage dynamic characteristics were retained without jeopardizing the hardware safety.

TEST INSTRUMENTATION

The measurements taken to detect the effects of the combustion instability can be divided into two categories: propulsion and structure.

The engines used for the bomb tests contained ports and fittings to measure much more than the standard instrumentation program. Because the pressure oscillations generated by the instability are transient, special instruments were used which were capable of sensing very high frequency disturbances. Water-cooled capacitance gauge and strain gauge type pressure transducers were used. Instruments to measure the pressure wave propagation were placed at various points in the oxidizer and fuel feed system of the engine. Also, pressure transducers were located upstream of the engine turbopump inlet in the feedlines between the tank and the engine. Similar measurements were placed in the propellant feedlines of adjacent engines to determine if pressure interchange through the tank bottoms occurred. Crystal oscillator vibration instruments were placed on the engine thrust chamber to measure vibration levels in the vertical (thrust application) direction and the horizontal direction. The same type of vibration measurements were located in the feedlines, turbopump inlets, and thrust chamber exits. No special vibra-

tion instruments were placed on the adjacent engines. There were already several accelerometers required by the standard stage measurement program. To correlate the single engine test data with the clustered engine stage data, measurement location and transducer type were consistent.

Recorders used to store the transducer outputs included Beckman Digital Recorders, oscillographs, direct inking graphic recorders, and magnetic tape units. These devices satisfactorily covered the frequency spectrum encountered.

The structural measurements complemented those on the propulsion system. They consisted of strain gauges and vibration accelerometers to monitor and record the response of the stage structure. A combination of axial and vesseette gauges were used on the base region of the thrust support beams to measure the increased thrust levels and thrust oscillation frequency. For recording abnormal vibration, a total of fifty-five accelerometers were used in an area below the tanks and lower thrust structure.

TEST RESULTS

Four tests were conducted; one test during which the engine in position 7 was disturbed and three tests where both positions 1 and 7 engines were bombed. This yielded seven sets of data. In all cases, the pressure oscillations generated by the explosion of the bomb were damped within the 100 millisecond time criteria established before the series. An automatic device would have terminated the test had it taken longer than 100 milliseconds to subside. Structural and engine mounted measurements taken during the instability tests are summarized below:

TABLE 1. MEASURED DATA COMPARISON

INDICATOR	STRUCTURE	ENGINE
MAXIMUM THRUST INCREASE (PERCENT)	31-51	43-66
INSTABILITY PERIOD (MSEC)	15-31	27-48
DISTURBANCE FREQUENCY (CPS)	133-154	145-155

The structural response to the shock was very localized and limited to the member attaching directly to the engine. No structural failures occurred

nor were structural limits exceeded. The vibration induced in the feed system propagated to the extent that it was felt by all pressure and vibration measurements on engines 1 and 7. There was no evidence that the fluid pressure wave contained sufficient energy to be transmitted to other engines. No vibration coupling of the feed system-structure-engine was detected as evidenced by the very short damping time. A typical thrust and structural disturbance is shown in figure 7. The structural curve shows the initial response was compression. However, some structural members underwent tension first, followed by compression.

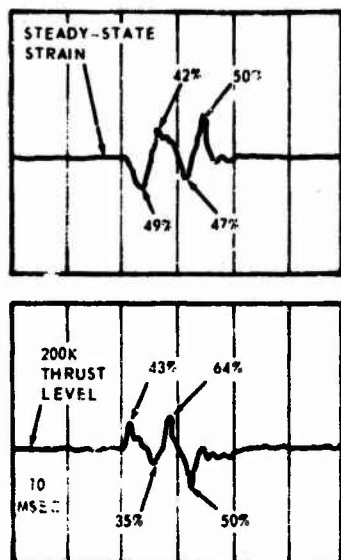


Fig. 7 - Typical thrust and structural oscillations

GENERAL CONCLUSIONS

The practice of stability rating an injector or engine configuration is not new and has become an accepted part of engine development testing. However, the test series described in the previous pages marks the first time an entire flight stage was tested for its combustion instability characteristics. Additionally, the flight worthiness of the stage was unaltered by this non-destructive means of testing.

The previous mathematical computer model of the S-IB Stage was formulated from analytical studies supplemented by non-firing dynamic shake tests of the stage. The instability tests afforded a means of energy input to excite the

stage structure and feedlines which was not obtainable in the dynamic shake tests. They served to verify and improve the structural math model.

Because the stage response to engine instability was quite different than the single engine test stand configuration, the practice of requiring that engines be inherently stable, as a design criteria, should be extended to include the stage design as well. The stage structure must be capable of accepting the thrust and frequency of the combustion instability produced by the engine without coupling or otherwise supporting the instability.

ACKNOWLEDGMENTS

The author wishes to acknowledge the assistance of Mr. J. K. Patterson, now of TRW Systems, Houston, Texas and Mr. J. R. Packard, Chrysler Space Division, Huntsville, Alabama.

DYNAMIC ANALYSIS OF A HIGH-SPEED LINKLESS AMMUNITION CONVEYOR SYSTEM

C. B. Basye and B. R. Scheller
Electronics and Space Division
Emerson Electric Company
St. Louis, Missouri

A dynamic analysis of the XM-53 conveyor feed system for the AH-56A Cheyenne helicopter has been completed. This feed system is required to transport ammunition through flexible chutes at a variety of chosen firing rates. Distributed friction along the conveyor was considered by utilizing an equation which related the load buildup resulting from the conveyor being pulled around a curved surface ("capstan" effect). Distributed mass along the conveyor was neglected, but appropriate mass was lumped with sprocket moments of inertia to account for conveyor mass. Results of the analysis compare favorably with available experimental information. Dynamic conveyor loads and power requirements were determined from the analysis. Effects of different coefficients of friction were evaluated. Effects of torsional flex shaft stiffness on natural frequencies and on dynamic response were also evaluated.

INTRODUCTION

The XM-53 nose mounted subsystem for the AH-56A Cheyenne helicopter provides installation and aiming means for the rotating six barrel 7.62mm machine gun. Linkless ammunition is stored in a vertically disposed magazine approximately 15 feet aft of the turret. The "linkless" conveyor system which transports ammunition to the gun is an integral part of the total weapon system. The conveyor is thus used for succeeding complements of ammunition, in contrast to "linked" ammunition systems where conveyor elements are discarded as rounds are fired. Travel limits for the gun are $+120^\circ$ in azimuth, 18° in elevation, and 70° in depression. Quadruple firing rates of 750, 1500, 3000, and 6000 shots per minute are provided for the weapon. Thus the conveyor feed system is required to transport the ammunition through flexible chutes at a variety of chosen firing rates.

Developmental progress relative to reliable performance regarding rate of fire and time to reach rate was slower

than desired. To accelerate this progress, and to increase the knowledge of dynamic subsystem behavior, an analysis of the conveyor feed system was performed.

Fig. 1 is a photograph of the AH-56A Cheyenne helicopter in flight. The XM-53 weapon is seen protruding from the nose of the aircraft.

Fig. 2 illustrates some of the component parts of the XM-53 subsystem. The vertical cylindrical ammunition drum is at the rear of the photo with the gun at the left foreground. The gun feeder is immediately under the gun. The long fixed polycarbonate conveyor chute is visible in the right foreground.

Fig. 3 is similar to Fig. 2. The streamlined cover is on the turret in Fig. 3, and the double sprocket (J_2 of Fig. 6) is visible at the bottom of the ammunition drum. The forward part of the polycarbonate conveyor chute has been removed in Fig. 3. Both the feed and return sides of the conveyor are enclosed in this polycarbonate chute.



Fig. 1 - AH-56A Cheyenne

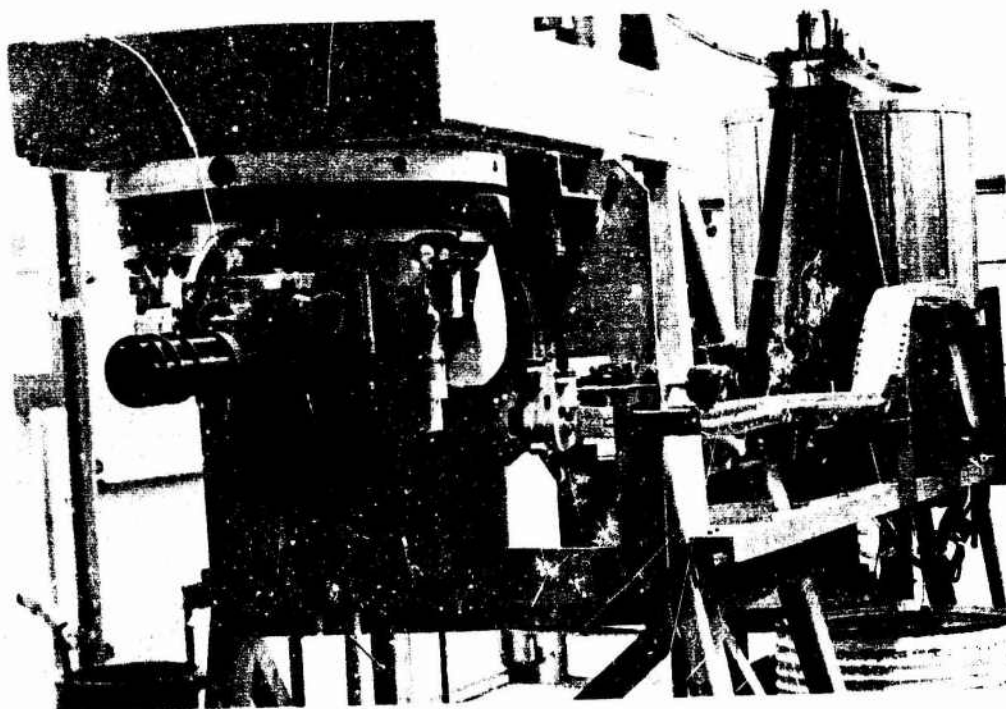


Fig. 2 - XM-53 subsystem

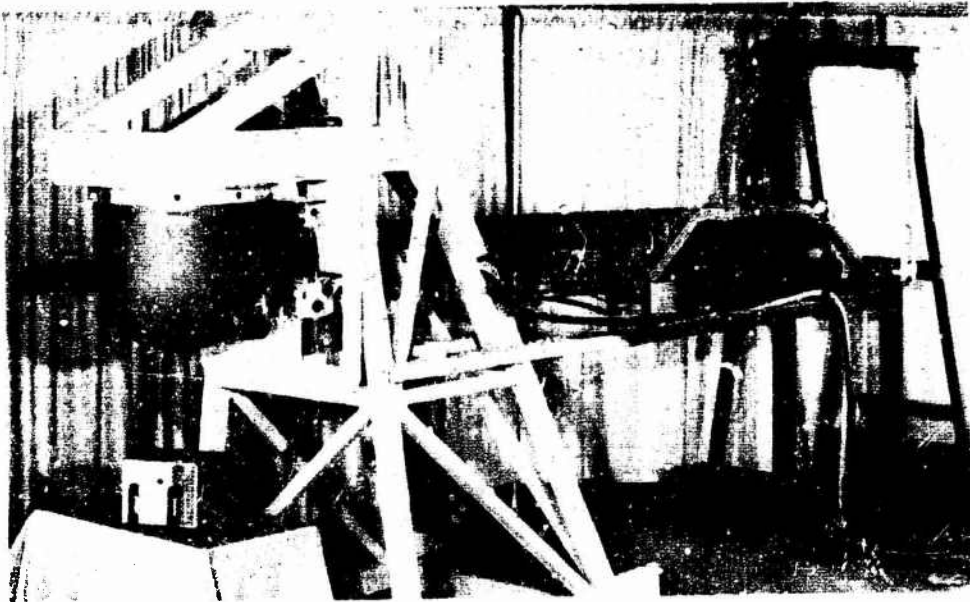


Fig. 3 - XM-53 subsystem with turret cover installed



Fig. 4 - XM-53 subsystem, left side view

Fig. 4 is a left side view of the XM-53 subsystem. The main power transmission shaft is visible in the left foreground. Power to drive the gun is transmitted through this main shaft and through the flexible shaft which is in the upper center of the photograph. The subsystem is driven by a single electric motor mounted inside the ammunition drum.

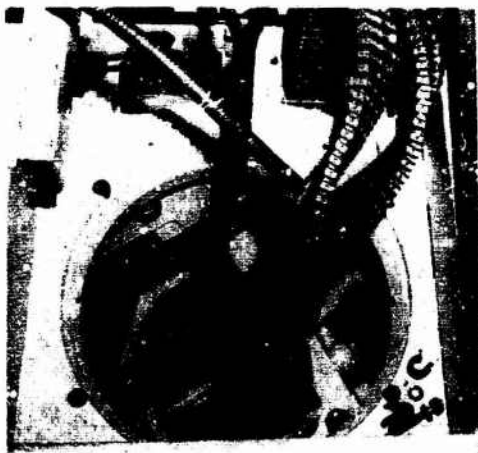


Fig. 5 - Forward flexible chute

Fig. 5 is a view looking down on the top of the turret. The complicated geometrical paths which the conveyor has to assume as the weapon is traversed through azimuth and elevation changes are illustrated here. Pictured are the flexible forward conveyor feed and return chutes when the weapon is rotated 120° left in azimuth. Also shown is the shaft housing enclosing the flexible shaft which provides power for the weapon-feeder combination.

ANALYSIS

Fig. 6 is a schematic of the XM-53 conveyor feed system. This schematic was used in deriving the equations of motion of the system. The descriptions in Table 1 apply to the schematic and to the analysis.

The driving torque T_p , on Fig. 6 shown acting on inertia J_1 , is furnished by the drive motor which powers the complete system. This motor is inside the ammunition drum of Fig. 2. The inertia J_1 includes the motor inertia, gearing, and the inertia of the ammunition and rotating drum com-

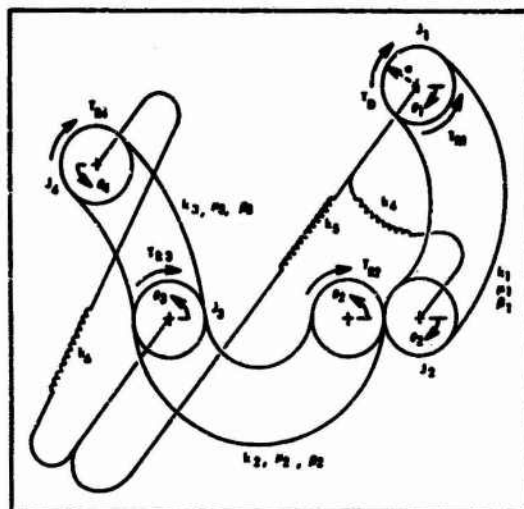


Fig. 6 - XM-53 conveyor feed system schematic

ponents. Thus the angular position function θ_1 gives the angular position of the motor, drum, gearing, and conveyor sprocket adjacent to the drum.

The inertia J_1 is much larger than the other three inertias, J_2 , J_3 , and J_4 . The shaft k_4 is a flexible shaft connecting inertias J_1 and J_2 , and the aft loop of the conveyor (k_1 area) connects these same two inertias.

The double sprocket, J_2 of Fig. 6, is visible at the aft end of the polycarbonate chute in Fig. 3. The long conveyor section enclosed in the polycarbonate chute of Figs. 2 and 3 is designated k_2 in Fig. 6. The conveyor section designated k_3 in Fig. 6 is enclosed in the flexible feed and return chutes of Fig. 5. The flexible shaft visible in Figs. 4 and 5 is designated as k_6 of Fig. 6. The shaft designated as k_5 of Fig. 6 consists of a flexible shaft adjacent to the drive motor in series with the long main power transmission shaft shown in Fig. 4.

The distributed friction along the conveyor was considered by utilizing an equation which related the load buildup resulting from the conveyor being pulled around a curved surface ("capstan" effect). The distributed mass along the conveyor was neglected, but appropriate mass was lumped with the sprocket moments of inertia to account for conveyor mass.

TABLE 1

Notation

k_1, k_2, k_3	Spring rates of the conveyor in the aft, polycarbonate, and forward flexible sections, respectively.
k_4, k_5, k_6	Torsional spring constants of appropriate system flex and line shafts.
J_1, J_2, J_3, J_4	Appropriate inertias lumped at the sprockets in drum conveyor transfer unit, double sprocket location, cartridge drive, and feeder-gun area, respectively.
$\theta_1, \theta_2, \theta_3, \theta_4$	Angular position functions at the four sprocket locations.
μ_1, μ_2, μ_3	Friction coefficients between the conveyor and the appropriate guidance surfaces.
$\beta_1, \beta_2, \beta_3$	Angle of contact between the conveyor and the conveyor track in the appropriate area. For instance, β_2 , in the polycarbonate chute, is about 180° , or π radians, when all of the angular bends of the polycarbonate chute are accounted for.
T_D	Driving torque for the conveyor.
$T_{R1}, T_{R2}, T_{R3}, T_{R4}$	Periodic resistance torques at each sprocket. These occur each time a conveyor element contacts a sprocket.

The equations of motion for this four degree of freedom system in matrix form are

$$[M]\{\ddot{\theta}\} + [K]\{\theta\} = \{F^1\} + \{F^2\} + \{F^3\} \quad (1)$$

where

$$[M] = \begin{bmatrix} J_1 & 0 & 0 & 0 \\ 0 & J_2 & 0 & 0 \\ 0 & 0 & J_3 & 0 \\ 0 & 0 & 0 & J_4 \end{bmatrix}, \quad (2)$$

$$\{\ddot{\theta}\} = \begin{bmatrix} \ddot{\theta}_1 \\ \ddot{\theta}_2 \\ \ddot{\theta}_3 \\ \ddot{\theta}_4 \end{bmatrix}, \quad \{\theta\} = \begin{bmatrix} \theta_1 \\ \theta_2 \\ \theta_3 \\ \theta_4 \end{bmatrix}, \quad \text{and}$$

$$[K] = \begin{bmatrix} k_{11} & k_{12} & k_{13} & k_{14} \\ k_{21} & k_{22} & k_{23} & k_{24} \\ k_{31} & k_{32} & k_{33} & k_{34} \\ k_{41} & k_{42} & k_{43} & k_{44} \end{bmatrix} \quad (3)$$

In Eq. (3),

$$k_{11} = k_4 + k_5 + k_1 a^2 + k_1 a^2 e^{\mu_1 \beta_1},$$

$$k_{12} = k_{21} = -k_4 - k_1 a^2 - k_1 a^2 e^{\mu_1 \beta_1},$$

$$k_{13} = k_{31} = -k_5,$$

$$k_{14} = k_{41} = k_{24} = k_{42} = 0,$$

$$k_{22} = k_4 + k_1 a^2 + k_2 a^2 + k_1 a^2 e^{\mu_1 \beta_1} + k_2 a^2 e^{\mu_2 \beta_2},$$

$$k_{23} = k_{32} = -k_2 a^2 - k_2 a^2 e^{\mu_2 \beta_2},$$

$$k_{33} = k_5 + k_6 + k_2 a^2 + k_3 a^2 + k_2 a^2 e^{\mu_2 \beta_2} + k_3 a^2 e^{\mu_3 \beta_3}, \quad \text{and}$$

$$k_{34} = k_{43} = -k_4 - k_6 - k_3 a^2 - k_3 a^2 e^{\mu_3 \beta_3}.$$

The forcing function, $\{F^1\}$, of Eq. (1) is

$$\{F^1\} = \begin{bmatrix} T_D + aT(1 - e^{\mu_1 \beta_1}) \\ aT(2 - e^{\mu_1 \beta_1} - e^{\mu_2 \beta_2}) \\ aT(2 - e^{\mu_2 \beta_2} - e^{\mu_3 \beta_3}) \\ aT(1 - e^{\mu_3 \beta_3}) \end{bmatrix} \quad (4)$$

where T is the conveyor preload and T_D is the driving torque. The forms of the matrix entries in Eqs. (3) and (4) were derived by drawing free body diagrams of the appropriate sprockets and applying Newton's Law. The static flat belt frictional relationship was utilized. A correction for the inertial effect of the mass of the belt as the belt moved around curved paths was considered but was of small magnitude and thus was not used. The same preload was assumed to exist in all sections of the conveyor. The driving torque is the torque necessary to overcome the resistance of the conveyor being moved through the system and does not include the torque required to bring the system up to speed.

The forcing function, $\{F^2\}$, of Eq. (1) is

$$\{F^2\} = \begin{bmatrix} A (1 - \cos \frac{2\pi}{\tau} t) \\ 0 \\ 0 \\ 0 \end{bmatrix} \quad (5)$$

where

$$A = \left[\frac{J_1 + J_2 + J_3 + J_4}{\tau} \right] \left[\dot{\theta}_{ss} \right]$$

and t is time with

τ = the accelerating time and
 $\dot{\theta}_{ss}$ = steady state angular velocity corresponding to the particular firing rate.

$\{F^2\}$ is considered to be zero after the accelerating time is over.

The forcing function, $\{F^3\}$, of Eq. (1) is

$$\{F^3\} = \begin{bmatrix} (K_4 + 2.06T + 14)(1 - \cos 6\dot{\theta}_{ss}t) \\ (-0.82T - 5.4)(1 - \cos 6\dot{\theta}_{ss}t) \\ (-0.97T - 5.7)(1 - \cos 6\dot{\theta}_{ss}t) \\ (-K_4 - 0.27T - 2.9)(1 - \cos 6\dot{\theta}_{ss}t) \end{bmatrix} \quad (6)$$

$\{F^3\}$ is considered to be zero during the accelerating time for reasons of mathematical convenience. $\{F^3\}$ consists of the resistance torques at each sprocket (T_{R1} , T_{R2} , T_{R3} , and T_{R4} of Fig. 6) which result from the conveyor elements contacting the six-toothed sprockets. The magnitudes of these torques were based on experimental data and were functions of the preload, T . The factor K_4 accounts for the torque necessary to drive a round through the feeder and weapon.

Damping as such was not incorporated in the analysis, but the influential distributed friction along the con-

veyor was utilized.

The equations of motion for this four degree of freedom system were solved by normal mode matrix methods. See References [1], [2], or [3]. Four natural frequencies, one zero frequency and three non-zero frequencies, result. The solutions for the angular position functions during the accelerating, or starting, time are of the form:

$$\theta_i = A_i + C_i t^2 + D_i \cos \frac{2\pi t}{\tau} + F_i \cos \omega_2 t + G_i \cos \omega_3 t + H_i \cos \omega_4 t \quad (7)$$

where i takes on the values 1, 2, 3, and 4 for the four sprockets and τ is the acceleration time. The solutions following the accelerating phase are of the form:

$$\theta_i = J_i + K_i t + L_i \cos 6\dot{\theta}_{ss}t + M_i \cos \omega_2 t + N_i \sin \omega_2 t + O_i \cos \omega_3 t + P_i \sin \omega_3 t + Q_i \cos \omega_4 t + R_i \sin \omega_4 t \quad (8)$$

where i again takes on values 1, 2, 3, and 4. The symbols A_i , C_i , ---, R_i are constants in these equations.

RESULTS

Table 2 includes analytical results of the XM-53 conveyor feed system analysis when appropriate values are used for the various parameters of the system. In other words, Table 2 is indicative of the system as is. It is important to realize, however, that the maximum loads predicted in the various sections of the conveyor are based on an undamped analysis. Effects of friction have been included, but effects of damping associated with conveyor oscillations have not been included. It is certain that these predicted maximum loads are higher than actually occur. These predicted loads reflect conveyor loads due to preload, friction buildup (capstan effect), and loads due to conveyor stretching as a function of sprocket oscillation. It is this latter load component which contributes more in these analytical results (due to absence of damping in the equations) than actually exists in the "real world" conveyor.

Table 3 illustrates predicted results if the k_4 -flex shaft of Fig. 6 is geared up so as to rotate six times its present speed. The spring constant k_4 would increase from its present value of 80 in.-lb./radian to six-squared times this, or 2880 in.-lb./radian.

TABLE 2

Analytical Results

μ_2 , Polycarbonate Chute Friction Coefficient (k_2 area) = 0.5
 k_4 , Flex Shaft Spring Constant = 80 in.-lb./radian

Rate, spm	Preload, T, lb.	Natural Frequency, rad/sec			Forcing Freq., rad/sec (6 δ_{ss})	Undamped Predicted Maximum Conveyor Load, lb.			Power Required for Con- veyor and Gun, HP
		ω_1	ω_2	ω_3		k_1 area	k_2 area	k_3 area	
750	10	90.3	530.1	127.2	78.5	120	136	45	0.43
750	2	90.3	530.1	127.2	78.5	43	42	12	0.15
900	10	90.3	530.1	127.2	94.2	195	204	45	0.51
900	2	90.3	530.1	127.2	94.2	101	94	14	0.18
1500	10	90.3	530.1	127.2	157.1	66	93	50	0.85
1500	2	90.3	530.1	127.2	157.1	17	22	17	0.29
1760	10	90.3	530.1	127.2	184.3	65	93	48	1.00
1760	2	90.3	530.1	127.2	184.3	16	21	14	0.35
1760	4	90.3	530.1	127.2	184.3	28	38	23	0.51
3000	10	90.9	530.7	130.1	314.2	73	99	45	1.71
3000	2	90.9	530.7	130.1	314.2	19	23	11	0.59
5300	10	90.9	530.7	130.1	555.0	71	99	47	3.26
5300	2	90.9	530.7	130.1	555.0	18	23	12	1.04
6000	2	90.9	530.7	130.1	628.3	18	23	11	1.17

TABLE 3

Analytical Results

μ_2 , Polycarbonate Chute Friction Coefficient (k_2 area) = 0.5
 k_4 , Flex Shaft Spring Constant = 2880 in.-lb./radian

Rate, spm	Preload, T, lb.	Natural Frequency, rad/sec			Forcing Freq., rad/sec (6 δ_{ss})	Undamped Predicted Maximum Conveyor Load, lb.			Power Required for Con- veyor and Gun, HP
		ω_1	ω_2	ω_3		k_1 area	k_2 area	k_3 area	
750	10	318.8	530.1	127.1	78.5	18	55	45	0.43
750	2	318.8	530.1	127.1	78.5	4	12	12	0.15
1500	10	318.8	530.1	127.1	157.1	18	59	52	0.85
1500	2	318.8	530.1	127.1	157.1	4	16	17	0.29
3000	10	320.4	530.7	130.1	314.2	44	77	45	1.71
3000	2	320.4	530.7	130.1	314.2	17	24	12	0.59
6000	10	320.4	530.7	130.1	628.3	17	53	44	3.44
6000	2	320.4	530.7	130.1	628.3	3	12	11	1.17

Table 4 illustrates the predicted effects of leaving the k_4 shaft as is, but reducing the friction coefficient in the polycarbonate chute (μ_2) from its presently assumed value of 0.5 to a value of 0.1.

Table 5 includes analytical predictions if both changes were incorporated, or if the timing shaft is stiffened up to a value of 2880 in.-lb./radian and the polycarbonate chute friction coefficient reduced to a value of 0.1.

TABLE 4

Analytical Results

μ_2 , Polycarbonate Chute Friction Coefficient (k_2 area) = 0.1
 k_4 , Flex Shaft Spring Constant = 80 in.-lb./radian

Rate, spm	Preload, T, lb.	Natural Frequency rad/sec			Forcing Freq., rad/sec (ω_{ss})	Undamped Predicted Maximum Conveyor Load, lb.			Power Required for Con- veyor and Gun, HP
		ω_1	ω_2	ω_3		k_1 area	k_2 area	k_3 area	
750	10	84.0	529.0	126.9	78.5	150	60	42	0.26
750	2	84.0	529.0	126.9	78.5	71	26	12	0.11
1500	10	84.0	529.0	126.9	157.1	38	21	50	0.52
1500	2	84.0	529.0	126.9	157.1	15	7	17	0.23
3000	10	84.5	529.7	129.8	314.2	32	20	43	1.05
3000	2	84.5	529.7	129.8	314.2	12	6	11	0.46
6000	10	84.5	529.7	129.8	628.3	34	21	42	2.09
6000	2	84.5	529.7	129.8	628.3	12	6	11	0.91

TABLE 5

Analytical Results

μ_2 , Polycarbonate Chute Friction Coefficient (k_2 area) = 0.1
 k_4 , Flex Shaft Spring Constant = 2880 in.-lb./radian

Rate, spm	Preload, T, lb.	Natural Frequency rad/sec			Forcing Freq., rad/sec (ω_{ss})	Undamped Predicted Maximum Conveyor Load, lb.			Power Required for Con- veyor and Gun, HP
		ω_1	ω_2	ω_3		k_1 area	k_2 area	k_3 area	
750	10	317.0	529.1	126.8	78.5	15	16	43	0.26
750	2	317.0	529.1	126.8	78.5	3	4	12	0.11
1500	10	317.0	529.1	126.8	157.1	15	17	50	0.52
1500	2	317.0	529.1	126.8	157.1	3	5	17	0.23
3000	10	318.7	529.7	129.8	314.2	51	29	43	1.05
3000	2	318.7	529.7	129.8	314.2	22	10	11	0.46
6000	10	318.7	529.7	129.8	628.3	14	16	42	2.09
6000	2	318.7	529.7	129.8	628.3	3	4	11	0.91

Fig. 7 illustrates the effect of preload on the relative windup of the k_4 shaft. It is noted that the lowest natural frequency (See Table 2) is 90.3 divided by 2π , or 14.4 Hz. These oscillations illustrated on Fig. 7 are predominantly at this low natural frequency.

Fig. 8 compares the analytical result for a preload of 4 lb. with experimental data. Firing rates for

both the experimental and analytical curves were 1760 shots per minute.

Figs. 9 and 10 include an experimental run (solid line) at the nominal 6000 rate. The actual rate was approximately 5300 shots per minute. Also shown on Figs. 9 and 10 are analytically predicted results (dashed lines), with preloads of 2 and 10 lb., at a rate of 5300 spm. Although the analytical result based on 2 lb. preload is closer to

the experimental result in the post-accelerating time period, it is noted that a peak angular windup during acceleration occurs which is similar to that predicted when a 10 lb. preload is utilized in the analytical study.

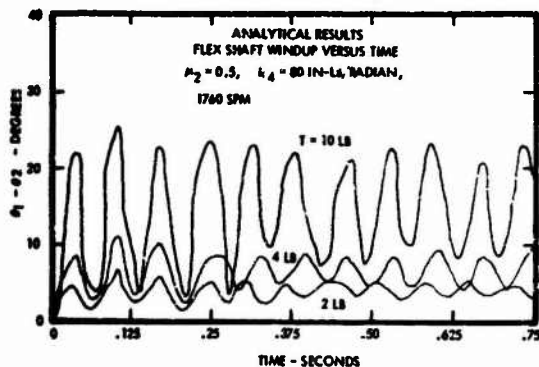


Fig. 7 - Effect of preload

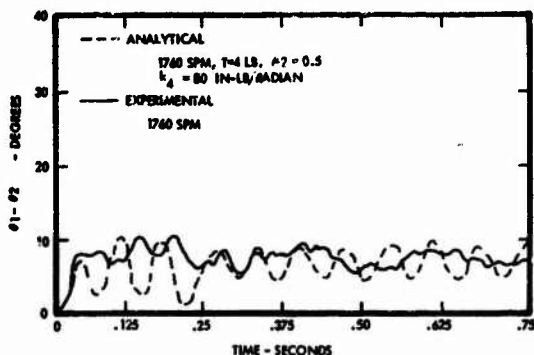


Fig. 8 - Flex shaft windup versus time

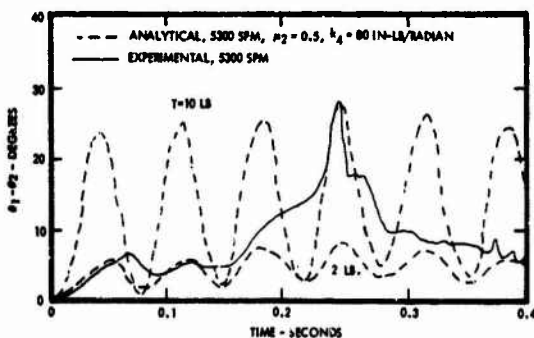


Fig. 9 - Flex shaft windup versus time during system startup

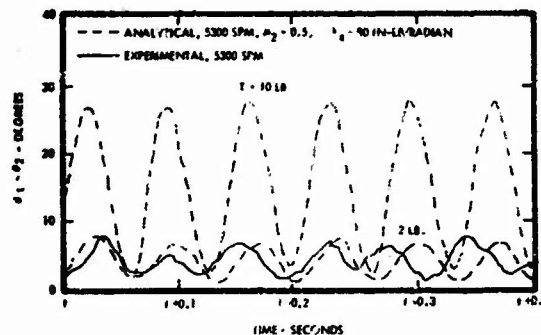


Fig. 10 - Flex shaft windup versus time after startup

Other experimental data were measured and compared with analytical predictions. Examples of these data included main power shaft torque and the angular velocities of inertia J₃, the gun, drive motor, and main power shaft as functions of time. Although not included herein, comparisons of these data with analytical predictions were satisfactory.

DISCUSSION OF RESULTS

Primary questions involved in this ammunition conveyor study include:

1. Will the conveyor system operate satisfactorily without jamming?
2. Are the loads sufficiently low so that satisfactory life will be realized in field operation? Not only must early fractures be guarded against, but the conveyor loads must be kept low enough to avoid fatigue failures.
3. Is excessive power required to drive the conveyor?

In connection with 1, above, it has been experimentally established that the XM-53 conveyor operates without jamming when appropriate preload is utilized. However, large preload has disadvantages as discussed herein, so conveyor dynamic behavior at lower preloads needs to be investigated.

As far as conveyor loads are concerned, the total load is considered to consist of the following:

1. Preload,
2. Spring load (function of wind-up between adjacent sprockets),
3. Friction buildup load (capstan effect), and

4. Stress waves and/or inertia loads.

The first three load categories are the ones with which this paper is concerned. The latter load category has been considered in detail by Maier [4]. Dr. Maier concluded that under simplifying assumptions of a straight belt section, no friction, and fully synchronous sprocket motion, a force of approximately 5 lb. would be induced in the XM-53 conveyor due only to the stress wave phenomenon.

Returning to the consideration of conveyor loads due to preload, relative sprocket motion, and friction buildup, it is enlightening to inspect Fig. 9. A relative windup of approximately 28° occurred during the acceleration phase of this experimental run. For a preload of 10 lb., it is calculated that the force in the conveyor is just over 70 lb. for this situation. If 5 lb. is added due to the stress wave effect, it is apparent that the load in the conveyor is close to the yield load of 85 lb. As noted earlier, although the post-acceleration experimental data agree much more closely with the 2 lb. preload analytical results, the maximum angular windup agrees closely with the 10 lb. preload analytical result.

As far as power requirements are concerned, the entries in Tables 2, 3, 4, and 5 illustrate the dependence of power on preload and friction level.

Two other points are pertinent as far as discussion of the results are concerned. One is the tremendous influence of resonance effects, and the other is the influence of damping. From Table 2, it is noted that the lowest natural frequency is 90.3 radians/second, or 14.4 Hz. At a firing rate of 750 spm, the forcing frequency due to conveyor elements contacting sprockets is 78.5 radians/second while at the 900 spm rate this forcing frequency is 94.2 radians/second. Note that the maximum predicted force in the aft conveyor loop at a preload of 10 lb. increases from 120 to 195 lb. due to this near resonant condition as the firing rate changes from 750 to 900 spm.

Of course, the forces cannot be as high as predicted, since the conveyor yields at 85 lb., but it is again emphasized that these maximum predicted forces are based on an undamped analysis as far as oscillations of the conveyor are concerned. However, examination of Figs. 8, 9, and 10 illustrates that this undamped analysis

gives reasonable qualitative results when compared with experimental results. It is observed that the analytical results for a 10 lb. preload indicate a larger periodic excursion than actually occurs. Further analytical investigation, with damping considered and therefore more technically involved, would lead to closer agreement between theory and experiment.

CONCLUDING REMARKS

1. The maximum conveyor loads increase as conveyor preload increases. To illustrate this point, the maximum loads in various sections of the conveyor at 10 lb. preload are calculated to be from 2 to 4 times the comparable maximum loads at 2 lb. preload.
2. Approximately three times as much power is required to run the conveyor system at 10 lb. preload as at 2 lb. preload unless friction levels are low. When friction levels are low, the effect of preload on power requirement is less pronounced, but power requirement still increases with preload.
3. Replacement of the k4 flex shaft by a shaft 36 times as stiff would decrease the maximum loads in the conveyor from their present value to lower levels. See Tables 2 and 3. However, large loads would still exist primarily at the 3000 spm rate because of the proximity of the ω_1 natural frequency and the forcing frequency at the 3000 spm rate. (320 versus 314 radians/second.)
4. Replacement of the polycarbonate chute by a chute with lower friction would also reduce the maximum conveyor loads. See Tables 2 and 4. However, if this action were taken without also stiffening up the k4 shaft, large loads would still exist at the 750 spm rate, again due to the proximity of a forcing frequency and a natural frequency.
5. It is apparent that low preload is desirable as far as keeping conveyor loads down is concerned.
6. Utmost care must be exercised to keep friction levels low in all parts of the conveyor system.
7. Early determination of component dynamic behavior is important for future analyses.

Torque-time characteristics of power sources during acceleration should be known in some detail. Investigation of various analytical damping simulations is definitely desirable.

REFERENCES

1. W. C. Hurty and M. F. Rubinstein, Dynamics of Structures, Prentice-Hall, Englewood Cliffs, N. J., 1964.
2. F. S. Tse, I. E. Morse, and R. T. Hinkle, Mechanical Vibrations, Allyn and Bacon, Boston, Mass., 1963.
3. W. T. Thomson, Vibration Theory and Applications, Prentice-Hall, Englewood Cliffs, N. J., 1965.
4. K. W. Maier, "Analysis of the Forces Induced in the XM-53 Conveyor Belt", Math + Metrik, Cheshire, Conn., 1969.

STRESS WAVES IN MULTILAYERED CYLINDERS AND CONICAL FRUSTRUMS

Jackson C. S. Yang and A. E. Seigel
U. S. Naval Ordnance Laboratory
White Oak, Maryland

The purpose of this paper is to report on an investigation of the spallation problem of multilayered conical structures by analyzing the propagation of elastic stress waves in multilayered cylinders and conical frustrums using the method of characteristics. Two approaches were utilized in the analysis of the propagation of elastic stress waves. The conical frustrum was first analyzed as a multilayered cylinder with step changes in area and varying impedances and then a numerical method was utilized to solve the characteristic equation as the area of the conical frustrum is changing continuously. Both approaches were effected by use of electronic computer programs.

The programs were verified as being correct and functioning properly by a comparison with experimental strain-time results in truncated cones impacted by spheres observed by V. Kenner and W. Goldsmith [1].

LIST OF SYMBOLS

A_1	cross-sectional area of (1)th layer	φ	impact function
a	Lagrangian coordinate	F	force
g	shift rate		
I_1	impedance of (1)th layer		
L_1	length of (1)th layer		
t	time		
T	applied pulse length		
E	modulus of elasticity		
X	Eulerian coordinate		
u	particle velocity		
ϵ	engineering strain		
ρ	mass density		
σ	engineering stress		
$(\sigma_T)_{\max}$	maximum tensile stress		
σ_0	applied stress		

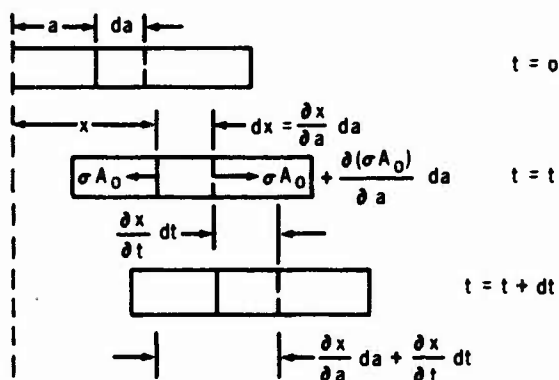
INTRODUCTION

A laboratory facility which has proved useful in the study of the aerodynamic behavior of vehicles is the ballistics range. In this type of facility small-scaled models of the vehicles of interest are shot from a gun into the range tube where their flight behavior may be observed. In recent years engineers have been required to design ballistics range models which are capable of being launched at hypersonic velocities for aerodynamic tests of ballistic missiles and spacecraft. At such velocities the designer is confronted with the dual problem of using materials which are structurally strong enough to withstand the severe loading conditions and materials which minimize the ablation of the missile nose due to aerodynamic heating. The spallation of many potential nose materials in developmental tests indicates that the analytical design tools presently in use are

inadequate; this spallation is evident in Fig. 1, which is an X-ray photograph taken of a cone model and sabot just after launch from the gun. The purpose of this paper is to report on an investigation of the spallation problem of multilayered conical structures by analyzing the propagation of elastic stress waves in multilayered cylinders and conical frustrums using the method of characteristics.

TECHNICAL DISCUSSION

The stress wave propagation theory used in this analysis was developed independently by T. von Karman [2] and G. I. Taylor [3] in 1942. It is a one-dimensional elastic-plastic theory used to determine the transient properties of solid materials under impulsive loading.



t = 0 unstrained
t = t strained
t = t + dt

The response of materials is governed by the equations of continuity and momentum which are given in the Lagrangian coordinate system as follows.

$$\frac{\partial u}{\partial a} = \frac{\partial \epsilon}{\partial t} \quad (1)$$

$$\frac{\partial u}{\partial t} = \frac{1}{\rho_0} \frac{d\sigma}{da} \quad (2)$$

The shift rate g , or speed of the disturbance is given by

$$g^2 = \frac{1}{\rho_0} \frac{d\sigma}{d\epsilon} \quad (3)$$

Defining the impact function φ as

$$d\varphi = g d\epsilon \quad (4)$$

it follows that

$$d\varphi = \frac{1}{\rho_0} \frac{d\sigma}{g} \quad (5)$$

From the above equations the characteristic equations may be written as follows.

$$\frac{\partial(u + \varphi)}{\partial t} + g \frac{\partial(u + \varphi)}{\partial a} = 0 \quad (6)$$

From calculus

$$\frac{d(u + \varphi)}{dt} = \frac{\partial(u + \varphi)}{\partial t} + \frac{\partial(u + \varphi)}{\partial a} \frac{da}{dt} \quad (7)$$

since the quantity $(u + \varphi)$ is a function of (a, t) . Thus, Eq. (6) is a one-dimensional elastic-plastic equation which indicates that the quantity $(u + \varphi)$ is constant when $da/dt = -g$. This property can be used to evaluate u and φ for the propagation of stress waves in solids, and the numerical technique has been illustrated by the example in Appendix A.

Multilayered Cylinders (Impedance Change)

In the case of multilayered cylinders interfaces exist where materials of different impedances are joined. The two assumptions used to solve for the properties across such interfaces are as follows.

$$u_A = u_B \quad (8)$$

and

$$F_A = F_B \quad (9)$$

where

$$F_1 = \varphi_1 \rho_1 g_1 A_1 \quad (10)$$

in the elastic region. Thus

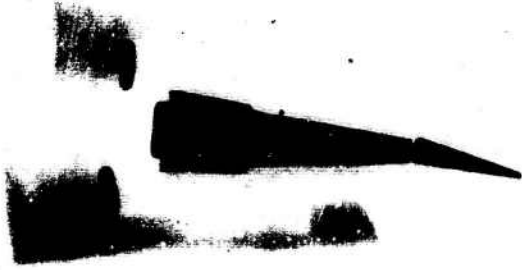
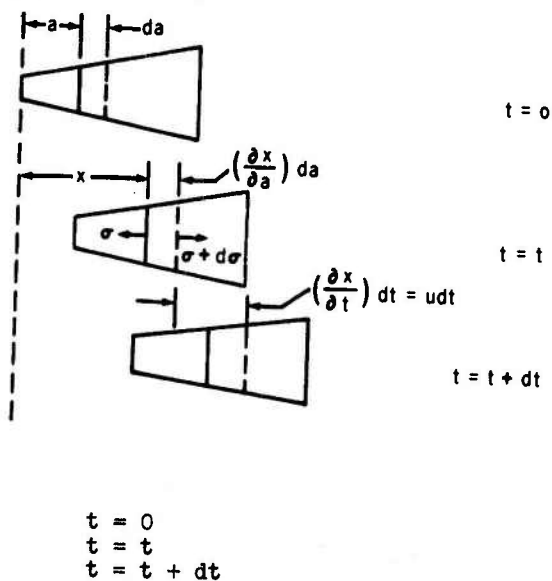


Fig. 1 X-ray photo of cone model and sabot just after launch

$$\varphi_A I_A = \varphi_B I_B \quad (11)$$

Figure 2 shows a typical ballistic model which may be analyzed using the above equations. The model has two interfaces with step impedance changes and three regions of continuously changing impedance. The regions of continuously changing area can be approximated by multilayered cylinders with step changes in area.



The equation of continuity remains the same as the bars with constant cross section. The momentum equation takes into account the varying cross section.

$$\frac{\partial u}{\partial a} = \frac{\partial \epsilon}{\partial t} \quad (12)$$

$$\frac{\partial u}{\partial t} = \frac{1}{\rho_0 A_0} \frac{\partial (\sigma A_0)}{\partial a} \quad (13)$$

The characteristic equations may be written as follows.

$$\frac{\partial (u+\varphi)}{\partial t} \mp g \frac{\partial (u+\varphi)}{\partial a} = \frac{\sigma}{\rho_0 A_0} \frac{\partial A_0}{\partial a} \quad (14)$$

The following notations were used to transform this equation into dimensionless form.

$$\bar{u} = \frac{u}{\varphi^*}, \quad \bar{\sigma} = \frac{\sigma}{\sigma^*}, \quad \varphi^* = \frac{\sigma^*}{\rho_0 g_e}$$

$$\bar{\varphi} = \frac{\varphi}{\varphi^*}, \quad \bar{a} = \frac{a}{a_0}$$

$$\bar{g} = \frac{g}{g_a}, \quad \bar{t} = \frac{t g_e}{a_0}$$

where $\sigma^* = \sigma_{\text{yield}}$

a_0 = initial length of bar

Therefore

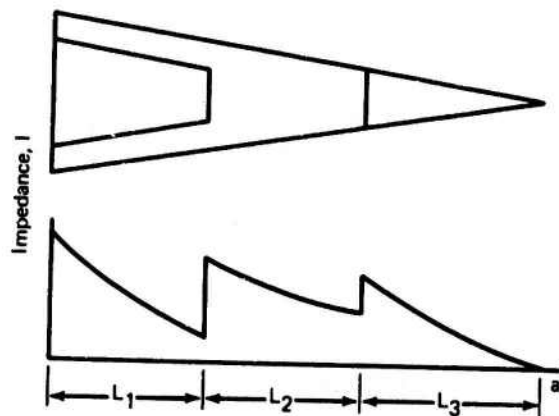


Fig 2 Conical ballistic model and impedance diagram

$$\frac{\partial(\bar{u}+\bar{\varphi})}{\partial t} + \bar{g} \frac{\partial(\bar{u}+\bar{\varphi})}{\partial \bar{a}} = \frac{\bar{\sigma}}{A_0} \frac{\partial A_0}{\partial \bar{a}} \quad (15)$$

For the elastic case

$$\bar{g} = 1, \quad \bar{\varphi} = \frac{\sigma}{\sigma^*} = \bar{\sigma}$$

$$\therefore \frac{\partial(\bar{u}+\bar{\varphi})}{\partial t} + \frac{\partial(\bar{u}+\bar{\varphi})}{\partial \bar{a}} = \frac{\bar{\sigma}}{A_0} \frac{\partial A_0}{\partial \bar{a}}$$

$$\frac{D(\bar{u}+\bar{\sigma})}{D\bar{t}} = \frac{\bar{\sigma}}{A_0} \frac{\partial A_0}{\partial \bar{a}}, \quad \frac{D\bar{a}}{D\bar{t}} = \pm 1 \quad (16)$$

The nondimensional characteristic equation for changing area may be written as follows:

$$\frac{D(\bar{u}+\bar{\sigma})}{D\bar{a}} = \mp \frac{\bar{\sigma}}{A_0} \frac{DA_0}{D\bar{a}}$$

The numerical technique to evaluate u and φ for the propagation of stress waves in cones has been illustrated by the example in Appendix B.

DISCUSSION OF RESULTS

A remote terminal multi-access computer was used in this analysis due to its availability and ease of operation. However, this system lacks the capacity for a thorough investigation for many of the problems capable of being solved by the program. A listing of the programs used in this analysis is given in Appendix C for the impedance approach and Appendix D for the continuous changing area approach. The programs were written in general, and they can give the complete stress-time history of multilayered conical frustrums for designated applied pulses.

Figure 3 gives the stress-time history for the midsection of a truncated cone experiencing an infinitely long unit input pulse. The specimen was approximated by twenty cylindrical layers of a homogeneous material with step changes in area (impedance change method). The response shows that the midsection experiences tension as the first reflection approaches the midsection. Also stress reversals occur as the first and second reflections pass the midsection.

The solution of this problem was also obtained by the continuous change in area method. Twenty points were used. The result was compared with the impedance change method; agreement was excellent and the two solutions were indistinguishable when plotted.

A drawing of the 5.38-degree truncated cone which Kenner and Goldsmith impacted with steel spheres is shown in Fig. 4. The cylindrical portion at the larger end was used to transmit and measure the input pulse. The sections where the strain-time histories were observed are indicated by the station numbers. The input strain pulse was approximated as

$$\epsilon = 0.320 \times 10^{-3} \sin^2(\pi t/35)$$

where

$$0 \leq t \leq 35.$$

The comparison of the approximated input strain with the experimental is also given in Fig. 4. The two methods of calculation were used; the truncated cone was approximated by 72 cylindrical layers with step changes in area, and for the second method a continuous change in area with 80 points. Again, the two analytical methods were in excellent agreement. The comparison of experimental to theoretical strain-time responses for Stations 1, 2, 3, 4, are given, respectively, by Figs. 5, 6, 7, 8. These figures show that the theoretical responses are in good agreement with the experimental responses.

CONCLUSION

The method of characteristics can be used to analyze the problem of spallation of multilayered cylinders and conical frustrums. Two electronic computer programs were developed to analyze the propagation of the elastic stress waves using two different approaches. Excellent agreement was achieved in the comparison of the theoretical to the experimental strain-time results observed by Kenner and Goldsmith in truncated cones. This comparison provides evidence that the programs are correct and functioning properly. However, the limited capacity of the computer system dictates the necessity of converting the programs to a larger computer prior to any extensive analysis of multilayered conical frustrums.

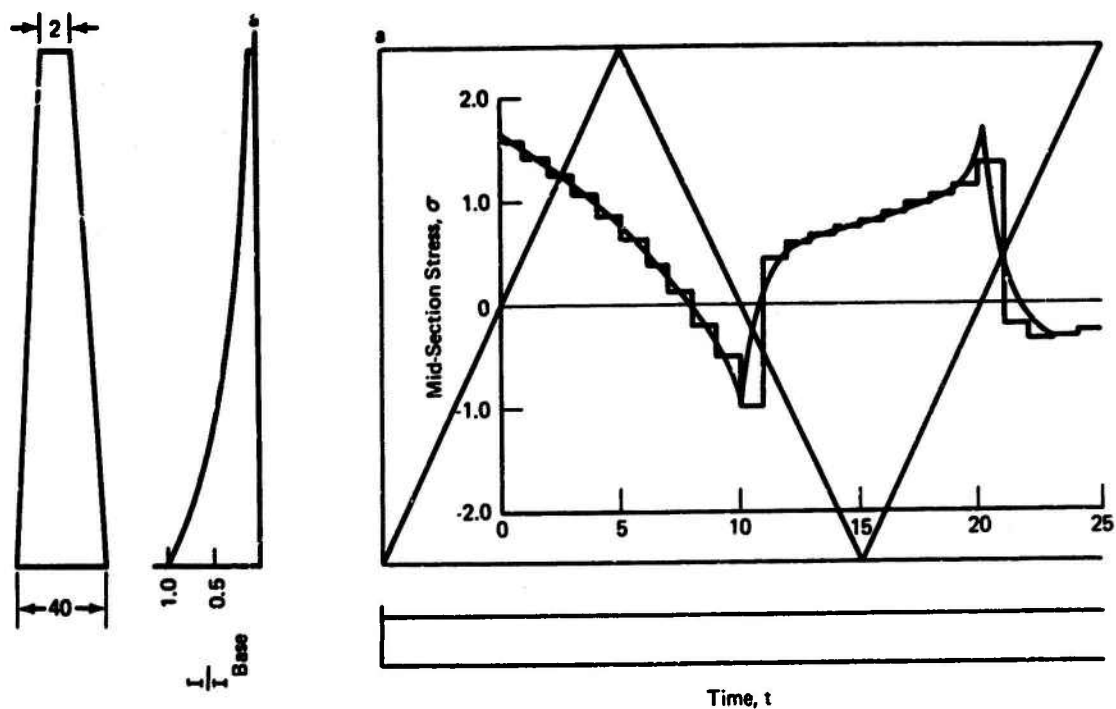


Fig. 3 Midsection stress vs time in a truncated cone for an infinitely long applied pulse

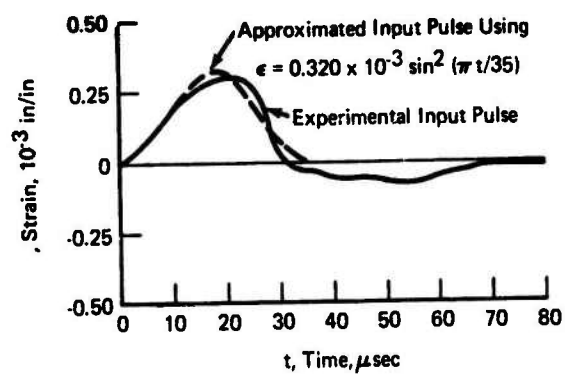


Fig. 4 Truncated 5.38-degree cone and applied strain pulse

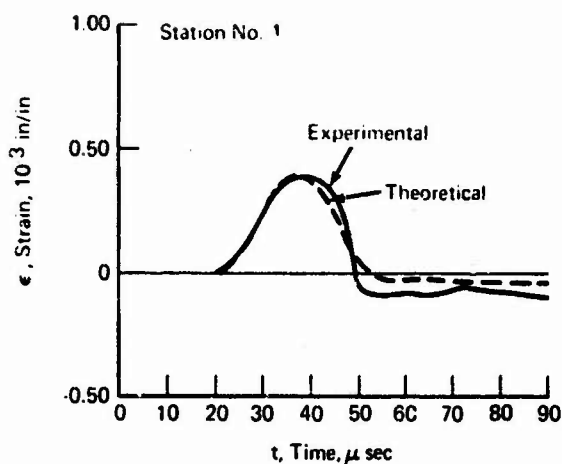


Fig. 5 Experimental and theoretical response vs time for the truncated 5.38-degree cone at Station No. 1

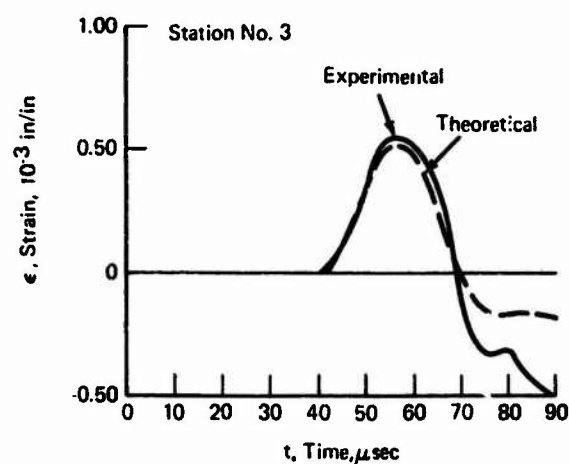


Fig. 7 Experimental and theoretical response vs time for the truncated 5.38-degree cone at Station No. 3

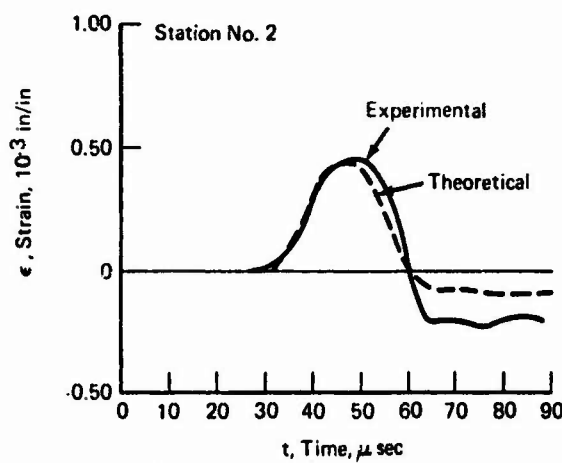


Fig. 6 Experimental and theoretical response vs time for the truncated 5.38-degree cone at Station No. 2

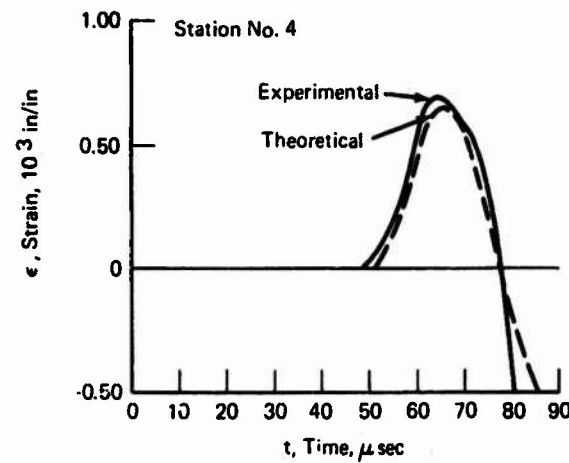


Fig. 8 Experimental and theoretical response vs time for the truncated 5.38-degree cone at Station No. 4

A preliminary analysis was made on a one-layered conical frustrum to gain some insight into its wave propagation properties. As mentioned previously, the structure goes into tension as the first reflection approaches the midsection, and stress reversals occur as the first and second reflections pass the midsection. A thorough consideration of such an investigation would be a significant contribution to the state of the art of the design analysis of ballistic models.

REFERENCES

1. V. H. Kenner and W. Goldsmith, "Elastic Waves in Truncated Cones," *Experimental Mechanics*, Vol. 8, No. 10, pp. 442-449, Oct 1968
2. T. von Karman, "On the Propagation of Plastic Deformation in Solids," NDRC Report A-29 (OSRD No. 365), 28 Jan 1942
3. G. I. Taylor, "The Plastic Wave in a Wire Extended by an Impact Load," R.C. Report No. 329, Jun 1942

APPENDIX A

Example of Solution Technique Using Method of Characteristics (Constant Cross Section)

The characteristic equation given by Eq. (6) indicates that the quantity $(U + \varphi)$ is constant when $\frac{da}{dt} = \mp g$. In

the elastic case the shift rate, g , is a constant. Thus the slope of the (+) g -lines in the a - t plane are constants as shown in the sketch below. If the properties in regions 1 and 2 are known, the properties in region 3 are determined as follows.

$$\text{Along the (+) } g\text{-line} \quad (A-1) \\ (U_1 - \varphi_1) = (U_3 - \varphi_3)$$

$$\text{Along the (-) } g\text{-line} \quad (A-2) \\ (U_2 + \varphi_2) = (U_3 + \varphi_3)$$

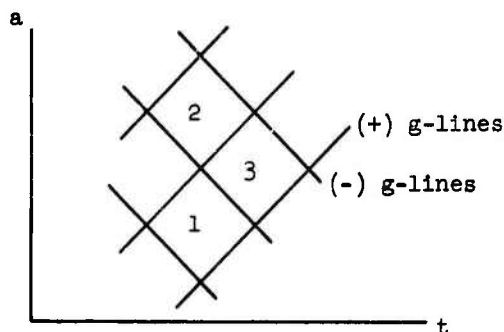
Solving (A-1) and (A-2) simultaneously gives

$$U_3 = (U_2 + \varphi_2 + U_1 - \varphi_1)/2$$

and

$$\varphi_3 = (U_2 + \varphi_2 - U_1 + \varphi_1)/2$$

The reiteration of this technique, including any appropriate boundary conditions, will give a complete solution of properties in the a - t plane.



APPENDIX B

Example of Solution Technique Using Method of Characteristics (Varying Cross Section)

If the properties at points 1 and 2 are known, the properties at point 3 are determined as follows.

From the characteristic equation given by Eq. (16).

$$\frac{D(\bar{u} \mp \bar{\sigma})}{D\bar{a}} = \pm \frac{\bar{\sigma}}{\bar{A}_0} \frac{D\bar{A}_0}{D\bar{a}}$$

where

$$\bar{A}_0 = f(\bar{a}).$$

By taking averages of $\bar{\sigma}$ and \bar{A}_0 , we have two equations applicable along \mp g-lines with the two unknowns \bar{u}_3 and $\bar{\sigma}_3$. Solving simultaneously gives the solution at point 3. For example: Let

$$\bar{A}_0 = \frac{A_0}{A_{0\text{bot}}} = e^{k\bar{a}}$$

$$\frac{D(\bar{u} \mp \bar{\sigma})}{D\bar{a}} = \pm \frac{\bar{\sigma}}{e^{k\bar{a}}} k e^{k\bar{a}}$$

$$D(\bar{u} \mp \bar{\sigma}) = \pm K \bar{\sigma} D\bar{a}$$

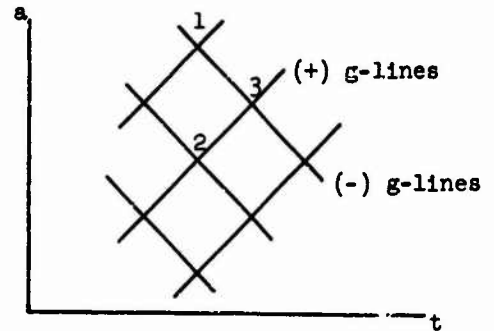
Along the (-) g-line from point 1 to point 3

$$(\bar{u} - \bar{\sigma})_3 - (\bar{u} - \bar{\sigma})_1 = k \left(\frac{\bar{\sigma}_1 + \bar{\sigma}_3}{2} \right) (\bar{a}_3 - \bar{a}_1)$$

Along the (+) g-line from point 2 to point 3

$$(\bar{u} + \bar{\sigma})_3 - (\bar{u} + \bar{\sigma})_2 = -k \left(\frac{\bar{\sigma}_2 + \bar{\sigma}_3}{2} \right) (\bar{a}_3 - \bar{a}_2)$$

Solving simultaneously gives the solution \bar{u}_3 and $\bar{\sigma}_3$. The reiteration of this technique, including any appropriate boundary conditions, will give a complete solution of properties in the a-t plane.



APPENDIX C

Program Listing Impedance Approach

```

5. REM SIC MOD 6
10 REM THIS PROGRAM CALCULATES PROPERTIES FOR A CYLINDER
20 REM WITH STEP IMPEDANCE CHANGES AND VARIOUS PULSE LENGTHS.
30 REM IT WILL PRINT OUT PROPERTIES AT A DESIGNATED SECTION,
40 REM SECTIONS EXPERIENCING TENSION, AND LIST THE MAXIMUM
50 REM STRESS FOR EACH SECTION.
60 LET S(2,K+1)=S(1,K+1)
70 REM LENGTH MUST BE AN INTEGER.
100 REM M=N0. OF REGIONS, T=PULSE LENGTH, I=IMPEDANCE,
110 REM L=EFFECTIVE LENGTH, Q1=SECTION TO PRINT OUT,
120 REM T1=N0. OF ROWS ANALYZED.
150 DIM U(1,75),S(2,75),J(75)
152 DIM D(75),E(75),A(75),N(75)
155 DIM T(75),M(75)
160 READ M,Q1
170 LET N1=0
180 FOR I=1 TO M
190 READ I(1),L(1)
200 IF I>1 THEN 220
210 LET L9=L(1)
220 IF L(1)>L9 THEN 240
230 LET L9=L(1)
240 NEXT I
250 GOSUB 1500
275 LET T1=2*N1
280 PRINT "T="
290 INPUT T
300 LET J=1
310 FOR I=1 TO N1
330 LET S(0,I)=0
335 LET S(2,I)=0
340 NEXT I
345 LET S(1,1)=1
350 GO TO 360
355 LET S(1,1)=0
360 LET U(1,1)=U(0,2)+S(0,2)-S(1,1)
380 LET L=1
390 FOR I=1 TO N1/2
400 LET K=2*I
430 LET N=N(1)
490 LET S(1,K)=(U(0,K+2)+S(0,K+2)-U(1,K-1)+S(1,K-1))*N/(N+1)
500 LET U(1,K)=U(1,K-1)-S(1,K-1)+S(1,K)
510 LET T(K)=S(1,K)*M(K)
530 IF S(1,K)<S(2,K) THEN 550
540 LET S(2,K)=S(1,K)
545 LET J(K)=J
550 LET S(1,K+1)=S(1,K)/N
555 LET T(K+1)=S(1,K+1)*M(K+1)
560 LET U(1,K+1)=U(1,K)
590 IF S(1,K+1)<S(2,K+1) THEN 610
610 IF K<>Q1 THEN 640
620 PRINT K,T(K)
630 GO TO 670
640 IF K+1 <> Q1 THEN 670
660 PRINT K+1,T(K+1)
670 IF N1=K+2 THEN 690
680 NEXT I
690 LET S(1,N1)=0
700 LET U(1,N1)=U(1,N1-1)-S(1,N1-1)
710 LET J=J+1
720 IF J=T1+1 THEN 780

```

```

730 FOR I=1 TO N1
740 LET S(0,I)=S(1,I)
750 LET U(0,I)=U(1,I)
760 NEXT I
765 IF J<T THEN 775
770 GO TO 355
775 GO TO 345
780 PRINT
790 PRINT
800 PRINT "CALCULATION COMPLETED"
810 GO TO X70
820 PRINT "ROW","COLUMN","MAX STRESS"
830 PRINT
840 FOR I=1 TO N1
850 PRINT I,J(1),S(2,1)
855 NEXT I
860 PRINT
870 PRINT "NEXT TIME PULSE"
880 GO TO 280
900 DATA 1,2
910 DATA 1,2
999 GO TO 9999
1500 REM THIS SUBROUTINE CALCULATES THE TOTAL IMPEDANCE RATIO
1510 REM FOR EACH DIVISION RESULTING FROM UNIFORM STEP CHANGES
1520 REM IN DIA. TO APPROXIMATE A CONICAL FRUSTUM.
1550 REM N9=N0. DIVISIONS FOR SMALLEST REGION
1560 REM P(1)=N0. DIVISIONS FOR (1)TH REGION
1570 REM D0=BASE DIA., D1=FREE SURFACE DIA.
1580 REM D(I)=TOP DIA. OF (I)TH DIVISION
1590 REM L8=TOTAL LENGTH, N(1)=(1)TH DIV. IMPEDANCE RATIO
1610 REM N8=TOTAL NO. OF DIVISIONS
1620 REM E(I)=AVG. DIA. OF (I)TH DIVISION
1630 REM A(I)=AVG. AREA OF (I)TH DIVISION
1650 PRINT "ENTER THE FOLLOWING"
1660 PRINT "DIV. FOR SMALLEST REGION, BASE DIA., FREE SURFACE DIA."
1670 INPUT N9,D0,D1
1675 LET N8=0
1680 LET L8=0
1690 FOR I=1 TO M
1700 LET L8=L8+L(I)
1710 LET P(I)=N9*L(1)/L9
1720 LET K(I)=2*P(I)
1730 LET N1=N1+K(I)
1740 LET C(I)=C(I-1)+K(I)
1760 NEXT I
1770 LET N8=N1/2
1775 LET L=1
1780 FOR I=1 TO N8+1
1800 LET D(I)=(D0-D1)*(N8+1-I)/N8+D1
1805 NEXT I
1807 FOR I=1 TO N8
1810 LET E(I)=(D(I)+D(I+1))/2
1820 LET A(I)=3.1416*(E(I)2)/4
1830 NEXT I
1840 FOR I=1 TO N8
1850 LET K=2*I
1860 IF K<C(L) THEN 1890
1870 LET N(I)=A(I+1)*I(L+1)/(A(I)*I(L))
1872 LET M(K)=I(L)
1874 LET M(K+1)=I(L+1)
1875 LET L=L+1
1880 GO TO 1910
1890 LET N(I)=A(I+1)/A(I)
1892 LET M(K)=I(L)
1894 LET M(K+1)=I(L)
1910 NEXT I
1920 RETURN
2260 PRINT "STATEMENT 260"
9999END

```

APPENDIX D

Program Listing Continuous Changing Area Approach

```

1 REM THIS PROGRAM CALCULATES THE STRESS VS TIME IN A TRUNCATED
2 REM CONE ASSUMING THE STRESS AT THE TOP IS ZERO ON THE 1 WAVE.
3 REM THE IMPULSE IS OF THE FORM SINE SQUARED AND THE STRESS
4 REM ALL ALONG THE FIRST WAVE IS ZERO.
10 DIM U(1,220) , S(1,220) , A(220)
15 PRINT "WHAT ARE K,C,T,S1,L"
20 INPUT K,C,T,S1,L
30 FOR I=0 TO K-1
35 LET A(I) = 1/K
40 LET S(0,I)=0
50 LET U(0,I) = -S(0,I)
60 NEXT I
62 LET A(K) = 1
64 LET S(0,K) = 0
66 LET U(0,K)= U(0,K-1) - S(0,K-1)
68 PRINT "J","S(1,0)","S(1,K/4)","S(1,10*K/24)","S(1,21*K/24)"
70 FOR J=1 TO L
78 IF J > T THEN 85
80 LET S(1,0)= S1*SIN(3.1417*J/T)+2
81 GO TO 90
85 LET S(1,0) = 0
90 LET U(1,0) = U(0,1) + S(0,1) - S(1,0)
95 LET U(1,0) = U(1,0) + (S(1,0)+S(0,1))*(A(0)-A(1))/(C-(A(0)+A(1))/2)
100 FOR I = 1 TO K-1
105 LET X = (A(I)-A(I+1))/(C-(A(I)+A(I+1))/2)
106 LET Y = (A(I)-A(I-1))/(C-(A(I)+A(I-1))/2)
110 LET S(1,I)=X*S(0,I+1)+Y*S(1,I-1)+U(0,I+1)+S(0,I+1)-U(1,I-1)
111 LET S(1,I) = (S(1,I)+S(1,I-1))/(2-X-Y)
120 LET U(1,I)=S(1,I)+U(1,I-1)-S(1,I-1)-Y*(S(1,I-1)+S(1,I))
130 NEXT I
230 LET S(1,K) = 0
240 LET U(1,K) = U(1,K-1)-(Y+1)*S(1,K-1)
250 PRINT J,S(1,0),S(1,K/4),S(1,10*K/24),S(1,21*K/24)
260 FOR I = 0 TO K
270 LET S(0,I) = S(1,I)
280 LET U(0,I) = U(1,I)
290 NEXT I
300 NEXT J
1000 END

```


DISCUSSION

Mr. Mains (Washington Univ.): What material did you use for the model tests?

Mr. Yang: We used steel and aluminum.

Mr. Mains: Are you familiar with the work that Carlos Riparabelli did at Cornell in the late 40's with plaster models?

Mr. Yang: No.

Mr. Mains: He showed this phenomenon and discussed it, I think, in the *Journal of Applied Mechanics* in 1948 or 1949. He went one step further and curved the models back on themselves. He hit the bar on one end and had it shoot back at him.

Mr. Yang: We did the same thing. We looked at the waves as they bounced back and forth in our conical frustum. Someone at NOL actually performed some tests on plastic materials, setting off explosives at the base of a polycarbonate cone. Many other tests have also been performed.

Mr. Fritz (General Electric Co.): Did you have a criterion to predict spalling? Do you have some engineering correlation to predict when you would expect spalling to occur?

Mr. Yang: Yes, from the theory one can calculate a stress-time history of the entire conical frustum. By doing this, you are able to know the stress at any time. If you go through the calculation, look at the stress, and find a time at a place where the tensile stress exceeds the tensile strength of the material, you probably will get spallation.

Mr. Fritz: Spalling is a surface fracture, and the maximum strain that you showed only went up to about 0.7 percent. It is my understanding that the materials that you were working with would have strains in fracture much in excess of 0.7 percent. If spalling or surface fracture occurred, some kind of strain rate effect must have been associated with it. One cannot mention a stress to cause fracture without considering the associated strain; but when the stress and the strain are both correlated possibly with the strain rate effect, there is an engineering or scientific basis for predicting when spalling would occur.

Mr. Yang: Yes, there are some problems with strain rate effects. As a matter of fact, this has been studied quite a bit. The theory of the characteristic method proposed by Von Karman and G. I. Taylor is for strain rate independence. In our particular case, the steel that we used was impacted at various strain rates. We examined the stress-strain curves and found that they are strain rate independent. Now, if spalling occurs, it is probably caused by the reflection from tip of the conical frustum which meets the unloading wave and increases the tensile stress. At that particular spot our material spalls.

CAVITY EFFECT ON PANEL FLUTTER - JUST HOW SIGNIFICANT?

N.H. Zimmerman and C.E. Lemley
McDonnell Aircraft Company
St. Louis, Missouri

A cavity that is enclosed behind a skin panel may alter the panel dynamics and hence, the panel flutter boundaries. The changes in dynamics, both in modeshapes and frequencies, are due to the introduction of effective stiffness and mass by the entrapped air volume. Analytical methods using assumed modes (Galerkin or Rayleigh-Ritz) have been used previously to study the cavity effect on vibration and flutter. This paper presents an exact solution of the cavity problem that was recently performed to check the validity of the modal analyses. The results to date indicate that the modal approach shows good agreement with the exact solution for zero airspeed frequency and modeshape changes; however, the reduction in flutter speeds indicated by the approximate methods appear to be overly conservative.

INTRODUCTION

Panel flutter is a troublesome offspring of supersonic flight that has raised many questions about the dynamic aeroelastic behavior of thin plates. Efforts to answer these questions have resulted in a large number of experimental and theoretical studies designed to improve our understanding of panel flutter. Difficulties that have been encountered in predicting the flutter speeds of panels have usually been attributed to the large number of parameters that significantly affect panel behavior; these include not only the geometry and material properties of the panel itself but also the panel's environment. A discussion of these factors is presented in Reference (1) together with guidelines for assessing their effects. The present paper deals with one such factor, a cavity enclosed behind a panel, and presents theoretical

results based on an exact solution technique indicating that cavity effect may be less destabilizing than previously indicated. References (2) and (3) are considered representative of previous efforts to assess the effects of a cavity. Modal representations presented in these references had been used as the basis for four-mode flutter studies that were made for Reference (1) but flutter boundaries thus obtained were suspected of being overly conservative. The present authors later found a more descriptive, exact flutter solution that could be applied to a two-dimensional (i.e., infinite width) panel. The initial studies are reported here and present a better analytical assessment of the effect of an enclosed cavity on panel flutter boundaries. In addition, vibration data obtained as a by-product of the flutter studies are discussed.

SYMBOLS LIST

D	$Eh^3/12(1-\nu^2)$, panel bending stiffness
E	modulus of elasticity
h	panel thickness
L	panel span
M	Mach number
p_l	pressure on lower panel surface
p_0	initial pressure in cavity
p_u	pressure on upper panel surface
p_∞	free airstream static pressure
q	$= \frac{1}{2} \rho v^2$, dynamic pressure
T	time function
s	complex frequency parameter
t	time
V_0	initial cavity volume
v	airflow velocity
w	gross panel loading per unit area
X	modal displacement function
x	distance downstream from forward panel support
z	deflection of panel from initial position, positive downward
β	$= \sqrt{M^2 - 1}$
γ	polytropic exponent
δ	cavity depth
η	$= x/L$ fraction of panel length aft of forward support
θ	eigenvalue
λ	$= \gamma \frac{p_0 L^4}{D\delta}$, cavity parameter
μ	panel mass per unit panel area
ν	Poisson's ratio
ρ	mass density of air
σ	$= \frac{2qL^3}{\beta D}$, dynamic pressure parameter
σ_{cr}	value of σ at flutter onset
ω	frequency of oscillation
ω_r	reference frequency

PHYSICAL PROBLEM

The influence of an enclosed cavity on the dynamics of a panel is due to the interaction between panel displacement and the entrapped air. Fig. 1 shows a side view of an infinitely wide panel enclosing a cavity. Assume that when the panel is in its neutral (undeflected) position, the pressure and volume of the enclosed air are p_0 and V_0 respectively. When the panel is deflected inward, as indicated in the lower sketch of Fig. 2, then the air pressure is increased to $p_0 + \Delta p$ in response to a decrease in volume represented by $V_0 - \Delta V$. For a "second-mode" deflection, represented for example by a full sine wave, the net volume change would be zero hence there would be no pressure change. The only cavity effect in this case would be due to a redistribution of the air to accommodate the new cavity shape. The presence of the enclosure therefore can be treated as (1) a "stiffening" effect as the entrapped air pressure varies in response to volume change and (2) an "inertia" effect as the air mass is redistributed during panel deformation. For panel and cavity sizes of practical interest, the stiffness effect alone is expected to give an accurate assessment of the cavity influence (2). The analyses presented here account for the cavity by assuming that a perturbation cavity pressure Δp is exerted everywhere on the cavity side of the panel in instantaneous response to panel displacement.

MATHEMATICAL DEVELOPMENT

We present here the salient features of the mathematical development. For the two dimensional plate problem consider a strip of unit width perpendicular to the paper in Fig. 1. The gross panel loading pressure w consists of the air pressure p_u on the upper surface, the air pressure p_l on the lower surface, and inertia loading

$$\mu \frac{\partial^2 z}{\partial t^2}$$

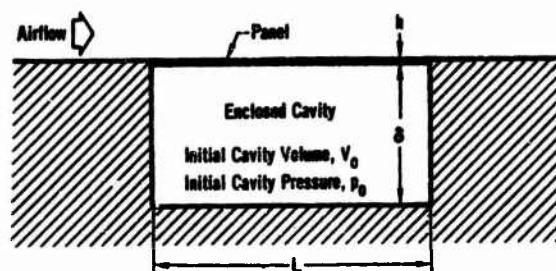


Fig. 1 - The Problem: Determine the Effect of an Enclosed Cavity on Panel Dynamics, Including its Influence on Panel Flutter

The panel deflection z is related to the loading by the relation

$$D \frac{\partial^4 z}{\partial x^4} = w(x,t) = p_u - p_l - \mu \frac{\partial^2 z}{\partial t^2} \quad (1)$$

(See Ref. (4), for example). The pressure p_u arises from the external airflow over the upper surface of the panel while the pressure p_l arises from the pressure within the enclosed cavity, see Fig. 2.

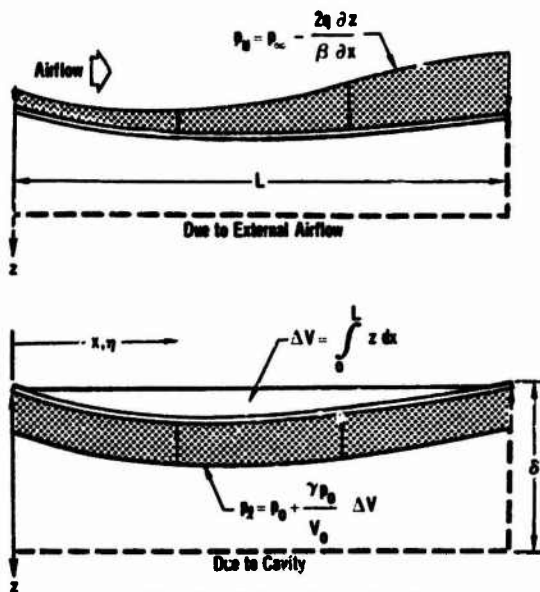


Fig. 2 - Air Loading on Panel

Assuming the adiabatic gas law ($pV^\gamma = \text{constant}$) holds in the cavity the pressure may be expressed

$$p_l = p_0 + \frac{\gamma p_0}{V_0} \Delta V = p_0 + \frac{\gamma p_0}{V_0} \int_0^L z dx. \quad (2)$$

The pressure p_u , based on the Ackeret theory of supersonic flow, is given by

$$p_u = p_\infty - \frac{2q}{\beta} \frac{\partial z}{\partial x}, \quad (3)$$

which in essence states that the pressure perturbations from freestream p_∞ are proportional to the local panel slope. With these expressions for the pressures the governing differential equation is

$$D \frac{\partial^4 z}{\partial x^4} + \frac{2q}{\beta} \frac{\partial z}{\partial x} + \mu \frac{\partial^2 z}{\partial t^2} + \frac{\gamma p_0}{V_0} \int_0^L z dx = 0, \quad (4)$$

where we neglect any effect due to static differential pressure, $p_\infty - p_0$, across the panel.

We assume the solution of Eq. (4) to have the form

$$z(x,t) = XT \quad (5)$$

in which X is a function only of the lengthwise coordinate x and T is a function only of time. Substitute equation (5) in equation (4), substitute $x = \eta L$ and multiply through by L^4/D to get

$$\frac{d^4 X}{d\eta^4} T + \frac{2qL^3}{\beta D} \frac{dX}{d\eta} T + \mu \frac{L^4}{D} \frac{d^2 T}{dt^2} X + \frac{\gamma p_0 L^5}{V_0 D} \int_0^1 X T d\eta = 0 \quad (6)$$

After making the substitutions

$$V_0 = L\delta$$

$$\lambda = \frac{\gamma p_0 L^4}{D\delta} \quad (\text{cavity parameter})$$

and

$$\sigma = \frac{2qL^3}{\beta D} \quad (\text{dynamic pressure parameter})$$

We divide each term in Eq. (6) by XT . The T inside the integral in the last term cancels because it is not a function of η . This operation separates the variables so that we can then write

$$\frac{1}{X} \frac{d^4 X}{d\eta^4} + \frac{\sigma}{X} \frac{dX}{d\eta} + \frac{\lambda}{X} \int_0^1 X d\eta = - \frac{\mu L^4}{DT} \frac{d^2 T}{dt^2} \quad (7)$$

The separated functions can only be equal to one another if they each equal a constant which we call θ . Therefore, Eq. (7) becomes

$$\frac{d^4 X}{d\eta^4} + \sigma \frac{dX}{d\eta} - \theta X = -\lambda \int_0^1 X d\eta \quad (8)$$

and

$$\mu \frac{L^4}{D} \frac{d^2 T}{dt^2} + \theta T = 0 \quad (9)$$

As a consequence of the definite limits of integration, the term on the right side of Eq. (8) does not vary with η . To emphasize this fact we define

$$K = -\lambda \int_0^1 X d\eta. \quad (10)$$

For the time function, we assume the form

$$T = e^{st} \quad (11)$$

in which we can think of s as a panel complex frequency parameter (for example, the solution $s = i\omega$ gives the familiar undamped free vibration solution). Substituting Eq. (11) into (9) gives

$$\theta = -\mu \frac{s^2 L^4}{D}$$

and θ becomes clearly defined as the problem eigenvalue.

The solution (X) of the fourth-order, non-homogeneous, ordinary differential equation (8) is expressed as the sum of particular (X_p) and complementary (X_c) solutions, i.e.,

$$X = X_p + X_c \quad (12)$$

The particular solution is simply the constant

$$X_p = -K/\theta = k \quad (13)$$

The complementary solution, which is the solution for the homogeneous equation obtained by equating the left-hand side of Eq. (8) to zero, can be expressed as

$$X_c = e^{-a\eta} (A' \sinh \eta + B' \cosh \eta) + e^{a\eta} (C' \cos \zeta \eta + D' \sin \zeta \eta) \quad (14)$$

in which (see Ref. (5)) the following relationships hold:

$$\left. \begin{aligned} \epsilon &= \left(\frac{\sigma}{4a} - a^2 \right)^{1/2} \\ \zeta &= \left(\frac{\sigma}{4a} + a^2 \right)^{1/2} \\ \theta &= \frac{\sigma^2}{16a^2} - 4a^4 \end{aligned} \right\} \quad (15)$$

At this point, the unique form of Eq. (8), particularly the fact that the integral equation has finite limits, allows us to express X_p in terms of X_c . We combine Eqns. (10), (12) and (13) to obtain

$$K = -\theta X_p = -\lambda \int_0^1 (X_p + X_c) d\eta = -\lambda X_p - \lambda \int_0^1 X_c d\eta.$$

Since $X_p = k$,

$$k = \frac{\lambda}{\theta - \lambda} \int_0^1 X_c d\eta. \quad (16)$$

The complete solution then is

$$X = e^{-a\eta} (A' \sinh \eta + B' \cosh \eta) + e^{a\eta} (C' \cos \zeta \eta + D' \sin \zeta \eta) + k \quad (17)$$

Using the boundary conditions for the pinned ends

$$X = 0 \text{ at } \eta = 0 \text{ and } \eta = 1$$

and

$$\frac{d^2 X}{d\eta^2} = 0 \text{ at } \eta = 0 \text{ and } \eta = 1$$

gives four simultaneous equations in the four constants, A' , B' , C' and D' . The determinant of the coefficient matrix of these constants is set equal to zero to yield a transcendental equation whose solutions give the eigenvalues as well as the values for a , ϵ and ζ required for Eq. (14). After specifying values for σ (the dynamic pressure parameter), and λ (the cavity parameter) we used an iterative solution technique that is described in Reference (5). The panel stability is indicated by the form of s , as follows:

If s is:	The panel motion is:
Pure imaginary	Natural free vibrations
Positive real	Static divergence instability
Complex	Oscillatory instability (flutter)

CAVITY EFFECT ON PANEL VIBRATION

The magnitude of the non-dimensional cavity parameter determines the extent of the cavity effect on the panel. Figure 3 shows how the natural vibration frequencies of the panel (normalized to the fundamental frequency obtained for $\lambda = 0$) vary with the cavity parameter. Note that $\lambda = 0$ indicates a "no cavity" condition that could be caused by a vacuum ($p_0 = 0$) or an infinite cavity depth ($\delta = \infty$). Increasing values of the cavity parameter then indicate increasingly severe interaction between panel motion and the enclosed air. Of special note are the following:

- The panel deflection shape designated as the first mode (at $\lambda = 0$) undergoes a drastic increase in frequency, asymptotically approaching that of the "no cavity" third mode.
- The third mode (at $\lambda = 0$) experiences a more gradual increase in frequency, asymptotically approaching that of the "no cavity" fifth mode.
- The frequencies of the second and fourth modes (as well as all still air even modes) are not changed at all.

These frequency trends, which however do not tell the story of modeshape change, can be anticipated by knowing the nature of the volumetric change induced in the cavity by each modeshape at $\lambda = 0$. The first such mode is a half sine wave which causes the largest volumetric change of any mode. The second and fourth such modes are a full sine wave and two full sine waves, respectively, and cause no volume change at all. Finally, the third mode (one and one-half sine waves at $\lambda = 0$) causes a net

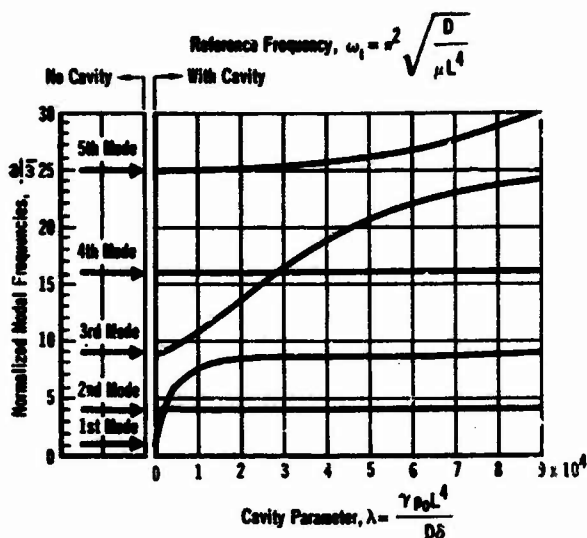


Fig. 3 - Modal Frequencies of a Panel as a Function of Cavity Parameter (Exact Solution)

volume change, but of a lesser amount than for the first mode. The plot shows another very interesting feature; it is possible to "lose" the fundamental mode still air deflection shape when testing a panel that encloses a cavity.

The variation of the fundamental modeshape with λ is indicated in Fig. 4. Note that the mode shape, as λ increases, takes on the character of the "no cavity" third mode. It is indeed found that as $\lambda \rightarrow \infty$ both frequency and panel deflection shape approach those of the "no cavity" third mode condition. Similarly, the mode that starts as the third at $\lambda = 0$ eventually approaches the "no cavity" 5th mode frequency. These effects are due to coupling through the enclosed air of the odd vibration modes.

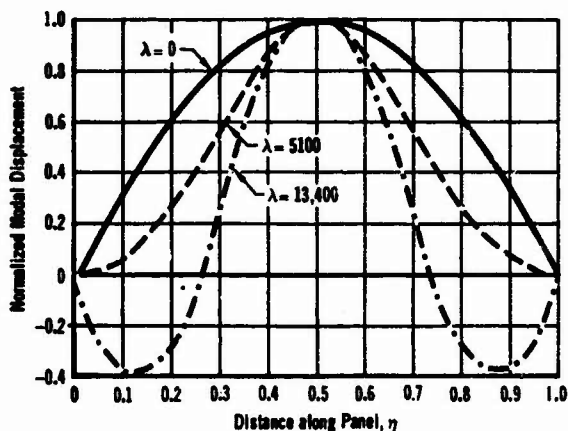


Fig. 4 - Change in the Fundamental Mode Displacement Function with Increase in Cavity Parameter (Exact Solution)

CAVITY EFFECT ON PANEL FLUTTER

Because of the pronounced cavity effect noted in the previous section we expected to find a correspondingly significant effect on panel flutter. The most critical configuration usually occurs when the frequency ratio between still air vibration modes is near unity. We were therefore especially thorough in examining flutter boundaries near $\lambda = 1800$ which Fig. 5 shows to be the crossover point of the two lowest still air vibration frequencies. In particular we were interested in the variation of panel dynamics with increase in the dynamic pressure parameter σ .

The variation in panel dynamics with σ is reflected by the three plots of modal frequency trends shown in Fig. 6.

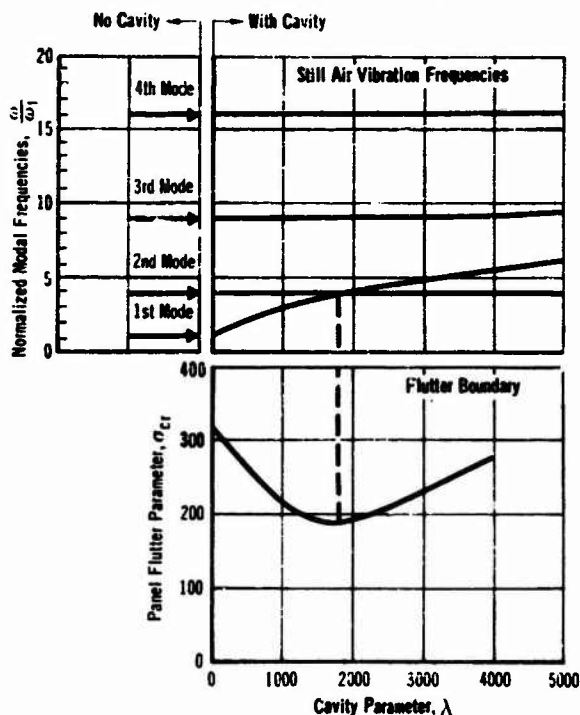


Fig. 5 - Effect of Cavity on Panel Flutter (Exact Solution)

Here we show plots of the lowest four frequency eigenvalues as a function of σ , and we indicate in each case the critical value σ_{cr} that is used to define the flutter boundary. Fig. 6(a), for $\lambda = 0$, shows the dynamic aeroelastic characteristics of the two dimensional panel without cavity effect. As air-speed (σ) is increased, the notable change is that the two lowest "natural frequencies," which are coupled aerodynamically, coalesce at the value $\sigma = \sigma_{cr}$ (about 320 in this case.) Mathematically, all frequencies are real for $\sigma > \sigma_{cr}$; for $\sigma < \sigma_{cr}$, the lowest two frequencies become a complex conjugate pair indicating oscillatory instability (flutter).

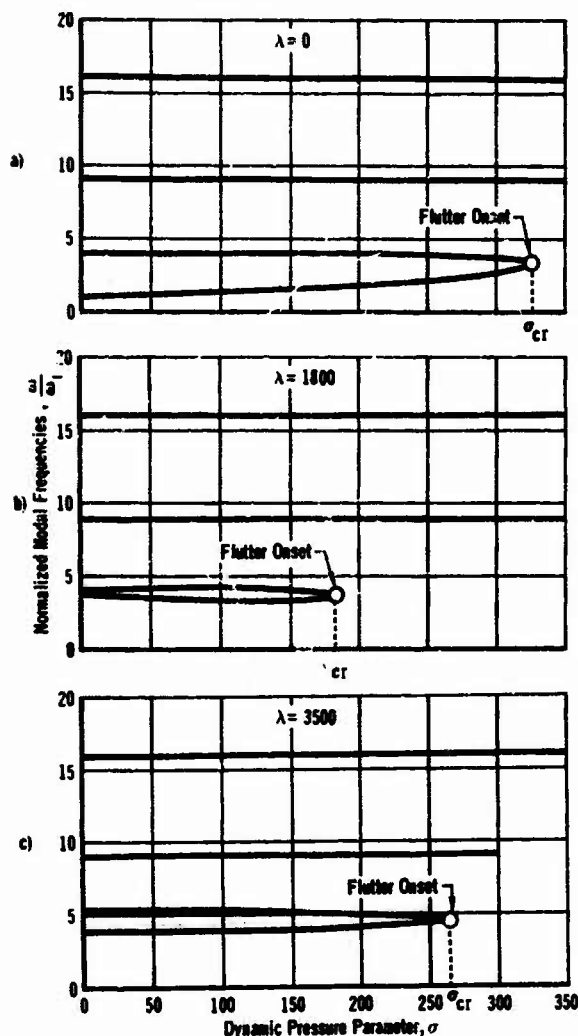


Fig. 6 - Effect of Dynamic Pressure on Modal Frequencies (Exact Solution)

Moving on to Fig. 6(b), we are very near the value of σ at which the still-air frequency crossover occurs; the interesting feature here is that the modal frequencies initially separate with increasing σ until a value of about 110, before starting to converge and coalesce at $\sigma_{cr} = 185$. Fig. 6(c) shows the behavior of the frequencies at a value of λ above the frequency crossover, and the overall plot is very similar to Fig. 6(a). Although not shown, we obtained flutter solutions for other values of λ near 1800 and verified the flutter boundary curve shown in Fig. 5.

COMPARISON OF RESULTS WITH THOSE BASED ON MODAL APPROACH

Prior theoretical studies investigating the effect of an enclosed cavity on panel flutter employed modal approach

approximation techniques. A cursory comparison of results obtained in those studies with the present exact solution results suggested that the cavity effect was not as destabilizing as previously thought.

In order to reach more valid conclusions, we have applied the modal approach solution to the identical problem analyzed herein by the exact solution technique. Problem definition and all assumptions employed were identical; the only difference was in the solution technique. Rayleigh-Ritz assumed mode solutions were used in the present studies employing two, four, and eight modes. These modes correspond to the zero airspeed "no cavity" vibration modes (sinusoidal mode shapes and corresponding frequencies). The comparisons are discussed below.

Zero Airspeed Vibrations

Results of the modal approximation solution using four assumed modes agreed quite well with the exact solution results. Only minor deviations from the results presented in Fig. 3. (for the first four frequencies) could be detected. The same applies with regard to change in fundamental mode shape with cavity, i.e., very nearly the same as that shown in Fig. 4.

Panel Flutter Speed

Figure 7 compares flutter speeds obtained from the exact solution with those obtained using the modal approach. In general, poor agreement is noted with the modal approximation technique showing a drastically more severe cavity effect than does the exact solution technique. Only in the range of small cavity effect ($\lambda < 300$) is there reasonable agreement. The greatest discrepancy occurs at $\lambda \approx 1800$ which is in the vicinity of the zero airspeed frequency crossover point of the first and second modes (see Fig. 3).

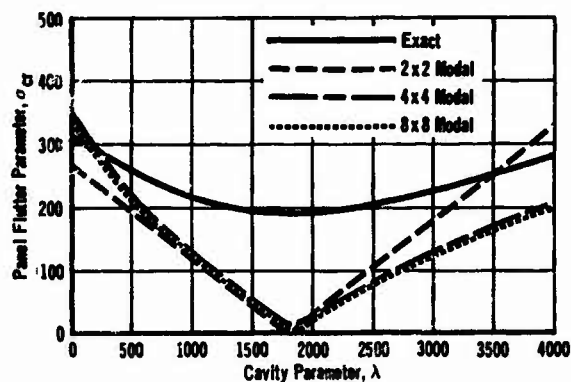


Fig. 7 - Comparison of Modal and Exact Flutter Solutions

CONCLUSIONS

1. Modal and exact solutions yield the same frequency and mode shape trends with cavity effect at zero airspeed.
2. The exact solution indicates that cavity effect is not as destabilizing as previously thought.
3. These results are only a beginning. Further assessment of the cavity effect would be desirable, such as:
 - a) The exact solution should be extended to account for finite panel width perpendicular to the airflow.
 - b) The modal solution to panel flutter employing zero-airspeed, cavity-affected modes and frequencies should be carried out and compared to the exact solution to see if better agreement can thereby be achieved.
 - c) Actual severity of cavity effect should be ascertained through experimentation and compared with the theoretical studies.

REFERENCES

1. C.E. Lemley, "Design Criteria for the Prediction and Prevention of Panel Flutter," AFFDL-TR-67-140, 1968.
2. E. Dowell, and H. Voss, "The Effect of a Cavity on Panel Vibration," AIAA Journal, Technical Note, January 1963.
3. E. Dowell, and H. Voss, "Experimental and Theoretical Panel Flutter Studies in the Mach Number Range 1.0 to 5.0," AIAA Paper No. 64-491, presented at the First Annual Meeting of the American Institute of Aeronautics and Astronautics, 1964.
4. S. Timoshenko and S. Woinowsky-Krieger, Theory of Plates and Shells (McGraw-Hill, Second Ed.), 1959.
5. Hedgepeth, J.M. "On the Flutter of Panels at High Mach Numbers," Reader's Forum, Journal of the Aeronautical Sciences, Vol. 23 No. 6, pp 609,610; June, 1956.
6. Weinberger, H.F., Partial Differential Equations (Blaisdell Pub. Co.), 1965, Chap. 4.

DISCUSSION

Mr. Michel (NASA Headquarters): When you had the dynamic characteristics of the plate with a cavity behind it, it appeared that you did not take into account the traveling wave. When you deflect the plate I think you are assuming that the pressure instantaneously changes over the whole cavity. Are you not?

Mr. Lemley: Yes.

Mr. Michel: Do you think that could be an effect if you considered a traveling wave in the gas?

Mr. Lemley: We think there would be an effect and that there would be some influence on that minimum point of the flutter curve. If I had to guess, I would say maybe 5 or 10 percent. I do not think it would come anywhere near consolidating these curves.

Mr. Michel: It would depend on whether you get a resonance there or not, wouldn't it?

Mr. Lemley: Yes, it would depend on it. If there were a cavity resonance, that would show up very drastically in the behavior of the panel.

Mr. Shore (NASA Langley Research Ctr.): I have a question regarding your last slide, where you show the modal results in comparison with your exact results. At the point where zero Q flutter is predicted from the modal solution, does the modal solution say that there are two frequencies that are equal at this value of the cavity parameter?

Mr. Lemley: Yes. We used a frequency coalescence criterion. There is a figure in the paper that I did not show here that shows how that coalescence occurs.

Mr. Shore: Could not this coalescence be due to the cavity parameter without the presence of the air flow? Is this what the figure is saying?

Mr. Lemley: It could, if you were just looking at equal frequencies as indicating flutter. We go beyond that point. We get complex conjugate pairs. So just the existence of a pair of frequencies that are equal would not tell us that this is flutter. That is not coalescence; it would just be a cross over.

Mr. Shore: The same thing happens when you have in-plane stress in the panel. You get these anomalous zero Q flutter points which can be removed by the addition of both structural and aerodynamic damping in the analysis. Did you consider any damping in your work?

Mr. Lemley: We tried to isolate this problem and treat it for the ingredients that we feel we need to understand better. We have made simplifications and assumptions on the problem, but the modal answers have the same ingredients and the same simplifying assumptions that the exact solution has. That is what puzzles us. It is not the membrane dilemma exactly, but it looks close.

AN EIGENVALUE PROBLEM SOLUTION OF A THREE DIMENSIONAL PIPING SYSTEM

Paul Bezler
Brookhaven National Laboratory
Upton L.I., New York

and

J. R. Curreri
Polytechnic Institute of Brooklyn
333 Jay Street
Brooklyn, New York

The eigenvalue problem solution of a three dimensional piping system is studied. The structure investigated consists of three mutually perpendicular legs, having fixed ends. The stiffness matrix and the mass matrix for the system are combined to establish the eigenvalue problem. Higher natural frequencies and corresponding normal modes are determined. The ratio of span lengths is altered over a wide range to show transitions and to check boundary cases. The results are normalized and plotted for the first modes. The three dimensional normal modes are plotted for some ratios of span lengths.

INTRODUCTION

There is a long history associated with the design and analysis of three dimensional piping systems. Advanced techniques are routinely used in the static design that consider thermal effects, pressure stresses and gravity loads.

The response of these systems to dynamic inputs, however, presents a more involved problem. Some sophisticated programs have been written regarding the response of such systems to dynamic inputs. These are complex, not easy to use and not widely known.

Very little information is available for guidance in the literature. The Design of Piping Systems, compiled by the M. W. Kellogg Company (1) discusses the vibration of piping systems. The treatment uses a Rayleigh type approximation for the fundamental mode for the case of a pipe bend with two legs. No information or guidance is given for the occurrence of higher modes.

This paper is intended to expand on the dynamic properties on a three legged, three dimensional piping system. Higher natural frequencies and corresponding normal modes, as well as the fundamental, are included. This is done by setting up the stiffness matrix which when combined with the mass matrix defines an eigenvalue problem. The various system force deflection routines were supplied as deflection routines to serve as inputs to obtain the stiffness matrix. From the eigenvalue problem, the natural frequencies and associated normal modes were obtained.

The computerized solution uses a corrected and expanded version of an available general matrix manipulation code "GEM" (3). As compiled, it will determine the stiffness matrix, natural frequencies and mode shapes of a linear, conservative, spring-mass system. The most important operation included in the program is the vibration eigenvalue routine. The routine will determine the natural frequencies and mode shapes of a spring-mass system if supplied with the system mass and stiffness matrices as input. The eigenvalue-eigenvector determination is made by application of the Jacobi Method (4), a numerical determination of the systems principal coordinates.

For the three dimensional piping system, the relative span lengths were varied over a wide range. Sufficient range is included to permit boundary cases to be checked. In particular, the three legged system can appear as a two legged system or even as a single span system. This can be viewed in several stages which permits the transitional effects to be studied. The results are normalized and plotted for the first three natural frequencies, as shown in the accompanying Fig. 2. The three dimensional normal modes are also plotted for some ratios of span lengths.

ANALYSIS

The differential equations describing an n degree of freedom, conservative, linear spring-mass system are represented in matrix form as

$$[M] \{\ddot{X}\} + [K] \{X\} = 0 \quad (1)$$

where

$$M = \begin{bmatrix} m_{11} & m_{12} & \dots & m_{1n} \\ m_{21} & & & \\ \vdots & & & \\ m_{ni} & \dots & \dots & m_{nn} \end{bmatrix} \quad \text{the square mass matrix}$$

$$K = \begin{bmatrix} k_{11} & k_{12} & \dots & k_{1n} \\ k_{21} & & & \\ \vdots & & & \\ k_{ni} & \dots & \dots & k_{nn} \end{bmatrix} \quad \text{the square stiffness matrix}$$

$$X = \{x_1, x_2, \dots, x_n\} \quad \text{deflection coordinate vector}$$

The symmetry characteristics of both the mass and stiffness matrices is dependent on the deflection coordinates chosen to describe the system.

There are n solutions to equation (1) of the form:

$$\{x_r\} = \{v_r\} e^{i\omega_r t} \quad \text{and} \quad \{\ddot{x}_r\} = -\omega_r^2 \{v_r\} e^{i\omega_r t}$$

where ω_r^2 is the r th eigenvalue, or natural frequency squared of the system, and v_r is the corresponding eigenvector, or mode shape vector. Each solution satisfies equation (1), therefore, the total solution can be expressed as n equations of the form:

$$-\omega_r^2 [M] \{v_r\} + [K] \{v_r\} = 0 \quad (2)$$

If the n eigenvalues are arranged as the diagonal spectral matrix

$$\Lambda = \begin{bmatrix} \omega_1^2 & & & 0 \\ & \omega_2^2 & & \\ & & \ddots & \\ 0 & & & \omega_n^2 \end{bmatrix}$$

and the corresponding eigenvectors are arranged into the square modal matrix

$$V = \begin{bmatrix} \vdots & \vdots & \dots & \vdots \\ v_1 & v_2 & \dots & v_n \\ \vdots & \vdots & \dots & \vdots \end{bmatrix}$$

the n equations describing the entire solution (2) can be expressed as the single matrix equation

$$-[M][V][\Lambda] + [K][V] = 0 \quad (3)$$

or on rearranging

$$[M][V][\Lambda] = [K][V] \quad (4)$$

The determination of the modal and spectral matrices is effected by a transformation of the chosen system descriptive co-ordinates to the systems' principal co-ordinates. Multiplication of equation (4) by the inverse of the mass matrix yields

$$[V][\Lambda] = [M]^{-1}[K][V] \quad (5)$$

Expressing this equation in principal co-ordinates results in the matrix product $[M]^{-1}[K]$ appearing as a diagonal matrix. Conversely, operations which result in the diagonalization of this product also effect the transformation to principal co-ordinates. The Jacobi Method achieves diagonalization by applying to the co-ordinate vector of the subject matrix a series of rotation transformations, each transformation resulting in the elimination of one off diagonal element pair. The applied transforms are of the form:

$$T_{ij} = \begin{bmatrix} 1 & & & \\ & c & s & \\ & s & c & \\ & & & 1 \end{bmatrix}$$

where

$$\begin{aligned} c &= \cos \theta & a_{ij}, a_{ii}, a_{jj} &\text{are} \\ s &= \sin \theta & &\text{elements of row} \\ \tan 2\theta &= \frac{2a_{ij}}{a_{ii} - a_{jj}} & &\text{order } i \text{ and column} \\ & & &\text{order } j \end{aligned}$$

and any one transform can be interpreted as a rotation of the plane represented by the i th and j th co-ordinates through an angle of θ degrees.

The symmetry restriction imposed by the Jacobi Method necessitates various matrix manipulations of the system equations prior to diagonalization. Expressing the equation as in (5) is not sufficient as the matrix product $M^{-1}K$ is not necessarily symmetric. The required formulation is as follows:

since

$$M = M^{\frac{1}{2}} M^{\frac{1}{2}}$$

equation (4) may be represented as

$$KV = M^{\frac{1}{2}} M^{\frac{1}{2}} V \Lambda \quad (6)$$

next using the identity

$$M^{-\frac{1}{2}} M^{\frac{1}{2}} = I$$

and inserting this relation between K and V , equation (6) becomes

$$K M^{-\frac{1}{2}} M^{\frac{1}{2}} V = M^{\frac{1}{2}} M^{\frac{1}{2}} V \Lambda$$

finally, multiplying by $M^{-\frac{1}{2}}$ yields

$$(M^{-\frac{1}{2}} K M^{-\frac{1}{2}}) (M^{\frac{1}{2}} V) = (M^{\frac{1}{2}} V) \Lambda \quad (7)$$

Now if the matrix product $(M^{-\frac{1}{2}} K M^{\frac{1}{2}})$ can be shown to be symmetric, equation (7) is in a form suitable for solution by the Jacobi Method. Note that the spectral matrix has not been affected.

Since M is symmetric, it can be shown that $M^{-\frac{1}{2}} K M^{-\frac{1}{2}}$ is also symmetric, or

$$(M^{-\frac{1}{2}} K M^{-\frac{1}{2}}) = (M^{-\frac{1}{2}} K M^{-\frac{1}{2}})^T$$

The matrix then actually diagonalized by the Jacobi Method has a spectral matrix identical to the original and a modal matrix related to the original by

$$M^{\frac{1}{2}} V_{(\text{orig})} = V_{(\text{diagonalized})} \quad (8)$$

Application of the above technique requires the determination of the inverse square root of the mass matrix $(M^{-\frac{1}{2}})$. This is easily done if the mass matrix is diagonal. If the mass matrix is symmetric but nondiagonal, the Jacobi Method is used to determine its modal and spectral matrices. The modal matrix is normalized, this being possible because the eigenvectors are orthogonal, and the inverse square root is given by

$$M^{-\frac{1}{2}} = T \Gamma^{-\frac{1}{2}} T^T$$

where T is the normalized mass modal matrix ($T T^T = I$), and Γ is the mass spectral matrix.

It should be noted that $\Gamma^{-\frac{1}{2}}$ is easily formed since Γ is diagonal.

The presentation to this point has dealt with the formulation and solution of the vibration problem given the mass and stiffness matrices. The development of the mass matrix is normally of little difficulty, the mass locations and their respective degrees of freedom being either obvious or at the analysts discretion. The development of the stiffness matrix on the other hand, can be quite arduous for anything but the simplest of structures.

The stiffness matrix may be obtained by inversion of the flexibility matrix or by direct derivation, starting with the principle of virtual work. The forces and deflections are related by

$$\{f\} = [k] \{d\} \quad (9)$$

$$\text{or } [F] \{f\} = \{d\}$$

where $[F]$ is the flexibility matrix.

For the elastic system, the forces f are associated with the deflections d . The system may be subdivided into basic elements, the division being such that each element is statically determinate. Application of the force group f generates forces within the basic elements. Let the column vectors p and v respectively represent the generated internal forces and deformations. There exists a relation of the form (9) between the internal forces and deformations of each element. Assembling these into one matrix equation results in

$$\{v\} = [F_v] \{p\} \quad (10)$$

where F_v is a symmetric, diagonally partitioned array of the basic element flexibility matrices. The body is also acted on by the support reactions, let the column vector X represent those reactions which are redundant. Now viewing the body as a statically determinate structure acted upon by two force groups X and f , the relationship between applied forces and internal forces may be expressed as

$$\{p\} = [B_0] \{f\} + [B_1] \{X\} \quad (11)$$

B_0 is a matrix of the coefficients relating the internal forces of the statically determinate structure to the external forces. The i th column of this matrix may be determined by subjecting the structure to the force f_i , the other forces being taken as zero, and solving for all internal forces. A similar interpretation applies to B_1 .

In accordance with the principle of work, the work done by the external forces must equal that stored in the structure, or

$$f^T d = p^T v \quad (12)$$

Substituting the various quantities into equation (12), and solving for the flexibility matrix (2) gives:

$$F = B_0^T F_v B_0 - (B_0^T F_v B_1) (B_1^T F_v B_1)^{-1} (B_1^T F_v E_0) \quad (13)$$

By following an analogous procedure, the stiffness matrix may be found to be (2):

$$K = A_0^T K_p A_0 - (A_0^T K_p A_1) (A_1^T K_p A_1)^{-1} (A_1^T K_p A_0) \quad (14)$$

where K_p is a diagonally partitioned array of the element stiffness matrices and A_0 and A_1 relate the element deflections to the kinematically determinate structure deflections.

RESULTS

The structure investigated consists of

three mutually perpendicular legs having fixed ends, as shown in Figure 1. A three mass point representation is taken, with the mass acting at the center of each span. Torsional and longitudinal degrees of freedom are neglected, resulting in a seven degree of freedom system.

In accordance with the procedure previously described, the structure is broken up into basic elements, in this case six cantilever beams.

The problem was non-dimensionalized for general usage. The resulting natural frequencies and associated normal modes are listed in Table 1. It should be noted that the

eigenvectors are interpreted as deflections in the applied force line directions, positive if in the positive force direction. The non-dimensional frequency coefficients α , from Table 1, appear in the equation

$$f = \alpha \left(\frac{EI}{mL^3} \right)^{1/2} \text{ cps} \quad (15)$$

where m = mass of one span (slugs)
 L = length of one span (in.)

A plot of Table 1 appears in Figure 2 for the first three natural frequencies only. A graphical representation of the first three eigenvectors is shown in Figures 3-5.

TABLE 1

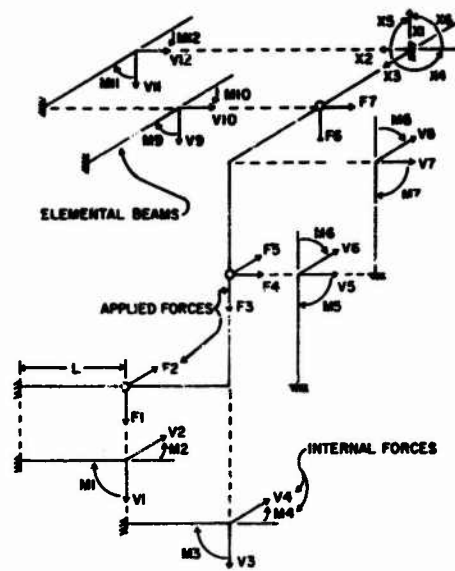
Frequency Order	1	2	3	4	5	6	7
Natural Frequency+ rad/sec	.839	2.87	3.27	13.91	16.69	23.98	27.60
rad/sec	.916	1.69	1.81	3.73	4.09	4.89	5.26
cps	.146	.270	.288	.594	.650	.779	.837
Normalized Eigenvectors++							
1	.357	-.606	-.219	.263	1.000	-1.000	1.000
2	.211	.588	-.780	1.000	-.684	-1.000	-.172
3	1.000	-.794	-.001	-.138	-.0002	.000	-.962
4	.490	1.000	1.000	-.482	-.316	-1.000	.326
5	.490	1.000	-1.000	-.482	.316	1.000	.326
6	.357	-.606	.219	.263	-1.000	1.000	1.000
7	.211	.588	.780	1.000	.684	1.000	-.172
Nondimensional Frequency Coefficients							
$f = \alpha \left(\frac{EI}{mL^3} \right)^{1/2} \text{ cps}$.414	.765	.816	1.680	1.840	2.200	2.370

+ Values apply to system where $L_{TOT} = 6$ in., $M_{TOT} = 3$ slugs, $EI = 1$

++ Listed in order of applied mass loadings (Ref. Fig. 1), positive value indicating a positive deflection in the applied force line direction.

REFERENCES

- (1) "Design of Piping Systems," M. W. Kellogg Company, 1956
- (2) "Matrix Methods in Elastomechanics," E. C. Pestel and F. A. Leckie, McGraw-Hill Book Company, 1963
- (3) "Gem," General Matrix Manipulation Program, J. A. Warrington KAPL-M-BC-33, March 1963
- (4) "Computational Methods of Linear Algebra," V. N. Faddeeva and D. K. Faddeeva, W. H. Freeman, 1963



BEAM STRUCTURE
FIGURE 1

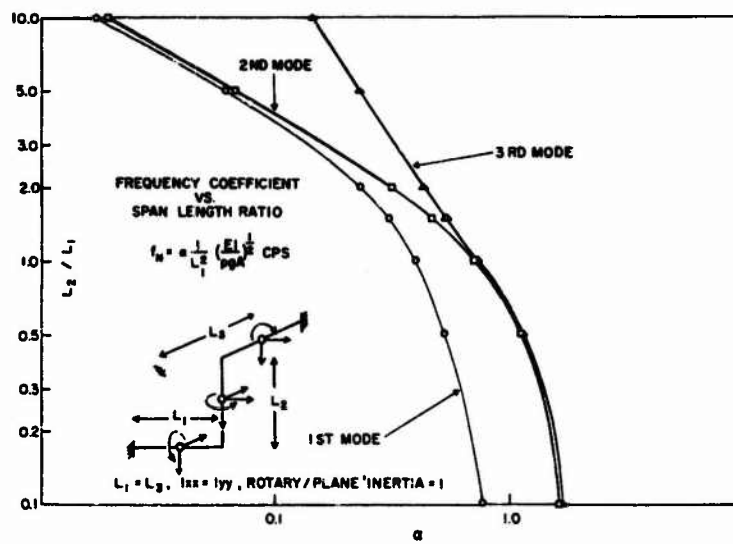


FIGURE 2

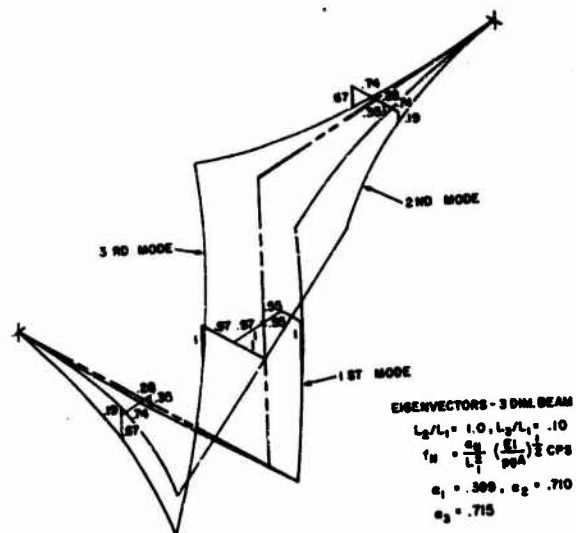


FIGURE 3

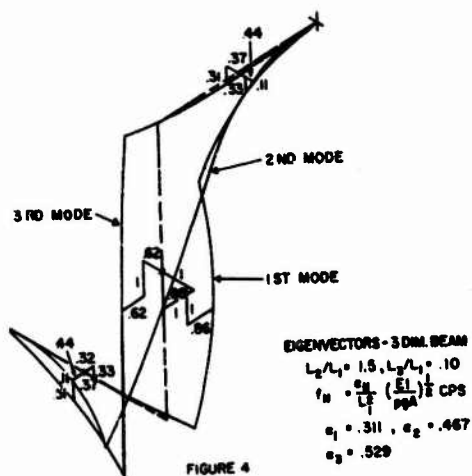


FIGURE 4

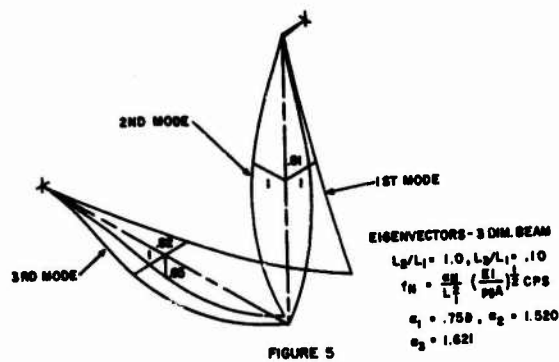


FIGURE 5

DISCUSSION

Mr. Monroe (Babcock & Wilcox Co.): Was the system that you modeled a uniformly lumped mass system?

Mr. Bezler: Yes.

Mr. Monroe: What guidelines were used to lump the masses and develop the mass matrix?

Mr. Bezler: I lumped the total mass of each leg at its center point.

Mr. Monroe: Did you apply the total mass in the middle of the span?

Mr. Bezler: Yes.

Mr. Monroe: Did you make any parametric studies on moving that mass to any other place?

Mr. Bezler: No. I might add that I have run later problems where I have used more mass points, and obtained virtually the same results. I find that if I put mass at the junction points, the results tend to change. I do not know if they are more correct. There was no parameter study.

DESIGN MODEL BASED ON OBSERVED MODES OF VIBRATION OF
AUSTRALIAN CSIRO 210-FT RADIO TELESCOPE

J.A. Macinante
Division of Applied Physics, National Standards Laboratory, CSIRO
Sydney, N.S.W. 2008, Australia

This paper describes qualitatively the simplest design model that is capable of representing the modes of vibration observed in an experimental vibration study [1] of the Australian CSIRO 210-ft Radio Telescope. The model is presented as three separate mass-spring systems. In the azimuth system the three observed torsional modes are represented by those of a series arrangement of three inertias connected by three springs. In the elevation system the three observed 'rocking modes' are represented by the first three flexural modes of a cantilever having non-uniform mass and stiffness. This cantilever is coupled to another representing the master column to provide a model for investigating the influence, on the pointing accuracy of the telescope, of unintentional coupling of the master column to the telescope structure. The observed 'walking' mode in elevation can be studied with a model based on a series arrangement of four inertias connected by three springs. The justification for making the considerable simplifications described in this paper is discussed in relation to the actual hardware.

INTRODUCTION

In the design of a radio telescope employing a servo-controlled driving system the designer must know the values of the natural frequencies that the structure will have, because it is desirable to arrange for these frequencies to lie outside the pass band of the control system. If it is intended that the servo pass band should lie below all the structural resonance frequencies, obviously it is the fundamental frequency in each manner of oscillation (e.g. torsion about azimuth axis, flexure in elevation plane, etc.) that is important. With increase in the size of a telescope of a particular type, the fundamental frequencies decrease and this increases the importance of making a reliable estimate of their values.

The mathematical model which is used for the calculation of natural frequencies is intended to separate the essential from the irrelevant or unimportant - it involves the use of simplifying assumptions which reduce the number of parameters that determine the dynamic behaviour of the system being studied. The greater the simplification, of course, the less information the model will yield. The art in deriving a design model is to know how far to carry the simplification.

In devising the model presented in this paper the author has the advantage of having observed experimentally the actual dynamic behaviour of the structure which the model is

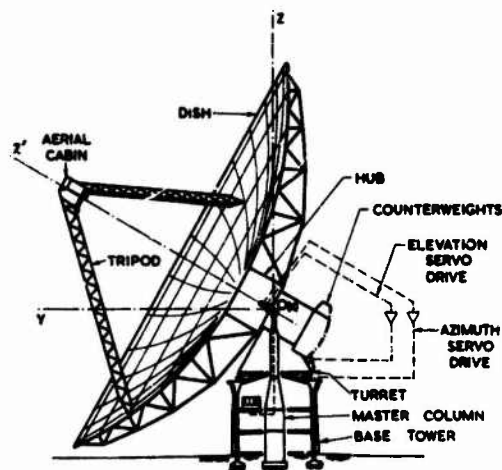


FIGURE 1. Nomenclature

TABLE 1
Observed Structural Resonance Frequencies

Mode	Resonance Frequency (Hz)	Part of Structure Primarily Involved
Torsional modes about azimuth axis OZ	1.2	Whole structure
	1.7	Tripod/aerial cabin assembly
	8.6	Lower structure
Cantilever modes in elevation plane YOZ	1.6	Whole structure
	3.0	Whole structure
	3.4	Whole structure
Cantilever modes in lateral plane XOZ	1.5	Whole structure
	2.5	Upper structure
Cantilever mode	6.5	Master column
Walking mode	0.4	Counterweight assembly and elevation drive

to represent. The model derived is the simplest that would be capable of representing the modes of vibration observed in tests made on the CSIRO 210-ft radio telescope at Parkes, Australia. Such a model may be of interest to designers of other radio telescopes of the same general type, that is an alt-azimuth steerable paraboloid on a cylindrical base tower.

The structural natural frequencies of this telescope were found by making resonance and free vibration tests for which excitation was provided through the driving system of the telescope itself. The results of the experimental study have been published elsewhere [1].

OBSERVED MODES OF VIBRATION OF CSIRO 210-FT RADIO TELESCOPE

The radio telescope has been described in detail by Bowen and Minnett [2, 3]. For convenience of reference the nomenclature used in the present paper is given in Fig. 1. The 210-ft parabolic dish is pointed in the required direction by being tilted about an elevation axis OX in a turret which is rotated about an azimuth axis OZ. These movements are produced by servo-controlled driving systems [4]. The pointing direction is nominated by a master equatorial instrument which is supported on the master column. Further descriptive matter is given later in context as required.

The results of the experimental vibration study which are relevant to the present paper are summarized in Table 1, and the observed modes of the structure as a whole are illustrated in Fig. 2. All the numerical values

are rounded to 0.1 Hz. The detailed observations were made with the dish at 0° z.a. (zenith angle ZOZ' in Fig. 1). Some observations made at 30° and 45° z.a. indicated that the resonance frequency in a given mode differed by less than 10% from the 0° z.a. value. Full details of the experimental procedures by which these results were obtained will be found in [1].

BASIS OF DERIVATION OF THE DESIGN MODEL

The model described in this paper has been derived on the following basis:

1. The term 'design model' refers to that part of the complete model of the telescope and its control system which represents the mechanical and structural elements whose properties determine the natural frequencies. The relationship of this part to the complete model of the driving and control system can be seen in [4].
2. The treatment is purely qualitative. No attempt is made to allocate to the model numerical values of its parameters based on calculated properties of the actual structure.
3. In the experimental study transient responses in elevation usually followed braking in azimuth, and transient responses in azimuth resulted from braking in elevation: these were attributed to uneven braking [see 1, p. 12-13, 22]. Steady-state excitation in azimuth or in elevation did produce a coupled response in the lateral plane, but for the purposes of the present

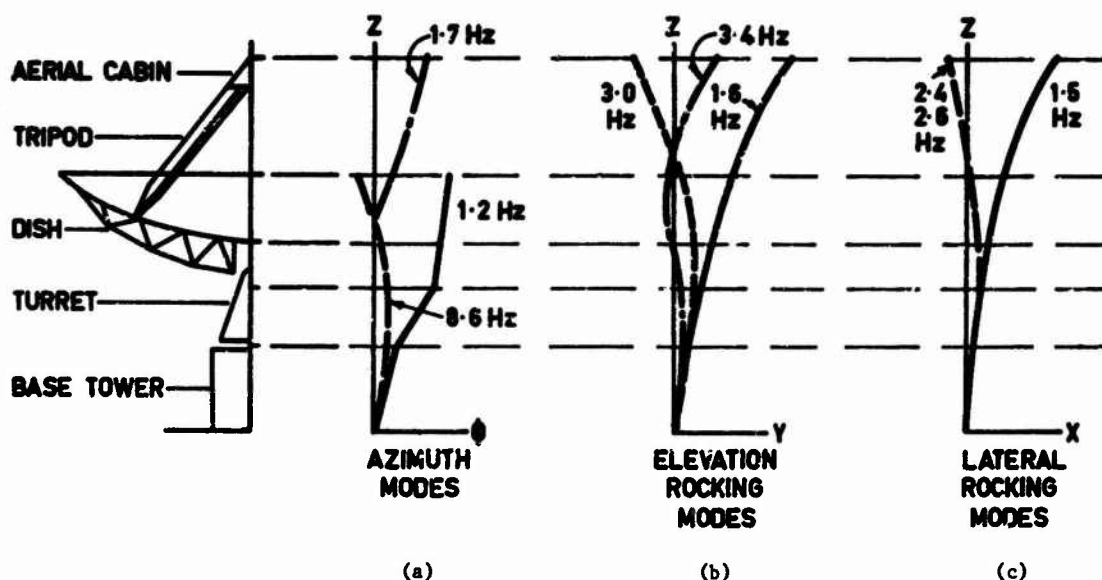


FIGURE 2. Diagrammatic Summary of Observed Modes

paper it is assumed that these systems are not coupled and hence may be represented by independent models.

4. The model is devised to represent only modes actually observed. Certain minor ones, e.g. flexural mode of tripod leg, are ignored. The model does not attempt to represent the dish modes: direct excitation of the dish for experimental study of its modes was not permitted [1, p. 6] because it would have involved risk of distortion of the dish surface.

AZIMUTH MODEL

First referring to Fig. 3, the complete dish assembly is represented by the equivalent system I_D, k_D . The experimental results indicate that the stiffness k_D of the dish itself about the azimuth axis is comparatively high. The aerial cabin/tripod assembly is shown as the separate system I_A, k_A attached to the dish system.

The turret stiffness is represented by the spring k_T . The experiments showed that the turret contributes the major compliance in azimuth. The turret inertia is shown partly as I_{T1} at the top of the turret, combined with I_C the inertia of the counterweight assembly, and the remainder as I_{T2} at the base of the turret.

The telescope is driven in azimuth by two motor-gearbox units, one of which is shown diagrammatically in Fig. 4. The effective inertias

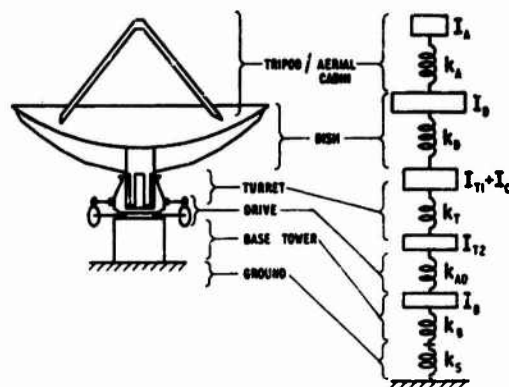


FIGURE 3. Azimuth System

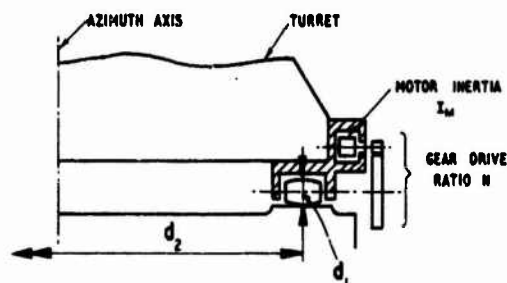


FIGURE 4. Azimuth Drive

of the azimuth drive I_{AD} referred to the azimuth axis is

$$I_{AD} = 2I_M(Nd_2/d_1)^2 \quad (1)$$

where I_M = the moment of inertia at the motor shaft;

N = gear ratio motor rpm/roller rpm;

d_1 = effective diameter of roller;

d_2 = effective diameter of track.

Because the reduction ratio Nd_2/d_1 has a very high value the total moment of inertia of the azimuth drive referred to the azimuth axis is about eight times greater than the total moment of inertia of the complete assembly that rotates on the azimuth track. Therefore the motor shafts can be assumed to be locked.

The supporting structure, comprising the base tower and azimuth track, is shown in Fig. 3 as the I_B, k_B system. Some response was observed experimentally at the ground level [see 1, p. 13]; the stiffness of the ground or site is represented by k_S .

In the vibration study the azimuth modes recognized in addition to the fundamental were a mode associated with the aerial cabin/tripod and one associated with the base tower. (See Fig. 2(a)). This suggests that the model could be reduced to a three-inertia system as shown in Fig. 5 by ignoring the inertia of the turret and counterweights, a total of about one-tenth that of the complete dish assembly above the counterweights. Consequently the stiffness of dish, turret and azimuth drive can be represented by that of a single spring denoted by k_2 .

Thus, Fig. 5 is presented as the simplest system that is capable of representing the three azimuth modes that were found experimentally.

ELEVATION AND LATERAL ROCKING MODEL

The model for the elevation system is required to represent the following features of the observed behaviour of the telescope:

- (i) Oscillation of the structure as a whole. Three rocking (flexural) modes were observed in the elevation plane YOZ and two in the lateral plane XOZ as shown in Figs 2(b) and 2(c) and Table 1.
- (ii) Oscillation of the master column resulting from some unintentional coupling to the telescope, as discussed in Section 2 below.
- (iii) 'Walking' oscillation of the counterweight assembly as discussed in Section 3 below.

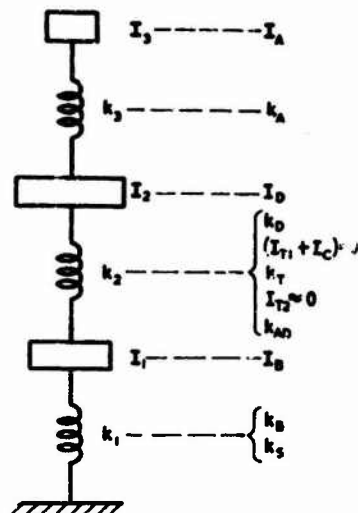


FIGURE 5. Azimuth Model

1. Flexural Oscillation of the Telescope Structure

The system involved in flexural oscillation in the elevation plane is shown diagrammatically in Fig. 6(a). This is first converted to Fig. 6(b) in which the model suggested is basically a cantilever. The suitability of this is obvious in relation to the flexure of the lower part of the structure from the ground to the base of the turret, and the upper part of the structure above the elevation bearings. The behaviour of the intermediate part comprising the turret, the counterweight assembly and the elevation drive requires some discussion.

The dish is represented by a lumped mass m_D and a flexure spring k_D . Superposed on m_D is an m_A, k_A system representing the aerial cabin/tripod assembly.

The counterweight assembly is treated as a lumped mass m_C on a flexural element k_C . The rack on the counterweight is connected through gearing to a motor attached near the base of the turret. Because of the very high drive ratio the total moment of inertia of the elevation driving system, referred to the elevation axis, is over 30 times greater than the moment of inertia of the complete elevation assembly about the elevation axis. Therefore the motor shaft can be regarded as locked. The torsional stiffness of the elevation drive is represented as that of a spring k_{ED} . Displacement of the counterweight mass m_C is opposed by springs k_C and k_{ED} acting in the configuration shown in relation to the turret k_T .

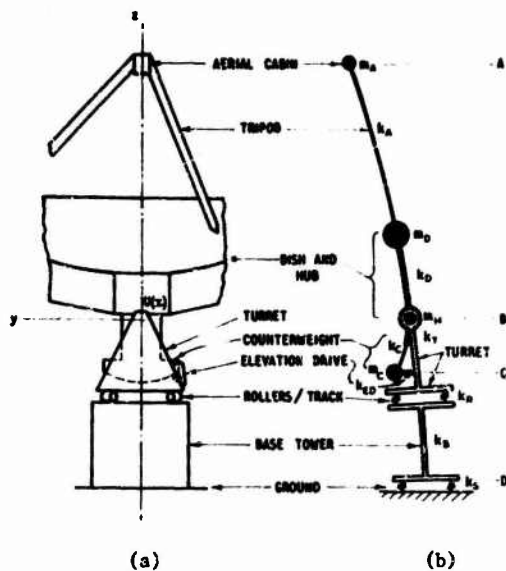


FIGURE 6. Elevation System

Referring now to Fig. 7(a) the elevation system ABC, which has just been discussed, is supported at the elevation bearings B by a system BD. For clarity the two systems are shown separated at the common point B. The system BD can be regarded as a cantilever having non-uniform stiffness, and also non-uniform mass distribution which might involve the use of lumped masses such as m_{T1} and m_{T2} for the upper and lower parts respectively of the turret, and m_B for the upper part of the base tower, and so on. The flexural stiffness is that associated with the ground or site (k_S), the base tower (k_B), the azimuth track and roller system (k_R), and the turret (k_T).

The model can be simplified to that shown in Fig. 7(b), if the stiffness k_{BD} is relatively high. For m_C and m_{T2} can then be combined, also k_T and k_C can be combined, as shown.

Therefore the model suggested for the rocking modes in elevation is a cantilever having non-uniform mass and stiffness as shown in Fig. 7(b). The three observed rocking modes can be represented by the first three modes of such a cantilever.

For flexural oscillations in the lateral plane the elevation drive stiffness is not involved and the hinge at B is irrelevant. Hence lateral modes can be represented by a system basically similar to that in Fig. 7(b).

2. Coupling of the Master Column with the Telescope Structure

Ideally the master column is completely isolated structurally from the surrounding

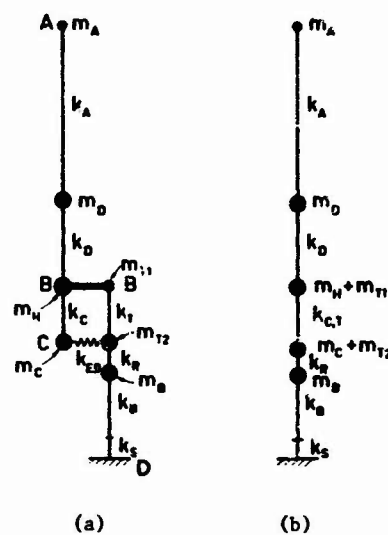


FIGURE 7. Development of Elevation Model

telescope. However, the experiments showed that the master column was not uncoupled: it responded as a vertical cantilever to excitation applied to the surrounding telescope structure, in the manner illustrated in Fig. 8 [see also 1, p. 17]. Such a coupled response of the master column in a telescope of this type could have an important influence on the pointing accuracy as discussed in 1, Part 4.

Therefore the design model might with advantage be extended to permit a study of the influence of structural resonances on the error detection system, for even though there may be no physical contact where the master column passes through the structure, some degree of coupling through the foundations is probably unavoidable. In such a study obviously the mode shapes as well as frequencies should be investigated.

The master column may be represented in the model by a cantilever which is weakly coupled to that representing the telescope structure as shown in Fig. 9. Direct coupling could be represented by a spring k_H and coupling through the ground by the spring k_S . The cantilever representing the column may have non-uniform stiffness and mass, or lumped masses, as appropriate.

Thus the model of the complete telescope in elevation is simply a pair of cantilevers with a small degree of coupling. Such a model is capable of representing features (i) and (ii) of the observed behaviour noted at the beginning of this Section. The third feature is now discussed.

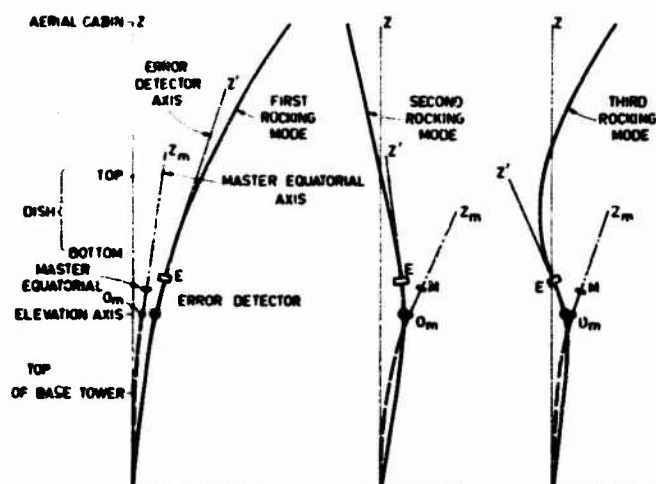


FIGURE 8. Coupled Response of Master Column

3. Walking Oscillation

The phenomenon observed experimentally is as follows. At a certain angular velocity ω of rotation in elevation, the two counterweights oscillated in phase about the elevation axis with the displacement of the right about twice that of the left. The frequency f_W of this oscillation is the walking frequency. In the CSIRO radio telescope $f_W = 0.42$ Hz was the lowest of the observed frequencies. At submultiple rates ω/n ($n = 1, 2, \dots$) the counterweights oscillated in a similar manner with the same frequency f_W but with smaller displacement.

At these particular rates at which walking occurred, the period T_R of the rack-tooth meshing cycle in the counterweights drive was observed to be an integral multiple of the period T_W of the walking cycle.

That is

$$T_R = n T_W, \text{ or } f_W = n f_R \quad (2)$$

where f_R = frequency of rack-tooth meshing cycle.

Dynamic load observations at the turret base throughout the range of elevation speed showed appreciable load fluctuations at the tooth meshing frequency.

The mechanism of the excitation of the walking motion is not fully understood; it is thought that non-uniformity of the velocity ratio may provide the excitation and that the control system, which applies to both sides

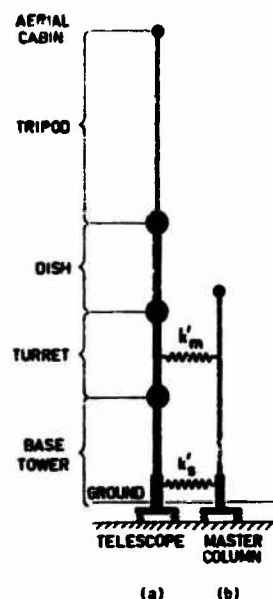


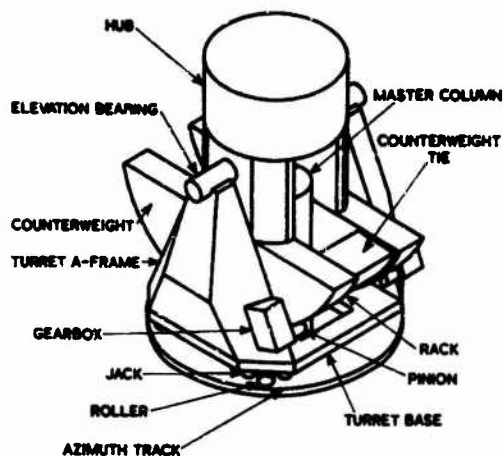
FIGURE 9. Elevation Model

a correction based on the error detected at one side, may tend to maintain a walking oscillation.

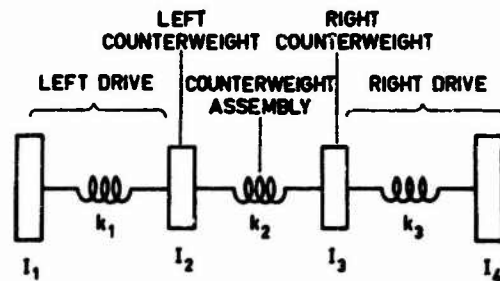
Although there is no experimental evidence of interaction between the walking oscillation and the servo-control system, the possibility of such an interaction should be considered in the design of any alt-azimuth mounted telescope which attains equatorial control through the use of a master instrument on a central column. With such an arrangement a walking oscillation is inherently possible because the counterweight assembly must be in the form of two separate counterweights that can be joined together at only one end (Fig. 10(a)).

For the design model, all that can be suggested on the basis of the experimental results is that the walking mode could be studied with a model having as its basic element the system shown in Fig. 10(b) in which the excitation originates. To this it would be necessary to add the other elements which participate in the walking mode, notably the turret, and possibly also the dish.

The system in Fig. 10(b) treats separately the two counterweights and their drives which were lumped together in the elevation model. The left counterweight I_2 is joined to the right I_1 by a spring k_2 having the stiffness of the counterweight assembly in torsion about the elevation axis. The inertias I_1 and I_2 are the drive inertias referred to the elevation axis, and k_1 and k_2 are the drive stiffnesses. Excitation representing that resulting from non-uniformity of the gear drive velocity ratio could be applied to I_2 and I_3 .



(a) Diagram of Counterweight Assembly



(b) Basic System for Walking Mode Model

FIGURE 10. Walking Mode

CONCLUDING REMARKS

A simple design model has been derived which would be capable of representing qualitatively the observed modes of vibration of the Australian CSIRO 210-ft radio telescope. The model comprises three separate spring-mass systems, one for the azimuth system, one for the elevation system and a supplementary system to represent the walking mode that occurs in elevation motion.

Although in these days of high speed computers the inclusion in any design model of a few more degrees of freedom than necessary 'just to be on the safe side' may not be unreasonable, the very simple model described in this paper may be of some interest if only to suggest a limit to the degree of simplification that may be contemplated in the design model for a telescope of this type.

ACKNOWLEDGMENTS

The experimental study [1] on which this paper is based was made by the author and colleagues in the CSIRO Division of Applied Physics at the request of the Division of Radiophysics who had undertaken a more general performance study of the telescope for the United States National Aeronautics and Space Administration (NASA Grant NSG-240-62).

REFERENCES

1. J.A. Macinante, B. Dorien-Brown, J.L. Goldberg, N.H. Clark, R.A. Glazier and K.M. O'Toole, "A Vibration Study of the CSIRO 210-ft Radio Telescope," Inst.

Mech.Engrs Lond., Mech.Eng. Science Monograph No. 6, 36 pp., Dec. 1967.

2. E.G. Bowen and H.C. Minnett, "The Australian 210-ft Radio Telescope," J.Br.Instn Radio Engrs, Vol. 23, No. 1, pp. 49-54, Jan. 1962.
3. E.G. Bowen and H.C. Minnett, "The Australian 210-foot Radio Telescope," Proc.Instn Radio Engrs Aust., Vol. 24, No. 2, pp. 98-105, Feb. 1963.
4. J. Rothwell, "The Control of a Radio Telescope," AEI Engng, Vol. 3, No. 1, pp. 15-21, Jan.Feb. 1963.

DISCUSSION

Mr. Michel (NASA Headquarters): Since they did not let you shake the full scale telescope, did they have any plans for a model that you could shake?

Mr. Macinante: No. At no time was there any discussion of the use of a scale model.

Mr. Mains (Washington Univ.): What kind of computers are available in Australia for doing this kind of work?

Mr. Macinante: In our own laboratory we have CDC 3200 and 3600 digital computers. We also have a large analog computer available in another part of the CISRO on which one could have done this work.

Mr. Mains: Had you desired to use several more degrees of freedom you could have, because you had the computer capability.

Mr. Macinante: Yes.

UPPER AND LOWER BOUNDS TO TORSIONAL FREQUENCIES OF NONUNIFORM SHAFTS AND APPLICATIONS TO MISSILES

N. Rubinstein, V. G. Sigillito, J. T. Stadter
Applied Physics Laboratory, The Johns Hopkins University
Silver Spring, Maryland

In this paper we compute upper and lower bounds to torsional frequencies of nonuniform shafts. The torsional rigidity and mass moment of inertia per unit length are approximated by piecewise constant functions. Nonuniform free shafts often serve as models for the study of missile torsional vibrations. The upper bounds are obtained from the Rayleigh-Ritz method; the lower bounds result from an application of recently developed procedures of Bazley and Fox. A brief theoretical description of the lower bound methods is included along with several illustrative examples.

INTRODUCTION

In missile development it is important to know precisely the frequencies of free vibration of elastic structures and structural elements. For a missile as a whole the frequencies and mode shapes in bending and torsion have a strong influence on the performance of the control system. The frequencies and mode shapes of such other structural components as wings, fins, and panels are crucial in their aeroelastic behavior in flight.

The nonuniform free shaft often serves as a model for the study of missile torsional vibrations; in this paper we assume the shaft to have piecewise constant torsional rigidity and mass moment of inertia per unit length, both of which are distributed rather than lumped.

Although in principle this problem can be solved exactly, it is generally impractical to do so. In order to obtain the exact frequencies of a shaft with only a few non-uniformities it is necessary to find the roots of a large order determinant with non-linear entries. Methods are available for finding these roots, however their use leads to many computational problems: they are quite sensitive to round-off error and usually require much computation time. Other existing methods, such as those which concentrate the mass and stiffness at points or apply difference techniques, give approximations of the frequencies but they do not provide error estimates. Consequently, one cannot be certain of how accurate these approximations are. The methods presented here, however, give upper and lower bounds

which bracket the true frequencies of the missile model, are computationally fast and accurate, can handle a large number of non-uniformities and can be extended easily to handle shafts with more complicated variations of stiffness and mass.

The well known Rayleigh-Ritz procedure is used to obtain the upper bounds. The problem of computing lower bounds is much more difficult, but recent work of Bazley and Fox has provided useful lower-bound procedures that are applicable to a wide variety of vibration problems [Refs. 1,2]. More recently the authors were able to apply these theoretical results to obtain lower bounds to frequencies of various beams and shafts [Refs. 3-7].

THEORETICAL BACKGROUND

The differential equation of the free torsional vibration of a free shaft is given by

$$-\frac{d}{dx} \left[GJ(x) \frac{du}{dx} \right] - 4\pi^2 f^2 \mu(x) u = 0,$$

$$0 \leq x \leq L$$

$$u'(0) = u'(L) = 0,$$

where

$GJ(x)$ is the torsional rigidity,
 $\mu(x)$ is the mass moment of inertia per unit length (we will sometimes abbreviate this as the mass moment of inertia),
 L is the length of the shaft,

f is the circular frequency of torsional vibration.

We assume the $GJ(x)$ and $\mu(x)$ are piecewise constant. Physical considerations dictate that the solution u and $GJ(x)u'$ be continuous over the length of the shaft.

Because the theoretical methods are naturally expressed in terms of operators in Hilbert space, we treat the missile as a free shaft of unit length whose torsional vibrations can then be described in the real Hilbert space $L^2(0,1)$ with inner product

$$(u, v) = \int_0^1 u v \, dx.$$

Let

$$h(x) = GJ(x)$$

and

$$B(x) = \mu(x).$$

Then the above eigenvalue problem becomes

$$-\frac{d}{dx} \left[h(x) \frac{du}{dx} \right] - \lambda B(x)u = 0 \quad (1)$$

$$u'(0) = u'(1) = 0,$$

where the eigenvalue λ is related to the frequency f by †

$$\lambda = 4 \pi^2 f^2.$$

The stiffness and mass moment of inertia functions are chosen to be piecewise constant and to satisfy

$$0 < h^0 < h(x) \leq H$$

$$0 \leq m < B(x) < M,$$

where h^0 , H , m , and M are constants.

We now describe the methods used to compute upper and lower bounds to the eigenvalues of Eq. (1).

* We denote $L^2(0,1)$ the space of all square integrable functions on the interval $(0,1)$.

† The frequency for a beam of length L can be obtained from the equation

$$\lambda = 4 \pi^2 L^2 f^2.$$

Lower Bounds

The lower bounds are obtained using the method of intermediate problems [Refs. 7-9] with special choice developed by Bazley and Fox [1].

The quadratic forms associated with the elastic (or strain) energy and the kinetic energy are given by

$$J_A(u) = \int_0^1 h(x) |u'(x)|^2 \, dx$$

$$J_B(u) = \int_0^1 B(x) |u(x)|^2 \, dx,$$

respectively.

As required by the method J_A can be decomposed as

$$\begin{aligned} J_A(u) &= J_{A^0}(u) + (T_1 u, T_1 u) \\ &= \int_0^1 h^0 |u'(x)|^2 \, dx \\ &\quad + \int_0^1 (h(x) - h^0) |u'(x)|^2 \, dx. \end{aligned} \quad (2)$$

Therefore the operator T_1 is given by

$$T_1 u(x) = (h(x) - h^0)^{\frac{1}{2}} \frac{du}{dx},$$

and its adjoint T_1^* is given by

$$T_1^* v(x) = \frac{d}{dx} [(h(x) - h^0)^{\frac{1}{2}} v(x)]$$

with domain of definition $\mathcal{D}_{T_1^*}$ given by

$$\begin{aligned} \mathcal{D}_{T_1^*} &= \{ v, (h(x) - h^0)^{\frac{1}{2}} v \in L^2(0,1) \mid v(0) = v(1) = 0, \\ &\quad [(h(x) - h^0)^{\frac{1}{2}} v(x)]_{\xi_i} = 0, \\ &\quad i=1,2,\dots,n \}. \end{aligned}$$

Here $[\cdot]_{\xi}$ denotes the jump in the function at the point ξ .

Also as required by the method, the quadratic form J_B can be decomposed as

$$\begin{aligned} J_B(u) &= J_{B^0}(u) - (T_2 u, T_2 u) \\ &= \int_0^1 M |u(x)|^2 dx \\ &\quad - \int_0^1 (M - B(x)) |u(x)|^2 dx. \end{aligned} \quad (3)$$

It therefore follows that the operator T_2 is given by

$$\begin{aligned} T_2 u(x) &= [M - B(x)]^{\frac{1}{2}} u(x) \\ \text{and its adjoint } T_2^* &\text{ is given by} \\ T_2^* v(x) &= [M - B(x)]^{\frac{1}{2}} v(x) \\ \text{with domain of definition} \end{aligned}$$

$$\mathcal{D}_{T_2^*} = \mathcal{L}^2(0,1).$$

The variational problem

$$\delta \left[\frac{J_{A^0}(u)}{J_{B^0}(u)} \right] = 0,$$

for variations taken in $\mathcal{D}_{J_{A^0}}$ gives rise to the eigenvalue problem

$$A^0 u - \lambda B^0 u = 0$$

which in our case is given by

$$\begin{aligned} u''(x) + \lambda \frac{M}{h} u(x) &= 0, \\ u'(0) = u'(1) &= 0. \end{aligned} \quad (4)$$

This eigenvalue problem, referred to as a base problem, is resolvable as it corresponds to the problem of torsional vibrations of a uniform shaft with constant stiffness h and constant mass moment of inertia per unit length M . Its eigenvalues λ_v^0 and corresponding normalized eigenvectors, u_v^0 , are given by

$$\begin{aligned} \lambda_v^0 &= \begin{cases} 0, & v=1 \\ \frac{h^0}{M} (v-1)^2 \pi^2, & v=2,3,\dots \end{cases} \\ u_v^0 &= \begin{cases} \frac{1}{\sqrt{M}}, & v=1 \\ \sqrt{\frac{2}{M}} \cos (v-1) \pi x, & v=2,3,\dots \end{cases} \end{aligned}$$

The eigenvalues λ_v^0 satisfy

$$0 \leq \lambda_1^0 \leq \lambda_2^0 \leq \dots$$

Since the quadratic form J_{A^0} is obtained from J_A by dropping the positive term $(T_1 u, T_1 u)$, and the quadratic form J_{B^0} is obtained from J_B by subtracting the positive term $(T_2 u, T_2 u)$, the eigenvalues λ_v^0 give crude lower bounds to the eigenvalues of problem (1); that is, the eigenvalues satisfy

$$\lambda_v^0 \leq \lambda_v, \quad v=1,2,\dots \quad (5)$$

The lower bound method described in detail in [1, pp. 8-11] uses the first k_1 elements of a given sequence $\{p_1^i, p_2^i, \dots\}$ of linearly independent vectors belonging to $\mathcal{D}_{T_1^*}$, $i=1,2$, to construct intermediate quadratic forms which satisfy

$$\begin{aligned} J_{A^0} &\leq J_{A^{k_1}} \leq J_{A^{k_1+1}} \leq J_A \\ J_{B^0} &\geq J_{B^{k_2}} \geq J_{B^{k_2+1}} \geq J_B \end{aligned} \quad (6)$$

Consequently, the operator eigenvalue problem

$$A^{k_1} u - \lambda B^{k_2} u = 0 \quad (7)$$

obtained from the variational equation

$$\delta \left[\frac{J_A k_1}{J_B k_0} \right] = 0, \text{ has ordered eigenvalues}$$

$\lambda_{\nu}^{k_1, k_0}$ which satisfy

$$\lambda_{\nu}^0 \leq \lambda_{\nu}^{k_1, k_0} \leq \begin{cases} \lambda_{\nu}^{k_1+1, k_0} \\ \lambda_{\nu}^{k_1, k_0+1} \end{cases} \leq \lambda_{\nu}, \quad (8)$$

$\nu=1, 2, \dots$

The operator eigenvalue equation (7) is given explicitly by

$$A^0 u + \sum_{i,j=1}^{k_1} (u, T_i^* p_i^1) b_{ij}^1 T_i^* p_j^1 \quad (9)$$

$$- \lambda \left\{ B^0 u - \sum_{i,j=1}^{k_0} (u, T_i^* p_i^2) b_{ij}^2 T_i^* p_j^2 \right\} = 0,$$

where the constants b_{ij}^1 and b_{ij}^2 are elements of the matrix inverse to that with elements (p_i^1, p_j^1) and (p_i^2, p_j^2) respectively.

The method of special choice requires us to find vectors $p_i^1 \in \mathcal{D}_{T_i^*}$ satisfying

$$T_i^* p_i^1 = \sum_{\sigma=1}^n \beta_{i\sigma}^1 B^0 u_{\sigma}^0, \quad i = 1, 2, \dots, k_1,$$

and vectors $p_i^2 \in \mathcal{D}_{T_i^*}$ satisfying (10)

$$T_i^* p_i^2 = \sum_{\sigma=1}^n \beta_{i\sigma}^2 B^0 u_{\sigma}^0, \quad i = 1, 2, \dots, k_0.$$

Such a set of vectors satisfying eqs. (10) is given by

$$p_i^1 = \begin{cases} 0, & i=1 \\ \sqrt{\frac{2M}{h(x) - h^0}} \sin (i-1) \pi x, & i=2, 3, \dots, k_1, \\ \sqrt{\frac{M}{M - B(x)}} & i=1 \\ \sqrt{\frac{2M}{M - B(x)}} \cos (i-1) \pi x, & i=2, 3, \dots, k_0, \end{cases}$$

where $\beta_{i\sigma}^1 = i \pi \delta_{i+1, \sigma}$, $\beta_{i\sigma}^2 = \delta_{i\sigma}$ and

$n = k_1 + 1 = k_0$. The integer n will correspond to the order of the matrix problem.

Equation (9) now becomes a linear algebraic eigenproblem

$$\sum_{\mu=1}^n \gamma_{\mu} \left\{ \lambda_{\mu}^0 \delta_{\mu\nu} + \sum_{i,j=1}^{k_1} \beta_{i\mu}^1 b_{ij}^1 \beta_{j\nu}^1 - \lambda \left[\delta_{\mu\nu} - \sum_{i,j=1}^{k_0} \beta_{i\mu}^2 b_{ij}^2 \beta_{j\nu}^2 \right] \right\} = 0, \quad (11)$$

or equivalently in matrix notation

$$\gamma \{ \Lambda^0 + \beta_1^* B^1 \beta_1 - \lambda [I - \beta_2^* B^2 \beta_2] \} = 0. \quad (12)$$

The eigenvalues $\lambda_{n+1}^0, \lambda_{n+2}^0, \dots$, together with those determined from (12) are, when ordered according to magnitude, the eigenvalues $\lambda_{\nu}^{k_1, k_0}$ that provide lower bounds according to (8).

The eigenvalue λ_{n+1}^0 is the lowest persistent eigenvalue (P.E.) of the base problem, and the eigenvalues $\lambda_{\nu}^{k_1, k_0}$ which provide lower bounds are, for simplicity, written as λ_{ν}^n . We observe that only the eigenvalues less than λ_{n+1}^0 (the P.E.) give improved lower bounds.

Upper Bounds

The upper bounds are obtained using the

well-known Rayleigh-Ritz procedure in which we diagonalize a symmetric matrix with elements $R_{\mu\nu} = J_A(\varphi_\mu, \varphi_\nu)$ relative to the matrix $Q_{\mu\nu} = J_B(\varphi_\mu, \varphi_\nu)$ where the trial vectors φ_ν are in \mathcal{D}_{J_A} and satisfy $(B \varphi_\mu, \varphi_\nu) = \delta_{\mu\nu}$.

Here we chose modified eigenvectors of the base problem, u_ν^0 's, as trial vectors φ_ν . These are given by

$$\varphi_\nu = \begin{cases} 1 & , \quad \nu=1 \\ \cos(\nu-1)\pi x & , \quad \nu=2,3,\dots \end{cases}$$

This leads to a symmetric matrix eigenvalue problem of order n given by

$$\sum_{\nu=1}^n \left[J_A(\varphi_\mu, \varphi_\nu) - \hat{\lambda}_\nu^n J_B(\varphi_\mu, \varphi_\nu) \right] \alpha_\nu = 0, \quad \mu=1,2,\dots,n. \quad (13)$$

This problem yields upper bounds $\hat{\lambda}_\nu^n$, i.e., the eigenvalues of (13) satisfy

$$\lambda_\nu \leq \hat{\lambda}_\nu^n, \quad \nu=1,2,\dots,n.$$

ILLUSTRATIVE EXAMPLES AND RESULTS

Digital programs which solve Eq. (12) for lower bounds and Eq. (13) for upper bounds have been written. The programs require only stiffness and mass moment of inertia data in standard engineering units. All necessary conversions, matrix constructions, arithmetic operations and inversions are done automatically by the programs. A detailed description of the programs and their use is given in our report [Ref. 5].

We now give the results of two sample problems. In both of these examples we have used as a model for the missile a shaft with piecewise constant torsional rigidity and mass moment of inertia.

The first example treats a simple case which illustrates the type of results obtainable from the procedure. Figures 1 and 2 give the torsional rigidity and mass moment of inertia per unit length. The bounds to eigenvalues and to the first six frequencies obtained from 15th-order calculations are given in Tables 1 and 2. Each of these calculations required .01 hours of running time on the 7094 IBM digital computer at the Applied Physics Laboratory.

Our second example treats a more realistic missile structure. We have used a model with 17 discontinuities in torsional rigidity and 15 in mass moment of inertia per unit length (see Figures 3 and 4). The bounds to frequencies resulting from 15th, 30th and 50th order calculations are given in Table 3. Notice

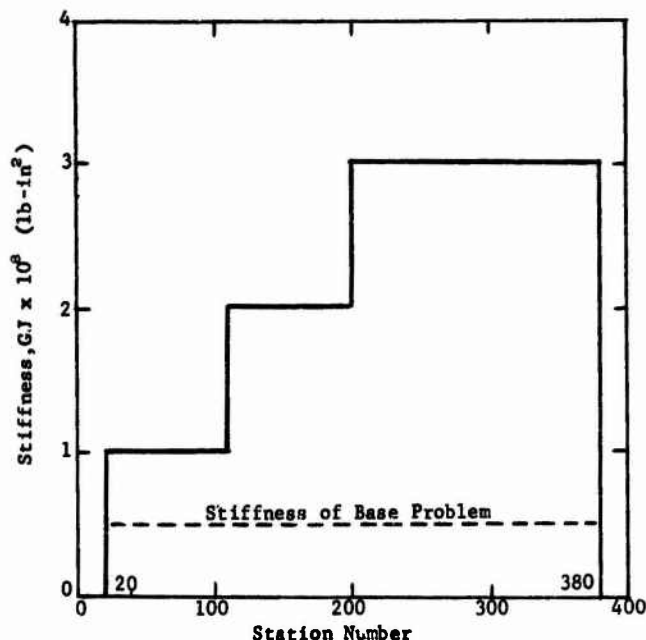


Fig. 1 TORSIONAL RIGIDITY OF A MISSILE

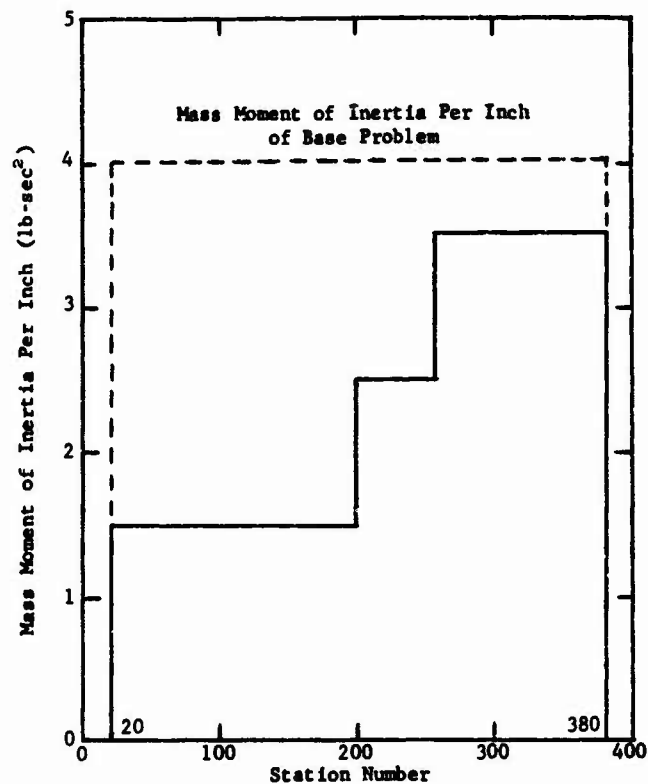


Fig. 2 MASS MOMENT OF INERTIA PER INCH

TABLE 1 TORSIONAL VIBRATION OF A MISSILE WITH PIECEWISE CONSTANT STIFFNESS AND MASS [Bounds to Eigenvalues]		
ν	15th order Lower Bounds λ_{ν}^{15}	15th order Upper Bounds $\hat{\lambda}_{\nu}^{15}$
1	0	0
2	10.086870	10.206404
3	36.843140	37.323944
4	79.572732	80.258881
5	148.77342	149.77740
6	230.09118	234.53120
7	323.11676	327.90150
8	450.40969	453.22798
9	593.77889	605.91167
10	726.20745	742.04673
11	916.55514	927.82328
12	1101.0237	1157.1484
13	1298.8136	1374.3641
14	1528.9682	1760.6615
15	1708.8686	1988.4073

that the higher order problems give imprc bounds. The theory dictates that all eige values of Eq. (12) which are less than λ_{n+1}^0 , the persistent eigenvalue of the base problem, provide lower bounds. Thus increas ing n (which increases λ_{n+1}^0) has a twofold

TABLE 2 TORSIONAL VIBRATION OF A MISSILE WITH PIECEWISE CONSTANT STIFFNESS AND MASS [Bounds to Frequencies (Hz)]		
ν	15th order Lower Bounds f_{ν}^{15}	15th order Upper Bounds \hat{f}_{ν}^{15}
1	0	0
2	14.040929	14.123880
3	26.834650	27.009179
4	39.436627	39.606291
5	53.923777	54.105422
6	67.060628	67.704564

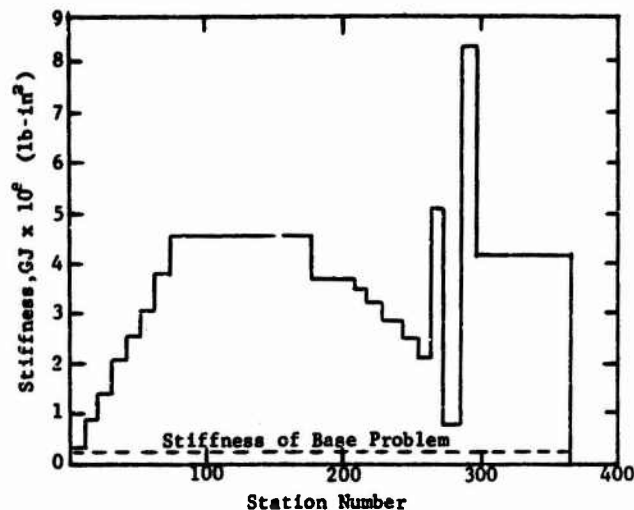


Fig. 3 TORSIONAL RIGIDITY OF A MISSILE

effect on the eigenvalues:

- (i) lower bounds to more eigenvalues are obtained,
- (ii) the lower bounds improve (see Eq.(8)).

The above can be summarized by simply stating that by increasing the order n of the matrix

calculation (Eq.(13) for the upper bounds and Eq. (12) for lower bounds) one obtains improved upper and lower bounds. This fact is clearly exhibited in Table 3.

The combined running time for the three cases, in Table 3, for both upper and lower bounds was .10 hours.

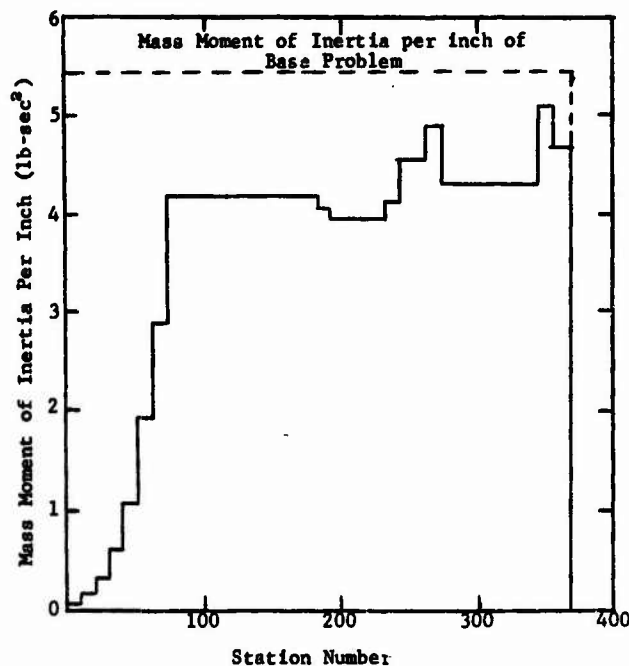


Fig. 4 MASS MOMENT OF INERTIA PER INCH

TABLE 3 TORSIONAL VIBRATION OF A MISSILE WITH PIECEWISE CONSTANT STIFFNESS AND MASS [Bounds to Frequencies (Hz)]						
ν	15th Order Lower Bounds $\hat{\nu}_{15}^L$	15th Order Upper Bounds $\hat{\nu}_{15}^U$	30th Order Lower Bounds $\hat{\nu}_{30}^L$	30th Order Upper Bounds $\hat{\nu}_{30}^U$	50th Order Lower Bounds $\hat{\nu}_{50}^L$	50th Order Upper Bounds $\hat{\nu}_{50}^U$
1	0	0	0	0	0	0
2	42.308842	47.197705	42.961492	46.692733	43.208092	45.007649
3	92.865038	100.42290	93.568213	99.285572	93.874986	96.454445
4			145.70238	146.72565	145.93122	146.69077
5			180.08932	191.69803	180.68884	186.07257
6			231.47309	242.07325	231.81773	235.93195
7					288.44201	291.61031
8					320.30658	325.83021
9					365.19466	369.46514
10					422.12678	430.20020

REFERENCES

1. N. W. Bazley and D. W. Fox, "Methods for Lower Bounds to Frequencies of Continuous Elastic Systems," Zeits. angew. Math. u. Phys., Vol. 17, No. 1, pp. 1-37, 1966.
2. N. W. Bazley and D. W. Fox, "Lower Bounds to Eigenvalues Using Operator Decompositions of the Form B*B," Archive for Rat. Mech. and Anal., Vol. 10, No. 4, pp. 352-360, 1962.
3. N. Rubinstein, "Frequencies of Beams on Partial Elastic Foundations," Appl. Phys. Lab. Tech. Rept. TG-804, Mar. 1966.
4. N. Rubinstein, V. G. Sigillito, and J. T. Stadter, "Torsional Frequencies of Uniform Shafts with Elastic Restraints and Elastically Attached Masses," Appl. Phys. Lab. Tech. Rept. TG-833, June 1966.
5. N. Rubinstein, V. G. Sigillito, and J. T. Stadter, "Bounds to Torsional Frequencies of Non-uniform Shafts, and Applications to Missiles," Appl. Phys. Lab. Tech. Rept. TG-958, Oct. 1967.
6. N. Rubinstein, V. G. Sigillito, and J. T. Stadter, "Upper and Lower Bounds to Bending Frequencies of Non-uniform Shafts, and Applications to Missiles," The Shock and Vibration Bulletin, Bull. 38, Part 2, pp. 169-176, August 1968; also published as Appl. Phys. Lab. Tech. Rept. TG-966, Feb. 1968.
7. N. Rubinstein and J. T. Stadter, "Bounds to Frequencies of a Simply Supported Rotating Beam," Appl. Phys. Lab. Tech. Rept. TG-1042, Oct. 1968.
8. N. Aronszajn, "Approximation Methods for Eigenvalues of Completely Continuous Symmetric Operators," Proc. Symp. Spectral Theory and Differential Problems, Okla. A. & M. College, Stillwater, Okla., pp. 179-202, 1951.
9. S. H. Gould, Variational Methods for Eigenvalue Problems, Second Ed., Univ. of Toronto Press, Toronto, 1966.
10. A. Weinstein, "Etudes des Spectres des Equations aux Derivées Partielles de la Théorie des Plaques Elastiques," Memorial des Sciences Mathématiques, fascicule No. 88, Gauthier-Villars, Paris, 1937.

* * *

* * *

DETERMINATION OF DYNAMIC LOADS AND RESPONSE
OF A SPACE VEHICLE USING FLIGHT DATA

Shou-nien Hou
Bellcomm, Inc.
Washington, D. C.

An analytical method has been developed, based on statistical properties of power spectral density functions obtained from actual flight, for determining maximum intensity level of the residual thrust oscillation and dynamic response of a space vehicle.

The method yields the expected intensity, the standard deviation, and the distribution of the maximum intensity across the ensemble of either excitation or response, which are treated as random processes. It is found that the square of such maximum intensity follows a Gumbel distribution. Thus, a limited number of flight records can provide sufficient information for structural design.

The proposed method may offer advantages of (1) an analytical base for establishing the residual thrust oscillation specification of space vehicle, (2) a direct estimate of maximum structural response level over combined loading effects, and (3) information for structural anomaly study as well as for structural design.

INTRODUCTION

An assessment of space vehicle structural capability under launch loads requires knowledge of the nominal force exerted on the vehicle, and the variation of this force as a function of time during the boost phase. This latter quantity, which has been referred to as residual thrust oscillation, is a random phenomenon, and as such should be treated statistically. Structural capability should also be assessed by a direct statistical evaluation of maximum structural response. Conditions can occur such that both excitation and response are a combination of random and deterministic oscillations, (i.e., POGO). Additional considerations, which are not included in this text, should be given for the additional effects of such deterministic excitations to the random process.

As we know, a power spectral density function across the ensemble of the process can be obtained directly

by the spectral analysis of the sample vibration records. It would be convenient if we could associate all the statistical properties of the process with the power spectral density function, $S(\omega)$. However, we expect that such a power spectral density function will be non-stationary, with time variation in its overall intensity and the power distribution.

In the following, analytical solutions are presented for solving the mean, variance, and distribution of the maximum oscillation of a random process, based on a fixed $S(\omega)$. Then, a piecewise stationary approach is introduced for extending such solutions to the process with time varying $S(\omega)$. The influence of the means, variances, and correlations of those dominant parameters on the distribution of the process so solved is found in approximate analytical terms.

STATIONARY PROCESS -- TIME-INVARIANT S(.)

A power spectral density function, $S(\omega)$, can be interpreted as a statistical average of frequency decomposed sample functions of a random process. By its physical meaning, the area under the curve of $S(\omega)$ is equivalent to the mean square value, x^2 , of the process:

$$x^2 = \int_{-\infty}^{\infty} S(\omega) d\omega, \quad (1)$$

where x may be considered as an averaged intensity of the process. However, for structural design and vibration studies, the extreme peak which may occur in a finite duration of time should receive more attention than just an averaged intensity alone. Since the value of x is directly associated with $S(\omega)$ and can be obtained easily through equation (1), let us choose x for expressing other statistical properties of the process.

Let excitation or structural response be a stationary random process, $Q(t)$, of zero-mean, and let $\dot{Q}(t)$ be the slope of $Q(t)$ at any time. For any arbitrary level of $Q=a$, the expected number of crossings per unit time with positive slope is designated as N_a , an ensemble average. According to S. O. Rice⁽⁴⁾

$$N_a = \int_0^{\infty} \dot{Q} p(a, \dot{Q}) d\dot{Q}, \quad (2)$$

where $p(a, \dot{Q})$ is a joint distribution of $Q(t)$ and $\dot{Q}(t)$, with $Q=a$, and is assumed to be a joint Gaussian distribution

$$p(Q, \dot{Q}) = \frac{1}{2\pi\sigma_Q\sigma_{\dot{Q}}} \exp\left[-\frac{1}{2}\left(\frac{Q^2}{\sigma_Q^2} + \frac{\dot{Q}^2}{\sigma_{\dot{Q}}^2}\right)\right], \quad (3)$$

where

$$\sigma_Q^2 = \int_{-\infty}^{\infty} S(\omega) d\omega = x^2 \quad (4)$$

$$\sigma_{\dot{Q}}^2 = \int_{-\infty}^{\infty} \omega^2 S(\omega) d\omega. \quad (5)$$

Let us designate ω_0 and T_0 as

$$\omega_0^2 = \frac{\int_{-\infty}^{\infty} \omega^2 S(\omega) d\omega}{\int_{-\infty}^{\infty} S(\omega) d\omega} = \frac{\int_0^{\infty} \omega^2 S(\omega) d\omega}{\int_0^{\infty} S(\omega) d\omega} = \frac{\sigma_{\dot{Q}}^2}{\sigma_Q^2}, \quad (6)$$

$$T_0 = \frac{2\pi}{\omega_0} = 2\pi \frac{\sigma_Q}{\sigma_{\dot{Q}}}, \quad (7)$$

which can be interpreted as the mean frequency and period of $Q(t)$, respectively. Thus, substituting these expressions into equation (2), we have:

$$N_a = \frac{1}{2\pi} \frac{\sigma_{\dot{Q}}}{\sigma_Q} \exp\left(-\frac{a^2}{2\sigma_Q^2}\right) \quad (8)$$

or

$$N_a = \frac{1}{T_0} \exp\left(-\frac{a^2}{2x^2}\right). \quad (9)$$

One approach for finding the expected extreme peak value, m , in a specific duration S is to let the expected number of crossings over the double levels, $Q(t) = m$ and $Q(t) = -m$, equal to one:

$$N_{|m|} S = (2N_m) S = \frac{2S}{T_0} \exp\left(-\frac{m^2}{2x^2}\right) = 1. \quad (10)$$

Solving for m , the expected extreme peak in a duration S is:

$$m = \left[2 \log_e\left(\frac{2S}{T_0}\right)\right]^{1/2} x. \quad (11)$$

Another approach, based on an additional assumption⁽³⁾ that the time $T^{(j)}$ for a sample function $q^{(j)}(t)$ to reach the double levels $q(t) = \pm a$ for the first time follows Poisson process across the ensemble, will lead to a similar conclusion as follows.

The probability distribution for n crossings in a duration S is:

$$P(n, N_{|a|} S) = \frac{(N_{|a|} S)^n}{n!} e^{-N_{|a|} S}. \quad (12)$$

Then

$$\begin{aligned}
 F(a) &= P \left[\begin{array}{l} \text{Extreme peak } < a \\ \text{in a duration } S \end{array} \right] \\
 &= P \left[\begin{array}{l} \text{No crossing over} \\ \text{double levels } |a| \\ \text{in a duration } S \end{array} \right] \\
 &= P(0, N|a|S) \\
 &= e^{-N|a|S}.
 \end{aligned} \quad (13)$$

Let $\tau = N|a|S$, we get

$$\begin{aligned}
 p(a) da &= dF(a) \\
 &= de^{-\tau} \\
 &= -e^{-\tau} d\tau.
 \end{aligned} \quad (14)$$

From equation (9), we get

$$\tau = N|a|S = (2N_a)S = \frac{2S}{T_0} \exp\left(-\frac{a^2}{2x^2}\right) \quad (15)$$

$$\begin{aligned}
 a &= \left(2 \log_e \frac{2S}{T_0} - 2 \log_e \tau\right)^{1/2} x \\
 &= \left[\left(2 \log_e \frac{2S}{T_0}\right)^{1/2} - \frac{\log_e \tau}{\left(2 \log_e \frac{2S}{T_0}\right)^{1/2}} \right. \\
 &\quad \left. - \frac{1}{2} \frac{\log_e^2 \tau}{\left(2 \log_e \frac{2S}{T_0}\right)^{3/2}} + \dots \right] x.
 \end{aligned} \quad (16)$$

Hence, the expected extreme peak in a duration S is:

$$\begin{aligned}
 m = E[a] &= \int_{-\infty}^{\infty} ap(a) da \\
 &= x \int_0^{\infty} \left[\left(2 \log_e \frac{2S}{T_0}\right)^{1/2} - \frac{\log_e \tau}{\left(2 \log_e \frac{2S}{T_0}\right)^{1/2}} \right. \\
 &\quad \left. - \frac{1}{2} \frac{\log_e^2 \tau}{\left(2 \log_e \frac{2S}{T_0}\right)^{3/2}} + \dots \right] e^{-\tau} d\tau
 \end{aligned}$$

$$\begin{aligned}
 &= \left[\left(2 \log_e \frac{2S}{T_0}\right)^{1/2} + \frac{C}{\left(2 \log_e \frac{2S}{T_0}\right)^{1/2}} \right. \\
 &\quad \left. - \frac{1}{2} \frac{\frac{\pi^2}{6} + C^2}{\left(2 \log_e \frac{2S}{T_0}\right)^{3/2}} + \dots \right] x,
 \end{aligned} \quad (17)$$

where

$$\begin{aligned}
 C &= - \int_0^{\infty} \log \tau \exp(-\tau) d\tau = 0.5772 \\
 &= \text{Euler's constant.}
 \end{aligned}$$

Notice that the solution given by Equation (11) is equivalent to the first term of the solution given by Equation (17). Generally, the ratio between S and T_0 is large. Thus these two solutions are very close (See Example 1, Appendix). Similarly, the mean square of "a" can be found as:

$$\begin{aligned}
 E[a^2] &= \int_{-\infty}^{\infty} a^2 p(a) da \\
 &= x^2 \int_0^{\infty} \left[2 \log_e \frac{2S}{T_0} - 2 \log_e \tau \right] e^{-\tau} d\tau \\
 &= \left[2 \log_e \frac{2S}{T_0} + 2C \right] x^2.
 \end{aligned} \quad (18)$$

Thus, the variance, σ^2 , of the extreme peak in a duration S is:

$$\begin{aligned}
 \sigma^2 &= E[a^2] - m^2 \\
 &= x^2 \left[\left(\log_e \frac{2S}{T_0} + 2C \right) \right. \\
 &\quad \left. - \left(2 \log_e \frac{2S}{T_0} + 2C + \frac{C^2}{2 \log_e \frac{2S}{T_0}} \right. \right. \\
 &\quad \left. \left. - \frac{\frac{\pi^2}{6} + C^2}{2 \log_e \frac{2S}{T_0}} + \dots \right) \right]
 \end{aligned}$$

$$= x^2 \left[\frac{\pi^2}{6} \frac{1}{2 \log_e \frac{2S}{T_0}} + \dots \right], \quad (19)$$

and the standard deviation of the extreme peak in a duration S is

$$\sigma = \frac{\pi}{\sqrt{6}} \left(2 \log_e \frac{2S}{T_0} \right)^{-1/2} x. \quad (20)$$

After completing the derivation of m and σ in terms of x for the extreme peak in a specific duration S , now let us study the probabilistic distribution for such peak to occur at any arbitrary level " a ". Let us designate

$$y = -\log_e N|a|S. \quad (21)$$

From equation (15), we have:

$$\begin{aligned} y &= -\log_e \left[\frac{2S}{T_0} \exp \left(-\frac{a^2}{2x^2} \right) \right] \\ &= \frac{a^2}{2x^2} - \log_e \frac{2S}{T_0} \\ &= \frac{1}{2x^2} \left[a^2 - 2x^2 \log_e \frac{2S}{T_0} \right]. \quad (22) \end{aligned}$$

Substituting into equation (13), we get

$$F(a) = e^{-e^{-\frac{1}{2x^2} \left[a^2 - 2x^2 \log_e \frac{2S}{T_0} \right]}}. \quad (23)$$

Thus, the cumulative probability distribution of extreme peak over any double levels of " $\pm a$ " can be expressed in the form of a Gumbel distribution⁽⁵⁾ as follows:

$$\begin{aligned} F(a) &= e^{-e^{-\alpha(a^2 - \mu)}} & \text{for } a^2 \geq 0 \\ &= 0 & \text{for } a^2 < 0, \end{aligned} \quad (24)$$

where $\alpha = \frac{1}{2x^2}$ and $\mu = 2x^2 \log_e \frac{2S}{T_0}$.

NONSTATIONARY PROCESS -- TIME-VARYING $S(\omega)$

The spectral analysis of vibration records from space vehicles indicates that the power spectral density function across the ensemble varies with time. However, such variations are in a gradual transition fashion, which means that the function usually maintains a certain degree of consistency in the overall intensity and the power distribution of its contained frequencies for successive time intervals. Such intervals may have durations ranging from several seconds to several tens of seconds. As we know, when a process has small intensity change in an interval, and such an interval is relatively much longer than the periods of its autocorrelation function, then "local stationarity" can be applied to the process. (1) Thus, equivalent solutions for statistical properties in each interval are obtained by using a nominal (averaged) power spectral density function and a fixed duration. The feasibility and accuracy of such solutions can be judged by the coefficients of variation of the statistical properties so obtained. These coefficients are derived in approximate analytical terms as follows:

According to the solutions of m and σ given in equations (11) and (20), their values are determined by three parameters:

1. duration, S ,
2. expected intensity, x , and
3. mean period, T_0 , of the process.

Since S is rationally fixed, only x and T_0 remain random variables. With a given time-varying power spectral density function (which can be expressed in the form of a three-dimensional model), the variances of x and T_0 , designated as σ_x^2 and $\sigma_{T_0}^2$ respectively, and their covariance can be

estimated numerically over duration S. Now, to find the coefficients of variations for m and σ in terms of known quantities σ_x and σ_{T_0} :

$$\frac{\partial m}{\partial x} = \left(2 \log_e \frac{2S}{T_0} \right)^{1/2} = \frac{m}{x}, \quad (25)$$

$$\begin{aligned} \frac{\partial m}{\partial T_0} &= -\frac{x}{T_0} \left(2 \log_e \frac{2S}{T_0} \right)^{-1/2} \\ &= -\frac{x^2}{T_0 m}, \end{aligned} \quad (26)$$

$$\frac{\partial \sigma}{\partial x} = \frac{\pi}{\sqrt{6}} \left(2 \log_e \frac{2S}{T_0} \right)^{-1/2} = \frac{\sigma}{x}, \quad (27)$$

$$\begin{aligned} \frac{\partial \sigma}{\partial T_0} &= \frac{\pi}{\sqrt{6}} \frac{x}{T_0} \left(2 \log_e \frac{2S}{T_0} \right)^{-3/2} \\ &= \frac{\sigma}{T_0} \left(2 \log_e \frac{2S}{T_0} \right)^{-1} = \frac{\sigma}{T_0} \left(\frac{x}{m} \right)^2. \end{aligned} \quad (28)$$

Thus, based on the theoretical explanation given in references (2) and (6), the variances for random functions m and σ are found in approximate analytical terms as:

$$\begin{aligned} \text{Var}[m] &= \left(\frac{\partial m}{\partial x} \right)^2 \sigma_x^2 + \left(\frac{\partial m}{\partial T_0} \right)^2 \sigma_{T_0}^2 \\ &\quad + 2 \left(\frac{\partial m}{\partial x} \right) \left(\frac{\partial m}{\partial T_0} \right) \text{Cov}[x T_0] \\ &= \left(\frac{m}{x} \right)^2 \sigma_x^2 + \left(\frac{x^2}{T_0 m} \right)^2 \sigma_{T_0}^2 \\ &\quad - \frac{2x}{T_0} \text{Cov}[x T_0], \end{aligned} \quad (29)$$

$$\begin{aligned} \text{Var}[\sigma] &= \left(\frac{\partial \sigma}{\partial x} \right)^2 \sigma_x^2 + \left(\frac{\partial \sigma}{\partial T_0} \right)^2 \sigma_{T_0}^2 \\ &\quad + 2 \left(\frac{\partial \sigma}{\partial x} \right) \left(\frac{\partial \sigma}{\partial T_0} \right) \text{Cov}[x T_0] \\ &= \left(\frac{\sigma}{x} \right)^2 \sigma_x^2 + \left(\frac{\sigma x^2}{T_0 m^2} \right)^2 \sigma_{T_0}^2 \\ &\quad + \frac{2\sigma^2 x}{T_0 m^2} \text{Cov}[x T_0]. \end{aligned} \quad (30)$$

The coefficients of variation are found as:

$$\begin{aligned} v_m &= \frac{1}{m} \sqrt{\text{Var}[m]} \\ &= \left\{ \left(\frac{\sigma x}{x} \right)^2 + \left(\frac{x^2 \sigma_{T_0}}{T_0 m^2} \right)^2 - \frac{2x}{T_0 m^2} \text{Cov}[x T_0] \right\}^{1/2}, \end{aligned} \quad (31)$$

$$v_\sigma = \frac{1}{\sigma} \sqrt{\text{Var}[\sigma]}$$

$$\begin{aligned} &= \left\{ \left(\frac{\sigma x}{x} \right)^2 + \left(\frac{x^2 \sigma_{T_0}}{T_0 m^2} \right)^2 \right. \\ &\quad \left. + \frac{2x}{T_0 m^2} \text{Cov}[x T_0] \right\}^{1/2}, \end{aligned}$$

where quantities of x, m, and T_0 are evaluated at the "nominal" condition.

CONCLUSIONS AND APPLICATIONS

The technique has applications to space vehicle structural design and anomaly studies, which depend on the correct prediction and maximum intensity level of excitation or response. Direct measurements of time varying engine thrust, acceleration, or displacement at any location of the vehicle should be used.

Based on the theories so derived, two alternative ways are presented to get the maximum peak distribution:

1. Setting data points on the standard Gumbel distribution plots (see Appendix, Example 2), the whole distribution may easily be defined by drawing a best-fit line.
2. Obtain power spectral density functions and compute the distribution analytically (see Appendix, Example 1).

Two alternative criteria for determining dynamic loads or response for design are presented, which allows for a determination of a probabilistic oscillation intensity level:

1. A maximum intensity of oscillation which is equal to the expected value plus certain standard deviations. Let $a = m + 3\sigma$ and use "a" for design.
2. An assigned probability which indicates the confidence level for the occurrence of the maximum intensity. Let $F(a) = 0.99$, which means that in 99 out of 100 chances the maximum intensity will fall within the design limit. Then, solve equation (24) for "a" and use "a" for design.

Since any unusual energy concentrations are reflected in the power spectral density functions and eventually affect the result of the maximum intensity distribution, this technique will yield information for structural anomaly studies, as well as for structural design. Because the maximum response is analyzed by records measured directly from the site, distribution of maximum response represents a combined effect of all possible loads to the site. Thus, it saves us from the tedious and complicated work of evaluating individual loading effects. As such, errors caused by unrealistic superpositions are eliminated.

In order to demonstrate the technique, two numerical examples are presented in the Appendix. Owing to a limited number of available flight records, the first example uses only four F-1 engine thrust records from the Apollo 6 flight. Their associated power spectral density functions are attached. Even though the number of samples used is small and some non-random excitation occurred during this time interval (i.e. "POGO"), at the 95% confidence level, the Komogorov-Smirnoff goodness of fit test indicates that the assumed distribution is acceptable. The second

example uses 1,000 stationary white noise samples generated by

A. G. Brady⁽⁹⁾. Since a large number of sample simulations are not only costly, but also time consuming, we will take advantage of his work to verify our maximum peak distribution theory. Results indicate that it does indeed follow the Gumbel distribution.

APPENDIX

Numerical Examples

Two numerical examples are presented to illustrate the techniques so derived in actual engineering applications: The first example shows the procedures of estimating the distribution of the maximum intensity of the residual thrust by either analytically using the power spectral density functions, or directly using oscillation records. Results of these two approaches are compared. The second example uses extreme peak values of structural response from 1000 simulated random excitations⁽⁹⁾, and verifies that the nature of the maximum intensity indeed follows the Gumbel distribution. Both examples are treated as stationary oscillations with finite durations. As explained in the main text, the non-stationary aspects can be dealt with similarly by means of piecewise stationary procedures.

I. Example 1:

Residual thrust oscillations measured from four F-1 engines of Apollo 6 at time slice +110.00 to +120.00 (10 second duration) are used as stationary samples (Figures 1-4). Their corresponding power spectral density functions are shown in Figures 5-8. Certain properties are observed in Table 1:

TABLE 1

Sensor No.	Mean Pressure (psi)	Maximum Pressure from mean	Area Under PSD curve
D8-101	1151.17	16.7	19.1
D8-102	1154.66	14.5	27.8
D8-104	1156.00	17.0	20.0
D8-105	1151.33	13.3	21.6

Thus, the mean pressure across the ensemble is:

$$\frac{1}{4} (1151.17 + 1154.66 + 1156.00 + 1151.33) = 1153.29 \text{ psi.} \quad (33)$$

A. Analytical solutions using Power Spectral Density Functions:

From equation (1), the area under PSD curve, $S(\omega)$, is equivalent to the mean square intensity of the residual pressure. Thus the mean square intensity across the ensemble is:

$$x^2 = \left(\int_{\omega} S(\omega) d\omega \right)_{\text{ave.}} = \frac{1}{4} (19.1 + 27.8 + 20.0 + 21.6) = 22.1 \text{ (psi)}^2. \quad (34)$$

From equations (6) and (7), the expected mean frequency and its corresponding period is estimated as:

$$\omega_0 = \left(\frac{\int_{\omega} \omega^2 S(\omega) d\omega}{\int_{\omega} S(\omega) d\omega} \right)^{1/2}_{\text{ave.}} \approx 5.5 \text{ cps.} \quad (35)$$

$$\tau_0 = \frac{1}{5.5} = 0.182 \text{ sec.} \quad (36)$$

The duration of records is 10 seconds,

$$S = 10 \text{ sec.} \quad (37)$$

Thus, by evaluating the following two parameters,

$$\alpha = \frac{1}{2x^2} = \frac{1}{2(22.1)} = 0.0226, \quad (38)$$

$$\begin{aligned} \mu &= 2x^2 \log_e \frac{2S}{T_0} \\ &= 2(22.1) \log_e \frac{(2)(10)}{0.182} \\ &= (44.2) (4.7) \\ &= 207.5, \end{aligned} \quad (39)$$

the expected cumulative distribution of the maximum residual pressure "a" is defined from equation (24) as:

$$F(a) = e^{-e^{-0.0226(a^2 - 207.5)}}, \quad (40)$$

which is plotted in Figure 9 as a straight line $a^2 = \mu + \frac{1}{\alpha}$.

The mean and standard deviation of the maximum residual pressure are computed using equations (17) and (20) as:

$$\begin{aligned} m &= E[a] \\ &= \left[\left(2 \log_e \frac{2S}{T_0} \right)^{1/2} \right. \\ &\quad \left. + \frac{0.5772}{\left(2 \log_e \frac{2S}{T_0} \right)^{1/2}} + \dots \right] x \end{aligned}$$

$$= \left(2x^2 \log_e \frac{2S}{T_0} \right)^{1/2} + \frac{0.5772x^2}{\left(2x^2 \log_e \frac{2S}{T_0} \right)^{1/2}} + \dots$$

$$= \frac{1}{2} + \frac{0.5772x^2}{\frac{1}{2}}$$

$$= \sqrt{207.5} + \frac{(0.5772)(22.1)}{\sqrt{207.5}}$$

$$= 14.4 + 0.885 = 15.29 \text{ psi}, \quad (41)$$

$$\sigma = \frac{\pi}{\sqrt{6}} \left(2 \log_e \frac{2S}{T_0} \right)^{-1/2} x$$

$$= \frac{\pi}{\sqrt{6}} \frac{x^2}{\left(2x^2 \log_e \frac{2S}{T_0} \right)^{1/2}}$$

$$= \frac{\pi}{\sqrt{6}} \frac{x^2}{\frac{1}{2}}$$

$$= 1.283 \left(\frac{22.1}{\sqrt{207.5}} \right) = 1.97 \text{ psi.}$$

(42)

Notice that the second term on the right in the computation of the mean is 0.885, which is much smaller in comparison with the first term, 14.4. Thus, equation (11) is an acceptable approximation of equation (17).

Based on information so computed, two criteria for determining maximum intensity level of engine thrust, which may be used in design are illustrated as follows:

- 1) Use the mean of maximum pressure plus certain (say 1) standard deviations. Thus,

$$\begin{aligned} 1153.29 + 15.29 + 1 \times 1.97 \\ = 1170.55 \text{ psi} \end{aligned} \quad (43)$$

is the design pressure. From equation (40) it represents a confidence level with a probability of 0.86:

$$(15.29 + 1.97)^2 = 300$$

$$F(\sqrt{300}) = 0.86. \quad (44)$$

- 2) Use assigned confidence level. Let the probability of occurrence be 0.8,

$$F(a) = 0.80. \quad (45)$$

Using equation (40) or curve in Figure 9 we get

$$\begin{aligned} a^2 &= 276 \\ a &= 16.6 \text{ psi}, \end{aligned} \quad (46)$$

Thus the design pressure is

$$1153.29 + 16.6 = 1169.9 \text{ psi}, \quad (47)$$

- B. Direct Solutions using Data Plotted from Oscillation Records:

The maximum pressures, one value per record and measured from mean value, are listed in ascending order. Their cumulative probabilities are computed as shown in Table 2.

N = total number of samples. Then plot the data points on the special Gumbel paper (see Figure 9) using computed a^2 and $F(a)$. Thus, a distribution of the maximum pressure may be obtained by drawing a best fit line through these data points.

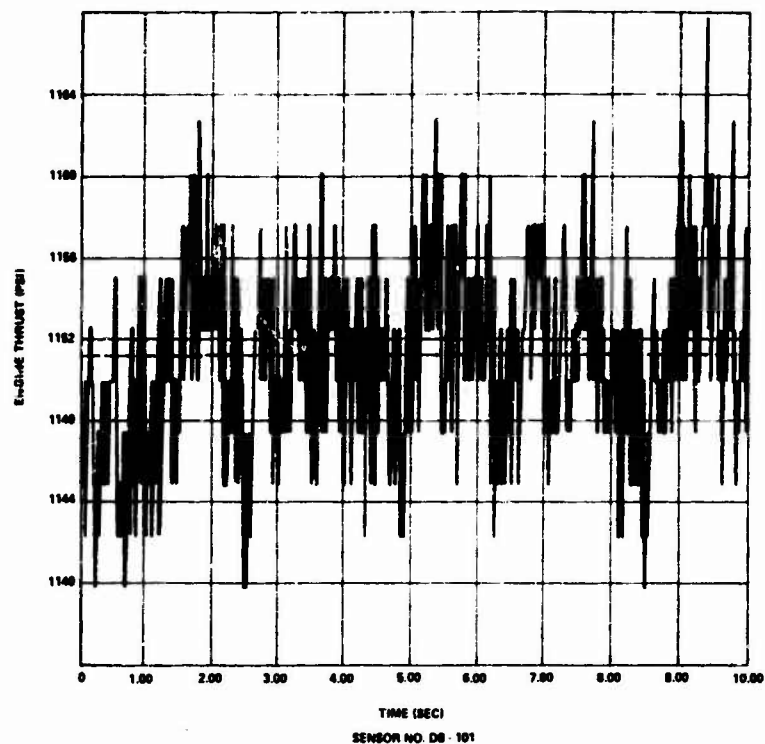


FIGURE 1-

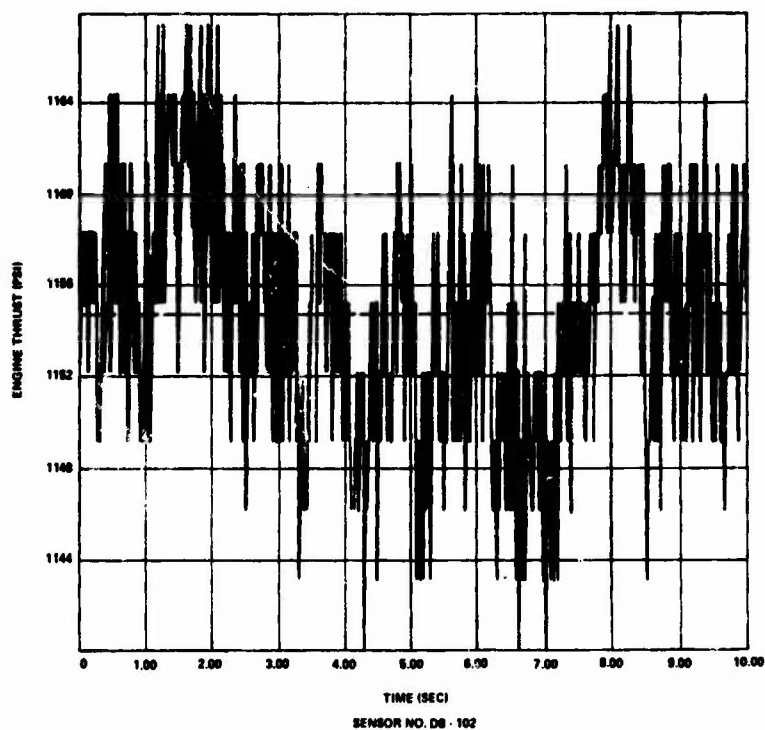


FIGURE 2-

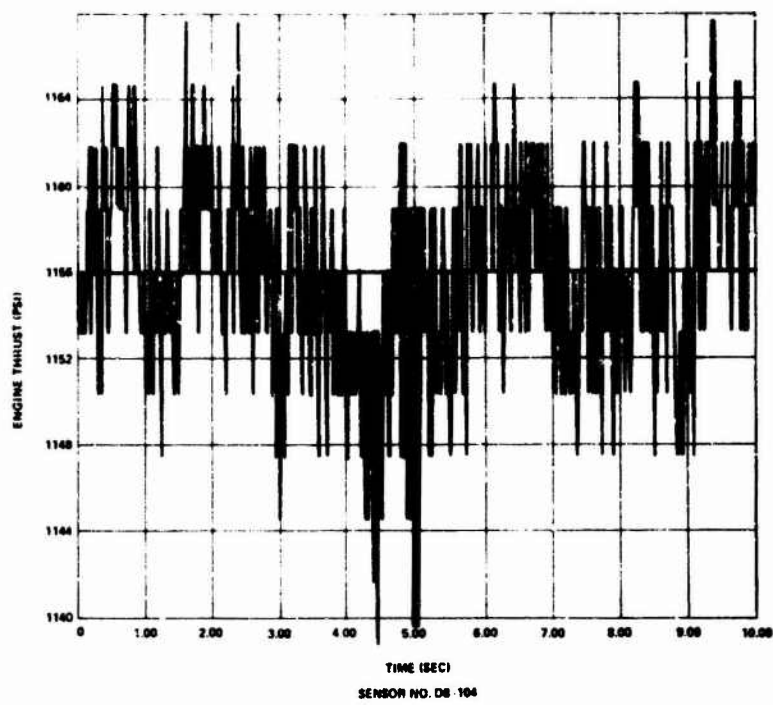


FIGURE 3-

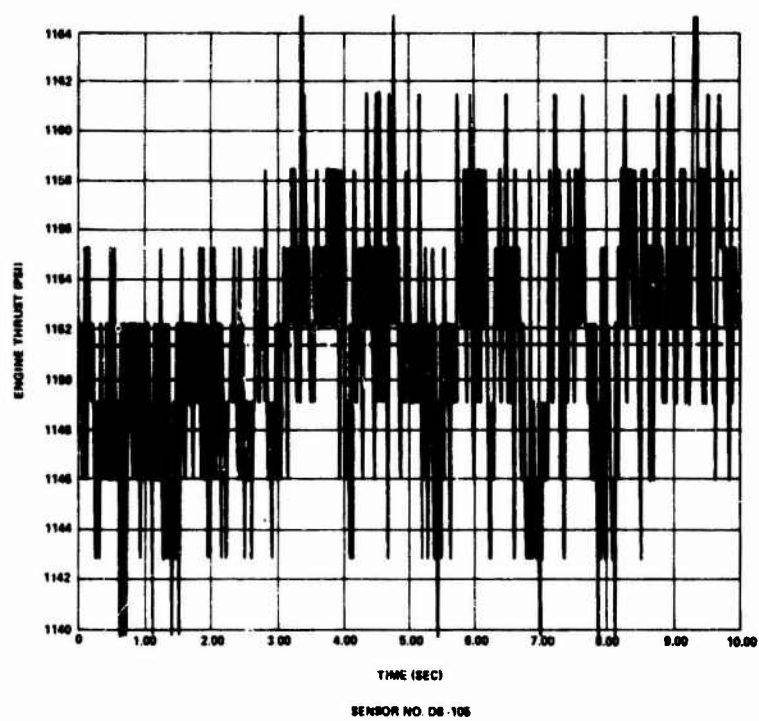


FIGURE 4-

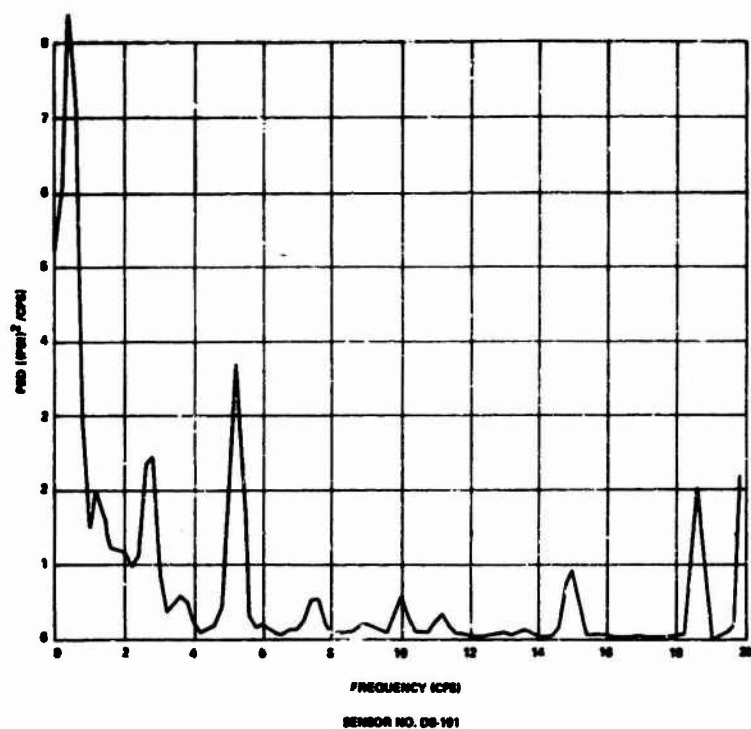


FIGURE 5-

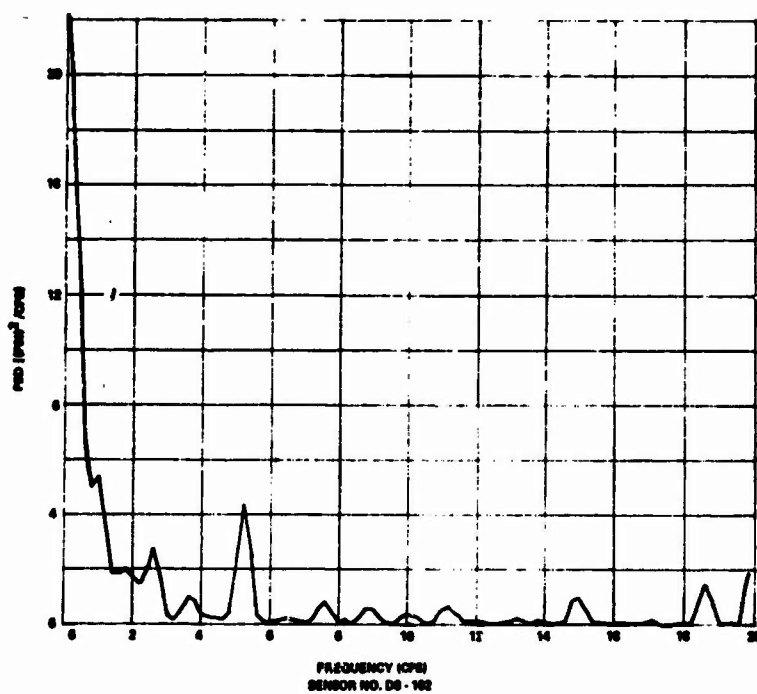


FIGURE 6-

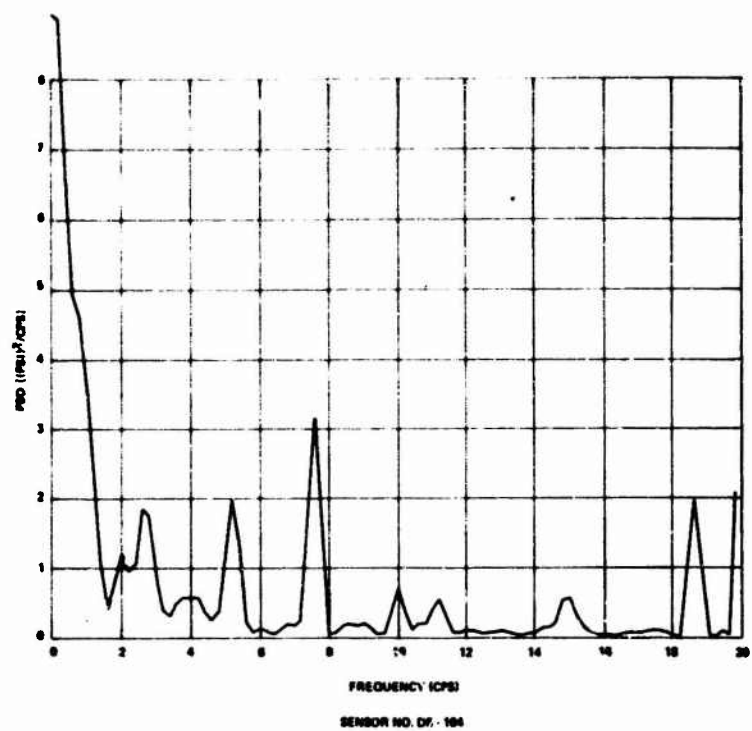


FIGURE 7-

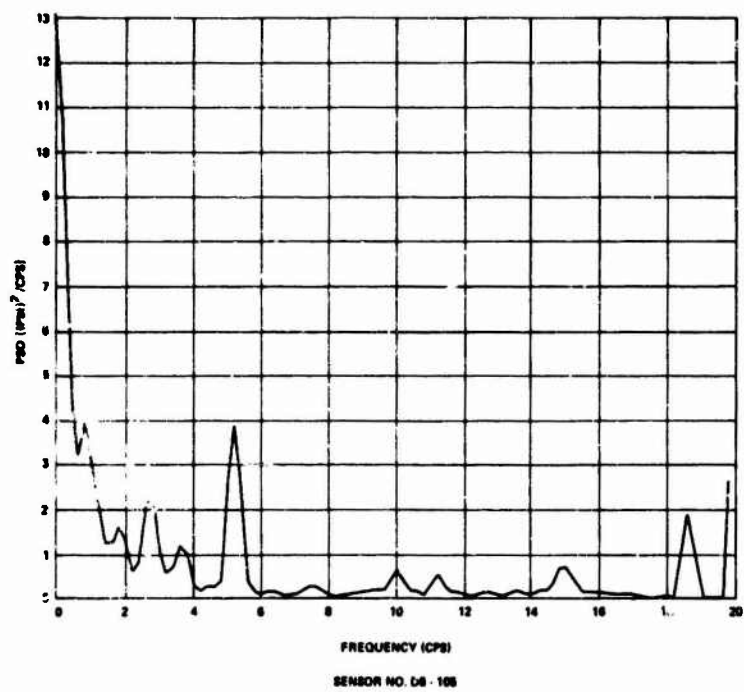


FIGURE 8-

TABLE 2

Order	Maximum Pressure		Freq. of Occurrence	Cumulative Freq. Ω	$F(a) = \frac{\Omega}{1+N}$
i	a	a^2			
1	13.3	176	1	1	0.2
2	14.5	210	1	2	0.4
3	16.7	278	1	3	0.6
4	17.0	288	1	4	0.8

The mean and standard deviation of the maximum pressure can also be computed directly from oscillation records as:

$$m = \frac{1}{4} (13.3 + 14.5 + 16.7 + 17.0) = 15.4 \quad (48)$$

$$\sigma = \frac{1}{4} \left[\overline{2.1^2} + \overline{0.9^2} + \overline{1.3^2} + \overline{1.6^2} \right]^{1/2} = 1.53. \quad (49)$$

C. Comparison between Analytical Solutions and Direct Solutions:

Even though the number of samples used is extremely small, the results are encouraging:

	Analytical Solution	Direct from Data
m	15.29	15.4
σ	1.97	1.53

The distribution of the maximum pressure obtained analytically is shown by a straight line in Figure 9. Now, comparing this line with the data points obtained directly from records, it is found that at 95% confidence level (or 5% significant level), the Kolmogorov-Smirnoff goodness of fit test indicates that the computed distribution is acceptable.

II. Example 2:

Now, let us study 1000 stationary samples simulated by A. G. Brady⁽⁹⁾. Values in Table 3 are from Brady's results of the maximum response of a single degree-of-freedom linear structure having a natural period of one second, with 2% of critical damping.

By plotting the square value of the maximum response " a^2 ", and their corresponding cumulative distribution " $F(a)$ " on the Gumbel paper (See Figure 10.), we can draw a best fit line of

$$a^2 = 275 + 12.34 y ,$$

which gives

$$\mu = 275 ,$$

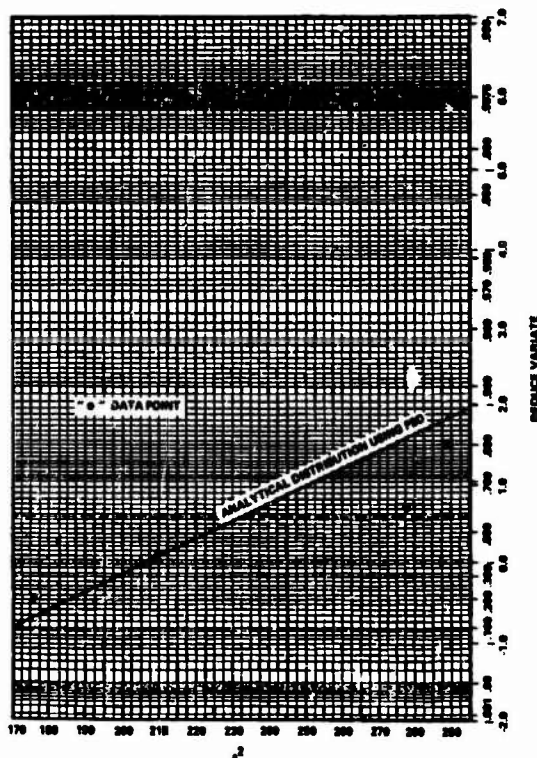


FIGURE 9-

TABLE 3

Maximum Response	a^2	Freq. of Occurrence	Cumulative Freq. Ω	$F(a) = \frac{\Omega}{1+N}^*$
a				
10	100	3	3	0.0029
11	121	8	11	0.0109
12	144	22	33	0.0329
13	169	49	82	0.0819
14	196	60	142	0.1418
15	225	91	233	0.2327
16	256	104	337	0.3366
17	289	112	449	0.4485
18	324	112	561	0.5604
19	361	104	665	0.6643
20	400	88	753	0.7522
21	441	56	809	0.8081
22	484	47	856	0.8551
23	529	37	893	0.8921
24	576	32	925	0.9240
25	625	25	950	0.9490
26	676	12	962	0.9610
27	729	14	976	0.9750
28	784	10	986	0.9850
29	841	3	989	0.9880
30	900	4	993	0.9920
31	961	4	997	0.9960
32	1024	2	999	0.9980
33	1089	1	1000	0.9990

*N = Total number of records = 1000.

$$\alpha = \frac{1}{12.34} = 0.0081.$$

$$F(a) = e^{-0.0081(a^2-275)}$$

The reading at point A is $a_A^2 = 275$, and at point B is $a_B^2 = 345$. Hence, the mean, standard deviation, and the distribution of the maximum response are:

$$m = \mu^{1/2}$$

$$= \sqrt{275} = 16.6,$$

$$\sigma = \sqrt{345 - 275} = \sqrt{70} = 8.37,$$

At 95% confidence level (or 5% significant level), the Komogorov-Smirnoff goodness of fit test indicates that the assumed distribution is acceptable.

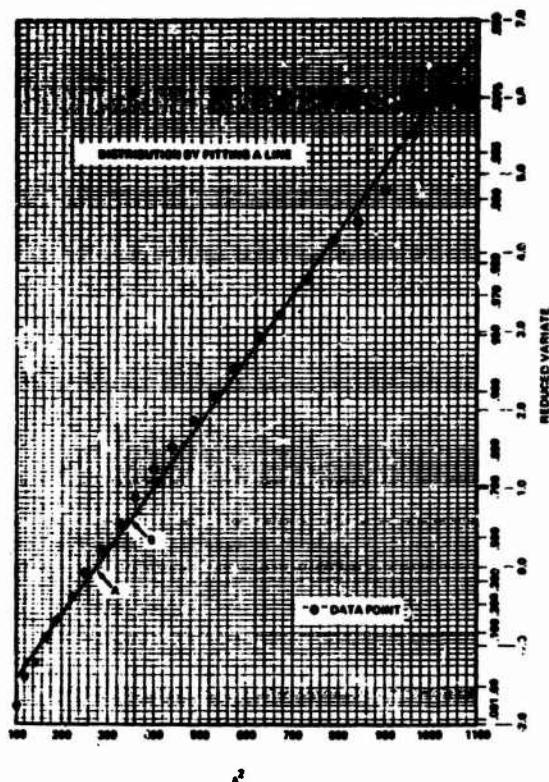


FIGURE 10-

NOTATIONS

- a An arbitrary intensity level for the process $Q(t)$.
- c Euler's constant.
- $E[a^2]$ Mean square of " a ".
- $F(a)$ Cumulative distribution of extreme peak up to an intensity level " a " in a duration S of the process $Q(t)$.
- m The expected intensity of extreme peak in a duration S of the process $Q(t)$.
- N_a The expected number of crossings of $Q(t)$ per unit time over an arbitrary intensity level ($Q(t)=a$) with positive slope.
- $p(Q, \dot{Q})$ The probability density function of $Q(t)$ and $\dot{Q}(t)$ in joint distribution.
- $Q(t)$ A stationary random process with Gaussian distribution and zero mean.

- $S(\omega)$ The power spectral density function of the process $Q(t)$.
- t Time.
- T_0 The equivalent period of frequency ω_0 .
- x Root mean square of the process $Q(t)$, or the averaged intensity of the process.
- α A parameter in Gumbel distribution, which is defined as $\frac{1}{2x^2}$ in the distribution of extreme peak of the process $Q(t)$.
- μ A parameter in Gumbel distribution, which is defined as $2x^2 \log_e \frac{2S}{T_0}$ in the distribution of extreme peak of the process $Q(t)$.
- v_m Coefficient of variation for m .
- v_σ Coefficient of variation for σ .
- σ The standard deviation of the extreme peak in a duration S of the process $Q(t)$.
- σ_Q Standard deviation of the process $Q(t)$.
- τ The expected number of crossings of the process $Q(t)$ with positive slope over double intensity levels ($Q(t)=+a$ and $Q(t)=-a$) in a duration S .
- ω Vibration frequency.
- ω_0 Mean frequency of the process $Q(t)$.

REFERENCES

1. Bendat, J. S. and A. G. Piersol, (1967). Measurement and Analysis of Random Data, John Wiley, (New York).
2. Cornell, C. A. and J. R. Benjamin, (1968). Probability, Statistics, and Decision for Civil Engineers, McGraw-Hill, (New York).
3. Cramer, H and M. R. Leadbetter, (1967). Stationary and Related Stochastic Processes, John Wiley, (New York).

4. Crandall, S. H. and W. D. Mark, (1963). Random Vibration in Mechanical Systems, Academic Press. (New York;).
5. Gumbel, E. J. (1958). Extreme Value Statistics, Columbia University Press, (New York).
6. Hou, S. N., (1968). Earthquake Simulation Models and Their Applications, Research Report, R68-17, MIT (Cambridge Mass.).
7. Lin, Y. K., (1967). Probabilistic Theory of Structural Dynamics, McGraw-Hill, (New York).
8. Parzen, E., (1962). Stochastic Process, Holden-Day, (San Francisco.).
9. Brady, A. G., (1966). Studies of Response to Earthquake Ground Motion, Calif. Inst. of Tech., Eng. Res. Lab., Ph.D. thesis, (Pasadena, California).

STIFFNESS MATRIX OF A BEAM - COLUMN INCLUDING SHEAR DEFORMATION

H. Saunders
Re-entry and Environmental Systems Division
General Electric Company
Philadelphia, Pennsylvania

This paper presents the derivation and stiffness matrices required for analyzing beam elements including shear deformation with in-plane loads used in stability and vibration problems. The previous published papers neglect the interaction between the in-plane load and the beam, thus the resulting stiffness matrices would be greatly in error when the axial load is an appreciable proportion of the compressive buckling load of the beam element. The consistent mass matrices (rotational and translational) are derived and can be employed in the solution of vibration problems.

INTRODUCTION

The extensive application to the dynamic analysis of vibrating continuous elastic systems implies writing the equation of motion for unrestrained modes of the structure as well as the support restraints. These equations of motion can be exhibited in matrix form. A considerable amount of pertinent theory has been developed and published in matrix analysis of structure; the pioneering efforts in the development of stiffness and flexibility methods were conducted by Argyris⁽¹⁾. The predominant applications to the "transfer matrix" approach is due to Pestel⁽²⁾ and his students.

Until recent years, very little attention was paid to the analysis of a combined axial load-beam problem. Silverstein⁽³⁾ investigated and published the first vibration analysis of a beam-column for a uniform beam including both shear deformation and rotary inertia in "transfer matrix" form. At about the same time, Saunders⁽⁴⁾ published the static case of a beam-column in "transfer matrix" form but did not include shear deformation. Saunders⁽⁵⁾ in a later publication extended Ref. (3) to a beam on many supports. Pestel and Leckie⁽²⁾ present the transfer matrix solution of a uniform beam containing rotary inertia and shear deformation but neglect any reference to axial loading. Martin⁽⁶⁾ furnishes an excellent history of beam-column theory but slants his analysis towards the buckling solution of beams where the in-plane axial loads are a mere fraction of the buckling load. Ross⁽⁷⁾ considers the axial load as being an integral part of the beam-column in a direct stiffness solution but neglects

shear deformation. Przemieniecki⁽⁸⁾ examined in detail, the three-dimension solution of a uniform beam-column including shear deformation but considered the axial loads to be extremely small and thus uncoupled from the general beam-column solution. The object of this paper is to extend the previous efforts by Ross and Przemieniecki by including shear deformation and axial load for a uniform beam in the "direct stiffness approach" to both static and dynamic problems.

McCalley⁽⁹⁾ and Archer⁽¹⁰⁾ have derived expressions for the "consistent mass matrix" for the uniform beam by employing the deformation function which originates in deriving the stiffness matrix. In a subsequent section, the "consistent mass matrix" is further considered and the translational and rotational matrix comprising the total mass matrix is derived in the Appendices.

The general theory of the direct stiffness method is first introduced. The equations of motion are expressed in matrix form and developed for use in problems of dynamics. By applying the known rules of finite element analysis, beam-columns having various types of support restraints may be solved on the digital computer.

MATHEMATICAL ANALYSIS

Determination of the Dynamic Equation of Motion

We consider an elastic system that is subjected to dynamic loading and has elastic displacements

which are functions of both coordinates and time. By proper application of d'Alembert's principle to the condition of equilibrium and upon further consideration of the inertia forces, the dynamic equation (7) can be expressed in matrix form

$$M\ddot{u} + Ku = N = N_d + N_a \quad (1)$$

where

N is a column matrix of equivalent forces: N_d represents the disturbing forces, N_a represents the aerodynamic forces, M is the mass matrix, and K is stiffness matrix.

For the case of free vibrations, $N = 0$. Eq. (1) becomes

$$M\ddot{u} + Ku = 0 \quad (2)$$

This differential equation can be solved by assuming a solution of the form

$$u = ae^{i\omega t} \quad (3)$$

where a is a column matrix of the amplitudes of the displacement u and ω is the circular oscillatory frequency.

Substituting Eq. (3) into (2), one obtains

$$(-\omega^2 M + K)a = 0 \quad (4)$$

In order for Eq. (4) to have a non-trivial solution, it is necessary that

$$|K - \omega^2 M| = 0. \quad (5)$$

This equation is commonly denoted as the frequency determinant from which the natural frequencies may be obtained. For a more detailed discussion, see Ref. 8.

Development of the Element Stiffness Matrix

Consider an idealized element of a uniform beam-column as shown in Figure 1. Development of an elemental stiffness matrix of the following form is desired:

$$\begin{bmatrix} V_1 \\ M_1 \\ V_2 \\ M_2 \end{bmatrix} = \begin{bmatrix} k_{11} & k_{12} & k_{13} & k_{14} \\ k_{21} & k_{22} & k_{23} & k_{24} \\ k_{31} & k_{32} & k_{33} & k_{34} \\ k_{41} & k_{42} & k_{43} & k_{44} \end{bmatrix} \begin{bmatrix} y_1 \\ \theta_1 \\ y_2 \\ \theta_2 \end{bmatrix} \quad (6a)$$

or in a simplified matrix notation

$$\{V\} = [K] \{y\} \quad (6b)$$

in which V_1 , M_1 , y_1 , and θ_1 represent the shear force, moment deflection and rotation due to beam bending respectively and k_{ij} signifies the elemental force (moment) at the end of the cantilevered beam due to a unit displacement (rotation) at its free end.

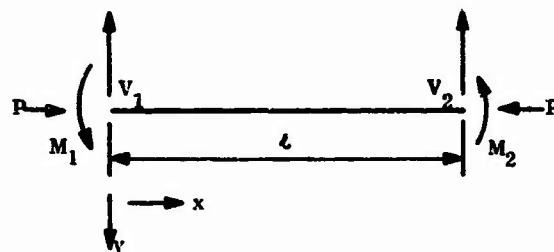


Fig. 1 - Idealized Element of a Uniform Beam-Column

at any point x

$$\frac{M_x}{EI} = \theta'_x \quad (7)$$

The total bending angle is expressed by

$$y'_x = \theta_x + \gamma_x \quad (8)$$

where γ_x is rotation due to shearing strain and

$$\gamma_x = -\frac{S_x}{KAG} \quad (9)$$

S_x is the total shear at point x on the beam-column and

$$S_x = V_1 - P \frac{dy}{dx} \quad (10)$$

$$\therefore \gamma_x = -\frac{V_1 - P \frac{dy}{dx}}{KAG} \quad (11a)$$

$$= -\frac{V_1}{KAG} + \frac{Py_x}{KAG} + \frac{P\theta_x}{KAG} \quad (11b)$$

thus

$$\gamma_x = -\frac{V_1}{KAG(1 - P/KAG)} + \frac{\theta_x}{[(KAG/P) - 1]} \quad (11c)$$

Differentiating Eq. (11c) and substituting into Eq. (8)

$$y_x'' = \theta_x' \left(\frac{1}{1 - P/KAG} \right) \quad (12)$$

The moment at any point x is expressed by

$$M_x = V_1 x - M_1 + P(y_1 - y_x) \quad (13)$$

Substituting Eq. (12) into Eq. (7) and simplifying

$$y_x'' + \frac{Py_x}{EI(1 - P/KAG)} = \frac{V_1 x - M_1 + Py_1}{EI(1 - P/KAG)} \quad (14)$$

Let

$$\beta^2 = \frac{P}{EI(1 - P/KAG)} = \frac{P}{EIR} \quad (15a)$$

where

$$R = 1 - \frac{P}{KAG} \quad (15b)$$

Equation (14) simplifies to

$$y_x'' + \beta^2 y_x = \beta^2 y_1 - \frac{M_1 \beta^2}{P} + \frac{V_1 \beta^2 x}{P} \quad (16)$$

The solution for Eq. (16) is

$$y_x = C \sin \beta x + D \cos \beta x + y_1 - \frac{M_1}{P} + \frac{V_1 x}{P} \quad (17)$$

Differentiating Eq. (17) and employing Eqs. (8) and (10)

$$\begin{aligned} \theta_x = y_x' - \gamma_x &= C\beta \cos \beta x - D\beta \sin \beta x + \frac{V_1}{P} \\ &+ \frac{V_1}{KAG} - \frac{P}{KAG} \left(C\beta \cos \beta x - D\beta \sin \beta x + \frac{V_1}{P} \right) \end{aligned} \quad (18a)$$

$$\begin{aligned} &= C\beta \left(1 - \frac{P}{KAG} \right) \cos \beta x - D\beta \left(1 - \frac{P}{KAG} \right) \sin \beta x \\ &+ \frac{V_1}{P} \end{aligned} \quad (18b)$$

$$= C\beta R \cos \beta x - D\beta R \sin \beta x + \frac{V_1}{P} \quad (18c)$$

Consider the beam-column to be cantilevered from sta. 2 with a unit deflection y_1 at sta. 1 ($x = 0$)

The boundary conditions for the slope and deflection as shown in Figure 2 are:

$$x = 0$$

$$y_x = y_1, \theta_x = \theta_1 = 0$$

$$x = l$$

$$y_x = y_2 = 0, \theta_x = \theta_2 = 0$$

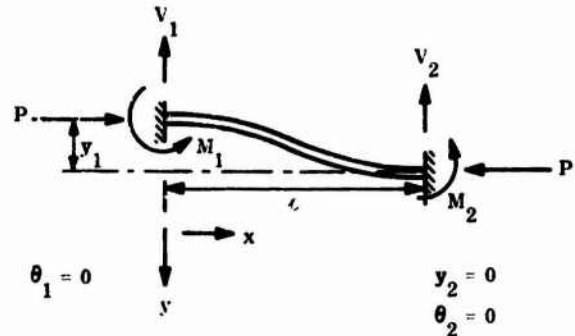


Fig. 2 - Beam-column Element Cantilevered From Sta. 2 With Unit Deflection at Sta. 1

Substituting the above boundary conditions for θ_1 and θ_2 into Eq. (18c), this results in

$$\theta_1 = 0 = C\beta R + \frac{V_1}{P} \quad (19a)$$

\therefore

$$C = - \frac{V_1}{P\beta R} \quad (19b)$$

$$\theta_2 = 0 = C\beta R \cos \beta l - D\beta R \sin \beta l + \frac{V_1}{P} \quad (20a)$$

\therefore

$$D = \frac{V_1}{P\beta R} \frac{(1 - \cos \beta l)}{\sin \beta l} \quad (20b)$$

In a similar manner, the values for y_1 and y_2 are substituted in Eq. (17) and yield

$$y_1 = D - \frac{M_1}{P} + y_1 \quad (21a)$$

or

$$D = \frac{M_1}{P} \quad (21b)$$

$$y_2 = 0 = C \cos \beta l + D \sin \beta l + \frac{V_1 l}{P}$$

$$- \frac{M_1}{P} + y_1 \quad (22a)$$

$$y_1 = \frac{M_1}{P} - \frac{V_1}{P} l - C \sin \beta l - D \cos \beta l \quad (22b)$$

or

$$y_1 = D(1 - \cos \beta l) - \frac{V_1}{P} l - C \sin \beta l \quad (22c)$$

Substituting the expressions for C and D as previously derived in Eqs. (19b) and (20b) into Eq. (22c), we obtain

$$y_1 = \frac{V_1}{P\beta R} \sin \beta l + \frac{V_1}{P\beta R} \frac{(1 - \cos \beta l)^2}{\sin \beta l}$$

$$- \frac{V_1}{P} l \quad (23a)$$

This can be further simplified to

$$y_1 = \frac{V_1 z}{P\beta R \sin \beta l} \quad (23b)$$

where

$$z = 2(1 - \cos \beta l) - l\beta R \sin \beta l \quad (24a)$$

$$= \sin \beta l (2 \times \tan \frac{\beta l}{2} - l\beta R) \quad (24b)$$

By definition, the expression for the stiffness coefficient k_{11} becomes

$$k_{11} = \frac{V_1}{y_1} = \frac{P}{z} (\beta R \sin \beta l) \quad (25)$$

The moment M_1 can be expressed in terms of V_1 by utilizing Eqs. (20b) and (21b).

$$\therefore \frac{V_1}{P} = \frac{M_1}{P} \frac{\beta R \sin \beta l}{1 - \cos \beta l} \quad (26)$$

A similar expression for stiffness coefficient k_{21} can be determined by substituting Eq. (26) into Eq. (23b)

$$k_{21} = \frac{M_1}{y_1} = \frac{P}{z} (1 - \cos \beta l) \quad (27)$$

In order to ascertain the stiffness coefficients associated with the rotation θ_1 , the beam is now subjected to the bending moments and shears (Figure 3).

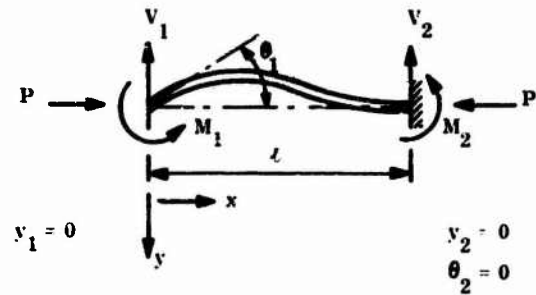


Fig. 3 - Beam-column Element Cantilevered From Sta. 2 With Unit Rotation at Sta. 1

The boundary conditions are illustrated in Figure 3.

Substituting the boundary conditions y_1 and y_2 into Eq. (17)

$$y_1 = 0 = D - \frac{M_1}{P} \quad (28a)$$

$$\therefore D = \frac{M_1}{P} \quad (28b)$$

$$y_2 = 0 = C \sin \beta l + D \cos \beta l - \frac{M_1}{P} + \frac{V_1}{P} l \quad (28c)$$

Employing Eq. (28c), we arrive at

$$-C \sin \beta l + D(1 - \cos \beta l) = \frac{V_1}{P} l \quad (28d)$$

In a similar manner by utilizing the value of θ_2 at $x = l$

$$\theta_2 = 0 = C\beta R \cos \beta l - D\beta R \sin \beta l + \frac{V_1}{P} \quad (29a)$$

\therefore

$$C\beta R \cos \beta l - D\beta R \sin \beta l = -\frac{V_1}{P} \quad (29b)$$

We obtain the equivalent expressions for C and D by solving Eqs. (28d) and (29b) simultaneously.

$$\text{i.e., } C = -\frac{V_1}{P\beta R} \left[\frac{l\beta R \cos \beta l - 1 + \cos \beta l}{1 - \cos \beta l} \right] \quad (30a)$$

and

$$D = -\frac{V_1}{P\beta R} \left[\frac{\ell\beta R \cos \beta\ell - \sin \beta\ell}{1 - \cos \beta\ell} \right] \quad (30b)$$

The important expression for θ_1 can be obtained by employing Eq. (18c).

$$\theta_1 = C\beta R + \frac{V_1}{P} \quad (31a)$$

Substituting the expression for C from Eq. (30a) and simplifying, one obtains

$$\theta_1 = \frac{V_1}{P} \left(\frac{z}{1 - \cos \beta\ell} \right) \quad (31b)$$

The stiffness coefficient k_{12} is derived from the above equation.

$$k_{12} = \frac{V_1}{\theta_1} = \frac{P}{z} (1 - \cos \beta\ell) \quad (32)$$

This checks Eq. (27) and also follows from the well known Maxwell reciprocal theorem (Ref. 7). By employing Eqs. (28b) and (30b), M_1 can be obtained in terms of V_1 .

$$\frac{V_1}{P} = \frac{M_1\beta R}{P} \left[\frac{1 - \cos \beta\ell}{\sin \beta\ell - \ell\beta R \cos \beta\ell} \right] \quad (33)$$

Substituting Eq. (33) into Eq. (31b), the stiffness coefficient k_{22} is

$$k_{22} = \frac{M_1}{\theta_1} = \frac{P}{z} \left[\frac{\sin \beta\ell}{\beta R} - \ell \cos \beta\ell \right] \quad (34)$$

The reactions for this beam-column element can be determined by applying equilibrium conditions to the force system (Ref. 12).

$$V_2 = -V_1 \quad (35)$$

$$-M_1 - M_2 + V_1\ell + Py_1 - Py_2 = 0 \quad (36a)$$

or

$$M_2 = -M_1 + V_1\ell + Py_1 - Py_2 \quad (36b)$$

The stiffness coefficient k_{31} can be obtained from Eq. (35).

$$k_{31} = \frac{V_2}{y_1} = -\frac{V_1}{y_1} = -\frac{P}{z} (\beta R \sin \beta\ell) \quad (37)$$

In a similar manner, the stiffness coefficient for k_{41} becomes

$$k_{41} = \frac{M_2}{y_1} = -\frac{M_1}{y_1} + \frac{V_1\ell}{y_1} + \frac{Py_1}{y_1} - \frac{Py_2}{y_1} \quad (38)$$

Since $y_2 = 0$, Eq. 38 can be simplified to

$$k_{41} = \frac{P}{z} (1 - \cos \beta\ell) \quad (39)$$

In a similar manner

$$k_{32} = -\frac{V_1}{\theta_1} = -\frac{P}{z} (1 - \cos \beta\ell) \quad (40)$$

The stiffness expression for k_{42} can be readily obtained by utilizing Eq. (36b) and noting that the derivation of θ_2 (Figure 3) requires that $y_1 = y_2 = 0$.

Therefore:

$$\begin{aligned} k_{42} &= \frac{M_2}{\theta_2} = \frac{-M_1 + V_1\ell}{\theta_2} \\ &= \frac{P}{z} \left[\ell - \frac{\sin \beta\ell}{\beta R} \right] \end{aligned} \quad (41)$$

Similarly if the beam-column is cantilevered from Sta. 1, Figure 4, the use of the differential equations for y_x , θ_x and the conditions of symmetry yield the following stiffness element coefficients.

$$k_{33} = k_{11} = \frac{P}{z} (\beta R \sin \beta\ell) \quad (42)$$

$$k_{34} = k_{43} = -k_{21} = -\frac{P}{z} (1 - \cos \beta\ell) \quad (43)$$

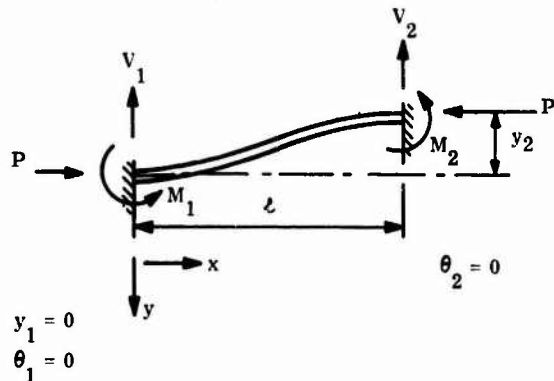


Fig. 4 - Beam-column Element Cantilevered From Sta. 1 With Unit Deflection at Sta. 2

if the deflection of the left side of the beam-column Figure 5 is equal to zero, it is immediately apparent from conditions of symmetry that

$$k_{44} = k_{22} = \frac{P}{z} \left(\frac{\sin \beta l}{\beta R} - l \cos \beta l \right) \quad (44)$$

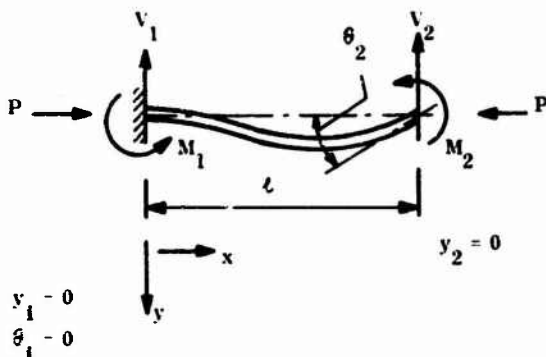


Fig. 5 - Beam-column Cantilevered From Sta. 1 With Unit Rotation at Sta. 2

The results obtained in the preceding subsections are now assembled into a matrix equation relating the elemental forces (moments) to their corresponding displacements (rotations) for the beam-column.

$$\begin{bmatrix} V_1 \\ M_1 \\ V_2 \\ M_2 \end{bmatrix} = \frac{P}{z} \begin{bmatrix} \beta R \sin \beta l & 1 - \cos \beta l & -\beta R \sin \beta l & 1 - \cos \beta l \\ 1 - \cos \beta l & \frac{\sin \beta l}{\beta R} - l \cos \beta l & -(1 - \cos \beta l) & l - \frac{\sin \beta l}{\beta R} \\ -\beta R \sin \beta l & -(1 - \cos \beta l) & \beta R \sin \beta l & -(1 - \cos \beta l) \\ 1 - \cos \beta l & l - \frac{\sin \beta l}{\beta R} & -(1 - \cos \beta l) & \frac{\sin \beta l}{\beta R} - l \cos \beta l \end{bmatrix} \begin{bmatrix} y_1 \\ \theta_1 \\ y_2 \\ \theta_2 \end{bmatrix} \quad (45)$$

Martin (12) and Gerard (13) employ different sign conventions for the positive moments and shears at the end of the beam element. This will affect some of the signs in the k_{ij} stiffness elements.

Consistent Mass Matrix

Although mass lumping at discrete points is in common use in depicting continuous structures for vibration analysis, McCalley (9) and Archer (10) claim that the use of the consistent mass matrix is more realistic. Mains (11) and a number of other investigators claim that the tremendous amount of additional work necessary in determining the terms of the translational and rotational mass matrices are

not worth the effort. To accommodate the adherents of the consistent mass matrix, the translation mass matrix (T_t) is derived in Appendix A and the rotational mass matrix (T_r) is derived in Appendix B. The mathematical handling and substitution of the various forms comprising the solution of the complete matrices is left to the interested reader. The total kinetic energy T for the beam-column element is the sum of the translational and rotational energy.

$$T = T_t + T_r \quad (46)$$

Series Expansion Technique

For digital computer applications, it is found that a polynomial expansion is much simpler to apply in numerical calculations. The original stiffness matrix, Eq. (45), is now expressed by expanding the trigonometric expressions in their equivalent series. After much mathematical manipulation and simplification, the stiffness elements of Eq. (45) reduce to

$$\begin{aligned} k_{11} &= \frac{P}{z} (\beta R \sin \beta l) \\ &= \frac{Pl}{R} \left\{ (1+R) \left(\frac{R}{l} \right)^2 - (\beta l)^2 \left(\frac{R}{l} \right)^2 \right. \\ &\quad \left. - \frac{(\beta l)^4}{120} \left(\frac{R}{l} \right)^2 \right\} \end{aligned} \quad (47)$$

$$k_{11} = -k_{13} = -k_{31} = k_{33} \quad (48)$$

$$\begin{aligned} k_{12} &= \frac{P}{z} (1 - \cos \beta l) \\ &= \frac{Pl}{R} \left\{ \frac{(1+R)}{2} \left(\frac{R}{l} \right) + \frac{(\beta l)^2}{2} \left(\frac{R}{l} \right)^2 \right. \\ &\quad \left. + \frac{(\beta l)^4 R}{24} \left[\frac{R}{5} - \frac{1}{6} \right] \right\} \end{aligned} \quad (49)$$

$$\begin{aligned} k_{12} &= k_{21} = -k_{32} = -k_{23} = k_{41} = -k_{43} \\ &= -k_{34} = k_{14} \end{aligned} \quad (50)$$

$$\begin{aligned} k_{22} &= \frac{P}{z} \left[\frac{\sin \beta l}{\beta R} - l \cos \beta l \right] \\ &= \frac{Pl}{R} \left\{ \frac{(1+R)}{(\beta l)^2} + \frac{4R^2 + 5R - 1}{12} \right. \\ &\quad \left. - \frac{(\beta l)^2}{360} (8R^2 - 5R + 3) \right\} \end{aligned} \quad (51)$$

$$k_{22} = k_{44} \quad (52)$$

$$k_{24} = \frac{P}{z} \left(4 - \frac{\sin \beta L}{\beta R} \right)$$

$$= \frac{P L}{R} \left\{ \frac{(R^2 - 1)}{(\beta L)^2} + \frac{(\beta L)^2}{12} (2R^2 + R + 1) \right.$$

$$\left. + \frac{(\beta L)^4}{360} (7R^2 - R + 3) \right\} \quad (53)$$

$$k_{24} = k_{42} \quad (54)$$

Dr. Ross (Ref. 7) explains at great length the significance of the series technique expansion for the beam-column element (no shear deformation). He points out the dependencies between a long beam approximation, short beam approximation, and the actual trigonometric stiffness relationships.

CONCLUSIONS

A matrix solution by the discrete beam element analysis for the static and vibration analysis of an elastic beam-column system having in-plane compressive load including shear deformation has been presented. The basic stiffness elements are then expanded into series approximations that can be applied in numerical calculations. Although not stated herein, the buckling of a beam-column in the static sense can be obtained by using the stiffness matrix. Since a number of analysts employ consistent mass matrix (translational and rotational), the matrix expressions are derived in the appendices. If the shear deformation is excluded, the stiffness matrices reduce to the well known relationship of a simple beam-column as detailed in the book by Weaver and Gere (Ref. 14).

ACKNOWLEDGEMENTS

The author would like to thank Drs. Ross, Przemieniecki, and McCalley for their illuminating discussions, aid, and information in making this paper a contribution to finite element theory.

REFERENCES

1. J. H. Argyris and S. Kelsey, *Energy Theorems and Structural Analysis*. Butterworth's Scientific Publications, London, 1960.
2. E. C. Pestel and F. A. Leckie, *Matrix Methods in Elastomechanics*. McGraw-Hill Book Company, N. Y., 1963.
3. S. Silverstein, "The Effect of Longitudinal Acceleration Upon the Natural Modes of Vibration of a Beam." Report No. TR-59-0000-00791, TRW Systems, 1959.

4. H. Saunders, "Beam Column of Non-Uniform Sections by Matrix Methods." *Journal of Aerospace Science*, Vol. 28, 1961.
5. H. Saunders, "Lateral Vibrations of a Beam on Many Supports with the Added Effect of an Axial Force." Presented at 65th Meeting of Acoustical Society of America, 1963.
6. H. C. Martin, "On the Derivation of Stiffness Matrices for the Analysis of Large Deflection and Stability Problems." *Matrix Methods in Structural Mechanics*, Report AFFDL-TR-66-80 Wright-Patterson AFB, Ohio, Dec. 1965.
7. A. L. Ross, "Effect of In-Plane Tensile Loads on Transverse Bending of Beams." GE Document No. 67SD264, 1967.
8. J. S. Przemieniecki, *Theory of Matrix Structural Analysis*. McGraw-Hill Book Company, N. Y., 1967.
9. R. B. McCalley, Jr., "Mass Matrix for a Prismatic Beam Segment." General Electric Company, KAPL-M-6913, 1968.
10. J. D. Archer, "Consistent Mass Matrix for Distributed Mass Systems." *Journal of the Structural Division*, Proceedings of the American Society of Civil Engineers, Vol. 89, No. ST-4, 1963.
11. R. M. Mains, "Comparison of Consistent Mass Matrix Schemes." *Shock and Vibration Bulletin*, No. 39, Part 3, 1969.
12. H. C. Martin, *Introduction to Matrix Methods of Structural Analysis*. McGraw-Hill Book Company, N. Y., 1966.
13. F. A. Gerard, "The Matrix Deformation Method of Analyzing Stiff - Jointed Frameworks." *Transactions of the Engineering Institute of Canada*, Vol. 4, No. 1, 1960.
14. W. Weaver and J. M. Gere, *Analysis of Framed Structures*. Van Nostrand, Princeton, N. J., 1965.

NOMENCLATURE

- | | |
|------|--|
| A | = cross-section area (in. ²) |
| C, D | = underdetermined coefficients in differential equation (Eq. 17) |
| E | = Young's modulus (lb/in. ²) |

F, G, H, K, N, Q, S	= matrix elements of consistent mass matrices (App. A & B)
I	= planar Moment of Inertia (in. ⁴)
K	= 4 × 4 bending and shear stiffness matrix
KAG	= beam shearing rigidity where K is numerical factor dependent on geometry of cross section
M _i	= bending moment at ends of beam element (in. -lb)
M _x	= total moment at point x of the beam element (in. -lb)
M = M _r + M _t	= total mass matrix
M _r	= rotational mass matrix
M _t	= translational mass matrix
N = N _d + N _a	= column matrix of equivalent forces
N _d	= disturbing forces
N _a	= aerodynamic forces
P	= axial load (lb.)
R	= $1 - \frac{P}{KAG}$ (Eq. 15b)
V _i	= shear force at end of beam element (lb)
S _x	= total shear at point x of the beam element (lb)
T = T _r + T _t	= total kinetic energy for vertical motion (in. -lb)
T _r	= rotational kinetic energy
T _t	= translational kinetic energy
x	= axial coordinate (in.)
y _x	= absolute deflection at point x (in.)
y _i	= absolute coordinate vector for beam ends

z	= $\sin \beta l (2 \tan \frac{\beta l}{2} - l \beta R)$ (Eq. 24b)
β	= $\sqrt{\frac{P}{EI R}}$ (Eq. 15a)
δ	= distance from neutral axis to point on cross-section (in.)
θ_x	= rotation of cross-section at point x (rad)
θ_i	= rotation of cross-section at ends of beam (rad)
ρ	= mass density of material

APPENDIX A - DERIVATION OF TRANSLATIONAL MASS MATRIX

R. B. McCsley (Ref. 9) has formulated a procedure for deriving the mass matrix of a prismatic-beam employing the deformation function emerging in the formulation of the stiffness matrix. This appendix extends the method by applying it to a beam-column.

If the constant mass per unit length for a uniform beam-column is denoted by ρA , the translational kinetic energy of the beam is represented by

$$T_z = \frac{\rho A}{2} \int_0^l \dot{y}_x^T \dot{y}_x dx \quad (A-1)$$

where

$$\dot{y} = \frac{dy}{dt}$$

The linear displacement y_x as previously derived in Eq. (17) is

$$y_x = C \sin \beta x + D \cos \beta x + y_1 - \frac{M_1}{P} + \frac{V_1 x}{P} \quad (A-2)$$

Substituting the boundary condition $y_x = y_1$ at $x = 0$ into Eq. (A-2).

$$y_1 = D - \frac{M_1}{P} + y_1 \quad (A-3)$$

$$\therefore D = \frac{M_1}{P} \quad (A-4)$$

The angular displacement θ_x was previously derived in Eq. (18c)

$$\theta_x = C \beta R \cos \beta x - D \beta R \sin \beta x + \frac{V_1}{P} \quad (A-5)$$

Substituting the boundary condition $\theta_x = 0$, at $x = 0$ into Eq. (A-5),

$$\theta_1 = C\beta R + \frac{V_1}{P} \quad (A-6)$$

$$\therefore C = \frac{\theta_1}{\beta R} - \frac{V_1}{P\beta R} \quad (A-7)$$

$$\therefore y_x = \left(\frac{\theta_1}{\beta R} - \frac{V_1}{P\beta R} \right) \sin \beta x - \frac{M_1}{P} (1 - \cos \beta x) + \frac{V_1}{P} x + y_1 \quad (A-8a)$$

$$= \left(\frac{\theta_1 \sin \beta x}{\beta R} \right) + y_1 + \frac{V_1}{P} \left(x - \frac{\sin \beta x}{\beta R} \right) - \frac{M_1}{P} (1 - \cos \beta x) \quad (A-8b)$$

and

$$\theta_x = \theta_1 \cos \beta x + \frac{V_1}{P} (1 - \cos \beta x) - \frac{M_1}{P} \beta R \sin \beta x \quad (A-9)$$

Employ the proper boundary conditions at $x = l$ i.e., $\theta_x = \theta_2$, $y_x = y_2$ and substitute into Eq. 's (A-8b) and (A-9). This yields

$$y_2 = \frac{\theta_1 \sin \beta l}{\beta R} + y_1 + \frac{V_1}{P} \left(l - \frac{\sin \beta l}{\beta R} \right) - \frac{M_1}{P} (1 - \cos \beta l) \quad (A-10)$$

$$\theta_2 = \theta_1 \cos \beta l + \frac{V_1}{P} (1 - \cos \beta l) - \frac{\beta R M_1}{P} \sin \beta l \quad (A-11)$$

By solving Eq. 's (A-10) and (A-11) simultaneously, the following expressions for V_1/P and M_1/P emerges,

$$\frac{V_1}{P} = \frac{y_1 \beta R \sin \beta l - y_2 \beta R \sin \beta l}{2(1 - \cos \beta l) - l \beta R \sin \beta l} \quad (A-12)$$

$$+ \frac{\theta_1 (1 - \cos \beta l) + \theta_2 (1 - \cos \beta l)}{2(1 - \cos \beta l) - l \beta R \sin \beta l}$$

$$\frac{M_1}{P} = \frac{y_1 (1 - \cos \beta l) - y_2 (1 - \cos \beta l)}{2(1 - \cos \beta l) - l \beta R \sin \beta l} + \frac{\theta_1 \left(\frac{\sin \beta l}{\beta R} - \frac{l \cos \beta l}{\beta R} \right)}{2(1 - \cos \beta l) - l \beta R \sin \beta l} + \frac{\theta_2 \left(l - \frac{\sin \beta l}{\beta R} \right)}{2(1 - \cos \beta l) - l \beta R \sin \beta l} \quad (A-13)$$

Substituting the expressions in Eqs. (A-12) and (A-13) into Eq. (A-10), we obtain

$$y_x = Fy_1 + G\theta_1 + Hy_2 + \underline{K}\theta_2 \quad (A-14a)$$

where

$$F = \frac{1}{z} \left[(\beta R \sin \beta l) \left(x - \frac{\sin \beta x}{\beta R} \right) - (1 - \cos \beta l) (1 - \cos \beta x) \right] + 1 \quad (A-14b)$$

$$G = \frac{\sin \beta x}{\beta R} + \frac{1}{z} \left[(1 - \cos \beta l) \left(x - \frac{\sin \beta x}{\beta R} \right) - \left(\frac{\sin \beta l}{\beta R} - \frac{l \cos \beta l}{\beta R} \right) (1 - \cos \beta x) \right] \quad (A-14c)$$

$$H = \frac{1}{z} \left[(\beta R \sin \beta l) \left(x - \frac{\sin \beta x}{\beta R} \right) - \left(l - \frac{\sin \beta l}{\beta R} \right) (1 - \cos \beta x) \right] \quad (A-14d)$$

$$\underline{K} = \frac{1}{z} \left[(1 - \cos \beta l) \left(x - \frac{\sin \beta x}{\beta R} \right) - \left(l - \frac{\sin \beta l}{\beta R} \right) (1 - \cos \beta x) \right] \quad (A-14e)$$

Obtain the velocity at any point on the beam by differentiating Eq. (A-14a) and substituting directly into Eq. (A-1). The translation matrix then reduces to

$$T_t = \frac{\rho A}{2} \int_0^l \begin{vmatrix} F^2 & FG & FH & FK \\ FG & G^2 & GH & GK \\ FH & GH & H^2 & HK \\ FK & GK & HK & H^2 \end{vmatrix} dx \quad (A-15)$$

By substituting the proper expressions for F , G , H and \underline{K} into Eq. (A-15), the translational mass matrix can be readily obtained.

APPENDIX B - DERIVATION OF ROTATIONAL KINETIC ENERGY

In Appendix A, the kinetic energy affiliated with vertical translation of the beam-column element was derived. Since most practical beam-columns in practice have depths which are comparable to their length, the rotational kinetic energy is derived for this condition.

Proceeding in a manner similar to McCsley (Ref. 9), consider a beam-column element of length dx , mass density ρ and slope θ_x . The volume $dV = dA dx$ is at a distance δ from the neutral axis and is measured in the same direction as the vertical deflection y_x . The total rotational kinetic energy for a segment of length l is

$$dT_r = \frac{1}{2} \rho dA dx [\delta \dot{\theta}_x]^2 \quad (B-1)$$

The total rotational kinetic energy of the cross-section yields

$$T_r = \frac{1}{2} \int_0^l \dot{\theta}_x^2 dx \int_A \rho \delta^2 dA \quad (B-2)$$

Consider the beam-column to be of constant mass density, Eq. (B-2) becomes

$$T_r = \frac{1}{2} \rho I \int_0^l \dot{\theta}_x^2 dx \quad (B-3a)$$

$$= \frac{1}{2} \rho I \int_0^l \dot{\theta}_x^T \dot{\theta}_x dx \quad (B-3b)$$

where

I is the planar moment of inertia and by definition

$$I = \int_A \delta^2 dA \quad (B-3c)$$

The appropriate slope equation derived in Eq. (A-8b) reduces to

$$\theta_x = \theta_1 \cos \beta x + \frac{V_1}{P} (1 - \cos \beta x) - \frac{M_1 \beta R}{P} \sin \beta x \quad (B-4)$$

Substitute the expressions for V_1 and M_1/P as previously derived in Eqs. (A-12) and (A-13) into

Eq. (B-4). After some mathematical manipulation, the equation reduces to

$$\theta_x = N y_1 + Q \theta_1 - N y_2 + S \theta_2 \quad (B-5)$$

where

$$N = \frac{\beta R \sin \beta l (1 - \cos \beta x) - \beta R (1 - \cos \beta l) \sin \beta x}{z} \quad (B-6a)$$

$$Q = \frac{z \cos \beta x + (1 - \cos \beta l) (1 - \cos \beta x)}{z} \quad (B-6b)$$

$$S = \frac{(\sin \beta l - l \cos \beta l) \sin \beta x}{z} - \frac{(1 - \cos \beta x)(1 - \cos \beta l) - (\beta R l - \sin \beta l) \sin \beta x}{z} \quad (B-6c)$$

The rotational velocity $\dot{\theta}_x$ at any point on the beam is obtained by differentiating Eq. (B-5) and substituting into Eq. (B-3b). After matrix multiplication, the rotational matrix simplifies to

$$T_r = \frac{\rho I}{2} \int_0^l \begin{vmatrix} N^2 & NQ & -N^2 & NS \\ NQ & Q^2 & -NQ & QS \\ -N^2 & -NQ & N^2 & -NS \\ NS & QS & -NS & S^2 \end{vmatrix} dx \quad (B-7)$$

By substituting the proper expressions for N , Q and S into Eq. (B-7), the rotational mass matrix is easily acquired.

LIQUID-STRUCTURE COUPLING IN CURVED PIPES

L. C. Davidson and J. E. Smith
Machinery Silencing Department
Naval Ship Research and Development Laboratory
Annapolis, Maryland

The coupled vibrational characteristics of a uniformly curved, liquid filled pipe (elbow) were investigated. The vibration transmission matrix (8x8) was computed by numerical methods. Significant intermedia coupling among all possible terminals is indicated. Good agreement between computed and measured results was obtained over a useful frequency range.

PROBLEM DEFINITION

Liquid transfer systems in general are noisy, water hammer and flow noise being familiar examples of noise sources. Periodic noise in piping systems often results from interactions among the working fluid and various mechanical parts of a pump, the fundamental frequency of the exciting forces being a low multiple of pump rotational speed. Because of the relatively low frequencies (typically 100-500 Hz), pump noise most often occurs in the form of plane wave pressure pulsations in the working fluid and beam type motion of the connected piping.

Pump noise transmission in piping systems has generally been treated as separate problems of liquidborne and structureborne noise. Experimental evidence, however, indicates that significant intermedia coupling is present in most pipe configurations [1]. The purpose of this work is to establish the mechanism and quantify the magnitude of such coupling in the uniformly curved pipe, a commonly occurring configuration which is fundamental to the general problem of liquid-structure coupling.

METHOD OF SOLUTION

The uniformly curved, liquid filled pipe (elbow) is shown in Fig. 1 along with a coordinate system for describing motion in the plane of the bend. The elbow is of uniform wall thickness and circular cross section throughout. (This would likely be the case for cast or forged elbows but not so for bent pipe).

The differential equations describing the elbow in the eight (8) degrees of freedom indicated by the coordinate system can be solved by a matrix iteration technique. Formulation of the coefficient matrix and a description of the computational method are presented in the Appendix.

The final result of this analysis is the (8x8) velocity transmission matrix relating forces and velocities at coordinate point 1 to those at point 2. This matrix is computed at logarithmically spaced frequencies, typically 144 over the range 20-2000 Hz and is available on magnetic tape for further use in systems analysis or for conversion to impedance or mobility form for experimental verification.

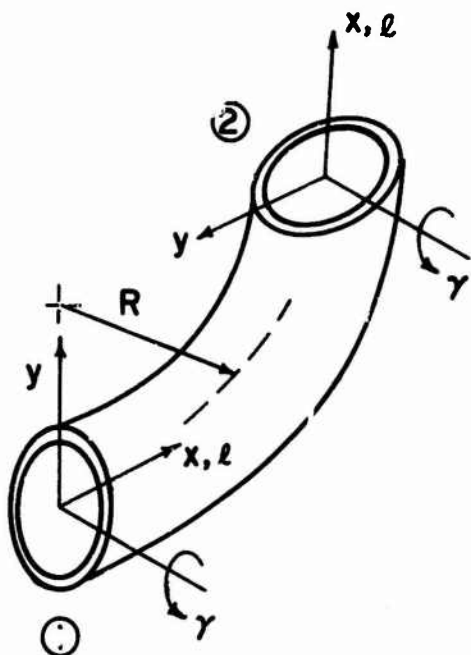


Fig. 1 - The uniformly curved, liquid filled pipe

EXPERIMENTAL METHOD

The purpose of an experimental program here is to verify the analytical model of the appendix. Accordingly, one would like to measure some of the frequency response parameters which are, or can be related to, elements of the computed transmission matrix.

In determining frequency response parameters of mechanical components, tractability of the experimental apparatus usually requires the application of mobility boundary conditions. The liquid terminals of the pipe elbow, however, introduce difficulties which preclude direct measurement of elements belonging to the total mobility matrix. Specifically, excitation of a liquid terminal cannot be accomplished without introducing excitation and/or constraint on the corresponding mechanical terminals. Thus, it is necessary to modify the computed results to correspond to what can be achieved experi-

mentally.

An acoustic mobility/impedance transducer (AMIT) has been shown to be a well defined single terminal acoustic source when operated under certain conditions of constraint [2]. This device contains a diaphragm supported piston which is attached to the pipe component under test by a concentric ring or flange. The piston is driven by an external force generator. Due to the transfer mobility across the diaphragm, the coupling ring also has a free response, requiring a multi-terminal representation of the device as a source. However, the coupling ring can be effectively blocked, shown schematically in Fig. 2, in which case the AMIT becomes a single terminal acoustic source. Then, it is only necessary to consider the effect of infinite constraint on the indicated terminals of the component under test.

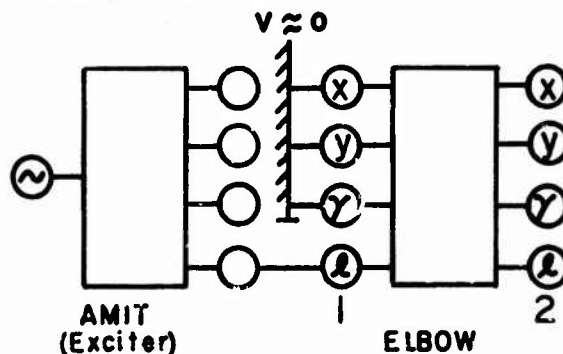


Fig. 2 - Exciter - elbow connection diagram

The resulting reduced mobility matrix (5x5) is obtained by inversion of the reduced impedance matrix which is simply a sub-matrix of the total impedance matrix for the elbow alone.

For a relatively short elbow one might expect both computational and experimental difficulties due to the stiffness of the structure. This was circumvented by including the elbow in a system of greater overall flexibility. A straight length of pipe was welded to each end of the elbow as shown in Fig. 3. From the measurement viewpoint, the straight pipes serve to amplify responses at the free end. Analytically, the structure is simple; the overall trans-

mission matrix is computed by pre and post multiplication of the elbow matrix by the pipe matrix, the pipe being treated as a mass loaded beam [3] and liquid column without liquid-structure coupling.

MEASUREMENTS

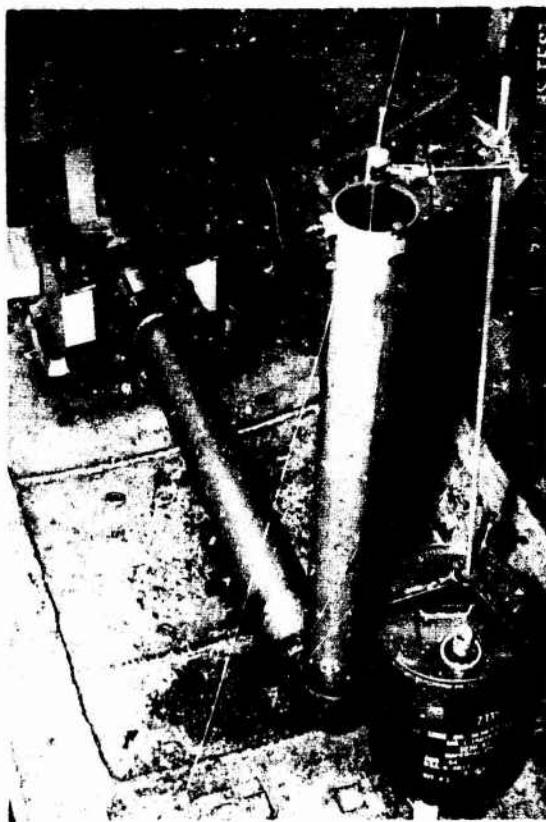
Five (5) mobility parameters are conceptually measurable with the apparatus of Fig. 3 (Fig. 2, where the elbow now comprises the total structure). The driving point mobility of the liquid terminal l_1 was determined directly with the AMIT which contains a hydrophone and accelerometer for that purpose. The AMIT also provided excitation for transfer measurements to l_2 , x_2 , y_2 and γ_2 .

The velocity response at l_2 was determined with a hydrophone placed one-half inch below the free liquid surface. The pressure at this point is proportional to acceleration at the

free surface because the one-half inch liquid column behaves as a simple in-ertance in the frequency range of interest.

Response in the y_2 direction (normal to pipe axis, in plane of bend) was determined directly with an accelerometer on the pipewall (not shown in Fig. 3). The x_2 response (along the axis of the pipe) was determined by summing accelerometers placed on opposite sides of the pipe, parallel to its axis and in the plane of the bend. These accelerometers can be seen in Fig. 3. The same two measurement positions, with one accelerometer reversed, were also used to determine the rotational response, γ_2 . Summing for the y_2 and γ_2 responses was accomplished with a passive adding network after a stage of amplification.

Measurement and readout of the mobility parameters were accomplished with the instrumentation shown schematically in Fig. 4.



PIPE: 70/30 CuNi, std wt
4.5" O.D. x 36" long (2 pc)

ELBOW: CuNi, Forged
4" radius of curvature

LIQUID: 2190 TEP oil
Combined bulk modulus
(liquid/pipe) determined
experimentally: 2.38×10^5 psi

Fig. 3 - Experimental Apparatus

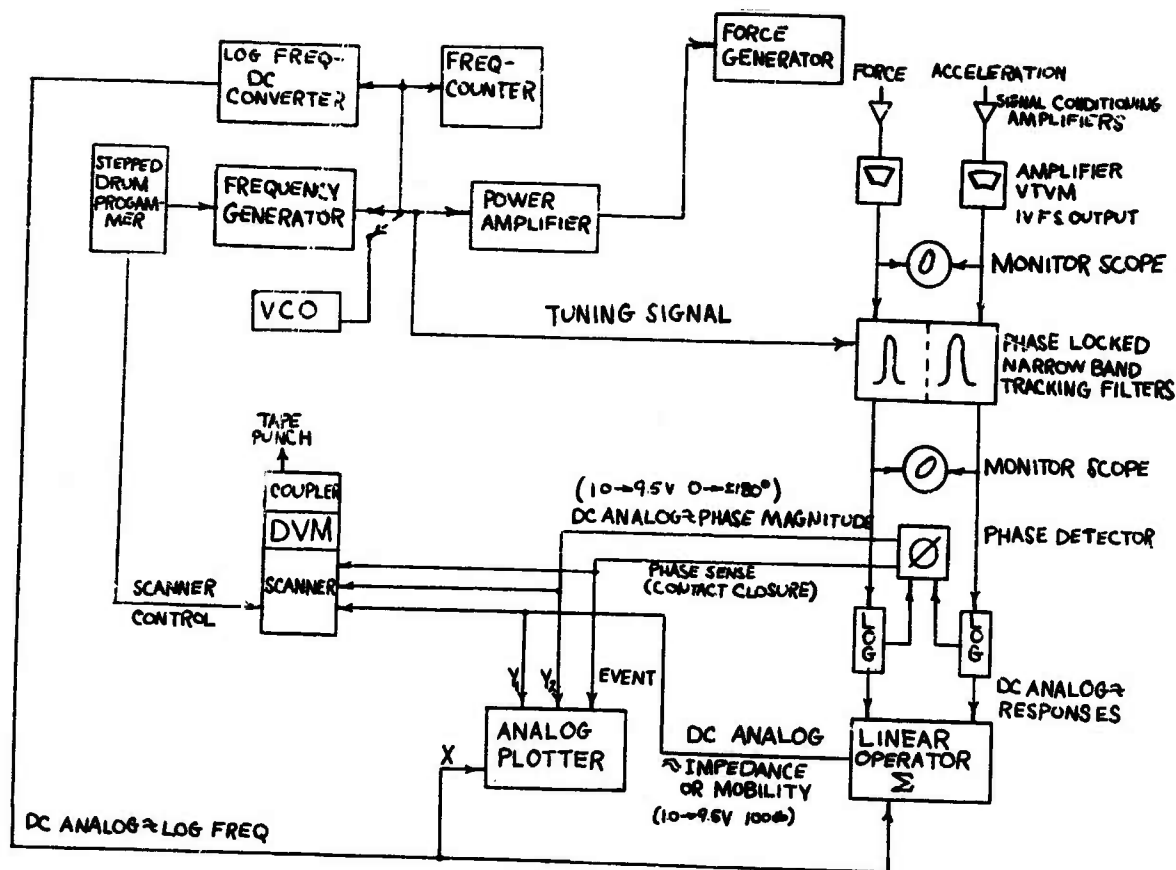


Fig. 4 - Measurement and readout instrumentation connection diagram

RESULTS

Computed and measured mobility parameters for the arrangement shown in Fig. 3 are presented in Figs. 5, 6 and 7.

The measured data were traced directly from analog curves obtained with the measurement apparatus onto the computer generated curves of calculated parameters. Note that the ordinates for measured and computed data are not to the same scale. For the transfer parameters, both computed mobilities were plotted (+, *). The breakdown in reciprocity occurring at about 500 Hz indicates that a smaller element is required in the iteration procedure.

In addition to the five (5) mobilities previously mentioned, the driving point mobility at y_2 is also presented. This measurement was accomplished with a conventional mechanical impedance transducer; however, the passive load of the AMIT on terminal ℓ_1 is a departure from the required boundary conditions.

In general the results confirm the analytical model which indicates a high degree of coupling among all possible terminals. Evaluating the significance of this coupling in terms of noise transmission however, requires consideration of the system in which the elbow occurs. Specifically, one is interested in the responses which develop in coupled systems at potential sound radiators.

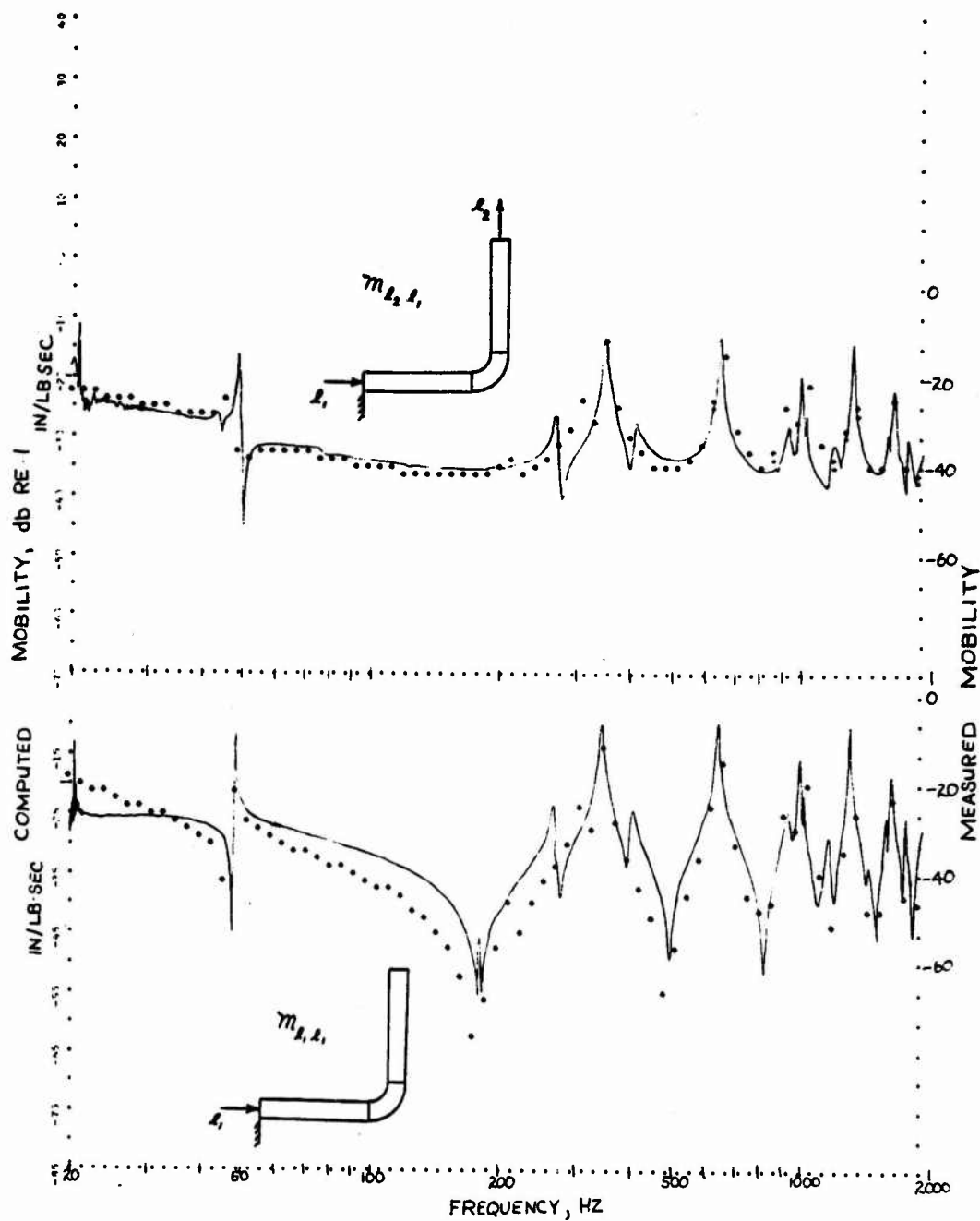


Fig. 5 - Mobility parameters, CuNi pipe configuration

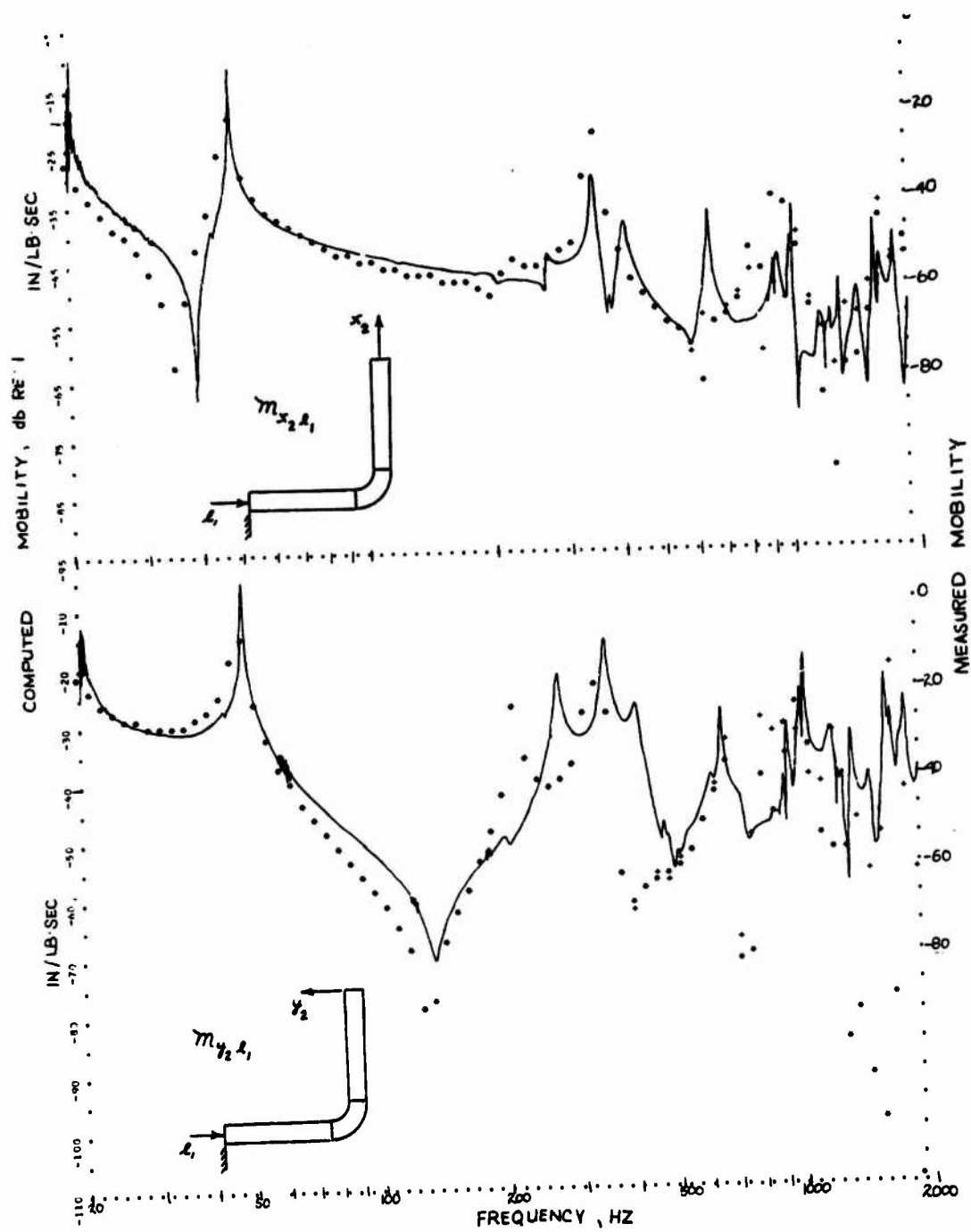


Fig. 6 - Mobility parameters, CuNi pipe configuration

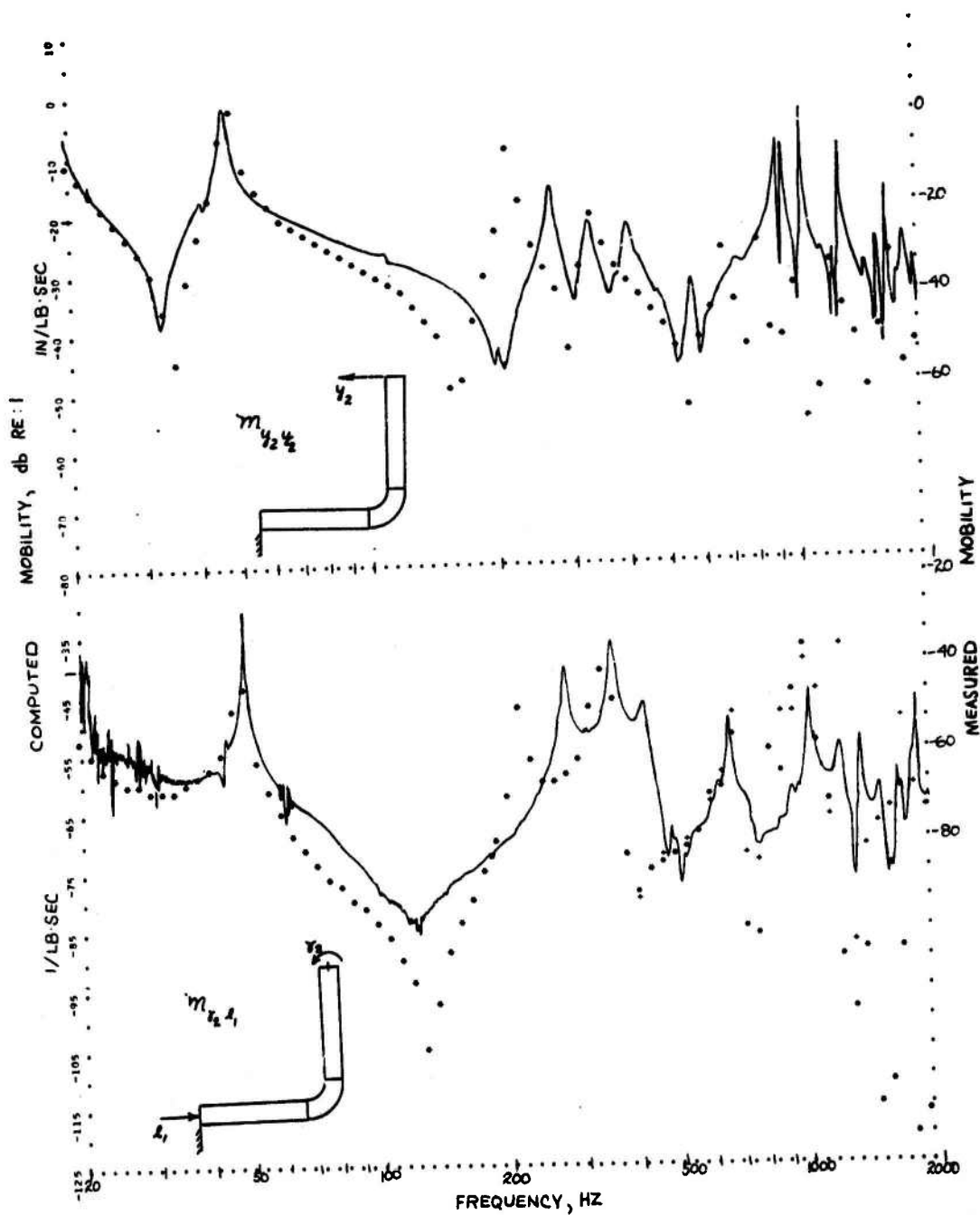


Fig. 7 - Mobility parameters, CuNi pipe configuration

Continuing work under this program is directed at the specific case of the sea connected system where responses of a ship's hull and of the liquid at the hull penetration are required. These responses can be computed from the application of known boundary conditions. Transfer factors relating these responses to radiated noise will then allow a quantitative comparison of the various liquid-structure paths as contributors to the total radiated signature.

Appendix

COMPUTATION OF THE TRANSMISSION MATRIX

It is required to determine the matrix describing, for a fluid filled

pipe of constant radius of curvature, the vibration transmission properties from input to output stations in the plane of the bend. The approach to the problem is to find the matrix A of coefficients for the system of linear ordinary differential equations $\frac{ds}{ds} = AS$ describing a differential element of the fluid filled pipe. The system of equations is then numerically solved for the transmission matrix U by the matrix exponential series for $e^{A\theta}$.

Postulating the existence of a system of linear ordinary differential equations describing the differential element shown in Fig. 8 we may write that the state vector change ΔS_0 from station (0) to station (1) is given by

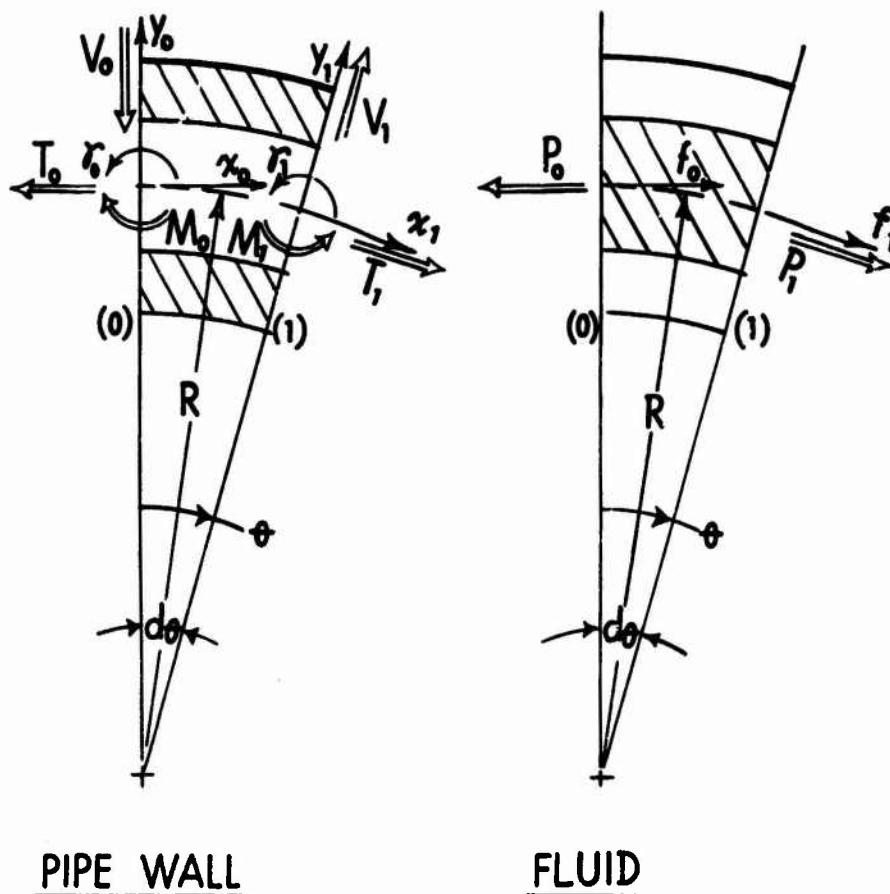


Fig. 8 - Differential element, curved liquid filled pipe

$$\Delta S_0 = S_1 - S_0 = A \Delta \theta S_0 \quad (1)$$

From Eq. (1) we obtain, therefore, that

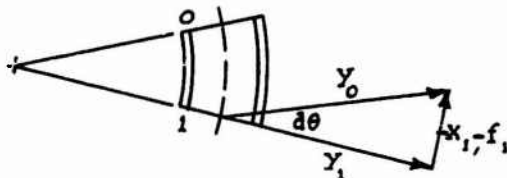
$$S_1 = A \Delta \theta S_0 + S_0 = (A \Delta \theta + I) S_0 \quad (2)$$

or

$$S_1 = B S_0 \quad (3)$$

where the matrix B is the transmission matrix for the differential element of Fig. 8 and relates the state vector at station (1) to that at station (0). This matrix can be determined by finding the images of the basis vectors across the matrix B, i.e. by determining the state vectors generated at station (1) when each coordinate axis at station (0), taken individually, undergoes a unit magnitude sinusoidal displacement motion or has applied a unit magnitude sinusoidal force quantity and all other coordinates at station (0) are held to zero motion or force. Since this is a one dimensional problem the element shown in Fig. 8 (shown with the fluid separated from the pipe wall for clarity) is treated in the same manner as a Timoshenko beam analysis where, as appropriate, shear deflection, rotary inertia and material damping are included. Taking each coordinate axis at station (0) in turn the following responses at station (1) are generated:

$$\underline{y_0 = e^{j\omega t}}$$

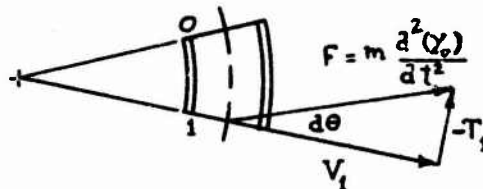


$$y_1 = y_0 \cos(d\theta) = e^{j\omega t}$$

$$x_1 = -y_0 \sin(d\theta) = -e^{j\omega t} d\theta$$

$$\gamma_1 = 0$$

$$f_1 = -y_0 \sin(d\theta) = -e^{j\omega t} d\theta$$



$$V_1 = F \cos(d\theta) = m (j\omega)^2 e^{j\omega t} \cos(d\theta) = -\gamma R d\theta \omega^2 e^{j\omega t} \cos(d\theta)$$

$$= -\gamma R \omega^2 e^{j\omega t} d\theta$$

$$T_1 = \gamma R d\theta \omega^2 e^{j\omega t} \sin d\theta = \gamma R \omega^2 e^{j\omega t} (d\theta)^2$$

or

$$T_1 = 0$$

$$M_1 = 0$$

$$P_1 = 0$$

These results follow from using the small angle trigonometric formulas and neglecting second order and higher terms. Employing similar force/motion diagrams the remaining sets of station (1) responses can be immediately written as

$$\underline{x_0 = e^{j\omega t}}$$

$$y_1 = e^{j\omega t} d\theta, x_1 = e^{j\omega t}, \gamma_1 = 0, f_1 = 0$$

$$V_1 = 0, T_1 = -\gamma' R \omega^2 e^{j\omega t} d\theta, M_1 = 0$$

$$P_1 = 0$$

$$\underline{\gamma_0 = e^{j\omega t}}$$

$$y_1 = R e^{j\omega t} d\theta, x_1 = 0, \gamma_1 = e^{j\omega t}, f_1 = 0$$

$$V_1 = 0, T_1 = 0, M_1 = -\gamma i_z^2 R \omega^2 e^{j\omega t} d\theta,$$

$$P_1 = 0$$

$$\underline{f_0 = e^{j\omega t}}$$

$$y_1 = 0, x_1 = 0, \gamma_1 = 0, f_1 = e^{j\omega t}$$

$$V_1 = 0, T_1 = 0, M_1 = 0,$$

$$P_1 = -\gamma'' R \omega^2 e^{j\omega t} d\theta$$

$$\underline{V_0 = e^{j\omega t}}$$

$$Y_1 = \frac{K_s R e^{j\omega t}}{GA} d\theta, \quad x_1 = 0, \quad \gamma_1 = 0, \quad f_1 = 0$$

$$V_1 = e^{j\omega t}, \quad T_1 = -e^{j\omega t} d\theta, \quad M_1 = -R e^{j\omega t} d\theta,$$

$$P_1 = 0$$

$$T_0 = e^{j\omega t}$$

$$Y_1 = 0, \quad x_1 = \frac{R e^{j\omega t}}{EK} d\theta, \quad \gamma_1 = 0, \quad f_1 = 0$$

$$V_1 = e^{j\omega t} d\theta, \quad T_1 = e^{j\omega t}, \quad M_1 = 0, \quad P_1 = 0$$

$$M_0 = e^{j\omega t}$$

$$Y_1 = 0, \quad x_1 = 0, \quad \gamma_1 = \frac{R e^{j\omega t}}{EJ_z} d\theta, \quad f_1 = 0$$

$$V_1 = 0, \quad T_1 = 0, \quad M_1 = e^{j\omega t}, \quad P_1 = 0$$

$$P_0 = e^{j\omega t}$$

$$Y_1 = 0, \quad x_1 = 0, \quad \gamma_1 = 0, \quad f_1 = \frac{R e^{j\omega t}}{B' A''} d\theta$$

$$V_1 = e^{j\omega t} d\theta, \quad T_1 = 0, \quad M_1 = 0, \quad P_1 = e^{j\omega t}$$

The above results can be arranged to form the matrix B which, after removing the common factor $e^{j\omega t}$, can be used with Eq.'s (1), (2) and (3) to obtain the system of ordinary linear differential equations for the element of Fig. 8. This system of equations is as follows:

where

μ' = mass per unit length of pipe

μ'' = mass per unit length of fluid

$$\mu = \mu' + \mu''$$

K_s = Timoshenko shear constant (.5)

E = Young's modulus (cis)

G = Shear modulus (cis)

B' = fluid/pipe wall bulk modulus (cis)

A' = pipe section area

A'' = fluid section area

i_z = radius of gyration

J_z = pipe section modulus

R = pipe radius of curvature

The above system of differential equation can be numerically solved by the CODAT computer program shown in Ref. 4 and the technique shown in Ref. 3. With this method the transmission matrix is given by the matrix series

$$\frac{d}{d\theta} \begin{bmatrix} y \\ x \\ \gamma \\ f \\ V \\ T \\ M \\ P \end{bmatrix} = \begin{bmatrix} 0 & 1 & R & 0 & \frac{RK_s}{GA} & 0 & 0 & 0 \\ -1 & 0 & 0 & 0 & 0 & \frac{R}{EA} & 0 & 0 \\ 0 & 0 & 0 & 0 & 0 & 0 & \frac{R}{EJ_z} & 0 \\ -1 & 0 & 0 & 0 & 0 & 0 & 0 & \frac{R}{BA''} \\ -\mu R \omega^2 & 0 & 0 & 0 & 0 & 1 & 0 & 1 \\ 0 & -\mu' R \omega^2 & 0 & 0 & -1 & 0 & 0 & 0 \\ 0 & 0 & -\mu'' R \omega^2 & 0 & -R & 0 & 0 & 0 \\ 0 & 0 & 0 & -\mu'' R \omega^2 & 0 & 0 & 0 & 0 \end{bmatrix} \begin{bmatrix} y \\ x \\ \gamma \\ f \\ V \\ T \\ M \\ P \end{bmatrix} \quad (4)$$

$$U = I + A\theta + \frac{1}{2} A^2\theta^2 + \frac{1}{6} A^3\theta^3 \dots$$

$$= \sum_{j=0}^{\infty} \frac{1}{j!} (A\theta)^j$$

The matrix U is the solution of Eq.'s (4) for any arc θ . i.e.

$$S_1 = U S_0$$

References

1. D. B. Callaway, F. G. Tyzzer and H. C. Hardy, "Resonant Vibrations in a Water-Filled Piping System", JASA. Vol. 23, No. 5, 1951.
2. L. C. Davidson, "Acoustic Mobility and Impedance Methods for Piping Systems", NSRDC, Machinery Laboratory Report 2683, May 1968.
3. J. E. Smith and R. J. Hanners, "Computation of the Mobility Properties of a Uniform Beam Foundation", NAVSHIPPRANDLAB Annapolis, Rept C2707, Feb 1969.
4. D. R. Jordan, "A General Digital Computer Program, CODAT, for Solving Noise Transmission Problems", MEL R&D Rept 548/66, Mar 67.

DISTRIBUTION OF EIGENVALUES IN CONICAL SHELLS

D. K. Miller and F. D. Hart
Department of Mechanical and Aerospace Engineering
North Carolina State University
Raleigh, North Carolina

Expressions for the cumulative number of eigenvalues and the eigenvalue density of a thin circular conical shell are obtained. These expressions are given for the frequency domain below the lower ring frequency and above the upper ring frequency of a conical shell. The results are presented in both analytic and graphic form. They are applicable for a wide range of cone geometries and materials, and are presented as functions of a dimensionless frequency parameter.

LIST OF SYMBOLS

C_0	velocity of a longitudinal wave in the shell material = $\sqrt{gE'/\rho}$	$n(\lambda)$	modal or eigenvalue density with respect to λ
D	stiffness of shell = $Eh/12(1-\nu^2)$	R	radius of a circular plate
E	modulus of elasticity of the shell material	r	radius of cone perpendicular to the cone axis
g	gravitational constant	w	displacement normal to shell surface
h	thickness of the shell	x	coordinate along shell surface
L	length of cone, apex to base slant length	α	truncation ratio = L_t/L
L_t	length of cone truncation, apex to top slant length	θ	coordinate around shell surface
m	number of circumferential waves	λ	dimensionless frequency
$N(\lambda)$	cumulative number of eigenvalues up to λ	ν	Poisson's ratio of shell material
n	number of one-half longitudinal waves	ρ	density of shell material
		Φ	stress function
		Ψ	one-half cone angle
		ω	angular frequency = $2\pi f$

INTRODUCTION

Knowledge regarding the eigenvalue distribution in various structural elements is a necessary prerequisite for the successful application of statistical energy methods to problems involving structures excited by random forces. Specifically, the eigenvalue density is one of the structural parameters which occurs in the statistical energy formu-

lation. Expressions for the eigenvalue density of such common structural geometries as beams, circular and rectangular plates, and cylindrical and spherical shells are presently available in the literature [1 - 4]. In addition, some work has been done on the conical shell geometry [5], which is applicable to the frequency range below the lower ring frequency of a thin conical shell.

In the paper presented here, the previous work on conical shell geometries is reinforced, and expressions are presented to cover the frequency range above the upper ring frequency of a thin conical shell. Since the conical shell is a very common structural element, the results of this paper are felt to have immediate engineering applications. Subsequently, as combined structures may also be considered [6], the statistical energy method is a practical method for handling complex structures excited by broad band random loads.

FREQUENCY EQUATION FOR CONICAL SHELLS

In order to obtain a frequency equation that is applicable to a thin conical shell, it is first necessary to write the differential equations governing the shell motion. The geometric parameters for the cone used in this analysis are illustrated in Fig. 1. The differential equations are obtained [7] by first writing the force and moment equilibrium equations for a typical shell element. The equilibrium equations are then combined with the conventional elasticity relationships in order to relate the internal forces and moments to corresponding stresses and strains, and then to the respective

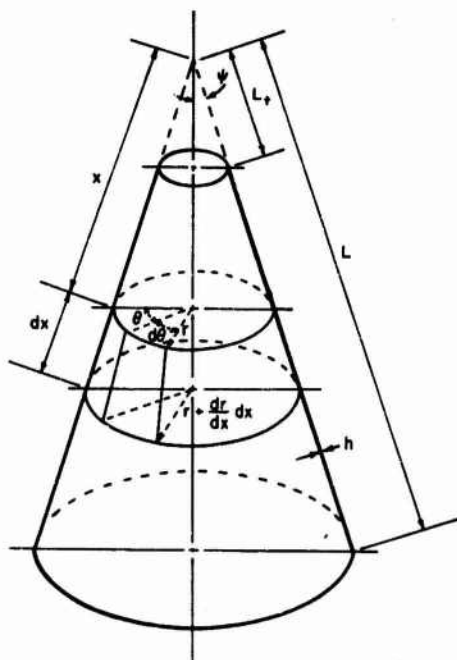


Fig. 1 - Conical shell geometry

elemental displacements. This together with continuity considerations makes it possible to express the differential equations in terms of the normal displacement (w) and the stress function (ϕ) as

$$\frac{1}{Eh} \nabla^2 \nabla^2 \phi - \frac{\cos \psi}{r} \frac{\partial^2 w}{\partial x^2} = 0 \quad (1)$$

$$\frac{\cos \psi}{r} \frac{\partial^2 \phi}{\partial x^2} + D \nabla^2 \nabla^2 w - \frac{\rho h \omega^2}{g} w = 0 \quad (2)$$

where

$$\nabla^2 = \frac{\partial^2}{\partial x^2} + \frac{\sin \psi}{r} \frac{\partial}{\partial x} + \frac{1}{r^2} \frac{\partial^2}{\partial \theta^2} \quad (3)$$

In obtaining the above differential equations both bending and extension of the middle surface are considered as well as transverse shear terms. The only body force considered is the inertia of the shell in the direction normal to the surface. It is assumed that the shell is of constant thickness (h), and that the value of the shell radius (r) remains much less than the shell thickness. The implications of this final assumption will be discussed later in this paper.

Solution of the differential equations (1) and (2) requires assumptions to be made concerning the mode shapes in the circumferential and longitudinal directions [8], in order to develop approximate expressions for the normal displacement and the stress function. The circumferential mode shape is assumed to be sinusoidal, and the longitudinal mode shape is approximated by a series expression. Also, it is assumed that the circumferential and longitudinal modes are independent. The Galerkin method is then used twice to reduce the differential equations to two simultaneous algebraic equations with the coefficients of the assumed series for the longitudinal variations as the unknowns. The condition that the coefficient matrix of these equations be equal to zero leads to the following approximate frequency equation for a thin conical shell.

$$\omega^2 = \frac{gE}{\rho L^2} \frac{\frac{D}{EL^2 h} \left\{ \frac{n^4 \pi^4}{10} \frac{(1-\alpha^5)}{(1-\alpha)^4} + \frac{n\pi}{(1-\alpha)} \left(1 + \frac{2m^2}{\sin^2 \psi} \right) \left(\frac{n\pi}{6} \frac{(1-\alpha^3)}{(1-\alpha)} - \frac{1}{2n\pi} \frac{(1-\alpha)^2}{(1-\alpha)} \right) \right\} + \left(\frac{\frac{m^4}{\sin^4 \psi} - \frac{4m^2}{\sin^2 \psi}}{2} \right) \frac{1-\alpha}{2} + \frac{n^4 \pi^4}{\tan^2 \psi} \left\{ \frac{1}{8} \frac{(1-\alpha^4)}{(1-\alpha)^2} - \frac{3}{8n^2 \pi^2} \frac{(1-\alpha^2)}{(1-\alpha)} \right\}^2}{\left\{ \frac{n^4 \pi^4}{10} \frac{(1-\alpha^5)}{(1-\alpha)^4} + \frac{n\pi}{(1-\alpha)} \left(1 + \frac{2m^2}{\sin^2 \psi} \right) \left(\frac{n\pi}{6} \frac{(1-\alpha^3)}{(1-\alpha)} - \frac{1}{2n\pi} \frac{(1-\alpha)^2}{(1-\alpha)} \right) \right\} + \left(\frac{\frac{m^4}{\sin^4 \psi} - \frac{4m^2}{\sin^2 \psi}}{2} \right) \frac{1-\alpha}{2} + \frac{n^4 \pi^4}{\tan^2 \psi} \left\{ \frac{1}{8} \frac{(1-\alpha^4)}{(1-\alpha)^2} - \frac{3}{8n^2 \pi^2} \frac{(1-\alpha^2)}{(1-\alpha)} \right\}^2} \quad (4)$$

where m is the number of circumferential waves ($m=2,3,4,\dots$); and n is the number of longitudinal waves ($n=1,2,3,\dots$).

The frequency equation (4) may be written in terms of a dimensionless frequency parameter as

$$\lambda^2 = \frac{\frac{D}{EL^2 h} \left\{ \frac{n^4 \pi^4}{10} \frac{(1-\alpha^5)}{(1-\alpha)^4} + \frac{n\pi}{(1-\alpha)} \left(1 + \frac{2m^2}{\sin^2 \psi} \right) \left(\frac{n\pi}{6} \frac{(1-\alpha^3)}{(1-\alpha)} - \frac{1}{2n\pi} \frac{(1-\alpha)^2}{(1-\alpha)} \right) \right\} + \left(\frac{\frac{m^4}{\sin^4 \psi} - \frac{4m^2}{\sin^2 \psi}}{2} \right) \frac{1-\alpha}{2} + \frac{n^4 \pi^4}{\tan^2 \psi} \left\{ \frac{1}{8} \frac{(1-\alpha^4)}{(1-\alpha)^2} - \frac{3}{8n^2 \pi^2} \frac{(1-\alpha^2)}{(1-\alpha)} \right\}^2}{\left\{ \frac{n^4 \pi^4}{10} \frac{(1-\alpha^5)}{(1-\alpha)^4} + \frac{n\pi}{(1-\alpha)} \left(1 + \frac{2m^2}{\sin^2 \psi} \right) \left(\frac{n\pi}{6} \frac{(1-\alpha^3)}{(1-\alpha)} - \frac{1}{2n\pi} \frac{(1-\alpha)^2}{(1-\alpha)} \right) \right\} + \left(\frac{\frac{m^4}{\sin^4 \psi} - \frac{4m^2}{\sin^2 \psi}}{2} \right) \frac{1-\alpha}{2} + \frac{n^4 \pi^4}{\tan^2 \psi} \left\{ \frac{1}{8} \frac{(1-\alpha^4)}{(1-\alpha)^2} - \frac{3}{8n^2 \pi^2} \frac{(1-\alpha^2)}{(1-\alpha)} \right\}^2} \quad (5)$$

where

$$\lambda^2 = \omega^2 \frac{\rho L^2}{gE} = (\omega L/C_0)^2 \quad (6)$$

In this form the frequency equation (5) is independent of the material properties of the cone, with the exception of small variation due to the shell stiffness (D). This variation will be neglected since Poisson's ratio is nearly constant (0.33) for most structural materials of interest. Frequency equation (5) is, however, dependent on the three dimensionless geometric parameters which appear. These are the cone angle (ψ), the thickness to length ratio (h/L), and the truncation ratio (α). The frequency equation presented is fairly general, and is only limited to some extent by the assumption concerning the shell radius (r). This assumption is obviously invalid for cones with small cone angles and little or no truncation. Hence, some care should be observed when applying the results of this paper to such geometries.

CUMULATIVE NUMBER OF EIGENVALUES

The frequency equation (5) is now used to obtain information regarding the eigenvalue distribution with respect to frequency. The usual procedure at this point is to employ the k -space integration method [2-4,5] which yields an integral expression for the cumulative number of eigenvalues as a function of dimensionless frequency. However, due to the complexity of Eq. (5) this method is found to be impractical from both an analytical and a computational point of view. Therefore, a purely numerical procedure is used.

Employing a high speed digital computer, frequencies corresponding to integer values of m and n are calculated and then filtered by means of a series of IF statements. In this manner, the number of eigenvalues occurring below certain selected values of dimensionless frequency can be counted. The values of m and n are incremented until the count in each specified frequency interval has terminated. This procedure is quite time consuming since the number of frequencies calculated is on the order of one-hundred thousand for each cone geometry studied.

The effect of each of the three dimensionless geometric parameters presented in the frequency equation is examined by successively holding two of the parameters constant and varying the third. The results of this parameter study are shown in Fig. 2, Fig. 3, and Fig. 4. The cumulative number of eigenvalues $N(\lambda)$ multiplied by $\pi/\sin\psi (1-\alpha)$ is shown versus the dimensionless frequency. The variation in geometric parameters presented in the figures is quite extreme, and it should not be concluded that the final results are necessarily this general.

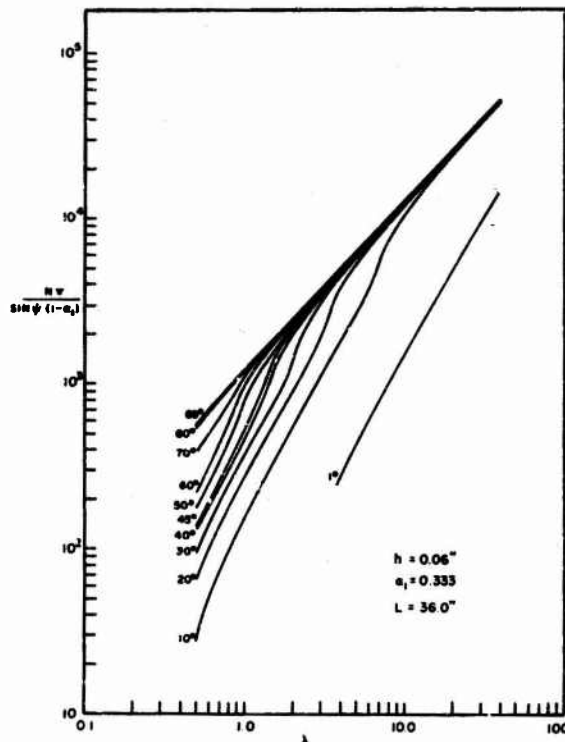


Fig. 2 - Effect of variations in cone angle

In order to effectively examine these results it is necessary to divide the frequency domain into three regions. The region above the upper ring frequency, the region below the lower ring frequency, and that between the two ring frequencies are considered. The upper ring frequency is defined as the frequency at which the longitudinal wave length in the shell material is equal to circumference of the small end of the

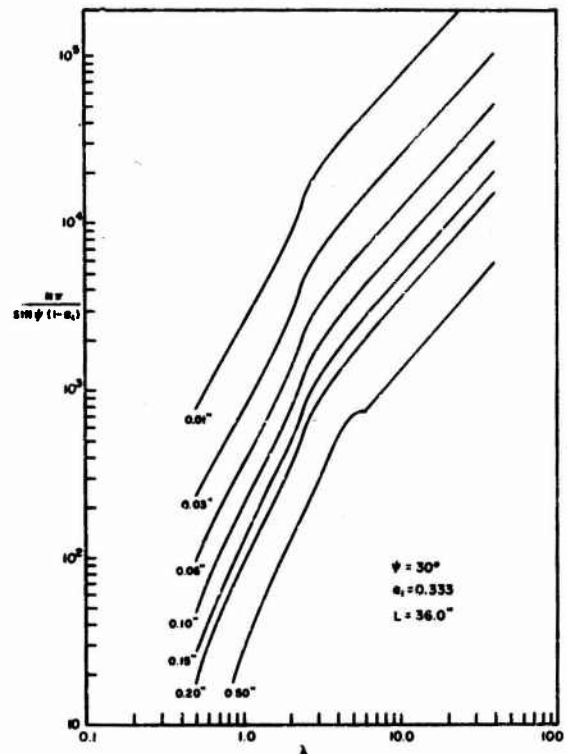


Fig. 3 - Effect of variations in cone thickness to length ratio

conical shell. In dimensionless form the upper ring frequency may be given as

$$\lambda \text{ (upper ring)} = 1/\alpha \sin\psi \quad (7)$$

The lower ring frequency is defined in a similar manner and may be given as

$$\lambda \text{ (lower ring)} = 1/\sin\psi \quad (8)$$

Examination of the results presented in Fig. 2, Fig. 3, and Fig. 4, in the range above the upper ring frequency, leads to the following conclusions. The results are independent of the cone angle. The results vary directly with the thickness to length ratio, and with the truncation ratio as $(1-\alpha)$ to the

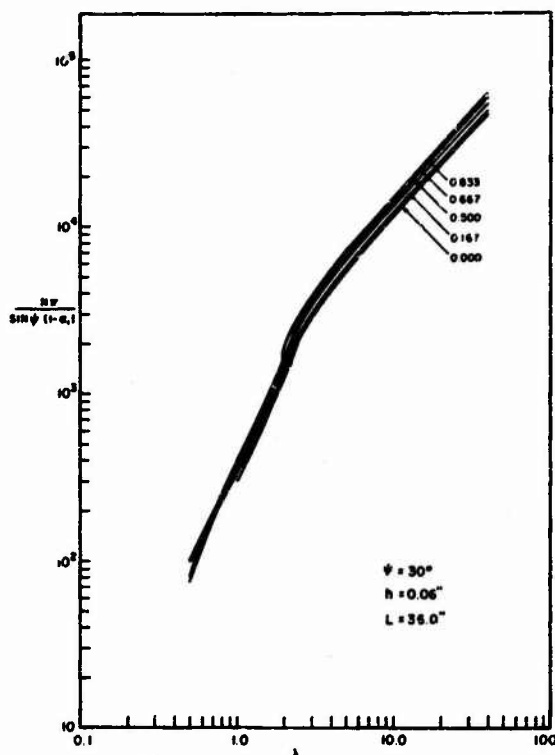


Fig. 4 - Effect of variations in the cone truncation ratio

one fifth. Therefore, the results may be normalized, and expressed in the following form.

$$N(\lambda) \frac{\pi}{\sin \psi (1-\alpha)} \frac{h}{L} (1-\alpha)^{\frac{1}{4}} = F(\lambda) \quad (9)$$

where $F(\lambda)$ now becomes a single straight line above the upper ring frequency for all cone geometries considered. $F(\lambda)$ is determined graphically from normalized plots of the results shown in Fig. 2, Fig. 3, and Fig. 4. This leads to an expression for the cumulative number of eigenvalues as

$$N(\lambda) \approx 2.0 \frac{L \sin \psi (1-\alpha)^{\frac{1}{4}}}{\pi h} \lambda \quad (10)$$

Eq. (10) is only valid for values of

dimensionless frequency above the upper ring frequency of a conical shell.

Below the lower ring frequency, the results shown in Fig. 2, Fig. 3, and Fig. 4 are in excellent agreement with similar curves presented in Ref. [5]. A normalization procedure similar to the one carried out above is performed in the reference cited, and the results are given as

$$N(\lambda) \approx 0.876 \frac{L \sin \psi \sqrt{\tan \psi} (1-\alpha)^{\frac{3}{4}}}{\pi h} \lambda^{\frac{1}{2}} \quad (11)$$

Eq. (11) is only valid for values of dimensionless frequency below the lower ring frequency of a conical shell.

Between the upper and lower ring frequencies the effect of variations in the geometric parameters is not clear. Therefore, it is not possible to normalize the curves in this region, and to obtain a single curve independent of cone geometry. However, even if this had been possible the complex behavior of the curves in this region makes it doubtful that the method used above could be employed to obtain a single analytic expression for the behavior of the curves in this region with respect to dimensionless frequency.

EIGENVALUE DENSITY

The eigenvalue density is obtained directly from the expressions for the cumulative number of eigenvalues. This is accomplished by simple differentiation of Eq. (10) and Eq. (11) with respect to the dimensionless frequency. Therefore, above the upper ring frequency the eigenvalue density expression is given as

$$n(\lambda) \approx 2.0 \frac{L \sin \psi (1-\alpha)^{\frac{1}{4}}}{\pi h} \quad (12)$$

and below the lower ring frequency the eigenvalue density [5] is given as

$$n(\lambda) \approx 1.31 \frac{L \sin \psi \sqrt{\tan \psi} (1-\alpha)^{\frac{3}{4}}}{\pi h} \lambda^{-\frac{1}{2}} \quad (13)$$

It should be noted that the expression for the eigenvalue density above

the upper ring frequency, Eq. (12), is independent of the dimensionless frequency. This implies that at high frequencies the conical shell exhibits a simple plate mode as would be expected.

As a limit check on the results presented, Eq. (10) may be extended to the limiting case of a circular plate. In this case the cone angle becomes a right angle, the truncation ratio goes to zero, and the length of the cone becomes the radius of a circular plate (R). Eq. (10) then becomes

$$N(\lambda) \approx 0.637 R\lambda/h \quad (14)$$

where the dimensionless frequency may now be expressed as $\omega R/C_0$. Expressing the results in terms of the circular frequency (ω), and then differentiating with respect to the circular frequency leads to the eigenvalue density expression for a circular plate as

$$n(\omega) = 0.637 R^2/hC_0 \quad (15)$$

Eq. (15) is identical to the expression given in Ref. [4] with the exception of the numerical constant. Due to degeneracy of eigenvalue effects in the formulation of the circular plate frequency equation, the actual value should be twice the value given in the reference cited, or 0.701. This is within ten percent of the value given in Eq. (15) which is considered to be excellent agreement. Unfortunately the results cannot be easily extended to the limiting case of a cylinder, since for the limiting case of the cone angle equal to zero, the geometry degenerates to a line, not a cylinder.

CONCLUSIONS

Expressions for the cumulative number of eigenvalues and the eigenvalue density are given in Eq. (10) and Eq. (12) respectively above the upper ring frequency, and in Eq. (11) and Eq. (13) respectively below the lower ring frequency. The results are also presented graphically in Fig. 5 and Fig. 6. Since the lower ring frequency is dependent only on the cone angle, it is shown as

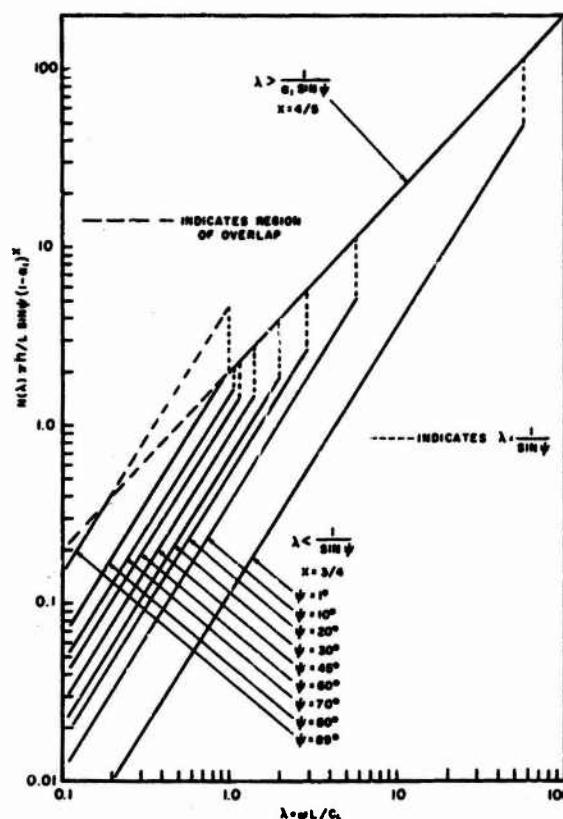


Fig. 5 - Cumulative number of eigenvalues for a conical shell

a vertical dashed line in the figures. The upper ring frequency is dependent on the truncation ratio as well as the cone angle, and must be determined for each cone of interest. The results presented are essentially independent of cone geometry and cone material, and should find a wide range of application.

There are several limitations regarding the application of the results presented in Fig. 5 and Fig. 6. First, for cones with large cone angles, the solution valid above the upper ring frequency becomes applicable even before the lower ring frequency is reached. In general the minimum value of the two solutions should be used for such cones. This type of behavior is indicated in Fig. 2, and is shown in Fig. 5 and Fig. 6 as a region of overlap.

Secondly, cones which have little or no truncation have a very high or infinite upper ring frequency. This

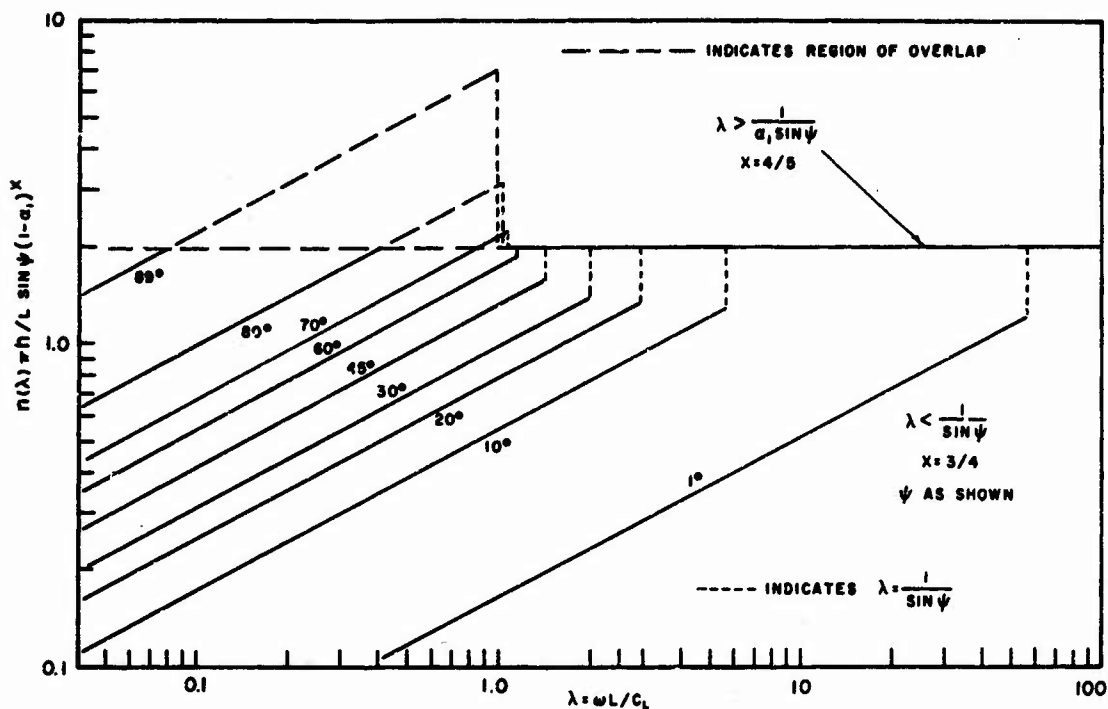


Fig. 6 - Eigenvalue density for a conical shell

type of behavior is indicated in Fig. 4. For computational purposes an artificial upper ring frequency of approximately ten times the lower ring frequency should be used in such cases.

Finally, it should be pointed out that the curves as given in Fig. 5 and Fig. 6 do not give values in the frequency domain between the two ring frequencies. Also, for low frequencies near or below the fundamental frequency, the results have no meaning. A lower cutoff frequency corresponding to a cumulative number of eigenvalues of approximately two should be employed when using the figures or the equations.

ACKNOWLEDGEMENT

This research was supported by the National Aeronautics and Space Administration, Langley Research Center.

REFERENCES

- 1 P.W.Smith and R.H.Lyon, Sound and Structural Vibration, NASA CR-160, Washington, D.C., 1965

- 2 V.V.Bolotin, "On the Density of the Distribution of Natural Frequencies of Thin Elastic Shells," PMM., Moscow, Vol.27, No.2, pp.362-364, 1963
- 3 V.V.Bolotin, "The Density of Eigenvalues in Vibrational Problems of Elastic Plates and Shells," Proc.Vibr. Probl., Vol.6, No.5, pp.342-351, 1965
- 4 D.K.Miller and F.D.Hart, Modal Density of Thin Circular Cylinders, NASA CR-897, Washington, D.C., 1967
- 5 D.K.Miller and F.D.Hart, "Eigenvalue Density of Conical Shells," Paper W-2, Presented at the 76th Meeting of the ASA, Cleveland, Ohio, November 1968
- 6 F.D.Hart and V.D.Desai, "Additive Properties of Modal Density for Composite Structures," Paper DD-11, Presented at the 74th Meeting of the ASA, Miami, Fla., March 1967
- 7 V.Z.Vlasov, General Theory of Shells and Its Applications in Engineering, NASA TT-F-99, Washington, D.C., 1949
- 8 V.G.Godzevich, "Free Vibrations of Circular Conic Shells," pp.339-343, NASA TT-F-341, Washington, D.C., 1962

DYNAMIC RESPONSE OF STRUCTURAL SHIELD TO A TRAVELING PRESSURE PULSE

A. M. Rodriguez and P. N. Mathur
The Aerospace Corporation
San Bernardino, California

A simplified quasi-static plate theory is presented for analyzing the dynamic response of an infinite plate half-space structural system subjected to a traveling side-on pressure pulse. The theory is applicable to the case of finite plate structure, and provides a method of calculation of the attenuation characteristics of the plate and the time histories of the stresses and motions transmitted to the foundation media. Validity of the theory has been checked against computer calculations based upon a more rigorous Fourier Transform solution and other known solutions.

INTRODUCTION

A concept utilizing a protective structural shield as a means of reducing the ground shock environment resulting from an expanding nuclear air blast pulse was investigated by the authors. Basically this technique introduces a high impedance structural plate on the ground surface to attenuate to low values the critical environment associated with the air-induced ground shock (ground or foundation peak stresses, velocities, and accelerations).

The general analytical problems of wave propagation in layered media have been extensively treated in the literature on seismology, acoustics, and electromagnetic wave theory [1] through [5]. However, there appear to be few publications dealing with the problem of traveling pressure pulse on a layered elastic half-space. The basic solution to the problem of a traveling load on a half-plane was introduced as early as 1904 by Lamb [6]. Sackman [7] treated the problem of multilayer media for the superseismic condition (traveling pulse velocities greater than the seismic velocity of both the plate media below) utilizing the ray-tracing technique for a progressively increasing number of shear and compressional waves.

A series of analytical investigations [8, 9] have been conducted to evaluate the effectiveness of the concept described above for superseismic and subseismic regimes. This paper presents some of the results of these investigations.

NOMENCLATURE

a	acceleration
C_p, C_s	seismic velocity, P-wave, S-wave
E	Modulus of elasticity
h	plate or layer thickness
I	impulse
k_n	Brode profile constants
p	airblast overpressure
p_a	steady moving load approximation
p_o	peak overpressure
p_s	interface pressure
P^*	foundation plasticity index
t	time
u	particle displacement in the half-space medium
u_x	horizontal displacement
u_z	vertical displacement
U	air shock velocity

v	particle velocity in the half-space medium
v_x	horizontal velocity
v_z	vertical velocity
w	vertical displacement of the plate
x, z	plane coordinates
α	U/C_p Mach number for P-wave
β	U/C_s Mach number for S-wave
ϵ	strain
ν	Poisson's ratio
ρ	density
σ	direct stress
τ	shear stress
ϕ	displacement potential, P-wave
ψ	displacement potential, S-wave

Subscript

a	refers to overpressure pulse
x	refers to quantities in horizontal direction
z	refers to quantities in vertical direction
s	refers to plate half-space interface
p	refers to plate shield

ANALYSIS OF QUASI-STATIC PLATE THEORY

Figure 1 illustrates an infinite plate half-space structural system subjected to a side-on pressure pulse $p(x, t)$ traveling with a velocity U . For a nuclear or high explosive surface burst, the airblast wave expands and the magnitude of the pressure pulse decreases with increasing distance x from ground zero. However, for a finite structural plate, the transit time (time for the pulse to engulf the plate) is negligibly small and the variation in the magnitude of the pulse during transit can be neglected. The actual airblast pulse is thus replaced by the steady moving pulse

$$p_a(t - x/U) = p(x_p, t - x/U)$$

where x_p is the location of the center of the plate from ground zero. The dynamic response of the plate half-space structural system for this case can be analyzed in two steps. First, the pressure $p_s(x, t)$ transmitted by the plate to the surface of the ground is determined by analyzing the motion of the plate on the half-space foundation. Second, the disturbances induced in the foundation media are determined by analyzing its response to the surface pressure loading p_s .

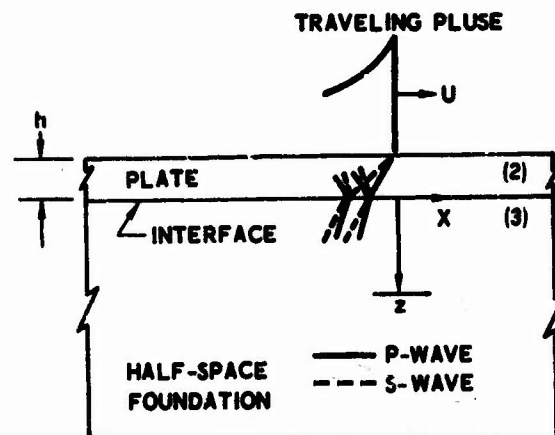


Figure 1. Analytical Model of Plate Half-Space Foundation.

Plate Elastic Half-Space Structural System

Equation of Motion

The equation of motion for an elastic plate of thickness h on an elastic half-space foundation, in terms of the vertical displacement $w(x, t)$ of the plate, is given as*

$$\rho_p h \frac{\partial^2 w}{\partial t^2} + D \frac{\partial^4 w}{\partial x^4} - I_o \rho_p \frac{\partial^4 w}{\partial x^2 \partial t^2} + \rho C_p \frac{\partial w}{\partial t} = p_a(t - x/U) \quad (1)$$

where $p_a(t - x/U)$ is the blast pulse loading and the subscript p refers to the quantities associated with the plate. Here, D and I_o are the flexural stiffness and the rotary moment of inertia of the plate respectively. Other symbols appearing in the above and following equations are defined in the Nomenclature.

This equation can be rewritten in terms of the time coordinate t , noting that $\partial/\partial x = -(1/U)(d/dt)$:

$$\frac{d^2 w}{dt^2} + \left[\frac{D}{\rho_p h U^4} - \frac{I_o}{h U^2} \right] \frac{d^4 w}{dt^4} + \frac{\rho C_p}{\rho_p h} \frac{dw}{dt} = \frac{p_a(t)}{\rho_p h}$$

The coefficient of the second term of this equation is small compared to the coefficients of the other terms and, if this term is neglected, the equation of motion is simplified considerably. An examination of the superseismic solution, with the second term included, indicated that this term introduces only small high frequency damped oscillations ahead of the ground shock. Hence, for predicting the medium structure interaction behavior, the second term of Eq. (2) can be dropped

*The equation is analogous to that for the beam on an elastic foundation [10, 11].

without introducing a significant error.

The vertical stress σ_z , or the pressure p_s , transmitted to the surface of the elastic half-space media is related to the vertical particle velocity v_z and the vertical particle displacement u_z of the media by the relation

$$p_s = \sigma_z = \rho C_p v_z = \rho C_p \frac{du_z}{dt} \quad (3)$$

Since the vertical displacements of the plate and the surface of the half-space foundation are continuous ($w = u_z$), Eq. (3) can be rewritten in the form

$$p_s = \sigma_z = \rho C_p \frac{du_z}{dt} \quad (4)$$

Based on the simplification considered above, Eq. (2) in conjunction with Eq. (4) reduces to the form

$$\frac{dp_s}{dt} + k' p_s = k' p_a(t) \quad (5)$$

where

$$T = \frac{1}{k'} = \frac{\rho_p h}{\rho C_p} \quad (6)$$

is the characteristic response time of the system. This plate equation can be readily solved for an arbitrary pressure pulse $p_a(t)$. The calculations presented in this paper pertain to the special case of a decaying step pulse.

Airblast Pulse

The decaying airblast pulse for a nuclear or high explosive surface burst is defined by Brode [12] as the sum of three exponential functions

$$p_a(t) = p_o \left(1 - \frac{t}{t_o}\right) \sum_{n=1}^3 A_n e^{-k_n t} \quad (7)$$

where p_o is the peak overpressure of the pulse and t_o is the duration of the positive phase of the pulse. The coefficients A_n and k_n for nuclear blast are defined in Reference 12.

A simplified form of the pressure pulse that can approximate the early time history (peak loading phase) of the Brode pulse Eq. (7) can be defined as

$$p(t) = p_o e^{-kt} \quad (8)$$

where p_o is the peak overpressure.

Plate Half-Space Interaction Pressure: Brode Pulse Solution

For the airblast overpressure pulse load described by Brode Eq. (7), Eq. (5) yields the solution:

$$p_s = p_o \sum_{n=1}^3 \frac{A_n}{\left(1 - \frac{k_n}{k'}\right)} \left[\left(1 + \frac{1}{(k' - k_n)t_o}\right) \left(e^{-k_n t} - e^{-k' t} \right) - \frac{t}{t_o} e^{-k_n t} \right] \quad (9)$$

The accumulated impulse required to calculate the displacements at the plate half-space interface is given as

$$I_s = p_o \sum_{n=1}^3 \frac{A_n}{k_n} \left[\left(1 - \frac{1}{k_n t_o}\right) \left(1 - e^{-k_n t}\right) + \frac{t}{t_o} e^{-k_n t} \right] - p_s/k' \quad (10)$$

Exponential Pulse Solution

For the simplified exponential pulse loading defined by Eq. (8), the solution of Eq. (5) yields

$$\frac{p_s}{p_o} = \frac{e^{-kt} - e^{-k't}}{1 - (k/k')} \quad (11)$$

The maximum value of the interface pressure p_s occurs at time t as defined by:

$$t_{\sigma} = (\ln k - \ln k') / (k - k')$$

and has the value

$$p_{s \max} = p_o e^{-k t_{\sigma}} \quad (12)$$

It should be noted that other loading pulse shapes can be constructed by linear superposition of the exponential pulses Eq. (8). For the elastic case, the solutions Eq. (11) can be superimposed accordingly to determine the response of the system to other pulse shapes.

Induced Stresses and Motions in Half-Space Foundation

The stresses and motions induced in the foundation medium can be calculated by analyzing the response of the medium to the surface load p_s . For the elastic half-space, the following wave solutions, in terms of the displacement functions, can be employed:

$$\phi = \phi \left(t - \frac{x}{U} - \frac{z}{U} \sqrt{\alpha^2 - 1} \right) \text{ for P-wave} \quad (13)$$

$$\psi = \psi \left(t - \frac{x}{U} - \frac{z}{U} \sqrt{\beta^2 - 1} \right) \text{ for S-wave} \quad (14)$$

where the coordinate x, z refer to Figure 2 which also illustrates the case of an unprotected half-space (without a structural plate).

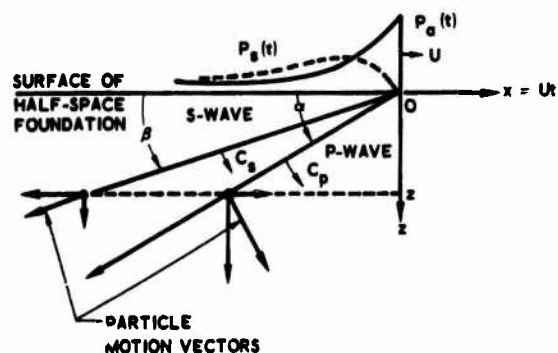


Figure 2. Free Field Induced in an Elastic Foundation with and without Plate Protection.

The field quantities (particle displacements, u ; velocities, v ; and stresses, σ , τ) at any point in the half-space are defined as follows:

$$u_x = \frac{\partial \phi}{\partial x} - \frac{\partial \psi}{\partial z} = -\frac{1}{U} \left(\phi' - \sqrt{\beta^2 - 1} \cdot \psi' \right) \quad (15)$$

$$u_z = \frac{\partial \phi}{\partial z} + \frac{\partial \psi}{\partial x} = -\frac{1}{U} \left(\psi' + \sqrt{\alpha^2 - 1} \cdot \phi' \right) \quad (16)$$

$$v_x = -\frac{1}{U} \left(\phi'' - \sqrt{\beta^2 - 1} \cdot \psi'' \right) \quad (17)$$

$$v_z = -\frac{1}{U} \left(\psi'' + \sqrt{\alpha^2 - 1} \cdot \phi'' \right) \quad (18)$$

$$\begin{aligned} \sigma_z &= \rho \left[C^2 \left(\frac{\partial u_x}{\partial x} + \frac{\partial u_z}{\partial z} \right) - 2b^2 \frac{\partial u_x}{\partial x} \right] \\ &= \rho \left[\left(1 - \frac{2}{\beta^2} \right) \phi'' + \frac{2}{\beta^2} \sqrt{\beta^2 - 1} \cdot \psi'' \right] \end{aligned} \quad (19)$$

$$\begin{aligned} \sigma_x &= \rho \left[C^2 \left(\frac{\partial u_x}{\partial x} + \frac{\partial u_z}{\partial z} \right) - 2b^2 \frac{\partial u_z}{\partial z} \right] \\ &= \left(1 - \frac{2\alpha^2}{\beta^2} \right) \sigma_z - \frac{4}{\beta^2} \left(1 - \frac{\alpha^2}{\beta^2} \right) (\rho U u_x) \end{aligned} \quad (20)$$

$$\begin{aligned} \tau_{xz} &= \rho b^2 \left(\frac{\partial u_x}{\partial z} + \frac{\partial u_z}{\partial x} \right) \\ &= \rho \left[\frac{2}{\beta^2} \sqrt{\alpha^2 - 1} \cdot \phi'' - \left(1 - \frac{2}{\beta^2} \right) \psi'' \right] \end{aligned} \quad (21)$$

where the primes denote differentiation with respect to the arguments of the functions ϕ and ψ .

Equation (20) states that σ_x is a linear combination of σ_z and v_x and is obtained by virtue of the relation $\frac{\partial}{\partial t} = -U \frac{\partial}{\partial x}$ for a steady moving load.

If ϕ_0 and ψ_0 are denoted as the value of ϕ and ψ at the surface of the half-space ($z = 0$), then, as a consequence of the boundary conditions

$$\begin{aligned} \tau_{xz_0} &= 0, \quad \sigma_{z_0} = -p_s \\ \phi_0'' &= - \left(1 - \frac{2}{\beta^2} \right) \cdot \left(\frac{1}{\rho \delta} \right) \cdot p_s \\ \psi_0'' &= - \left(\frac{2}{\beta^2} \cdot \sqrt{\alpha^2 - 1} \right) \cdot \left(\frac{1}{\rho \delta} \right) \cdot p_s \end{aligned} \quad (22)$$

where

$$\delta = \left(1 - \frac{2}{\beta^2} \right)^2 + \frac{4}{\beta^4} \sqrt{\beta^2 - 1} \cdot \sqrt{\alpha^2 - 1} \quad (23)$$

If the accumulated impulse is denoted as

$$I_s(t) = \int_{-\infty}^t p_s(t) \cdot dt \quad \text{and} \quad \begin{aligned} \xi &= \left(t - \frac{z}{U} \sqrt{\alpha^2 - 1} \right) \\ \eta &= \left(t - \frac{z}{U} \sqrt{\beta^2 - 1} \right) \end{aligned} \quad (24)$$

then the displacement time histories at depth z along the vertical line $x = 0$ are given as:

$$u_x = A \left(\frac{I_s(\xi)}{\rho U \delta} \right) - B \left(\frac{I_s(\eta)}{\rho U \delta} \right) \quad (25)$$

$$u_z = A \sqrt{\alpha^2 - 1} \left(\frac{I_s(\xi)}{\rho U \delta} \right) + \frac{B}{\sqrt{\beta^2 - 1}} \cdot \left(\frac{I_s(\eta)}{\rho U \delta} \right) \quad (26)$$

where

$$\begin{aligned} A &= \left(1 - \frac{2}{\beta^2} \right) \\ B &= \frac{2}{\beta^2} \sqrt{\alpha^2 - 1} \cdot \sqrt{\beta^2 - 1} \end{aligned}$$

and the remaining field quantities are given as:

$$v_x = A \left(\frac{p_s(\xi)}{\rho U \delta} \right) - B \left(\frac{p_s(\eta)}{\rho U \delta} \right) \quad (27)$$

$$v_z = A \sqrt{\alpha^2 - 1} \left(\frac{p_s(\xi)}{\rho U \delta} \right) + \frac{B}{\sqrt{\beta^2 - 1}} \cdot \left(\frac{p_s(\eta)}{\rho U \delta} \right) \quad (28)$$

$$-\sigma_z = A^2 \left(\frac{p_s(\xi)}{\delta} \right) + \frac{2B}{\beta^2} \left(\frac{p_s(\eta)}{\delta} \right) \quad (29)$$

$$-\sigma_x = A \left(1 - \frac{2\alpha^2 - 2}{\beta^2} \right) \left(\frac{p_s(\xi)}{\delta} \right) - \frac{2B}{\beta^2} \cdot \left(\frac{p_s(\eta)}{\delta} \right) \quad (30)$$

$$-\tau_{xz} = A \left(\frac{2}{\beta^2} \cdot \sqrt{\alpha^2 - 1} \right) \left[\frac{p_s(\xi)}{\delta} - \frac{p_s(\eta)}{\delta} \right] \quad (31)$$

If we set $z = 0$ in Eq. (28), the vertical velocity on the surface of the half-space becomes

$$v_z(t) = \frac{\sqrt{\alpha^2 - 1}}{\alpha \delta} \cdot \left(\frac{p_s(t)}{\rho C_p} \right) \quad (32)$$

Quasi-Static Plate Theory (Inelastic Foundation)

General Inelastic Media

The quasi-static plate solution can be extended to include the inelastic behavior of the foundation, represented by a general stress-strain relation

$$\epsilon = f(p_s); \quad \frac{d\epsilon}{dp_s} = f'(p_s) \quad (33)$$

The relation between the vertical velocity and the pressure at the surface of the inelastic half-space for the loading phase can be derived from the differential equations of the characteristics of the disturbances in the hodograph and physical planes. The resulting relationship is given by

$$\frac{dv_z}{dt} = \sqrt{f'} / \rho \cdot \frac{dp_s}{dt} \quad (34)$$

The equation of motion Eq. (5) for the inelastic foundation then modifies to the form

$$\frac{dp_s}{dt} = \frac{1}{\rho_p h} (p_a(t) - p_s) \sqrt{\frac{\rho}{f'}} \quad (35)$$

The nonlinear differential equation can be solved by numerical integration with the initial condition $p_s(0) = 0$. The solution must, however, be terminated at the end of the pulse-loading phase since Eq. (35) is not valid for the unloading phase.

Elastoplastic Media

The equation of motion can be linearized if the stress-strain behavior of the foundation medium is represented by an analytical expression (elasto-plastic relation)

$$\epsilon = f(p) = \frac{(\phi/E_0)}{(1 - p/p^*)} ; \left(\frac{d\epsilon}{dp}\right) = f' = \frac{1}{E_0(1 - p/p^*)^2} \quad (36)$$

where p^* is the foundation plasticity index and E_0 is the initial modulus of the foundation material as defined in Figure 3.

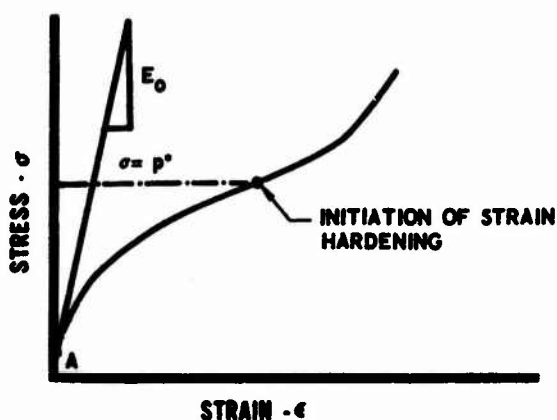


Figure 3. Elastoplastic Stress-Strain Representation for Inelastic Foundation.

Substitution of f' from Eq. (36) into Eq. (35) yields

$$\frac{dp_s}{dt} = k' \left(\frac{1 - p}{p^*} \right) (p_a(t) - p_s) \quad (37)$$

which can be reduced to a linear ordinary differential equation if we perform the substitution

$$p = p^* \left(1 - \frac{1}{y} \right) \quad (38)$$

Equation (37) then becomes

$$\frac{dy}{dt} + k' \left(1 - \frac{p_a(t)}{p^*} \right) y = k'$$

subject to the initial condition $y(0) = 1$. The solution of this equation is readily obtained by quadrature [9].

RESULTS AND DISCUSSION

Comparison of the Theory with Other Solutions

The validity and accuracy of the quasi-static plate theory can be checked against exact solutions obtained for special cases. Figure 4 presents a comparison of the response (interface pressure) of a liquid layer on an elastic half-space to a step wave based on the exact solution (superseismic case) and the quasi-static plate theory solution. The liquid layer in this case is essentially an elastic layer of zero shear strength. It is noted that the two results are in good agreement. The step increments in the interface pressure for the exact solution represent the cumulative pressure increments resulting from the multiple reflections of the superseismic waves within the liquid layer (zero-shear elastic plate). The quasi-static solution, on the other hand, represents an averaged cumulative pressure increase.

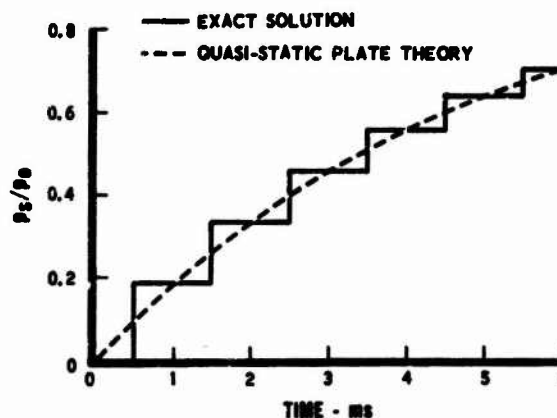


Figure 4. Comparison of Quasi-Static Plate Theory with Exact Solution for Liquid Elastic Layer Half-Space System, Subjected to a Non-decaying Step Pulse.

The quasi-static plate theory was further checked, for the elastic case, against the computer solutions based upon a rigorous Fourier Transform solution. Figure 5 shows a typical case comparing the two solutions. It is noted that, except for some oscillatory disturbances ahead of the primary wave, the two solutions are in good agreement. These oscillatory disturbances represent the contribution of the plate flexure (neglected in the plate theory).

Typical Results

Figures 6 through 11 present typical comparative time histories of the stresses and motions transmitted to the half-space medium for the protected (with structural plate shield) and the unprotected conditions. In all cases except where noted, the data given in Table 1 are used for numerical calculations.

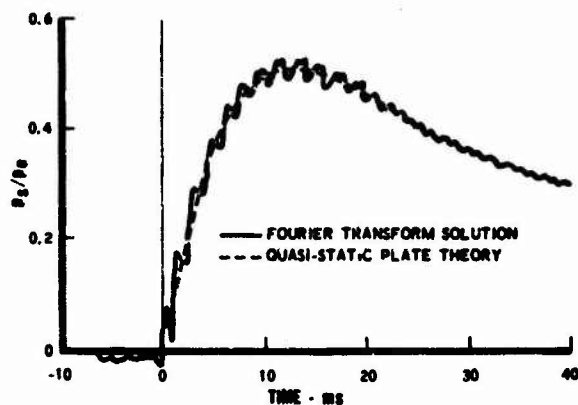


Figure 5. Comparison of Quasi-Static Plate Theory with Fourier Transform Solution for Interface Pressure for an Infinite Plate Elastic Half-Space System.

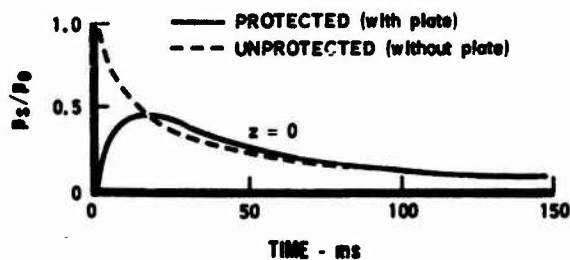


Figure 6. Vertical Stress Time Histories at the Surface of Elastic Space Foundation with and without Plate Protection.

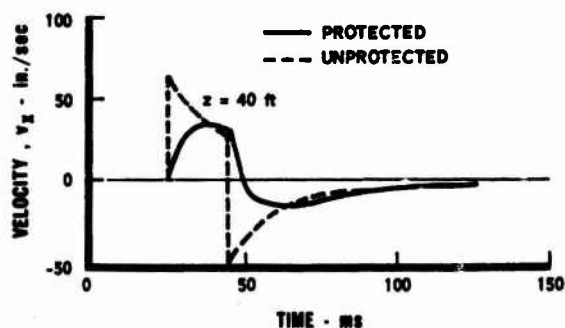


Figure 7. Horizontal Particle Velocities in the Elastic Foundation at 40-Foot Depth (Velocity is zero at surface, $z = 0$).

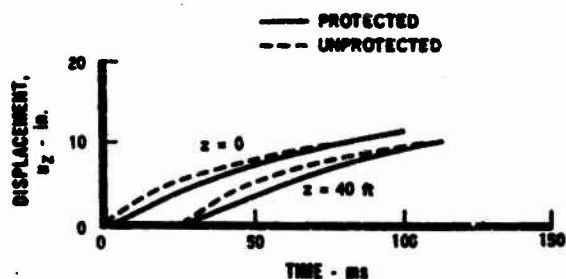


Figure 8. Vertical Particle Displacements in the Elastic Foundation at Surface and at a 40-Foot Depth.

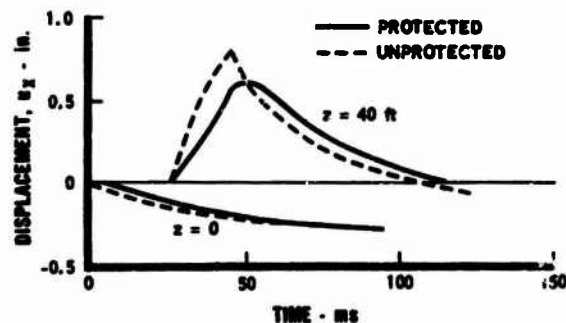


Figure 9. Horizontal Particle Displacements in the Elastic Half-Space Foundation at the Surface and 40-Foot Depth.

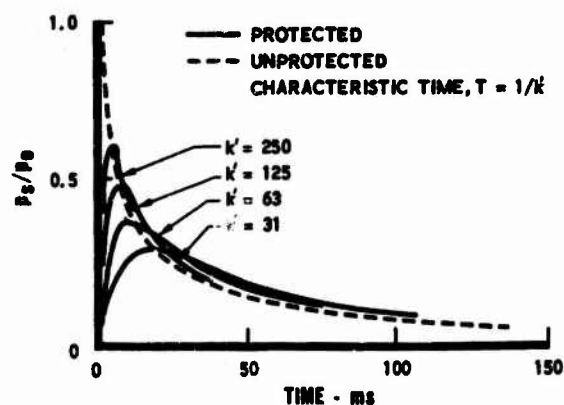


Figure 10. Interface Pressure Time Histories for Parametric Values of k' for Plate Elastic Half Space System.

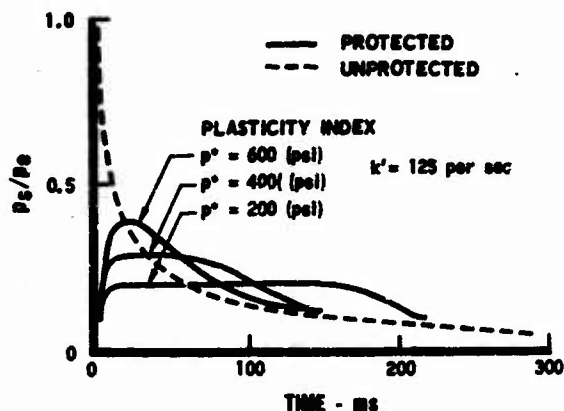


Figure 11. Interface Pressure Time Histories for Parametric Values of the Plasticity Index for Inelastic Foundation Media.

Item	Value
Plate Thicknesses	6 ft
Plate Material	8000 fps seismic velocity
Foundation Medium	1500 fps seismic velocity
Plate Foundation Medium Density Ratio	2.0
Plate Foundation Interface	Not bonded; free to slip
Pressure Pulse	1000-psi Brode pulse

Table 1. Structural Properties of the Plate on a Half-Space System.

Figure 6 presents a comparison of the time histories of the vertical stress at the plate-foundation interface for the elastic medium for the protected and the unprotected cases. It is noted that the peak pressure is reduced roughly by a factor of 2 at the interface due to the protection provided by the plate. The stress time histories are identical at other locations in the medium below the interface except for the time lag. Similar conclusions are derived for the vertical particle velocity since, for elastic media, the vertical velocity is directly proportional to the vertical stress.

Figure 7 shows a similar attenuation in the peak horizontal velocity as a result of the protection provided by the plate. The reversal in the direction of the particle velocity in this case is due to the contribution of the shear wave which lags the primary compression wave, as may be noted in Figure 2. Figures 8 and 9 show that the plate does not provide any significant reduction in the peak particle displacements in the foundation.

The effect of the characteristic response time T , defined by Eq. (6), on the attenuation of the peak

pressure is given in Figure 10. The attenuation of the peak pressure increases with increasing mass per unit area of the plate and decreases with increasing impedance of the foundation. The interface pressure builds up due to transmitted impulses resulting from the multiple reflections of the waves in the structural plate. The attenuation of peak pressure will therefore be larger for shorter duration pulses.

Figure 11 illustrates the effect of the foundation inelasticity on the attenuation of the peak pressure.

REFERENCES

1. M. Ewing, W. Jardetzky, and F. Press, Elastic Waves in Layered Media, McGraw-Hill Book Company, Inc., New York. (1957)
2. R. Stoneley, Proceedings of the Royal Society of London, Series a, Volume 106, p. 15 (1924).
3. P. G. Bergmann, "The Wave Equation in Medium with Variable Index of Refraction," Journal of the Acoustical Society of America, Volume 17, p. 329 (1946).
4. B. Salzberg, "Propagation of Electromagnetic Waves through a Stratified Media," Journal of the Optical Society of America, Volume 49, p. 465 (1950).
5. L. M. Brekhovshilch, Waves in Layered Media, ed. by F. N. Frenkel, Academic Press, New York, New York (1960)
6. H. Lamb, Philosophical Transaction of the Royal Society of London, Series A, Volume 203, p. 1 (1904).
7. J. L. Sackman, "Uniformly Moving Load on a Layered Half Plane," Transactions of the American Society of Civil Engineers, Volume 13, 1p. 404 (1948).
8. P. Mathur and A. Rodriguez, A Protective Concept for Hardness Improvement of Ground Systems Design, TOR-669(S6923-24)-1, The Aerospace Corporation., San Bernardino, California (November 1965).
9. A. Rodriguez and P. Mathur, Dynamic Response of Shock Shield to Nuclear Air Blast Pulse, ATM-67(s2930-31)-2, The Aerospace Corporation, San Bernardino, California, (January 1967).
10. Private communication from S. B. Batdorf to P. Mathur and A. Rodriguez, June 1965.
11. C. Harris and C. Crede, Shock and Vibration Handbook, Volume 1, "Basic Theory and Measurements," McGraw Hill Book Company, Inc., New York, New York, (1961).
12. H. L. Brode, A Review of Nuclear Explosion Phenomena Pertinent to Protective Construction, R-425-PR, The Rand Corporation, Santa Monica, California (May 1964).

ANALYSIS OF THE RELATIVE MOTION OF THE PEM MOD-IV TETHERED CANISTER AND THE ATLAS BOOSTER

Thomas L. Alley
The Aerospace Corporation
San Bernardino, California

ABSTRACT

The relative motion of the Atlas booster and a tethered PEM Mod-IV canister was analyzed for the period subsequent to canister deployment. This was accomplished by writing the equations of motion of the system and solving these equations on a digital computer. The solution of numerous cases indicated that, if early booster/canister collision could be avoided, the canister tended to remain as far away as possible from the booster.

Introduction

The PEM Mod-IV is a particular auxiliary payload ejection mechanism for use on Atlas boosters. This device consists of an orientable launch tube from which a canister is ejected by means of pressurized gas. The launch tube is in a stowed configuration pointing aft on the vehicle and enclosed by a shroud during launch. The shroud is ejected and the launch tube is oriented by means of its orienting mechanism after the booster has left the dense atmosphere and during the sustainer engine firing. The canister ejection sequence is initiated just after vernier engine cutoff and primary reentry vehicle separation. The canister opens after exit from the launch tube and releases the auxiliary payload. The tether brake, by means of a steel cable connecting the brake and the canister, then brakes the canister to a stop relative to the booster. This process is indicated schematically in Figure 1.

It is a requirement that extraneous bodies or fragments not be present in such a position as to interfere with radar observation of the payload during reentry. Thus, it is important that the tether cable not fail and permit the canister to reenter with the payload. Also, the canister should not strike the booster as this might cause the booster to explode, filling the area with fragments.

As it is important to avoid collision between the Atlas booster and the canister, any solution procedure must incorporate the possibility of the tether

cable being wrapped onto the surface of the booster. It was suspected that the cable would simply be wound onto the rolling booster until collision was inevitable. The provision for booster wrap was one of the difficult aspects of the study.

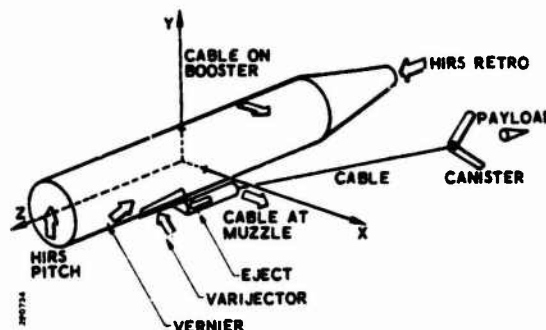


Figure 1. Schematic of Payload Deployment by Means of PEM Mod-IV

Analysis

The booster was idealized as a smooth, frictionless, cylindrical body of finite length. Various disturbing forces and moments act on this body. As it was desired to permit the booster to move in a general manner, the booster was

permitted to have three rotational and three translational degrees of freedom. Since the normal booster axes are nonprincipal axes, the rotational equations of motion have the form

$$\left. \begin{aligned} I_{xx} \dot{\omega}_x - I_{xy} \dot{\omega}_y - I_{xz} \dot{\omega}_z - I_{yz} (\omega_y^2 - \omega_z^2) \\ + (I_{xy} \omega_z - \omega_y I_{xz}) \omega_x - (I_{yy} - I_{zz}) \omega_y \omega_z = L_x \\ - I_{xy} \dot{\omega}_x + I_{yy} \dot{\omega}_y - I_{yz} \dot{\omega}_z - I_{xz} (\omega_z^2 - \omega_x^2) \\ + (I_{yz} \omega_x - \omega_z I_{xy}) \omega_y - (I_{zz} - I_{xx}) \omega_z \omega_x = L_y \\ - I_{xz} \dot{\omega}_x - I_{yz} \dot{\omega}_y + I_{zz} \dot{\omega}_z - I_{xy} (\omega_x^2 - \omega_y^2) \\ + (I_{xz} \omega_y - \omega_x I_{yz}) \omega_z - (I_{xx} - I_{yy}) \omega_x \omega_y = L_z \end{aligned} \right\} \quad (1)$$

where

x, y, z are axes imbedded in the booster,
 I_{xx} , etc. are inertia coefficients,
 ω_x , etc. are angular velocity components along x, y, z , and
 L_x , etc. are applied moment components along x, y, z .

The translational equations of motion for the booster have the form

$$m \begin{Bmatrix} \ddot{X} \\ \ddot{Y} \\ \ddot{Z} \end{Bmatrix} = A \begin{Bmatrix} F_x \\ F_y \\ F_z \end{Bmatrix}, \quad (2)$$

where

m = mass of the booster,
 \ddot{X} , etc. are inertial accelerations,
 F_x , etc. are applied force components along x, y, z and
 A = rotation matrix to transform force components from the x, y, z system to the X, Y, Z inertial system.

The canister was idealized as a mass particle. Hence, its equations of motion have the same form as Equation (2).

The tether brake on which the tether cable was wound was modeled as a single-degree-of-freedom flywheel so that its equation of motion is of the form

$$I \ddot{\theta}_B = -\tau_C - \tau_B + r_2 F_{CAB} \quad (3)$$

where

I = effective brake moment of inertia,
 θ_B = brake rotation,
 τ_C = brake drag torque,

τ_B = desired brake torque,

r_2 = brake radius, and

F_{CAB} = tether-cable force just forward of the brake.

The specification of the parameters and forces of Equation (3) is rather involved; the reader is referred to a more complete exposition for details.^[1] The brake torque as a function of cable pay-out, x_{3BR} , is indicated in Figure 2. Braking of the canister is initiated at point A and the canister is braked to a stop at point B. The brake shoes are then mechanically disengaged which permits additional cable to be payed-out before braking begins during the HIRS jerk, to be defined below, at point C. In general, the tether cable is pressed against the launch tube rim during the period that the cable is in tension. As the rim is considered a rough friction surface, the specification of F_{CAB} is particularly complex.

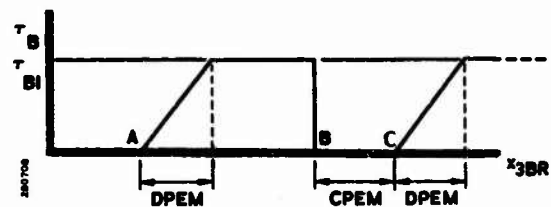


Figure 2. Braking Torque as a Function of Cable Pay-Out

There are various forces and moments which act on the booster and canister during the time period of interest. First, the cable force results in forces and moments on the booster which will appear in the right-hand sides of Equations (1) and (2). Also, the cable force will act on the canister. The magnitude of the cable force is computed by first computing the strain in the cable in the appropriate manner and then multiplying by an appropriate modulus.

A second disturbance is the vernier thrust. Although the vernier engines are cut off just prior to canister ejection, the tail-off thrust, acting through the vernier control system, exerts a significant effect on the booster motion.

A third disturbance is the gas eject force which forces the canister out of the launch tube. This obviously acts on both the booster and the canister.

A fourth disturbance is caused by the firing of two sets of small rocket motors mounted on the launcher base. The firing of the first set is intended to counteract the roll disturbance to the booster

[1] "Analysis of the Relative Motion of the PEM Mod-IV Tethered Canister and the Atlas Booster," by T. L. Alley, SAMSO TR-68-242, May 1968.

caused by the gas eject force and the second set is intended to counteract the roll disturbance caused by the braking force.

The last disturbance is the HIRS rocket firings. The HIRS system is intended to force the booster to a different trajectory from that of the payload so that the booster will not interfere with observation of the payload. A pitch-rocket fires, translating the booster upward and pitching it nose-down. After the booster has pitched through a predetermined angle, a retro-rocket fires, forcing the booster upward to a new trajectory. The tether cable has been slack during this period but it is suddenly drawn taut during the retro-rocket firing. This is called the HIRS jerk and represents a critical period in the functional life of the tether brake system.

Figure 3 is an end-on view of the Atlas booster showing the position of the muzzle and the canister.

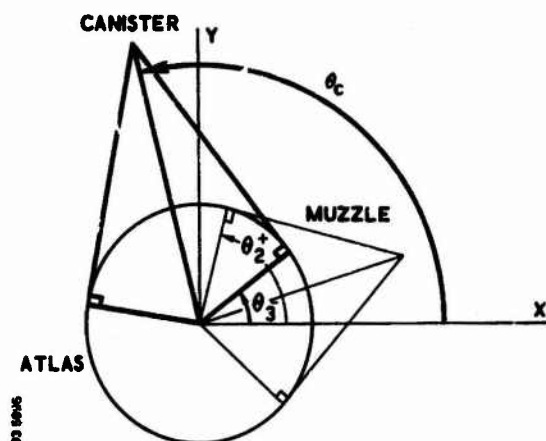


Figure 3. Geometry of Muzzle and Canister Positions

The angle θ_c tracks the angular position of the canister. Thus, not only the instantaneous position of the canister is known, but also the path traversed to reach that position. This is important as the tether cable trails along behind the canister. It is obvious from the figure that if θ_3 is greater than θ_2 , then the canister does not have a direct line-of-sight to the muzzle. A condition of "intersection" is then said to exist. It is postulated that the cable always assumes the minimum path-length position between the canister and the muzzle for purposes of computing the cable force. In the absence of a direct line-of-sight, the cable must assume a curved path, with a portion of the cable lying on the booster surface. It was hypothesized that this curved minimum path consists of

- a straight portion from the muzzle to the rear contact point on the booster,
- a helix on the booster from the rear contact point to the forward contact point, and
- a straight portion from the forward contact point to the canister.

If it is further assumed that path smoothness exists at the two contact points, then sufficient information is available to find the length of this curved minimum path. The path length is compared to the expended cable to compute cable strain. Since the booster is assumed frictionless, the cable force is constant everywhere forward of the muzzle, even though a portion of the cable is in contact with the booster.

Computer Program

The equations of motion were programmed for a digital computer and solved as an initial-value problem with a fourth-order Runge-Kutta integration procedure. The program was written in modular form, with subroutines performing specialized functions. Both printed and plotted output were obtained from the program.

The flow chart for the subroutine that sets the equations of motion for the period when the canister has exited the launch tube is shown in Figure 4. The equations are first set assuming zero cable force. Then tests for intersection are made. If there is no intersection, the possibility of a cable force is investigated. If there is a cable force, this force is added in the appropriate equations and the procedure is complete. The curved-cable path must be used in the case of intersection, but the logic flow is the same as the straight-cable path.

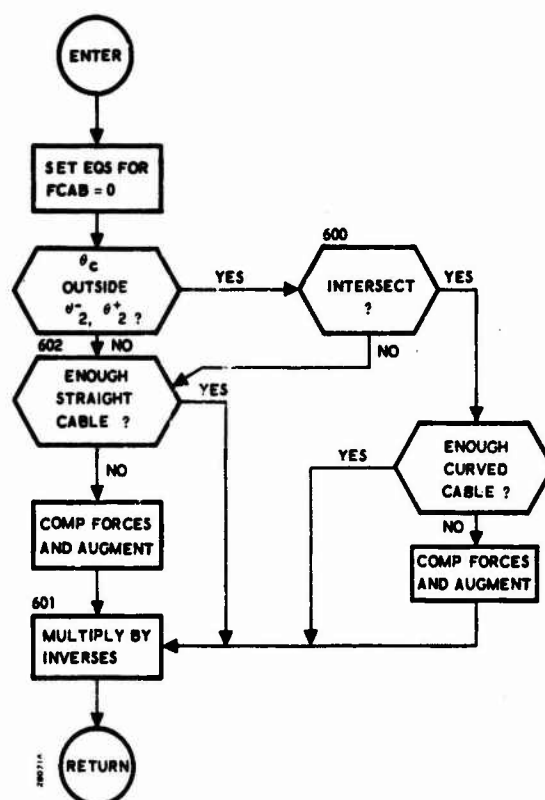


Figure 4. Logic Flow for Subroutine to Set Equations of Motion

Results

The first flight configuration analyzed by means of the developed program was a 50-pound payload launched at 40 ips from an Atlas D/Chalktalk missile. The launch direction was chosen as upward and forward from the booster. The canister weight was 110 pounds and the tether cable was 3/16-in. steel braided aircraft cable.

The most severe cable loads are experienced during HIRS jerk. This load history is shown in Figure 5. The process is one repeatedly of

- the cable becoming taut, applying a torque to the brake, and
- the brake accelerating and paying out cable so rapidly that the cable becomes slack for a time.

As the failure load for this cable is about 900 pounds, the program predicts survival of the cable.

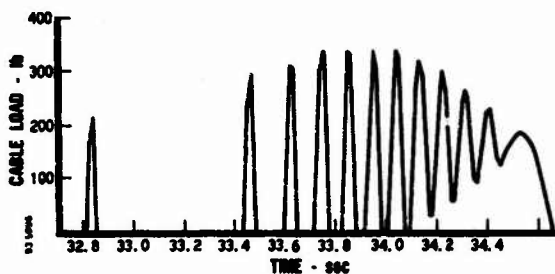


Figure 5. Load in Tether Cable during HIRS Jerk

Figure 6 indicates the initial phase of the canister motion subsequent to ejection. The process is displayed in booster-fixed coordinates, so that the booster appears fixed and the canister is in motion. A side view and head-on view are presented of the same motion. The triangles denote the position of the canister at one-second intervals, with "T" denoting the first position and "L" denoting the last position on a given chart. The line merely connects the canister positions. Here are displayed the initial rapid ejection, braking of the canister to a stop, and rebound toward the booster. The canister path in the side view is curved because the

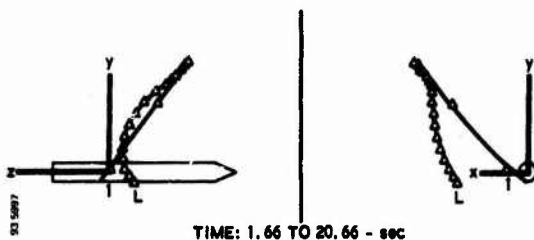


Figure 6. Initial Phase of Canister Motion Showing Ejection and Rebound

booster is now starting to pitch in the HIRS maneuver. The path is curved and offset in the head-on view because the booster is rolling and translating laterally.

Figure 7 is a continuation of the motion of Figure 6. This covers the period of retro-fire (the first break in the curve) and HIRS jerk (the second break in the curve).

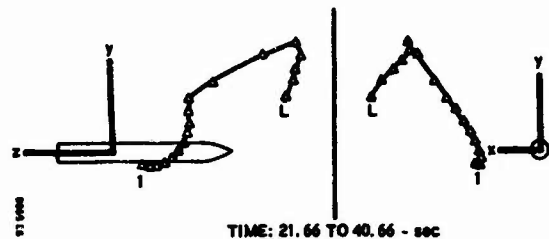


Figure 7. Continuation of Initial Phase of Canister Motion Showing HIRS Jerk

After the initial phase, the canister enters a somewhat stable phase of motion in which it tends to remain as far from the booster as possible, usually off the forward end or off the aft end. Figure 8 shows typical motion off the forward end of the booster. Figure 9 shows typical motion off the aft end of the booster. Figure 10 indicates a transition phase as the canister moves toward the forward end, but still remains at a large distance from the booster.

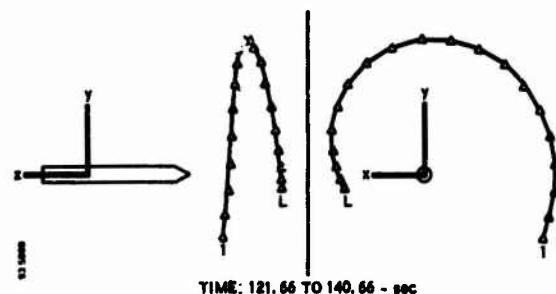


Figure 8. Intermediate Phase of Canister Motion Indicating Motion at Front of Booster

Very little wrap-up of the cable onto the booster occurred in this problem. Other runs indicated as much as two complete wraps before unwrapping began.

It was concluded that collision would not occur for at least 400 seconds after deployment for the present problem. This was judged a sufficient interval of time.

In all of the cases investigated, it was found that if early collision could be avoided, the canister

tended to remain away from the booster. A late-time collision was never obtained. In certain applications an early-time collision was obtained. In these latter cases the launch parameters were altered to avoid early collision.

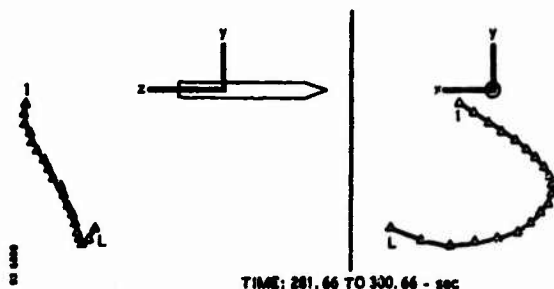


Figure 9. Late Phase of Canister Motion Indicating Motion at Rear of Booster

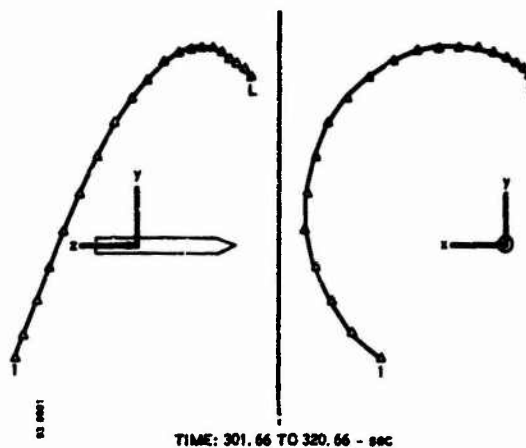


Figure 10. Late Phase of Canister Motion Showing Transition from Rear to Front

Conclusion

A computer program was developed to analyze the relative motion of the PEM Mod-IV canister and the Atlas booster. The program was initially applied to a proposed launch configuration on an Atlas D booster. The results indicated that the tether system would remain intact and that if

collision were to occur it would not take place until well after payload ejection. Application of the program to later flights resulted in changes to launch parameters in order to avoid collision. The results of many computer runs indicate that, if early-time collision can be avoided, the canister tends to remain at the end of the tether, as far away from the booster as possible.